Volcanic Gas Studies by Multi Axis Differential Optical Absorption Spectroscopy

Nicole Bobrowski

Dissertation
submitted to the
Combined Faculties for the Natural Sciences and for Mathematics
of the Ruperto Carola University of Heidelberg, Germany
for the degree of
Doctor of Natural Sciences

presented by
Diplom-Physicist: Nicole Bobrowski
born in: Hennigsdorf

Oral examination: 23.11.2005

Volcanic Gas Studies by Multi Axis Differential Optical Absorption Spectroscopy

Referees: Prof. Dr. Ulrich Platt
Prof. Dr. Mauersberger

Untersuchungen von Vulkangasemissionen mit Multi-Axis-DOAS

Die Chemie in Vulkanfahnen kann Einblicke in vulkanische Prozesses geben, welche die Vorhersage von Vulkanausbrüchen verbessern könnten. Als Quelle für Aerosole und Spurengase haben Vulkane ausserdem atmosphärische Relevanz und können signifikant das Klima beeinflussen. Obwohl beide Aspekte von grosser Wichtigkeit sind, ist die Chemie in Vulkanfahnen bisher unzureichend untersucht. Im Rahmen dieser Arbeit wurden Messungen mit Mini-MAX-DOAS Instrumenten an acht Vulkanen durchgeführt. Brommonoxid (BrO), Chlormonoxid (ClO), Chlordioxid (OClO), Formaldehyde (HCHO) und Schwefeldioxid (SO_2) Flüsse wurden bestimmt. Für BrO wurde ein globaler vulkanischer Fluss von 1.2-13 Gg/y berechnet. Der Fokus der Arbeit lag auf Messungen von BrO und SO_2. Das Verhältnis dieser beiden Spurengase wurde bezüglich verschiedener Vulkane, in Abhängigkeit vom Abstand zur Emissionsquelle und der Vulkanaktivität untersucht. Am Ätna konnten die verschiedenen Fahnen der aktiven Krater anhand ihrer unterschiedlichen Gaszusammensetzungen unterschieden werden. In unmittelbarer Kraternähe wurde kein BrO identifiziert. Experimentelle Studien des BrO/SO_2 Verhältnisses zeigten einen Anstieg mit steigender Distanz zur Quelle. ClO and OClO konnten zum ersten Mal als weitere reaktive Halogenspezies, neben BrO, in Vulkanfahnen identifiziert werden. Starke ClO Absorptionsstrukturen konnten schon in unmittelbarer Kraternähe beobachtet werden, aber nicht der beim BrO beobachtete Anstieg im Verhältnis zu SO_2 mit steigender Entfernung. Durch das in dieser Doktorarbeit neu entwickelte Mini-MAX-DOAS Instrument war es auch möglich für den Ollague Vulkan in Bolivien erstmals einen SO_2 Fluss zu bestimmen (2.2 t/d). Das weiteren wurde versucht erste Abschätzungen zur Lichtwegslänge in Vulkanfahnen durchzuführen, die die Unsicherheiten heutiger Auswerte- und Messtechniken deutlich machen.

Volcanic Gas Emission Studies by Multi Axis DOAS

The chemistry of volcanic plumes can give insights into volcanic processes, which could help with improving the forecast of volcanic eruptions and is also of atmospheric relevance as the volcanic source of aerosols and trace gases can have a significant climatic impact. Although both are very important aspects, the chemical processes in volcanic plumes are inadequately understood. In this thesis, measurements by ground based Mini-MAX DOAS systems were carried out to study gas emissions from eight volcanoes. Bromine monoxide (BrO), chlorine monoxide (ClO), chlorine dioxide (OClO), formaldehyde (HCHO) and sulphur dioxide (SO_2) abundances were measured. A global volcanic BrO flux of 1.2 - 13 Gg/y was determined. The study was focused on the measurements of BrO and SO_2. The ratio between both trace gases was investigated at different volcanic sites, as well as the dependence on the distance to the source and the volcanic activity. Additional attempts were made to distinguish the different summit craters of Mt. Etna. No BrO was detected in proximity of the active vents of the volcanoes. An experimental study of the increase of the BrO/SO_2 ratio with the aging plume was also conducted. ClO and OClO were measured in a volcanic plume for the first time. In contrast to BrO, ClO was detected near the volcanic source, and the distance dependency of ClO/SO_2 ratio did not exhibit the increase found for the BrO/SO_2 ratio. The miniaturized instrument developed in this thesis made possible to determine an SO_2 flux (2.2 t/d) for the remote volcano Ollague. The length of the average light path through a volcanic plume and the problems of determining it was discussed. A comparison between an SO_2 flux calculation assuming no scattering due to the volcanic plume and an SO_2 flux estimating the enhancement of light path by scattering in the plume illustrate the present uncertainty.

Contents

Chapter 1

Introduction

Volcanoes are a major source for a number of reactive atmospheric trace gases - in particular species containing sulphur and halogens. In fact, during the early ages of the earth, volcanic processes were mainly responsible for building up the atmosphere of our planet after the first atmosphere was "lost" [*Arthur* 2000]. Today volcanic emissions of gases and particles into our atmosphere still have local, regional and even global effects, on both short and longer time scales [*Robock* 2000; *Oppenheimer et al.* 2003; *Oman et al.* 2005].

Besides this very important influence on atmospheric composition, the released gases can also provide valuable information for the understanding of volcanic processes. It was shown recently that ratios between halogens and sulphur in plumes might serve as an indicator of changes in the activity of a volcano [*Oppenheimer et al.* 2003; *Aiuppa and Frederico* 2004; *Burton et al.* 2004], which, in turn, has implications for the prediction of volcanic activity. Therefore, it is very important to study the gas composition and the chemistry within volcanic plumes.

One powerful class of methods are optical remote sensing techniques. After early developments marked by COSPEC (correlation spectrometer) instruments [*Millán et al.* 1969; *Davies* 1970] in the end of 1960s, which could measure only one trace gas at time; especially the development of remote sensing techniques which can simultaneously measure several trace gases, as the Differential Optical Absorption Spectroscopy (DOAS), [*Platt* 1994] or Fourier Transform Infrared Spectroscopy (FTIR) (e.g. *Notsu et al.* [1993]) became very interesting for the research of volcanic gases. During the last decade significant progress has been made, for example new observation geometries were introduced and adapting these instruments for field measurements in the rough and hostile environments usually prevailing around volcanoes. Since the first DOAS measurements near a volcano were performed in Italy by *Edner et al.* [1994], size and weight of available spectrometers and the power consumption of the DOAS instruments have decreased dramatically. With the DOAS method, applied in this thesis, several trace species (which are not all emitted by

volcanoes in large quantities) can be observed, including SO_2, CS_2, NO_2, HCHO, BrO, ClO and OClO. This work focusses on the determination of SO_2 and BrO concentrations, but also investigates the possible abundance of the other trace species mentioned before. In the course of this study measurements at eight different volcanic sites were carried out. SO_2, as one of the main gas species emitted from volcanoes and a very important trace gas in the context of the climatic influence of volcanoes, was measured at each site. BrO, a reactive halogen compound, was measured at a volcanic site for the first time by *Bobrowski et al.* [2003] at the Soufriere Hills volcano (Montserrat) and since then a number of other investigations by *Bobrowski and Platt* [2005], *Lee et al.* [2005], *Galle et al.* [2005] and *Oppenheimer et al.* [2005] were carried out. At five of the eight studied sites BrO was detected. This demonstrates that Soufriere Hills is not an exceptional volcano with respect to emission of reactive bromine. Two other reactive halogen species ClO and OClO could be detected for the first time in a volcanic plume.

Outline of the thesis

This thesis is divided into nine chapters. It starts with a short overview on volcanic terms, followed by a description of the chemistry of volcanic gases in the third chapter, especially regarding the chemistry of sulphur and bromine in our atmosphere. The measurement technique is explained in chapter four and in chapter five the instruments applied in this thesis are described. Chapter six deals with the analysis procedure for the different trace gases considered in this work. Then a detailed description of the field campaigns is given with a description of every volcanic site. The discussion in chapter eight mainly focusses on the measurements at Mt. Etna, since this is the site studied in most detail within this thesis. In the last chapter the results of this thesis are summarized and an outlook for possible future research is given.

Chapter 2

Volcanoes - a Short Overview

2.1 Definition

A volcano can be described as a place on the surface, where molten rock and gases erupt through the earth's crust. Volcanoes vary in their structure - some are fissures in the earth's crust where lava erupts, and some are domes, shields, or mountain-like structures with a crater at the summit. The structure of a volcano contains a vent or cluster of vents fed by magma[1] which is rising directly from great depth within the earth, generally well below than 30 km.

Volcanism is the transport of matter and energy from the inner side of a celestial body to its surface.

The temperature inside the earth increases from the surface to the inner core of the earth. The center of the earth has a temperature of around 4700°C, but because of the high pressure it is probably in a solid phase. Three different processes cause the high temperature:

- since the formation of the earth 4.5 billion years ago - the impact of cosmic matter contained a huge amount of kinetic energy, which was converted to thermal energy and a rest of that is still existing

- more matter leads to an increasing mass of the earth. That increased the gravitational pressure inside the planet, therefore the temperature increases.

- the radioactive decay of certain isotopes like uranium, thorium and potassium convertes kinetic energy to thermal energy.

[1] Magma is molten rock under the earth's surface from which igneous rock forms. Magma is formed from many types of rocks, including basalt, andesite, dacite and rhyolite

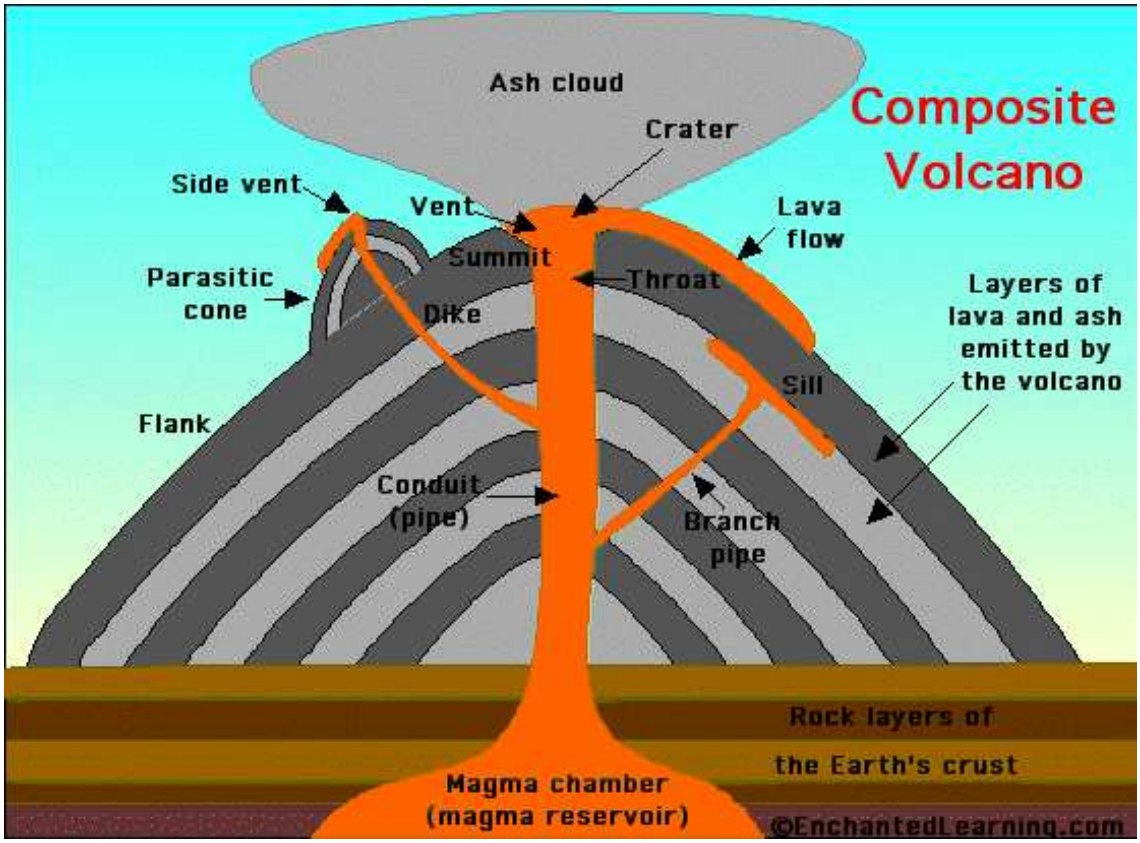

Figure 2.1: *Sketched cross section of a volcano with important parts shown. Adapted from http://www.EnchantedLearning.com/subjects/volcano/*

2.2 Birth, Life and Death of Volcanoes

The state of a volcano can be described using terms like active, alive, dormant or dead. The 'birth' of a volcano often follows the same pattern. First, over days and weeks earthquakes can be recognized. Then the earth's surface is more arched and cracks form, gases and water vapor start to escape. The vent gets free with an explosion, which removes the country rocks, then the magma starts to flow, degassing takes place combined with ash[2], lapilli[3] and bombs[4] eruption. The eruption of matter extends the vent, therefore more degassing takes place and the explosive eruption changes into an effusive one.
Most volcanic activity is interrupted by times of silence. The range of that time can vary

[2]Ash: - Fine particles of pulverized rock blown from an explosion vent. Measuring less than a few mm in diameter, ash may be either solid or molten when first erupted. By far the most common variety is vitric ash (glassy particles formed by gas bubbles bursting through liquid magma).

[3]Lapilli: - Literally, "little stones." Round to angular rock fragments, measuring from a few mm to 50 mm in diameter, which may be ejected in either a solid or molten state.

[4]A volcanic bomb is a chunk of viscous lava ($\varnothing > 64$ mm) that is ejected (thrown) from a volcano. Since they are still viscous when ejected, they often have rounded, aerodynamic shapes.

from some minutes like at the volcano Stromboli in Italy to more than 1000 years like for El Chichon in Mexico or even longer. During these breaks the volcano is described as dormant. The velocity of the magma uprises and the structure for the volcanic building can change and therefore also the time range of the breaks. Explosive eruptions are usually shorter than effusive eruptions, because an eruption stops when the energy is lost faster than can be replaced by new magma. The lifetime of a volcano can be many millions of years.
Destruction by erosion of the volcano takes place from the beginning of a volcano 'life', but during breaks and especially near the end of a volcano 'life' no rebuilding takes place. Erosion takes over, more and more cracks destruct the building of the volcano and lead to so called relief-reversal - Valleys. The valleys, which are filled with cold lava[5] flows, change to mountain ridges. At the place of the old crater a cone shaped dome is formed. A dying volcano will not only be destroyed from the outside, but also from the inside. When the lava flow stops, the roof of the magma chamber can collapse and the volcano mountain becomes a caldera[6], which can have a diameter of several kilometers.

2.3 Classification of Volcanoes

Volcanoes can be classified in different groups with respect to their attributes. They are mostly divided according to their different shapes, but since this will not always lead to a clear definition a more differentiated overview is given in this section. It starts with a description of different eruption types, followed by the types of bursts, classification based on geological settings and ends with the typical distinction of different shapes.

1. Types of Eruptions

Eruptions can be classified by their explosiveness. The fragmentation and the dispersion of tephra[7] can serve as a measure of explosiveness. The part of the fragmentation which consist of particles smaller than 1 mm is determined at the distance where the tephra has 10% of the maximum thickness. For an overview of this classification see Figure 2.2. The fragmentation strongly depends on the degassing state of the magma and its composition (see also section 2.4). Below are six different eruption categories described:

[5]Lava is molten rock, that has already reached the surface of the earth. It usually comes out of erupting volcanoes.

[6]caldera: - Spanish word for cauldron, a basin-shaped volcanic depression; by definition at least a mile in diameter, such large depressions are typically formed by subsidence of volcanoes.

[7]tephra: - is a general term for air fall material produced by a volcanic eruption regardless of composition or fragment size. It can be divided into Ash, Lapilli and volcanic bombs

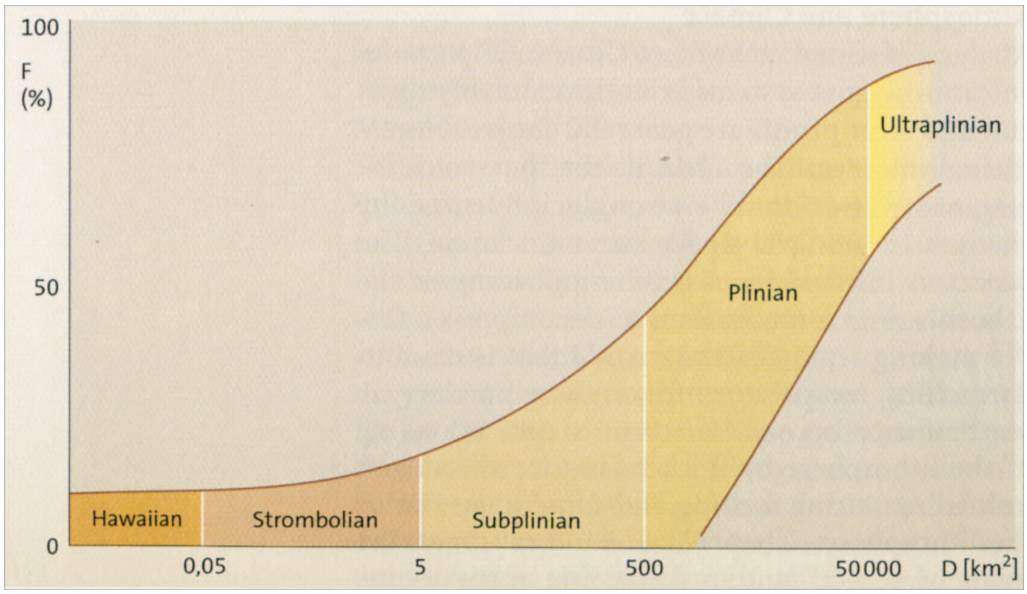

Figure 2.2: *Classification of explosive volcanic eruptions, based on the area distribution of their tephra deposits D(inside that isopach, which represents 0.01% of the maximum thickness) and degree of tephra fragmentation F (= % < 1mm), adapted from Schmincke [2004]*

- Hawaiian and chasm eruption:
  These kinds of eruptions are characterized by very fluid eruption. It cause sometimes spectacular high lava fountains and red glowing lava streams. Due to low viscosity of the lava and often central conduit, see Figure 2.1, mostly so called shield volcanoes are formed. These are mountains with very slow rises (see more below), the classical example is the Mauna Loa at Hawaii island. When the central conduit, which is typical for classical volcano mountains, is missing, fissure eruption occurs. The difference is the huge amount of very fluid lava, which comes out of the fissures and can flow several km long. The lava is spread over wide areas and lava plateaus are built. Such lava plateaus are found in India or Iceland.

- Strombolian eruption:
  Strombolian eruption are named after the Stromboli volcano in Italy. They are characterized by the eruption of so called pyroclastic[8] and lava flows resulting in longer periods of change between effusive and explosive eruptions mechanisms. Concave Strato volcanoes are formed, for example Fujiyama or Etna.

- Vulcanian eruption:

[8]pyroclastic: - pertaining to fragmented (clastic) rock material formed by a volcanic explosion or ejection from volcanic vent

The vulcanian eruption is characterized by strong explosive bursts which develop cauliflower clouds composed of water vapor, volcanic gases and stone fragments. After the explosive phase in the beginning these eruptions produce inert and viscous lava flows."Layer and strato volcanoes" (see below) with steep edges are built, due to variation of ash deposits and lava layers.

- Peleanian eruption
  Named after Mount Pelee at the Caribbean Island Martinique. This type of eruption is very destructive, because of hot lava avalanches. These are also called nuees ardentes[9] which run with a velocity of more than 100 km/h downward. The bottom and high density part of the nuees ardentes is called ash flow[10]. These ash flows form often wide sedimentary fans around the strato volcano, where they come from. The combination of two geomorphological structures makes clear that at such volcanoes different burst mechanisms take place. The acidic lava is viscous during peleanian actions and often forms plug domes[11]during the lava release from the conduit. The lava can actually plomb the conduit totally and the gases are trapped. The pressure increases more and more until an explosion takes place and destroys the plug dome.

- Plinian eruption
  These are very explosive eruptions like the burst of Vesuvio in 79 AD. The eruption is named after Plinius the Younger, who described this kind of eruption event for the first time. A fundamental feature is the long period of the blowing out of ashes. Ashes and volcanic gases reach even the stratosphere and can so influence the weather and climate global. Further features are pyroclastic flows and calderas are often formed.

- Explosive eruption
  The eruption appears suddenly and is often only of a short time range. Very high amounts of gases and high pressure occur during the building of the crater. Ash, bombs and rock fraction of different size are erupted into the air. Around the explosion funnel a wall of pyroclastic products can sometimes be observed.

2. Types of Bursts

[9]nuess ardentes: - French term applied to a highly heated mass of gas-charged ash which is expelled with explosive force and moves with hurricane speed down mountainside

[10]ash flow: - turbulent mixture of gas and rock fragments, most of which are ash-sized particles, ejected violently from a crater or fissure. The mass of pyroclastics is normally of very high temperature and moves rapidely down the slopes or even along a level surface

[11]plug dome: - steep-sided, rounded mound formed when viscous lava wells up into a crater and is too stiff to flow away. It piles up as a dome-shaped mass, often completely filling the vent from which it emerged

- Effusive volcanic bursts:
  The magma contains a small amount of gas and is relatively fluid, which leads to quiet lava flows and lava fountains. Effusive eruptions are characteristic for basaltic lavas with high temperatures of 1000 - 1200°C and less silicic acid contents. A classical example is Mauna Loa at Hawaii.

- Submarine volcanic burst:
  The pressure of water in the deep seas does not allow a fast distribution of gases, therefore the eruptions are mostly effusive. Only in shallow water the eruptions are much more violent. The mixture of magma and water at low water pressure produces suddenly vapor, which leads to vapor explosions.

- Explosive volcanic burst:
  Explosive eruptions take place if the magma has a high gas content and is very viscous. That is the case mainly for special acidic, rhyolitic magma. Rhyolitic magma has a high content of silicic acid and already melts at 800 - 1000°C, which leads to comparably viscous magma. Due to pressure decrease soluble gases can explosively release the magma and breaks to pieces of hot fraction of magma. A mixture of rock fraction, hot ash and expanding gases is released by the volcano. In the case that this cloud has a smaller density than air it rises up as a huge formation, higher density of the mixture leads to a pyroclastical flow moving down the mountain.

3. Classification Based on Geologic Settings

The distribution of the volcanoes over the earth and their origin can only be explained by the theories of plate tectonics and sea floor spreading. Both is based on the idea of a mobil dynamic earth by Alfred Wegener in 1912. Figure 2.3 gives a short overview of the different volcanic origins, which are than shortly described in this subsection.

- Volcanism at middle ocean ridge:
  At places where tectonic plates are moving apart volcanoes fill the gaps, mostly with basaltic lava flows. These are so called constructive plate boundaries. New ocean ground and middle ocean ridges are formed. The fissures reach down to the hot asthenosphere[12]. This form of volcanism is named Rift volcanism and has the highest amount of lava eruptions. Sometimes the basaltic mass reaches over the ocean surface and forms little islands, for example Iceland. Due to this kind of volcanism the ground of the oceans is globally not older than 200 million years.

- Island-arches and volcanism at continental edge:
  The most dangerous volcanoes can be found where a plate of lithosphere[13] moves

[12] asthenosphere: weak zone below the top of the mantle, which is overlain by the lithosphere
[13] lithosphere: the rigid outer shell of a planet, consisting of the crust and the uppermost mantle

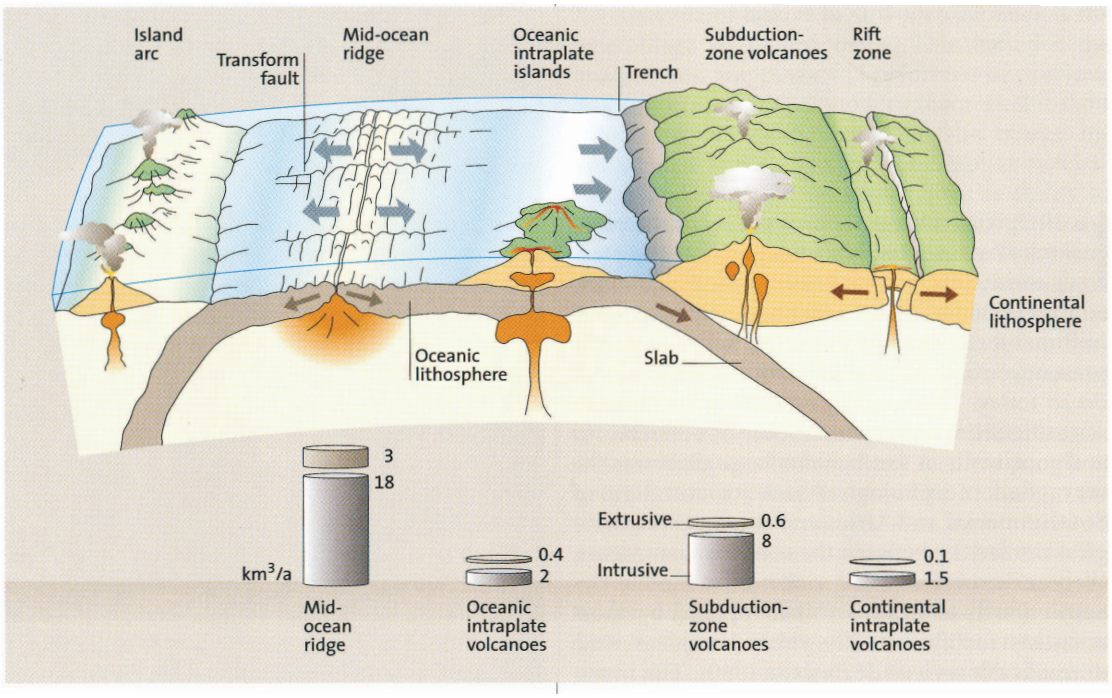

Figure 2.3: *Divergent (mid-ocean ridges) and convergent (subduction or Wadati-Benioff zones) plate margins. Annual magma production rate (km^3/a) adapted from Schmincke [2004] and references therein*

under another plate of the lithosphere and submerges in the asthenosphere - so called destructive plate boundaries. The volcanoes are usually located several tens of kilometers from the plate edge of the upper plate and are formed because of partial melting of rocks from the underlying plate. The eruptions are often explosive and characterized by mud flows and soot rains. Different kinds of rocks get to the surface - basaltic and andesitic lava. When one oceanic plate moves under another conspicuous arches are built. Examples are the Japanese island arch with Fujiyama and the arch of the Philippines. When an oceanic plate gets under a continental plate volcanic mountain chains appear for instance the Anden or the Cascade-mountains with Mount St. Helens in North America.

- Continental riftvulcanism:
  Rift-vulcanism happens when a continent is divided into different parts. It is often characterized with fissure formation, formation of a Rift-Valley and it consists of basaltic lava. A famous example is the east African Rift-Valley. The fissure formation and the volcanism are obviously signs of the beginning of a new ocean.

- Volcanism away from tectonic plate boundaries:
  Some volcanoes are far away from their classical places - edges of plates. Examples

are the hawaiian volcanoes and the volcanoes in India. This kind of volcanism is represented by Hot spots. Hot spots are volcanic appearances of so called mantle-diapirs, which consist of a beam of hot material with small density. The magma melts the plate at one place and forms a magma bubble. This finally breaks through the lithosphere. The hot spot doesn't change its place, but the plates move. Thus a row of volcanoes is formed, because the lava reaches the surface in portions over long periods of time.

4. Types of Volcano Shape

- Shield volcanoes:
  A shield volcano has gently sloping sides with a slope of less than 10°C. Shield volcanoes are composed mostly of basalt. Often the lava flows not only from a central pipe, but also run from fissures at the mountain side. The biggest volcanoes on Earth (like those on the islands of Hawaii) are shield volcanoes.

- Strato-volcanoes (Composite cone volcanoes):
  These are the most common volcanoes on earth. A composite volcano is a volcano that has a steep volcanic cone that is built up by dense lava flows and pyroclastic debris. The cold lava flows act as a protection layer for the pyroclastic material. They have a slope angle between 10° and 30°, an example is the well-known Fudschijama volcano.

- Tephra-volcanoes:
  Tephra volcanoes are formed by explosive eruptions of material which mostly falls down close by the crater. They have a steep mountain side of 30° or more and consist of lava rocks and adjoining rock. A layer which is composed of loose pyroclastic material is called tephra. Examples of tephra-volcanoes can be found in the German Eifel.

2.4 Types of Lava

Magma reaches the earth's surface (then it is called Lava) with ascending forces, sometimes as a calm lava stream, other times as an explosion. The consistency of lava varies from fluid to a highly viscous material. This is due to differences in minerals, water content, different amount and composition of gases of the magma and the different temperature. Alkaline basalt lava is very fluid because of the high temperature, which is necessary for basalt melting, 1000 to 1200 °C, and the relatively low amount of silicic acid (45% - 52%). Therefore it can spread fast over large areas. Rhyolitic lava has an extreme high amount of silicic acid (more than 66 %) and melts already between 800

and 1000 °C. As Rhyolitic lava is very viscous, it is more likely that the lava piles up than that it spreads over wide areas. During the ascending process the basaltic lava can take up country rock, which has a lower melting point than itself. Especially under the continents the country rocks, which are melted, contain more silicic acid - the consistency of magma changes and becomes a magma between basaltic and rhyolitic that is called andesitic, named after the south American mountain range.

An Overview of the mineralogical composition and the major groups of igneous rocks is given in Figure 2.4. In many cases magma is formed when an oceanic plate sinks under a continental plate, so water rich sediments are melted and the water content is much higher than from basaltic lava. Experimental experience shows that melts which have a low water content become more fluid when the pressure decreases during ascend. On the other hand water rich melts become more viscous under these conditions. Due to this fact andesitic lava can cause explosive eruptions. Lava flows (which tend to be basaltic) are divided into three kinds of lava - pahoehoe-, 'a'a-lava and pillow lava. Pahoehoe lava is a Hawaiian term for lava having a smooth or rope-like surface when it is solid. 'A'A lava is a lava flow that has a rough, broken-up, spiny surface. It is composed of broken lava blocks called clinkers. The interior of 'a'a is very dense. Pillow lava has a characteristic morphology and is mostly seen when the eruption took place under water.

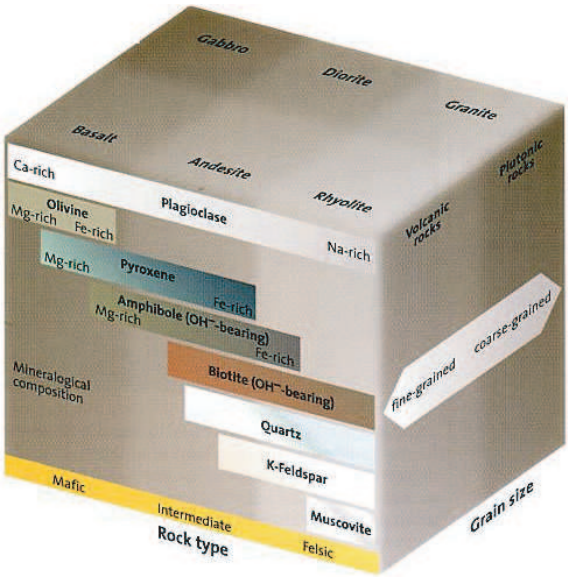

Figure 2.4: *Major groups of igneous rocks and their mineralogical composition adapted from Schmincke [2004].*

2.5 Volcanoes and Climate

After the primitive atmosphere of the earth was lost to space, volcanic eruptions were the main source of gases for the atmosphere of our planet and even for the ocean. Water (H_2O), carbon dioxide (CO_2)and nitrogen (N_2) are typically the most abundant components of volcanic gas emissions. Volcanoes contributed largely to the origin of our earth's atmosphere. The water was condensed to the ocean and the CO_2 was partly converted by plants to O_2. Today the earth's atmosphere consists of 78 % N_2 and 21 % O_2 [*Robock*

2000]. CO_2 and H_2O are greenhouse gases, but the amount, which is released into the atmosphere from volcanos at present is negligible compared to the global concentration. The volcanic influence on the climate has always been a topic of discussion. Volcanoes inject tens of teragramms of chemically and microphysically active gases and solid aerosol particles into the stratosphere and affect very likely the earth's radiative balance and climate and frequently disturb the stratospheric equilibrium. Therefore it is important to study the response of climate to volcanic eruptions. This also offers the possibility to comprehend the radiative and dynamical processes that respond in the climate system to both natural and anthropogenic forces. It serves to improve climate models, which lead to a more precise view on anthropogenic effects.

During many eruptions huge ash clouds ascend from a volcano which have a dramatic impact on the weather, but in most cases only locally near the volcano. It is possible that the ash clouds spread several hundreds of kilometers, however they often have no influence on the climate. For the climate, the gaseous emissions, especially sulphur compounds are of much higher importance. The sulphur species which are mainly emitted are H_2S (a gas smelling like addle eggs) and SO_2 (a sharp smelling gas). The decrease in surface temperature following a major volcanic eruption is proportional to the amount of sulphur which is released by eruption into the atmosphere [*Pinto et al.* 1989]. The residence time of sulphur compounds which are injected into the stratosphere is about a year, sometimes up to two or three years, depending on the injection height into the stratosphere. The emitted sulphur species react with OH and H_2O (see chapter Chemistry of Sulphur) to form H_2SO_4 on a timescale of weeks. Coagulation processes limit the number of particles which are formed. The resulting aerosol produces the dominant radiative effect from volcanic eruptions. The sulphur aerosol is fast advected around the globe, - after Krakatau it needed only two weeks [*Symonds et al.* 1988], after Pinatubo three [*Bluth et al.* 1992], but also other climatic relevant trace gases like bromine and chlorine compounds are emitted [*Pinto et al.* 1989]. In Table 2.1 an overview is given for gas emissions of volcanoes with less silicic magma content. Investigations at volcanoes fed by magma with a higher silicic content are more difficult, as they have more explosive eruptions (see above section Types of Lava). The amount of aerosol released by a volcanic eruption can be huge, several millions of

Table 2.1: *Characteristic composition of volcanic gases at the vent (e.g., Symonds et al. [1988], Cadle [1980], Symonds et al. [1994], and Chin and Davis [1993].*

Species	H_2O	CO_2	SO_2	H_2S	COS	CS_2	HCl	HBr	HF
%vol	50-90	1-40	1-25	1-10	10^{-4}-10^{-2}	10^{-4}-10^{-2}	1-10	?	$< 10^{-3}$
Tg/year	?	75	1.5-50	1-2.8	0.006-0.1	0.007-0.096	0.4-11	0.0078-0.1	0.06-6

tons and can significantly change the aerosol optical depth in the stratosphere (see Figure 2.5). For climate effects a minimum of 3 million tons of sulphur has to be emitted [*Sachs*

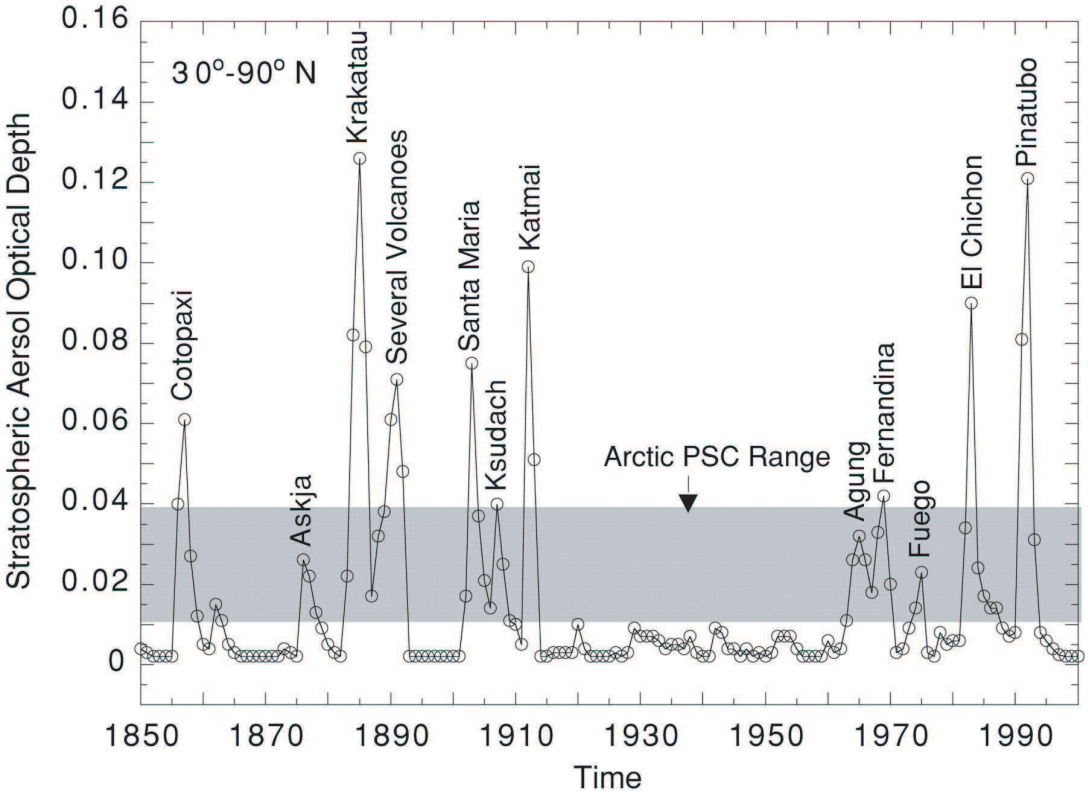

Figure 2.5: *Time series of stratospheric aerosol indicating the importance of major volcanic eruptions. Adapted from Tabazadeh et al. [2002]*

and Graf 1998]. Aerosols play an important role in our climate, they influence the global radiation balance directly, by scattering and absorbing light, and indirectly by inducing cloud formation and providing surfaces for heterogeneous chemistry. The sulphur aerosol in the lower stratosphere scatters solar radiation. It reflects sunlight back to space, but also scatters terrestrial radiation and thus impacts on shortwave and long-wave radiation, which results in a net heating of the lower stratosphere [*Robock* 2000]. As most volcanoes are situated in tropical regions the rise in temperature of stratospheric regions is higher at low latitudes than at high latitudes, leading to a temperature gradient from pole to equator especially in winter. This phenomenon causes a more stable polar vortex in the Northern Hemisphere (NH) compared to years without volcanic eruptions. The resulting stronger jet-stream produces characteristic stationary wave patterns of tropospheric circulation. This indirect advective effect on temperature is stronger than radiative cooling, which dominates lower latitudes in summer. In general the net planetary albedo is increased, it reduces the amount of solar energy which would reach the earth's surface and lead to a cooling effect, a decrease of global temperature in the troposphere [*Bissoli* 1985]. A huge volcanic eruption can change the global temperature around 1 K or even more. After the

eruption of Mt.Pinatubo 1991 (VEI [14] = 6) the global average temperature decreased by ∼ 0.5 K [*Sachs and Graf* 1998]. 20 million tons of sulphur dioxide were emitted. The eruption

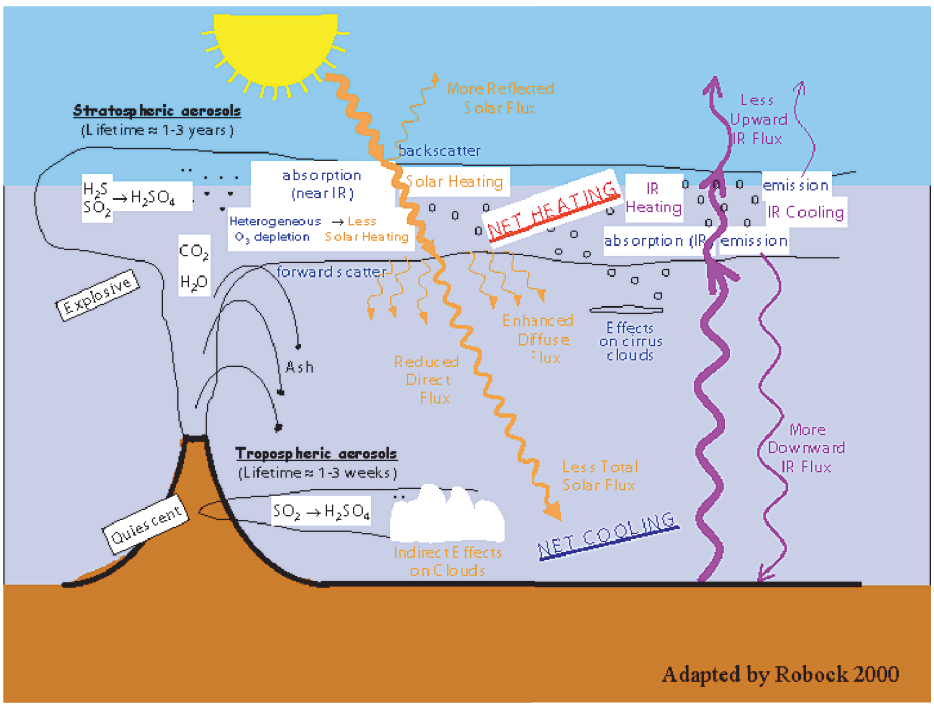

Figure 2.6: *Volcanic influences on the atmosphere, adapted from Robock [2000].*

of Toba 71000 years ago caused a cooling between 3 and 5 K for several years [*Yang et al.* 1996]. Additionally the sulphur aerosol provides surfaces for heterogenous reactions, the most important one is related to ozone destruction. Production and destruction of ozone is dependent on UV-flux, temperature and present surfaces which can all be changed by volcanic aerosol. The destruction of ozone lowers the UV-absorption in the stratosphere and therefore more shortwave radiation would reach the earth's surface. This causes a heating of the troposphere. The anthropogenically emissions caused higher concentration of chlorine compounds (e.g. by CFC's) which likely increased the destruction of ozone after the large volcanic eruption in the last years.

It is not possible to separate climatic effect of large volcanic eruptions from anthropogenic effects at the present time. Ozone losses would also be enhanced if HBr was present in the range of the bromine to chlorine ratio measured in volcanic gases [*Sugiura and Y. Mizutani* 1963], but could not be proven until now. Pinto, Turco and Toon [*Pinto et al.* 1989]

[14] VEI : Volcanic Explosivity Index, a scale for comparing the sizes of explosive eruptions (1 - 10) based on the volume of erupted material and the height of the eruption column

suggest that halogenide emission could be of higher importance in the clouds produced by increasingly alkalic volcanoes for example Etna, El Chichon and Erebus. Alkalic magma is richer in chlorine and also in sulphur [*Woods et al.* 1985]. Because of large differences between volcanoes (see above), a global estimation of emissions and the subsequent influence on climate is still difficult to predict.

Chapter 3

Chemistry of Volcanic Gases

The chemistry of volcanic plumes is still fairly unknown at the present time. The lack of suitable measurement techniques up to recent years in the vicinity of volcanoes can be regarded as one of the main reasons. The chemistry inside a volcanic plume differs substantially from "normal" atmospheric chemistry, because of the difference in composition with high amounts of H_2O, CO_2 and SO_2. Therefore the knowledge about ambient atmospheric chemistry is not directly transferable. A volcanic plume is also a very complex environment itself, because of a dense mixture of trace gases and aerosol particles, which provide a large surface area for heterogeneous chemistry. The higher temperatures and acidity in volcanic plumes also can accelerate reactions or even enable reactions that are in a normal ambient environment of no unimportance. Thus, high uncertainties remain and a large number of questions must still be answered, but already in the last 30 years the knowledge about volcanoes increased about orders of magnitude from "Next to nothing is known about the sources of the volatile components of magmas or how they are distributed" [*Williams and McBirney* 1983] to a "first understanding..." [*Carroll and Holloway* 1994].
Sulphur dioxide and bromine monoxide within volcanic plumes are the main focus of this study. Therefore, an introduction to the sulphur chemistry and afterwards to the halogen chemistry, in particular to the bromine chemistry, and its impact on the atmosphere is given. The third section give a brief overview about volatiles in melts and finally about the main gas components released by volcanoes.

3.1 Sulphur in the Atmosphere

Sulphur is the 14th most abundant element in the Earth's crust and an essential element of all creatures. Many compartments on Earth contain sulphur compounds, and exchange processes take place between the lithosphere, biosphere, hydrosphere and atmosphere all the time. In the atmosphere, sulphur compounds can be found as gas and in aerosols. Sulphur influences chemistry as well as climate and can negatively affect our health. It

has been known for long time that sulphur compounds are naturally released to the atmosphere through volcanism (mainly as SO_2 and H_2S) or biological processes - decay of organic matter (H_2S, CH_3SH or CH_3SCH_3) and sea spray (SO_4^{-2}).
Sulphur compounds affect the radiation balance of the atmosphere directly (i.e. cooling by sulphate particles) and indirectly by acting as cloud condensation nuclei (CCN). SO_2, SO_3, H_2SO_4 are aerosol precursors, which lead to cloud formation and serve as surfaces for heterogeneous chemistry. The modification of the cloud properties by sulfate aerosol is associated with a cooling effect [*Lohmann and Feichter* 2005]. The sulphur particles enhance the number of aerosols and therefore increase the albedo. The result is a reduction of the direct incoming sunlight radiation. In comparison to carbon, oxygen and nitrogen, the abundance, sources, sinks, budgets and photochemistry of atmospheric sulphur compounds are still poorly understood. The influence of sulphur on the climate is still fairly uncertain [*Albritton and Meira Filho* 2001]. Measurements of cloud microphysical parameters are very limited even a lot of effort has been already undertaken.
Figure 3.1 summarizes the known emission, transformation and deposition processes of

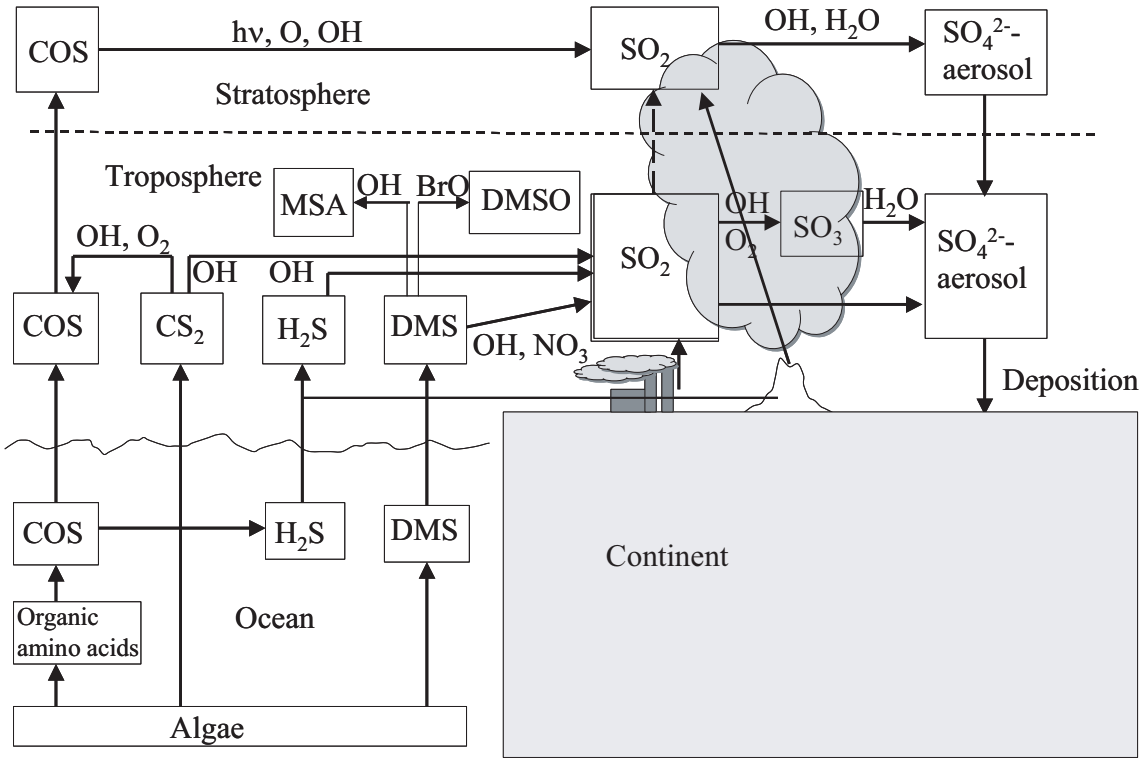

Figure 3.1: *Atmospheric Sulphur Cycle adapted from U. Platt*

the major atmospheric sulphur compounds. Volcanoes are the largest natural source of sulphur. SO_2 is the main sulphur species emitted from the magma, besides H_2S, COS and CS_2 are also released by volcanic activities [*Textor et al.* 2004]. Volcanoes are often able

to emit the sulphur compounds into the free troposphere. During an eruption more than 80% of the volcanic plumes reach a height of more than 6 km and more than 20% of the eruption plumes a height of more than 15 km [*Halmer et al.* 2002]. Therefore, volcanic

Table 3.1: *Observed Mixing Ratios of Atmospheric Sulphur Gases, source: Berresheim et al. [1995] and references therein.*

Compounds and Location	Average Mixing Ratio (ppt)	Average Lifetime
H_2S		2 days
Marine surface layer	3.6 - 7.5	
Coastal regions	65	
Forests	35 - 60	
Wetlands	450 - 840	
Urban areas	365	
Free troposphere (2 - 5 km)	6 - 8.5	
CH_3SCH_3 (DMS)		0.5 days
Marine surface layer	80 - 100	
Continental surface layer	8 -60	
Free troposphere (2 - 5 km)	1.5 - 15	
CS_2		1 week
Marine surface layer	2 -18	
Continental surface layer	35 - 120	
Free troposphere (2 - 5 km)	5 - 7	
COS		3 years
Total troposphere	500	
Marine surface layer	500	
Continental surface layer	545	
SO_2		2 days
Marine surface layer	50	
Free troposphere ($>$ 5 km)–	50	
Europe/North Sea/Arctic		
North America clean continent	160	
Coastal Europe	260	
Polluted continental air	1500	

emissions play a very important role in the global sulphur budget of the troposphere as well as the stratosphere.

After industrialization anthropogenic sources have increased and have at least been comparable in magnitude to natural ones since the early 20th century. For example, the well known London smog (sulphuric acid aerosol) or the problems of Forest dieback due to acid rain (lower pH in rainwater due to H_2SO_4) are still in mind as well as partly still ongoing and illustrate the anthropogenic contribution to sulphur emissions to the atmosphere.

Boucher and Lohmann [1995] describe an enhancement of cloud particles between 0-20% for the Southern Hemisphere and and up to 100% for the Northern Hemisphere since the beginning of the Industrial Revolution.
In the second part of the 20th century, sulphur emissions decreased significantly in the industrialized countries, because of desulphurization actions. However, on a global scale, the emissions are still increasing. The reason for this increase is fast economic developments in several Asian countries like China [*Seinfeld and Pandis* 1998].
Today, sulphur compounds are generally found with higher concentrations over the continents than over the oceans. Table 3.1 gives an overview of the typical mixing ratio of several sulphur compounds in various regions and typical lifetimes. For the most important known sulphur compounds in the atmosphere, estimated source and sink fluxes are given in Table 3.2.

3.1.1 Sulphur Sources and Sinks

The sulphur compounds in the atmosphere have oxidation states of S(-2), S(-1), S(0) S(+4) or S(+6). The sulphur in the oxidation state S(+6) is the most stable and therefore preferred one in Earths atmosphere. The primer oxidizers for sulphur gases are OH (for the gas phase), H_2O_2 and O_3 (mainly important for the liquid phase). The water solubility of the sulphur compounds increases with the increasing oxidation number. The lifetime of sulphur compounds is determined by chemical reactions and also physical processes.
Tropospheric sulphur originate from both, anthropogenic and natural sources. The anthropogenic sulphur emissions are caused by:

1. Industrial exhaust gas, which contains sulphur as carbonyl sulfide (COS), carbon disulfide (CS_2), low molecular weight mercaptans (e.g. CH_3SH) and thiophene
2. Natural and refinery gases which contain sulphur as mercaptans, COS and thiophene
3. Synthesis gas (mainly CO + H_2O) containing sulphur as COS and CS_2
4. Emissions from vehicle exhausts.

Further relevant anthropogenic sources are the emission of SO_2 by coal fired power stations, oil refinery operations, oil-fired energy generation, copper smelting, biomass burning and sulphuric acid manufacturing, which actually represent the major contribution of the anthropogenic sulphur release into the atmosphere.[*Zellner et al.* 1999; *Seinfeld and Pandis* 1998]

Anthropogenic sources play most likely a minor role as stratospheric sulphur sources. Although anthropogenic sources provide more than 80% of the total sulphur emission, the major chemical species is SO_2 that is emitted into the lower troposphere. Because of

Table 3.2: *Sources and Sinks of sulphur compounds in Terragramms sulphur per year Lelieveld et al. [1997] (a) Watts [2000] (b) Rasch et al. [2000] (c) Boucher et al. [2003] (d) Chin et al. [2000].*

	CS_2	DMS	H_2S	COS	SO_2	$SO^{2-}{}_4$
Sources[Tg S/year]	$0.66 \pm 0.19^{(a)}$	$24.5 \pm 5.3^{(a)}$	$7.7 \pm$	$1.3^{(a)}$	$79^{(b)}$	$55^{(b)}$
Anthropogenic	0.34 ± 0.17 (51.5%)	0.13 ± 0.04 (0.5%)	3.30 ± 0.33 (42.7%)	0.12 ± 0.06 (9.2%)	$75^{(d)}$	-
Biomass burning	-	-	-	0.07 ± 0.05 (5.3%)		
Ocean [1)]	0.18 ± 0.04 (27.3%)	20.77 ± 5.20 (84.8%)	1.80 ± 0.61 (23.3%)	0.30 ± 0.18 (22.9%)	biogenic	
Terrestrial	0.09 ± 0.08 (13.6%)	3.59 ± 1.01 (14.7%)	1.49 ± 0.43 (19.3%)	0.05 ± 0.03 (3.8%)	$14^{(d)}$	
Volcanism	0.05 ± 0.04 (7.6%)	-	1.05 ± 0.94 (13.6%)	0.05 ± 0.04 (3.8%)	$6\text{-}20^{(d)}$	
Precipitation	-	-	-	0.13 ± 0.08 (9.9%)		
DMS oxidation	-	-	-	0.17 ± 0.04 (13.0%)		
CS_2 oxidation	-	-	-	0.42 ± 0.12 (32.1%)		
Gas phase prod.	-	-	-	-	-	$14^{(d)}$
In cloud prod.	-	-	-	-	-	$22.5^{(d)}$
Sinks						
Gas phase oxidation					12%	
Reaction with OH	0.57 ± 0.25 (56.4%)	$11.4\text{-}19.4$ (42-71%)$^{(c)}$	8.50 ± 2.80	0.13 ± 0.10 (7.8%)		
Reaction with NO_3	-	6.2 - 15.7 (22-58%)$^{(c)}$	-	-		
Reaction with BrO	-	$7.8^{(c)}$	-	-		
Reaction with O	-		-	0.02 ± 0.01 (1.2%)		
In cloud oxidation		$1.7(\mathrm{DMS} + O_3(\mathrm{aq}))^{(c)}$			56%	
Dry deposition		-			$42^{(d)}$	$5^{(d)}$
					(31%)$^{(b)}$	(7%)$^{(b)}$
Oxic soils	0.44 ± 0.38 (43.6%)	-	-	0.92 ± 0.78 (55.4%)		
Vegetation	-	-	-	0.56 ± 0.10 (33.7%)		
Wet deposition		-			$10^{(d)}$	$35^{(d)}$
					(2%)$^{(b)}$	(93%)$^{(b)}$
Photolysis	-	-	-	0.03 ± 0.01 (1.8%)		
Total	1.01 ± 0.45	24 - $27^{(c)}$	8.50 ± 2.80	1.66 ± 0.79	$52^{(d)}$	40 $^{(d)}$

its short lifetime, SO_2 produced in the boundary layer is seldom transported up to the stratosphere or upper troposphere and is therefore of less stratospheric relevance than the contributions of natural sources. Only industrial areas located in higher altitudes could significantly contribute to the stratospheric sulphur budget.

The main sources of natural sulphur emissions are:

1. biogenic sources (DMS, H_2S, COS)
2. sea spray (SO_4^{2-})
3. volcanoes (SO_2)

Biogenic sources are hydrogen sulphide (H_2S) from bacterial reduction of sediments in the sea and dimethyl sulfide (DMS) released from organisms in the ocean. Most of H_2S is transformed by bacterial oxidation, so that dimethyl sulfide is the major biogenically produced sulphur compound in the ocean.

Volcanoes are the main natural source of sulphur dioxide. The source strength is still very badly known as illustrated in Table 3.3, which shows the differences between various literature values. This estimates vary over one order of magnitude, or neglecting citations before 1980 still about a factor of five. As mentioned above, volcanoes also emit

Table 3.3: *Annual global SO_2 fluxes from volcanoes to the atmosphere from literature data arranged by increasing magnitude. Adapted by Textor et al. [2004].*

SO_2, [Tg/a]	Reference
1.5	*Kellogg et al.* [1972]
4	*Friend* [1973]
6	*Granat et al.* [1976]
7.78	*Cadle* [1975]
9	*Halmer et al.* [2002]
10	*Stoiber and Jepsen* [1973b]
13	*Bluth et al.* [1993]
13	*Andres and Kasgnoc* [1998]
15.2	*Berresheim and Jaeschke* [1983]
18.7	*Stoiber et al.* [1987]
20	*Graf et al.* [1997]
50	*Le Guern* [1982]
50	*Lambert et al.* [1988]

H_2S, CS_2 and COS, but for these species the source strength is even less known than of SO_2.

The dominant natural stratospheric sulphur source is COS, which is mainly emitted from the sea and represents a sulphur compound that has a lifetime long enough to be transported from the lower troposphere into the stratosphere. Volcanoes also contribute to stratospheric sulphur because they may emit sulphur compounds through the tropopause.

The tropospheric sink for the most sulphur compounds is the oxidation of sulphur compounds to SO_2 (in the gas phase) and SO_4^{2-} (in the liquid phase) which are deposited on the earth's surface by wet- and dry-deposition. The SO_2 is removed from the troposphere: (a) in gas phase by formation of sulphuric acid, which forms condensation nuclei for aerosols and clouds and acidifies the rain, (b) directly, by uptake on aerosols and clouds, which leads to dry and wet acid depositions.
The main stratospheric sink for sulphur is the exchange with the troposphere. The dominance of stratospheric tropospheric exchange is illustrated by measurements of stratospheric sulphur following big volcanic eruptions (VEI[1] > 3). After 1 - 2 years the concentration of sulphur compounds is in most cases nearly on the same level as before eruption. This time scale is the same as is needed to mix stratospheric gases into the troposphere.

3.1.2 Sulphur Dioxide - SO_2

Sulphur dioxide is a colorless gas with a sharp smell. It is soluble in water through a reaction that forms sulphurous acid (H_2SO_3). It is a dangerous gas to human health in high concentrations, it has a lifetime of the order of some days in the troposphere and much longer in the stratosphere.
An overview of the sources of sulphur dioxide is given in Table 3.4. The values are taken from the MOZART model (Model for Ozone and Related chemical Tracers).
Anthropogenic activities like the combustion of fossil fuels in power plants and the smelting of non-ferrous metal ores contribute to the emission of SO_2 to the atmosphere. Between 1960 and 1980 the emission rate of sulphur dioxide increased considerably. [*Dignon and Hameed* 1989]. With the realization of negative environmental impact of industrial emissions, stringent precautions were taken in Europe and North America and a decreasing emission rate of SO_2 can be observed since 1980 [*Gschwandtner et al.* 1986; *Mylona* 1996]. Estimates of source strengths can have large uncertainties, which is illustrated by the volcanic emission data in Table 3.3. Significant natural SO_2 sources are oxidation of DMS emitted from the ocean and direct emission of SO_2 from volcanoes. *Berresheim and*

[1]VEI : Volcanic Explosivity Index, a scale for comparing the sizes of explosive eruptions (1 - 10) based on the volume of erupted material and the height of the eruption column

Jaeschke [1983] suggest a mean emission rate of 7.5 Tg/yr from volcanoes, but one major eruption can cause a contribution of the same amount. For example an estimate of the Mt. Pinatubo eruption is 10 Tg sulphur (20 Tg SO_2) [*Fiocco et al.* 1996]. Nevertheless, today the main source of SO_2 is anthropogenic, contributing to at least 75 % [*Chin and Davis* 1993] or more to the global emissions 3.4. Most of the sulphur dioxide undergoes

Table 3.4: *Sulphur Dioxide emission are presented for natural and anthropogenic sources. The anthropogenic part dominates in the emissions of SO_2 The values are adapted from MOZART [http://acd.ucar.edu/models/MOZART/emissions/tables/table_so2.html].*

Emission Sources	Total Emitted (Tg S /yr)
Power generation	27.9
Industry	14.8
Non-iron	8.6
Residential	6.6
Other transf.	5.4
International Shipping	2.5
Road transport	2.0
Chemicals	1.7
Cement	0.9
Non-road transport	0.5
Industrial biofuel	0.5
Iron and Steel	0.4
Other biofuel	$8.4 \cdot 10^{-4}$
Total industrial	71.8
Continuous volcanoes	2.7
Forest + Savanna burning	1.3
Agricultural waste	0.6
Fuelwood	0.34
Total	76.74

wet or dry deposition processes to Earth's surface. When sulphur dioxide is converted to sulphuric acid, dry deposition plays a minor role. Washout takes place as sulphuric acid, known as acid rain, leading to acidic soils and to higher dissolution of metals that consequently pollute ground water reserves. For the production and destruction processes for SO_2 see also Table 3.2.

The main contribution to the SO_2 in the stratosphere is formed by COS oxidation [*Zellner et al.* 1999]. But also major volcanic eruptions, having a VEI of more than 3 can directly inject huge amounts of SO_2 into the stratosphere.

Sulphur dioxide is converted to sulphuric acid:

$$SO_2 + OH \longrightarrow HSO_3 \tag{3.1}$$
$$HSO_3 + O_2 \longrightarrow HO_2 + SO_3 \tag{3.2}$$
$$SO_3 + H_2O \longrightarrow H_2SO_4 \tag{3.3}$$

or alternatively in clouds:

$$SO_2 + H_2O \longrightarrow H_2SO_3 \tag{3.4}$$
$$H_2SO_3 + H_2O_2 \longrightarrow H_2SO_4 + H_2O \tag{3.5}$$

Sulphuric acid condenses and forms aerosols. It can stay in the stratosphere for several years. Most sulphur compounds in the stratosphere are situated in the Junge-layer[2].

3.1.3 Other Sulphur Compounds

Sulphur compounds are mostly oxidized through homogeneous and heterogeneous processes in the atmosphere and end up in sulphuric acid or sulfates. Often OH radicals play an important role in such processes.

Hydrogen Sulphide - H_2S

The source strength of hydrogen sulphide is not known and it is still difficult to estimate its destruction rate. The production mechanism of H_2S remains uncertain as well. Biological processes in plants emit hydrogen sulphide into the surrounding area. The hydrolysis of COS is another source. Anaerobic bacterial reduction of sulphate is a well known mechanism for the production of H_2S in sulphate rich soils. The emission from soil is influenced by vegetation and is also temperature dependent. A further important source for H_2S could be the continuous degassing of volcanoes. That H_2S is not as fast converted to SO_2 as maybe assumed (H_2S has a lifetime of about two days see Table 3.1) is also indicated by measurements at Etna and Vulcano [McGonigle et al, 2004]
The oxidation of H_2S starts by reaction with OH:

$$H_2S + OH \longrightarrow H_2O + SH \tag{3.6}$$

The next reaction steps is uncertain. The reaction

$$SH + O_2 \longrightarrow OH + SO \tag{3.7}$$

[2]Junge-layer: discovered by Chr. E. Junge, a stratospheric aerosol layer at about 20 kilometer altitude. The aerosol particles have a diameter between several tenth of μm and two μm. The aerosol in this layer is composed to $\sim 80\%$ or more of sulphuric acid droplets or sulphate particles.

is probably very slow k $< 4 \cdot 10^{-19}$ cm^3/(molec $\cdot$ s) [*Stachnik and Molina* 1987], an alternative would be:

$$SH + O_3 \longrightarrow HSO + O_2 \tag{3.8}$$
$$\longrightarrow OH + SO_3 + O \tag{3.9}$$

with k $= 3.5 \cdot 10^{-12}$ cm^3/(molec $\cdot$ s) [*Friedl et al.* 1985].
HSO radicals could further react with oxygen or ozone and lead to SO-radicals [*Zellner et al.* 1999]:

$$HSO + O_2 \longrightarrow HO_2 + SO \tag{3.10}$$
$$HSO + O_3 \longrightarrow OH + SO + O_2 \tag{3.11}$$

Finally SO reacts with oxygen or ozone to form SO_2:

$$SO + O_2 \longrightarrow SO_2 + O \tag{3.12}$$
$$SO + O_3 \longrightarrow SO_2 + O_2 \tag{3.13}$$

Carbon Disulphide - CS_2

One main source of carbon disulphide is the ocean. Mixing ratios of about 20 ppt occur over the open ocean and 10 times more (200 ppt) are found in coastal regions [*Zellner et al.* 1999]. Further sources are emissions by soil and plants, but due to the high variability these source strengths are difficult to estimate on a global scale. The same is valid for the emission of CS_2 from volcanoes. Also rotting organic matter leads to the emission of CS_2. The anthropogenic source is of same order of magnitude as the oceanic source (0.03 Tg/yr)[*Chin and Davis* 1993]. The respective sources are factories that regenerate cellulose rayon and cellophane.
The most important sink of CS_2 is probably the formation of COS:

$$CS_2 + OH \longrightarrow COS + SH \tag{3.14}$$

Dimethyl Sulphide - CH_3SCH_3

At the end of the 1980s *Charlson et al.* [1987] proposed that DMS could play a major role in climate control (CLAW Theory see below). DMS is primarly released into the atmosphere through production processes by phytoplankton [*Andrea et al.* 1990]

in the ocean and represents on a global scale the main natural sulphur source of all reduced sulphur compounds in the troposphere. The global annual flux estimates have still a large uncertainty of a factor of two. It is known and already considered that there are seasonal [*Turner and Liss* 1985], diurnal [*Andreae and Barnard* 1984], depth and location dependent [*Andreae and Raemdonck* 1983] variations of the oceanic fluxes of DMS. The flux from continental sources is of minor importance compared to the ocean. The concentration in the upper layer of the ocean varies between a few nanograms (ng) S per liter to a few micrograms (μg) per liter [*Sebastian* 2004]. The average sea-water concentration of DMS is approximately to 100 ng S per liter [*Andreae and Raemdonck* 1983; *Lovelock et al.* 1972]. Destruction pathways of atmospheric DMS are still under investigation. Reaction of DMS with the free radicals OH and NO_3 are the main reactions. But also the reaction of DMS with BrO, which results in the DMSO as product could be of importance. For a more detailed overview about DMS see *Sebastian* [2004].

Carbonyl Sulphide - COS

Carbonyl sulfide has a lifetime of about 3 years [*Berresheim et al.* 1995] in the troposphere. Therefore, only small variations of its concentration occur and it is nearly uniformly distributed among both hemispheres. The photolysis of organic sulphur compounds (amino acids) or the direct emission from the ocean are the main sources for COS. A further source is the emission of volcanoes with an annual flux up to 0.1 Tg [*Textor et al.* 2004]. COS is produced by the destruction of CS_2 by the reaction with OH and represents a sink for OH.

$$CS_2 + OH \longrightarrow SCSOH \tag{3.15}$$

$$SCSOH + O_2 \longrightarrow COS + SO_2 + H \tag{3.16}$$

COS is also formed by low temperature combustion processes, especially in biomass burning. OH is not only responsible for the formation of COS, but also for its destruction:

$$COS + OH \longrightarrow CO_2 + SH \tag{3.17}$$

The dominant sinks of COS are the assimilation by plants, and the absorption by soil as well as the reaction with OH (Equation 3.17).
In contrast to most other sulphur containing gases, which are comparatively short-lived, the long-lived COS, can be transported up to the stratosphere.

Sulphur Hexafluoride - SF_6

Sulphur Hexafluoride has a lifetime of about 3200 years. It has a large cross section for the absorption of terrestrial infrared radiation, consequently it is a potent

greenhouse gas. Presently, SF_6 generated by out-gasing processes of fluorides, leads to a natural background concentration of 0.01 ppt. Measurements show a total background of 4.2 ppt in 1998. SF_6 concentrations increased about 7% per year during the 1980s and 1990s. Anthropogenic sources are found predominantly in the Northern Hemisphere. Sinks constitute photolysis and ion reaction in the mesosphere. Today anthropogenic SF_6 plays also a role as a source of sulphur compounds in the stratosphere.

3.1.4 Sulphur Species and Climate - the CLAW-Theory

Sulphuric acid and methane sulphonic acid condense rapidly after their formation in the gas phase. They form small particles, which can serve as cloud condensation nuclei (CCN). In 1987, Charlson, Lovelook, Andreae and Warren developed a theory, the so called CLAW-theory [*Charlson et al.* 1987]. It states that the biological activity in the ocean (mainly phytoplankton) forms volatile sulphur compounds, mainly DMS. Due to air chemical oxidation processes, DMS is transformed into sulphuric acid or methane sulphonic acid. The low vapor pressure of H_2SO_4 and CH_3SO_3H lead to the formation of small particles with an average size of 0.07 μm, which serve as CCN's. In wide parts of the oceans the CCN concentration is so low that cloud formation is limited not by water vapor, but by the CCN concentration. Hence, DMS emission leads to increased cloud albedo. Enhanced cloud-cover cools the surface ocean leading to less DMS production. Because DMS and ocean surface temperature are positively correlated, according the CLAW-hypothesis, the ocean causes a negative feedback which stabilizes the Earth's temperature. If correct, it means that the phytoplankton is able to regulate the climate via production of DMS (included in GAIA[3]). This theory has not been proven and is still under discussion. One could argue that the concentration of sulphur compounds in the northern hemisphere has increased significantly in the last century due to anthropogenic emissions and has a larger abundance than the natural DMS emissions. It could not be shown that the cloud albedo or temperature has obviously changed for that reason [*Schwartz* 1988].

3.2 Halogens in the Atmosphere

Halogens can be found in the 7th column of the periodic table. They have 7 electrons in the valence shell and need only one electron more to reach an inert gas configuration, therefore they are very reactive species. There are 5 halogens - Fluorine (F), Chlorine

[3]GAIA: In the 1970s first released as a hypothesis by J. E. Lovelock as the notion of the biosphere as an adaptive control system that can maintain the earth in a stage that is comfortable for life. It evolved into theory as a numerical basis was introduced. In its latest formulations, the theory proposes that life and the abiotic earth have evolved together (as the single entity Gaia) with emerging regulatory feedback mechanisms that kept surface environmental conditions. Lovelock named the science of Gaia Geophysiology. Although the Gaia theory is still being controversially discussed, it has been influential in the rise of earth system science.

(Cl), Bromine (Br), Iodine (I), Astatine (As), but only chlorine, bromine and iodine are of atmospheric importance [*Wayne et al.* 1995].

The importance of halogens in the atmosphere was revealed after the discovery of the ozone hole in the stratosphere.

Even after the discovery of the stratospheric ozone hole, halogen compounds were not thought to play a role in tropospheric chemistry. When sudden ozone losses were found in the PBL (Planetary Boundary Layer) and halogens were recognized to be responsible for the 'polar tropospheric ozone hole', this opinion had to be changed [*Barrie et al.* 1988].

The impact of halogens on the sulphur cycle and the mercury chemistry was also found to be significant [*Schroeder et al.* 1998; *von Glasow and Crutzen* 2003]. Reactive bromine is involved in the oxidation of DMS, and therefore influences the CCN budget and the oxidation of elemental mercury (Hg^0). The latter leads to the formation of highly toxic bioaccumulative Hg(II), which has a negative influence on human health and the ecosystem [*Ebinghaus et al.* 2002; *Lindberg et al.* 2002] in particular in regions enriched in reactive bromine like Arctic and Antarctica (see [*Platt and Hönninger* 2003; *von Glasow and Crutzen* 2003; *Simpson et al.* 2005], but could also play a role in vicinity of volcanoes.

Strong sources for the troposphere, especially of bromine and chlorine, were found and recycling mechanisms where discovered, which lengthen the lifetimes of active compounds in the troposphere. Discussions of the lifetime are far from complete and might be longer

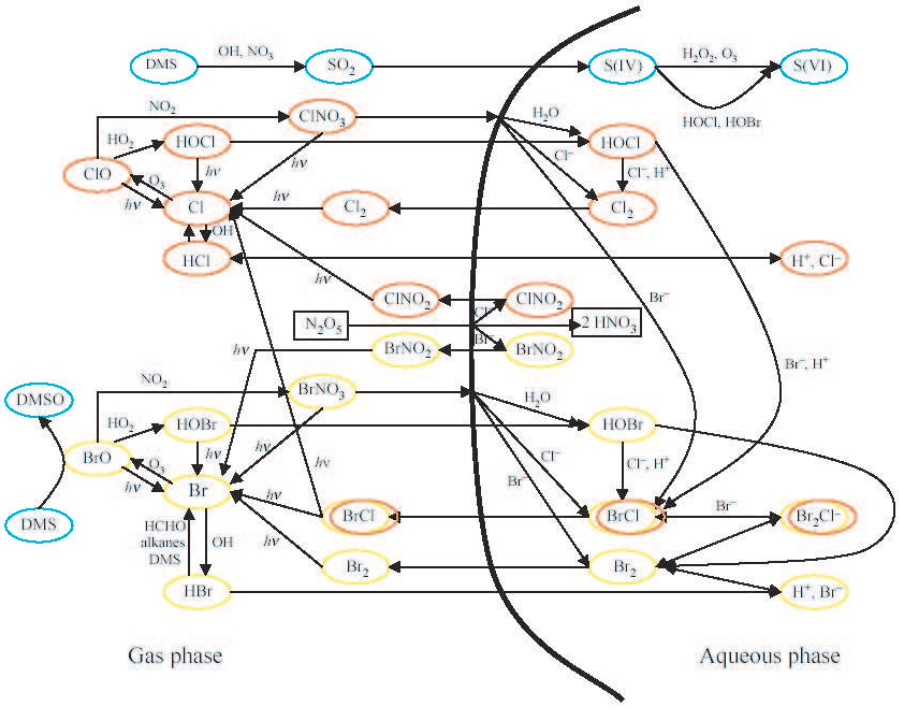

Figure 3.2: *The major homogeneous and heterogeneous reactions of bromine and chlorine. Adapted from von Glasow and Crutzen [2003]*

than originally thought because of several recycling processes. In the free troposhere, the lifetime of BrO was shown *Hollwedel* [2005] to be at least several days by, who could detect BrO several 1000 km from the expected source, due to transport processes.
Comparably low concentrations of halogens can already have a strong influence on tropospheric chemistry. Beside the interaction with the sulphur and mercury chemistry, they influence the oxidation power of the atmosphere, by the destruction of ozone and therefore the amount of OH available, and by indirectly and directly reacting with hydrocarbons [*von Glasow and Crutzen* 2003]. Figure 3.2 shows the main reaction pathways for chlorine and bromine in the troposphere. Also in the following sections the discussion will focus on the halogens chlorine and bromine, because they are the species of interest in this thesis. For a review on iodine chemistry see *Peters* [2005].

3.2.1 Reactive Halogen Species (RHS) in the Troposphere

Halogens and their oxides are key species in mechanisms that cause destruction of ozone [*Wayne et al.* 1995; *Tuckermann et al.* 1997; *LeBras and Platt* 1995; *Finlayson-Pitts et al.* 1990; *Barrie and Platt* 1997]. Halogen atoms X or Y (X, Y = Cl, Br,I), their oxides XO_n the hypohalous acids HOX, halogen molecules X_2, and the inter-halogens XY_n belong to the sum of Reactive Halogen Species (RHS). Reservoir species can be distinguished from the RHS due to the much lower reactivity. Reservoir species are halogen-NO_x (XNO_x) or hydrogen halides (HX). There are two main reaction cycles for ozone destruction in the PBL, one based on XO self- or cross-reactions, the other on reactions of XO with hydroperoxy radicals, HO_2. The main reaction schemes of Cl_2 and Br_2 are quite similar regarding tropospheric chemistry, therefore X or Y will be used as symbols for all halogen atoms (X, Y = Cl, Br, I). They can be distinguished because of differences in rate constants and different reaction channels. The most rapid reaction of halogen atoms is in fact a null-cycle

$$X + O_3 \longrightarrow XO + O_2 \tag{3.18}$$
$$XO + h\nu \longrightarrow X + O \tag{3.19}$$
$$XO + O \longrightarrow X + O_2 \tag{3.20}$$
$$O_2 + O + M \longrightarrow O_3 + M \tag{3.21}$$

In self or cross-reaction of XO instead of photolysis, two ozone molecules are converted into three oxygen molecules. However, this reaction cycle is only of importance for high amounts of XO

Cycle I (XO-cycle):

$$X + O_3 \longrightarrow XO + O_2 \tag{3.22}$$
$$Y + O_3 \longrightarrow YO + O_2 \tag{3.23}$$
$$XO + YO \longrightarrow \text{products} \quad (\text{eventually } X + Y + O_2) \tag{3.24}$$
$$2O_3 \longrightarrow 3O_2 \tag{3.25}$$

BrO + ClO can also lead to OClO or BrCl [*Sander et al.* 2000]. The formation of OBrO was shown to be unimportant [*Rowley et al.* 2001]. For bromine this reaction cycle has first been suggested for ozone destruction in the stratosphere already in 1975 [*Wofsy et al.* 1975], but is not of a real significance there. Later it was proposed by *Barrie et al.* [1988] for the arctic troposphere. For chlorine, this reaction cycle plays a minor role for the troposphere but it is of importance in the stratosphere.
Cycle II is initiated by the reaction between XO and HO_2. It is preferred if the mixing ratio of XO is below 30 ppt. Hypohalous acid (HOX) is formed by reaction of halogen monoxide radicals (XO) with hydroperoxy radicals. HOX can then be photolyzed to produce halogen atoms, who can destroy ozone. The second product OH may also contributes to ozone destruction. HO_2 and XO are recycled, cycle II a catalytic destruction cycle of ozone.
Cycle II (HOX-cycle)

$$XO + HO_2 \longrightarrow HOX + O_2 \tag{3.26}$$
$$HOX + h\nu \longrightarrow X + OH \tag{3.27}$$
$$X + O_3 \longrightarrow XO + O_2 \tag{3.28}$$
$$OH + O_3 \longrightarrow HO_2 + O_2 \tag{3.29}$$
$$2O_3 \longrightarrow 3O_2 \tag{3.30}$$

The rate constants of Cycle I and Cycle II are summarized for Cl and Br in Table 3.5. XO can also react with organic peroxy radicals (RO_2, R = organic group) instead of HO_2, e.g. methyl peroxy radical (CH_3O_2)

$$XO + CH_3O_2 \longrightarrow HOX + CH_2O \tag{3.31}$$

For X = Br this reaction takes place in 80 % of the cases. An overview about the main reactions of bromine and chlorine is shown in Figure 3.2

Table 3.5: *List of rate constants and photolysis frequencies for reactions in two ozone destruction cycles. Photolysis frequencies are calculated for a solar zenith angle of 70 at 80 N and surface albedo of 0.9.*

Reaction	Rate constant k [$\frac{cm^3}{molec \cdot s}$] Photolysis frequency j [s^{-1}]	Reference
ClO + ClO → Products	k=1.2*10^{-14}	[Atkinson et al. 2003]
BrO + ClO → Products	k=1.3*10^{-11}	[Atkinson et al. 2003]
IO + ClO → Products	k=1.3*10^{-11}	[Atkinson et al. 2003]
BrO + BrO → Products	k=3.2*10^{-12}	[Atkinson et al. 2003]
BrO + IO → Products	k=6.9*10^{-11}	[Atkinson et al. 2003]
Cl * O_3 → ClO + O_2	k=1.2*10^{-11}	[Atkinson et al. 2003]
ClO + HO_2 → HOCl + O_2	k=5.6*10^{-12}	[Atkinson et al. 2003]
BrO + HO_2 → HOBr + O_2	K=2.1*10^{-11}	[Atkinson et al. 2003]
Cl_2 + hv → 2Cl	j=0.0021	[Röth et al. 1996]
BrCl + hv → Br + Cl	j=0.012	[Röth et al. 1996]
Br_2 + hv → 2Br	j=0.044	[Röth et al. 1996]
ClO + hv → Cl + O	j=4.2*10^{-6}	[Röth et al. 1996]
BrO + hv → Br + O	j=0.035	[Röth et al. 1996]
HOCl + hv → Cl + OH	j=1.8*10^{-4}	[Röth et al. 1996]
HOBr + hv → Br + OH	j=7.6*10^{-4}	[Röth et al. 1996]

3.2.2 Sources of RHS

There are still uncertainties about the sources of RHS, however three dominant sources in the troposphere are known:

1. halogens release from sea salt
2. photolysis of halogenated organic compounds
3. emission of volcanoes.

1) Halogen Release from Sea Salt

The first to propose halogen release from sea salt was *Holland* [1978]. A mechanism with a main role of heterogeneous reaction was described first by *Fan and Jacob* [1992], followed more comprehensively by *Mozurkewich* [1995], and then by *Sander and Crutzen* [1996], *Vogt et al.* [1996] and *Platt and Lehrer* [1997]. During the last years *Kirchner et al.* [1997], *Oum et al.* [1998] and *Fickert et al.* [1999] could prove them in laboratory measurements.
Sea salt consists of 55.7% Cl^-, 0.19% Br^- and 2 × 10^{-5}% I^- [*Holland* 1978]. The input

of halogens from sea salt into the atmosphere is certain, particularly over the oceans in form of aerosols or at coastlines and over sea ice surfaces, but the total amount remains uncertain [*Platt and Lehrer* 1997; *Wennberg* 1999].
Three different processes for the release of halogens from sea salt are possible. The first one is based on the release of trace gases like NO or N_2O_5 [*Finlayson-Pitts and Johnson* 1988; *Behnke et al.* 1993]. Therefore it is a very effective process in polluted areas with high NO_x concentrations.

$$(N_2O_5)_g + (NaX)_{aerosol} \longrightarrow (XNO_2)_g + (NaNO_3)_s \tag{3.32}$$

$$2(NO_2)_g + (NaX)_{aerosol} \longrightarrow (XNO)_g + (NaNO_3)_s \tag{3.33}$$

For heterogeneous reactions "*aerosol*" denotes aqueous species, "*g*" denotes gas phase compounds, "*s*" denotes solid compounds. In that case X is defined as Br or Cl. The first reaction is only a nighttime reaction, because N_2O_5 is rapidly destroyed (N_2O_5 thermalizes to NO_3 and NO_2, NO_3 is photolyzed) during daytime. The second reaction is very slow. This source of RHS is the only nighttime source ('dark soure'). XNO_2 and XNO can be photolyzed in the early morning hours

$$XNO_2 + h\nu \longrightarrow X + NO_2 \tag{3.34}$$

The second possibility is the release of halogen molecules from dissolved sea salt due to a halogen catalyzed mechanism. The sea salt aerosol has to be acidic and HOX must be taken up to the aerosol surface [*Vogt et al.* 1996; *Fan and Jacob* 1992].

$$HOX + X^- + H^+ \longrightarrow X_2 + H_2O \tag{3.35}$$

$$(X_2)_{aerosol} \longrightarrow (X_2)_g \tag{3.36}$$

$$(X_2)_g + h\nu \longrightarrow (2X)_g \tag{3.37}$$

Atmospheric reaction of halogen oxides with peroxy radicals leads to hypohalous acid (see Equation 3.25). For every HOX-molecule two halogen atoms are released, therefore it is an autocatalytic process and very effective for bromine.

The Bromine Explosion Mechanism

Uptake of HOBr on acidic salt surfaces leads to formation of halogen molecules (Reaction 3.35 X = Br).

$$HOBr + Br^- + H^+ \longrightarrow Br_2 + H_2O \tag{3.38}$$

When Br_2 is in the gas phase, it is photolyzed and oxidized (see reactions 3.22 and 3.37), the reaction can be summarized to:

$$BrO + (Br^-)_{aq} + (H^+)_{aq} + HO_2 + 2O_3 \longrightarrow 2BrO + H_2O + 3O_2 \tag{3.39}$$

Platt and Lehrer [1997]. Because of the exponential growth in BrO, the name 'bromine explosion' mechanism is often used. Acidity of pH < 6.5 (HCl, HNO_3, H_2SO_4) is required [*Fickert et al.* 1999]. According to the current understanding bromine is mainly released by autocatalytic processes and even preferred against chlorine, although much more chlorine is available. A chlorine explosion is unlikely because Cl is very ineffectively converted into HOCl. An iodine explosion couldn't be observed, probably because the concentration of iodine in sea salt is too low.
The third release mechanism is the attack of strong acids on halides.
For example:

$$H_2SO_4 + 2(NaX)_{aerosol} \longrightarrow 2HX + NaSO_4 \tag{3.40}$$

Because of heterogeneous reactions on (sea salt) aerosols of HX into reactive halogen species is possible. These are important in polar regions [*Vogt et al.* 1999; *McFiggans et al.* 2000] and in the marine boundary layer (MBL) [*Seisel and Rossi* 1997]

$$HOX + HX \longrightarrow X_2 + H_2O \tag{3.41}$$

2) Halogenated Hydrocarbons as a Source of RHS

Halogenated hydrocarbons (HHC) are emitted by natural and anthropogenic sources. Presently more than 3800 halogenated hydrocarbon species are known. An important natural source is the emission from algae in the ocean [*Schall and Heumann* 1993], but also volcanoes and other geothermal sources are not negligible [*Jordan* 2003]. A dominant anthropogenic source of HHC is biomass burning in the tropics. HHC can be photolyzed at low UV intensity in the PBL or upper troposphere. HHC are for example CH_3Br or $CHBr_3$ etc (see also Table 3.6). A large uncertainty remains in the global estimation.

3) Volcanoes

The third source of halogens - the volcanoes, will be discussed in detail in Chapter 9.3. Halogen Chemistry in Volcanic Plumes.

3.2.3 Sinks of RHS

The sinks of RHS can be divided into wet and dry deposition. Wet deposition means removal after solution in water-droplets of clouds or fog or on aerosol surfaces. Dry deposition of gaseous forms can be due to sedimentation processes or due to surface reactions. In that case, surfaces are not only the Earth's surface but also buildings, trees, etc. The first step

for a dominant removal of RHS in the atmosphere is the reaction with hydrocarbons (RH, R = organic radical, e.g. CH_3) or peroxy radicals (Hydroperoxyl, HO_2 and organic peroxy radicals, RO_2). These lead to the formation of hydrogen halides (HX). HX is soluble in water and wet deposition follows. The reaction with hydrocarbons is an important sink for chlorine:

$$Cl + RH \longrightarrow HCl + R \tag{3.42}$$

This reaction is very fast and for RH larger than CH_4 the only limitation is gas kinetics [*Atkinson et al.* 1997]. Bromine atoms react only with unsaturated hydrocarbons (olefines) or already oxidized compounds (e.g. C_2H_4), for instance formaldehyde (HCHO), forming hydrogen bromide [*Atkinson et al.* 1997; *Platt and Stutz* 1998]. Br atoms can be also added to the $C = C$ double bond of olefins, leading to organic bromine species or HBr. Bromine is mostly deposited as HBr. Reactions with nitrogen oxides are possible loss reactions for all halogen oxides. This reaction leads to the formation of $XONO_2$

$$NO_2 + XO + M \longrightarrow XONO_2 + M \tag{3.43}$$

This is, however, in most cases only a temporary sink, because the photolytic lifetime and also the lifetime due to collision of $XONO_2$ is of the order of minutes at tropospheric temperatures. Hydrolysis of $XONO_2$:

$$XONO_2 + (H_2O)_{liquid} \longrightarrow HNO_3 + HOX \tag{3.44}$$

3.2.4 BrO in the Atmosphere

A dramatic effect of bromine species in the remote boundary layer on ozone was discussed after measurements of *Barrie et al.* [1988], *Hausmann and Platt* [1994], *Tuckermann et al.* [1997] and *Martinez et al.* [1999]. BrO is a key species of tropospheric ozone destruction. Satellite and ground-based measurements showed that in both hemispheres at polar regions low ozone episodes are observed during high BrO events [*Wagner and Platt* 1998; *Wagner* 1999; *Richter et al.* 1998; *Hollwedel* 2005]. High bromine monoxide concentrations coincidencing with ozone depletion were also detected at salt lakes like the Dead Sea, Great Salt Lake and the Salar de Uyuni [*Hebestreit et al.* 1999; *Stutz et al.* 1999; *Matveev et al.* 2001; *Hönninger et al.* 2004] as well as in mid altitudes during the Polarstern traverse [*Leser* 2001] at the Caspian Sea [*Wagner et al.* 2001] and at volcanic sites [*Bobrowski et al.* 2003; *Bobrowski and Platt* 2005; *Lee et al.* 2005; *Galle et al.* 2005]. It appears likely that a background concentration of 1 - 2 ppt BrO exists in the free troposphere [*Platt and Hönninger* 2003]. Evidence for free-tropospheric BrO comes from balloon-borne measurements and from comparison with satellite data [*Fitzenberger et al.* 2000; *Harder et al.* 1998]. Many investigations have already been carried out, but still several questions remain

for source and sink mechanisms and the total influence of reactive bromine, especially at mid latitudes. For a detailed review see *Platt and Hönninger* [2003] and *von Glasow and Crutzen* [2003].

3.2.5 Sources and Cycles of BrO

Halocarbons are emitted from natural sources (for a detailed review see *Gribble* [2003]) and can serve as precursors for reactive bromine compounds in the troposphere. Typical mixing ratios and lifetimes of halocarbons are given in Table 3.6. Volatile brominated organic substances are emitted by macroalgae and phytoplankton in the ocean. Supersaturation of volatile brominated organic substances is quite common at the ocean surface. Due to the ocean-atmosphere exchange bromohydrocarbons get into the troposphere [*Reifenhäuser and Heumann* 1992]. Methyl bromide (CH_3Br), the most simple form of bromohydrocarbons, has both natural and anthropogenic sources. Anthropogenic sources of halocarbons are fumigation of soils, burning of leaded gasolines [*Thomas et al.* 1997] and biomass burning. Also volcanoes are observed to be emitter of organohalogens, besides their emission of inorganic halides. The volcanic emission of organohalogens play probably no important role for the global atmospheric budget, but on a regional scale, the volcanic emissions can exceed most other sources - e.g. a mean mixing ratios of 218 ppb CH_3Br was measured at Mauna Loa [*Jordan* 2003]. For a more detailed review see *Jordan* [2003].
The lifetime of organobromine compounds is of the order of a month to about one year.
Sudden increases of reactive bromine up to 10 ppt/h observed in the arctic boundary layer

Table 3.6: *Lifetimes and typical mixing ratios of brominated hydrocarbons.*

compound	typ. mixing ratio [ppt]	approx. lifetime
CH_3Br	10^a	8 $month^a$
CH_2Br_2	$< 1.5^c$	4 $month^b$
CH_2BrCl	$< 0.5^c$	5 $month^d$
$CHBr_2Cl$	0.8^f	1.2 $month^d$
$CHBr_3$	6^f	1.2 $month^e$
$CHBrCl_2$	$< 0.5^c$	1.2 $month^d$

[a] *Yvon and Butler* [1996] [b] *Mellouki et al.* [1992]
[c] *Schall and Heumann* [1993] [d] *Bilde et al.* [1998]
[e] *Moortgat et al.* [1993] [f] *Carpenter et al.* [1999]

during polar spring and the measured mixing ratios of up to 180 ppt BrO at the Dead Sea [*Matveev et al.* 2001; *Hebestreit et al.* 1999; *Hebestreit* 2001] cannot be explained by atmospheric abundances and degradation rates of organobromine compounds. The details of the processes leading to such high reactive bromine releases are still under investigations, but the main sources seem to be the surfaces of sea ice in polar regions (sea salt) or

salt pans in the case of the high values in midlatitudes. It is presently assumed that the bromine explosion mechanism is responsible for these high reactive bromine amounts.
An exponential increase of BrO is only possible as long as the release of Br_2 is preferred to that of BrCl [*Fickert et al.* 1999] and enough ozone is available. In addition for the bromine explosion mechanism to proceed, special conditions are needed that prevent mixing of air of the PBL with air from the free troposphere. These conditions are satisfied during strong inversion layer conditions such as occur in late winter and early spring season in polar regions. Light and surfaces are also essential components for this reaction cycle and further a small amount of BrO to initiate the mechanism. The source of these small amount of "seed" BrO to start the explosion is of much debate.
Volcanoes were recently discovered as source of reactive bromine [*Bobrowski et al.* 2003] and are under investigation in this thesis. Therefore, a more detailed description regarding the volcanic processes is presented in Chapter 8.4.

3.2.6 Sinks of BrO

The main sink reactions of BrO are summarized here:

$$BrO + BrO \longrightarrow 2Br + O_2 \tag{3.45}$$
$$BrOh\nu \longrightarrow Br + O \tag{3.46}$$
$$BrO + HO_2 \longrightarrow HOBr + O_2 \tag{3.47}$$
$$BrO + NO \longrightarrow NO_2 + Br \tag{3.48}$$
$$BrO + HCHO \longrightarrow HOBr + CHO \tag{3.49}$$
$$BrO + NO_2(M) \leftrightarrow BrONO_2 \tag{3.50}$$
$$BrONO_2(OH^- surface) \longrightarrow NO_3^- + Br \tag{3.51}$$
$$BrONO_2(h\nu) \longrightarrow NO_3 + Br \tag{3.52}$$
$$BrONO_2(H_2O) \longrightarrow HNO_3 + HOBr \tag{3.53}$$

The HOBr is photolyzed to Br and OH quite rapidy.
Figure 3.2 shows a more detailed set of reactions forming bromine radicals or bromine molecules. Photolysis limits the lifetime of BrO to 30-100 s for typical daytime UV levels. The BrO self reaction is inversely proportional to the square of the BrO concentration and leads to a lifetime in the order of minutes for concentrations of several 10s of ppt. As long as ozone is available, the bromine atom reacts to BrO in less than a second [Zellner, 1999] and therefore BrO is the main bromine species. The reaction of bromine atoms with ozone does not depend on sunlight and can lead to bromine destruction during night as long as the BrO is formed back to Br. The reaction to Br_2 leads to termination of the ozone destruction cycle because Br_2 serves as a nighttime reservoir for bromine species. Measurements in the field show that BrO rapidly decays to zero approximately 30 min

after sunset [*Peters* 2005]. However, soon after sunrise the Br_2 reservoir provides a source for single bromine atoms that are quickly converted to BrO.
Most of the bromine radicals react with ozone. Other reaction with bromine are:

$$Br + HCHO \longrightarrow HBr + CHO \tag{3.54}$$

$$Br + HO_2 \longrightarrow HBr + O_2 \tag{3.55}$$

and reactions with other aldehydes, alkenes [*Bedjanian et al.* 1998] or olefins. They lead to the only relevant loss mechanism by dry or wet deposition of HBr and therefore to a lifetime of BrO of several hours. Additionally HBr can be recycled by the reaction with OH but this is a rather slow reaction. Up to this point only gas phase reaction have been considered, but since heterogeneous reactions play a role, deposited bromine can be recycled by HOBr reactions as in the bromine explosion. BrO could be an important species for DMS losses [*Toumi* 1994; *Platt and Stutz* 1998]).

$$BrO + DMS \longrightarrow Br + DMSO \tag{3.56}$$

Additionally reactive bromin species oxidize Hg^0 in reactions that may act as sinks of Br as well as BrO. The presence of so many reactions makes a straight forward calculation of the atmospheric lifetime of BrO difficult. Model studies by von Glasow et al. [2004] show a lifetime of 1-2 weeks for inorganic bromine in the free troposphere.
For more detailed description of atmospheric bromine chemistry see *Platt and Hönninger* [2003] or *von Glasow and Crutzen* [2003] and references therein.

3.3 Volatiles and exsolved Gases of Melts

Volcanic gases contribute to the characteristics, the time and the nature of volcanic eruptions. To interpret the gas composition measured at volcanic sites it is necessary to consider the sources and solubility of volatile compounds in melts. The rate of emissions are further controlled by the physical mechanism of (a) transfering of magma to or at least near to the surface and (b) separating the gas from the bubbly magma. The gases emitted by volcanic activity can affect the atmosphere on Earth for years and also in time ranges of more than 1 Myr. They can impact climate, the hydrosphere, the biological as well as the terrestrial cycle. The volcanic gases are responsible for the development of the Earths life. For the climatic influence today, the emitted sulphur species play the most significant role, especially the emission into the upper atmosphere. Studying the volcanic gases is not only of interest for the atmosphere, volcanic gases can be also seen as "telegrams from Earths interior" as expressed by *Matsuo* [1975] and they are a hazard for the health of humans, animals and plants, due to the effects on the respiratory system. The origin of the volcanic gases is the earths interior, but they are also strongly influenced by recycling processes.

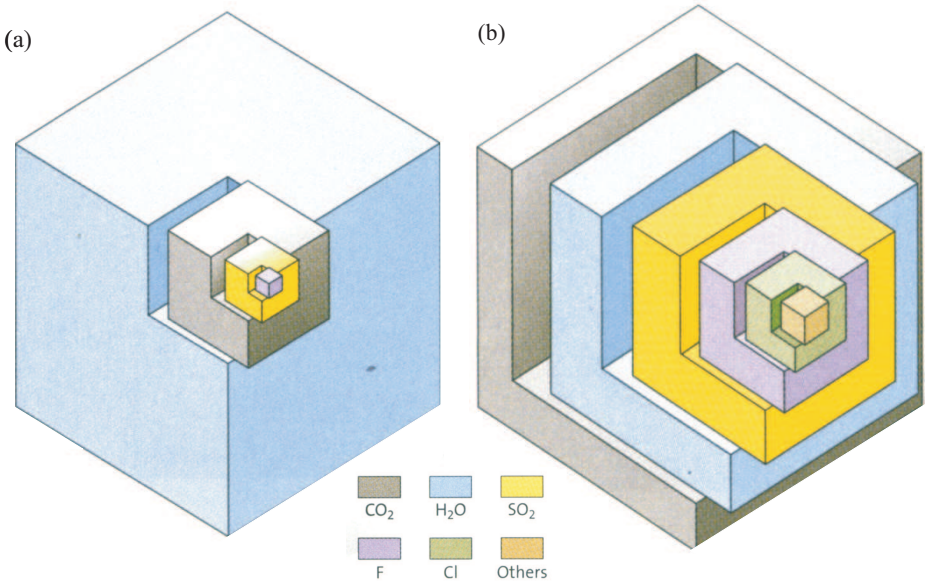

Figure 3.3: *Volatile composition of (a) basaltic and (b) rhyolitic magmas. Adapted from Schmincke, 2004*

Nevertheless, at least a trend between the tectonic environment and the emitted volatiles can be observed (see Table 3.7 for a summary of current knowledge). Convergent plate volcanoes tend to have a higher water and chlorine content than rift volcanoes and hot-spot volcanoes. The magma source of convergent plate volcanoes is usually influenced by crustal material. Divergent plate volcanoes are mainly fed from magma originating in the mantle. As illustrated in Figure 3.3, water is the principal volatile species in the magma, followed by CO_2, H_2S, SO_2, H_2, Cl, F, and more minor species like heavy metals. A short overview about the main volatile compounds and their properties will be given in following section. This overview is not providing a complete state of the current knowledge, but will give a "feeling" for the present and the missing parts of the impact of volcanic gases.

3.3.1 Water - H_2O

The impressive view of a steaming volcano is mainly caused by water vapor. But usually only to a minor fraction of this vapor is of magmatic origin, a much larger part results from heated ground, surface or atmospheric water. Nevertheless the water content of magma plays a fundamental role because it determines the acceleration and mass rate of an explosive eruption column and exerts a fundamental content over the style of eruptive activity. In the magma body the water can be found in the form of H_2O or hydroxyl ions OH^-. At low dissolved water (H_2O and OH^-) concentration, nearly all of it occurs in the form of

Table 3.7: *Summary of typical volatile abundances of magmas in different tectonic settings. The values reported in the Table are generally for the melt phase (dissolved) though true bulk volatile abundances for a magma would sum additionally volatiles in the crystallized phase and separated gas phase. Adapted from Oppenheimer [2004] and references therein.*

	Mid-ocean ridge basalt (MORB, e.g., Mid Atlantic Ridge, East Pacific Rise)
H_2O	<0.4-0.5 wt %, typically 0.1-0.2 wt.%; enriched MORB (E-MORB) up to < 1.5 wt.%
CO_2	50 - 400 ppm; typically saturated at eruptions (gas phase almost pure CO_2) leading to vesiculation
S	800 - 1500 ppm; immiscible Fe-S-O liquids indicate saturation at eruption
Cl	20-50 ppm in most primitive MORB, occasionally much higher due to assimilation of hydrothermal altered rocks
F	100-600 ppm
	Ocean island basalt (OIB, e.g., Kilauea, Galapagos, Reunion)
H_2O	0.2-1 wt. %; e.g. Hawaii 0.4-0.9 wt. % (Dixon et al)
CO_2	2000-6500 ppm for Hawaii
S	up to 3000 ppm; 200-2900 ppm for Hawaii
Cl	comparable to MORB; Kilauea estimate around 90 ppm
F	comparable to MORB; Kilauea estimate around 35 ppm
	Arc basalt (island arc basalt and continental margin basalts, e.g., Cerro negro, Marianas)
H_2O	up to 4-6 wt. % (e.g., see Roggensack et al (1997 on Cerro Negro), largely sourced from subducted slab; crustal assimilation another potential source, especially for arcs built on continental crusts
	Back arc basin basalt (BABB, e.g., Lau Basin)
H_2O	1-3 wt. %; generally speaking, intermediate between MORB and island arc basalts
	Andesites (e.g, Soufriere Hills Volcano) Note that it is particularly difficult to quantify pre-eruptive volatile contents of adesites because most are erupted subaerially (i.e., at atmospheric pressure) after significant degassing has taken place, and contain abundant phenocrysts (e.g., > 30 wt. %) such that liquid composition are more silicic (often rhyolitic) than bulk rock. Also, good host minerals for melt inclusion (e.g. olivine and quartz) are rare, and mineral disequilibria hamper experimental work
H_2O	> 3 wt. %
CO_2	10 - 1200 ppm
S	< 1000 ppm; typically 200-400 ppm
Cl	can be high, e.g., 1500 ppm not unusual; (5000 ppm or more in phonolites)
F	< 500 ppm
	Dacites and rhyolites (e.g., Mount St. Helens 1980, Pinatubo, 1991, Bishop Tuff)
H_2O	typically 3-7 wt. %; e.g., 4.6 wt % dissolved for Mount St. Helens 1980, 6-7 wt. % for pinatubo 1991; there is strong evidence for vertical gradients in both dissolved and exsolved H_2O and CO_2 in preeruptive magmas
CO_2	often below detection limits
S	typically < 200 ppm (75 ppm for Pinatubo, 1991) but melt often saturated with sulfide (pyrrhotite) or sulfate (anhydrite) crystalline phases
Cl	600 - 2700 ppm in metaluminous dacites and rhyolites ; 67000 ppm in trachytes; 9000 ppm in peralkaline rhyolites (pantellerites); 1100 ppm for Pinatubo 1991
F	200 - 1500 ppm in metaluminous dacites and rhyolites; up to 1.5 wt. % in peralkaline rhyolites (oantellerites)

OH^-. By analysis of the crystallization (content of Amphibole, Mica) the water content of the magma can be at least qualitatively determined. There exists a high variability of the water content between different magma types. The solubility is higher in more evolved magma and is proportional to the square root of pressure [*Burnham* 1979]. Magma along subduction zones is rich in water, but depleted in CO_2. Today a good qualitative knowledge about the water content in magma is achievable, but quantitative measurements are still difficult and only estimations can be given (see Table 3.8).

Table 3.8: *Approximate H_2O - concentrations in natural magmas derived from the analysis of quenched glasses, glass inclusions in minerals and of experimental studies on the stability of OH-containing phases and the maximum solubility of H_2O in natural magmas. Adapted from Schmincke [2004].*

Magma Composition	H_2O conncentration wt %
MORB (tholeiites)	0.1 - 0.2
Island tholeiites	0.3 - 0.6
Alkali basalts	0.8 - 1.5
Basalts above subduction zones	2 - 4
Basanites and nephelinites	1.5 - 2
Andesites - dacites(island arcs)	1 - 3
Andesites - dacites (convergent continental margin)	2 - 5
Rhyolithes	up to ca. 7

3.3.2 Carbon Dioxide - CO_2

Regarding its mass, CO_2 is the most important volatile compound in magma. The CO_2 degassing of volcanoes is in comparison to other CO_2 sources rather small with only 0.4% of the anthropogenic emissions [*Gerlach* 1991]. CO_2 has a high partial pressure and a very low solubility, which is highly dependent on the magma composition [*Sigurdssun* 2000]. Depending on the pressure, CO_2 can be found in gaseous form or, at low pressure as CO_2 anions and metal carbonate (CO_3^{2-}). The solubility of the CO_2 shows a negative temperature dependence [Blank 1999].
That CO_2 emissions have a large potential of hazard which was displayed by two catastrophic CO_2 releases in Cameroon during the 1980s, - Lake Monoun (1984) and Lake Nyos (1986). CO_2 emission are also a good measure of the activity state of a volcano, but can up to now hardly be used as indicator due to the technical problems of remote sensing methods to detect CO_2 in the presence of the high atmospheric background. Continous monitoring is a desirable but not an easy goal to achieve.

3.3.3 Sulphur Dioxide SO_2 and Hydrogen Sulfide H_2S

Most easily noticeable by our senses and also by measurement instruments are the sulphuric gases. The sulphur content of a magma is strongly dependent on the abundance of iron and silica. Although a lot of measurement techniques can be applied to measure sulphur bearing gases, exact values for pre-eruption concentrations are difficult to achieve. The solubility of sulphur is highly complicated because of the formation of sulfides as well as sulfates [*Sigurdssun* 2000]. In general, sulphur is abundant in magma in the reduced

form (S(2-) or as sulfide) but mostly the magma is enough oxidized that the abundant sulphur in the magma is dominated by the abundance of S(4). Sulphur degasses mainly as SO_2 or H_2S, but only a minor fraction of the degassing sulphur can usually be explained from the solution found in magma. It is assumed that SO_2 and other sulphur gases are enriched by a separated gas phase which can be released prior to or during eruptions. The ratio of SO_2 to H_2S strongly depends on the composition, the degree of oxidation and the temperature of the magma. It is assumed that during increasing differentiation of magma the oxidation increase and therefore also the S(6+)/S(2-) ratio increases. Beside SO_2 and H_2S also minor fractions of CS_2 and COS are emitted by volcanoes. The increased emission of SO_2 is often an evidence of rising magma, because the decreasing pressure when magma rises, the solubility of sulphur decreases and bubbles are formed. A decrease of the SO_2 flux is much more difficult to interpret, since it could either be a sign of depletion of volatiles in the magma body, in the case of no new magma replacements, or it could show a decrease of the permeability of the plumbing system, which leads to increasing pressure and enhancement of eruption probability.

3.3.4 Halogens

The primary emitted halogens are HCl, HF and HBr. Trace quantities of HI are also emitted [*Aiuppa et al.* 2005]. Data for halogen emission of volcanoes are sparse (See Table 3.9). The relative abundance of halogens in the gas phase cannot simply be explained by

Table 3.9: *Parameters determining the abundance of halogens in magmatic gases and fluxes of hydrogen halides. Adapted from Jordan [2003] and references therein. In some settings (for example Etna) the concentration might be higher; (a) Aiuppa et al. [2005].*

	F	Cl	Br	I
concentration in magmatic rocks (ppm)	basalt: 50 - 300 andesites: 240 - 640 rhyolithes: 400 - 640	basalt: 50 - 200 andesites: 1000 - 1800 rhyolithes: 600 - 1900	50 ppb-2500 ppb	4 - 11 ppb
Fluid/melt partitioning coefficient	$\ll 1$	8 - 10	3.7 - 17.5	104
Global hydrogen halide fluxes [kt/a]	60 - 6,000	400 - 11,000	1 - 50	0.03 - 1 [0.1[a]]
Molar ratio chlorine/ other halogen	2 - 100	1	75 - 2500	10000
Bond dissociation energy (kJ mol^{-1})	569.9	431.6	366.3	298.4

the content in the magma, several factors including reactivity and solubility will affect the emission and are therefore included in Table 3.9. The halogen content of alkaline basalt shows lower values in comparison to subalkaline (Tholeithe) magma. Investigated composition of glasses and melts indicate HCl emissions between 10^{-3} kt to 1 kt for mid ocean ridge basalts and between 1 kt to 100 kt in andesite rhyolitic magma [*Sigurdssun* 2000]. Halogens have a high solubility in magma, which increases with an increasing ratio of (Na + K)/M. The magma is often not saturated in its chlorine content and therefore a release of only 20 - 50 % during an eruption is observed. Fluorine is even more soluble than chlorine and therefore thought to be even less released during eruptions.

Chapter 4

The DOAS Technique

Differential Optical Absorption Spectroscopy (DOAS) is a widely applied method for the detection of a large number of trace gases (see Figure 4.3), e.g. NO_2, NO, NH_3, ClO, IO, O_3, SO_2, CS_2, HCHO and most aromatic hydrocarbons. A number of species were detected with the DOAS technique for the first time: HONO, OH, NO_3, BrO, IO in the troposphere and OClO and BrO in the stratosphere. A great advantage of the DOAS is its ability to determine the concentration of several trace gases simultaneously without disturbing their chemical behaviour. In this chapter the principle of DOAS will be introduced, starting with a short general introduction on absorption spectroscopy and followed by a mathematical description and explanation of some atmospheric and electronic side effects. Finally the Multi-AXis-DOAS (MAX-DOAS) measurement technique, which was applied during this study, is described in more detail.

4.1 Absorption Spectroscopy

Spectroscopy is well suited to analyze the chemical composition of gases. It has played an important role in the discovery of the physical and chemical properties of the Earth's atmosphere for more than the last 100 years. Most studies used the analysis of atmospheric absorptions and this is still the case in most current applications of atmospheric spectroscopy. However, the use of emission bands is also possible, but is restricted to the thermal infrared wavelength region or to the excited gas molecules in the upper atmosphere. These molecules also emit light at higher energies, i.e. shorter wavelengths. Both of these applications are in use today, but are not the focus of this thesis.

4.2 Beer-Lambert Law

The basis of spectroscopic measurements is Beer-Lambert's law, which describes the absorption of electromagnetic radiation by matter (Figure 4.1). In this case the absorption

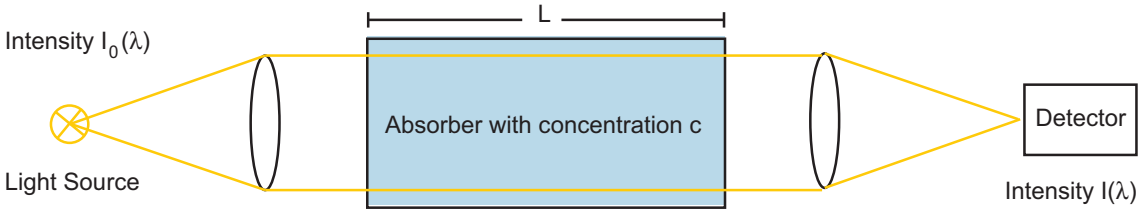

Figure 4.1: *Light with the initial intensity $I_0(\lambda)$ is emitted by a light source. After passing through a volume of air containing an absorber with concentration c, the detector measures the reduced intensity $I(\lambda)$. Adapted from [Sebastian 2004].*

of light occurs by passing through the atmosphere. A simplified form of the Beer-Lambert law can be written as:

$$I(\lambda) = I_0(\lambda) \cdot e^{-L \cdot \sigma(\lambda) \cdot c} \tag{4.1}$$

where $I_0(\lambda)$ denotes the initial intensity of a light beam emitted by a suitable light source. $I(\lambda)$ is the radiation intensity of the beam after passing through a layer of thickness L which contains the absorber at a uniform concentration c. The absorption cross section $\sigma(\lambda)$ at the wavelength λ is a characteristic property of all species. If the light-path length L and the cross section σ of a trace gas for the given wavelength is known (and if a constant temperature can be assumed for the light path), the average trace gas concentration c can be calculated from the measured ratio $I_0(\lambda)/I(\lambda)$:

$$c = \frac{ln\left(\frac{I_0(\lambda)}{I(\lambda)}\right)}{\sigma(\lambda) \cdot L} = \frac{D}{\sigma(\lambda) \cdot L} \tag{4.2}$$

The intensities, $I_0(\lambda)$ before and I(λ, L) after the light passing through the matter, are directly proportional. The negative exponent of the proportionality factor is the so-called "Optical Density" of a layer of a given absorber:

$$D = ln\left(\frac{I_0(\lambda)}{I(\lambda)}\right) \tag{4.3}$$

Equation 4.3 is the basis of most absorption spectroscopic applications in the laboratory. In this ideal situation the intensities $I(\lambda)$ and $I_0(\lambda)$ can be simply determined by measurements with and without the absorber in the light beam. But in the open atmosphere, the true intensity $I_0(\lambda)$, as it would be received from the light source in the absence of any atmospheric absorber, is difficult to determine. The absorbing gas cannot be simply removed from the air. The DOAS method overcomes this problem by measuring the so called "differential" absorption, i.e. the difference between the absorption at two different wavelengths. This principle - the DOAS principle - will be described in the following sections.

4.3 The DOAS Principle

As mentioned in section 4.2 the fundamental equation of absorption spectroscopy is the Beer-Lambert's law. When measuring atmospheric trace gases in the open atmosphere, the simple version of Beer - Lambert's law has to be modified. In order to describe the processes in the earth's atmosphere correctly, we have to account for multiple absorbers and scattering processes e.g. Mie scattering from aerosol particles and Rayleigh scattering from air molecules. Including these processes the equation of Beer-Lambert law changes to:

$$I(\lambda, L) = I_0(\lambda) \cdot exp(-\int_{l=0}^{l=L} (\sum_i \sigma_i(\lambda, T, p) \cdot c_i(l) + \epsilon_M(\lambda, l) + \epsilon_R(\lambda, l))\, dl) \qquad (4.4)$$

where for each trace gas i σ_i denotes the absorption cross section (which depends on the temperature T, the pressure p, and the wavelength λ). $c_i(l)$ is the concentration at the position l along the light path of total length L. The Rayleigh- and Mie-extinction coefficients are described by $\epsilon_R(\lambda, l)$ and $\epsilon_M(\lambda, l)$, respectively.

Another difficulty arises from the determination of the true intensity of $I_0(\lambda)$. It would

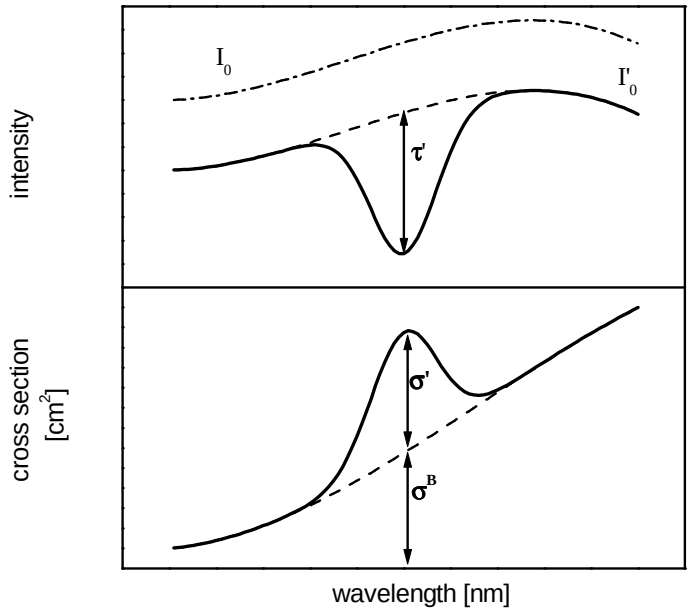

Figure 4.2: *The basic principle of DOAS. Only narrow absorption structures are considered. The differential cross section σ' corresponds to the differential optical density D'.*

be required to remove the atmosphere in order to determine $I_0(\lambda)$ exactly (or in the case of using the sun as light source, $I_0(\lambda)$ would have have the possibility to be measured from space). Therefore the basic idea of DOAS is to separate the narrow band differential

absorption of trace gases $\sigma^{'}(\lambda, T, p)$ from the broad band contribution $\sigma_B(\lambda, T, p)$ which varies only slowly with wavelength as illustrated in Figure 4.2.

$$\sigma(\lambda, T, p) := \sigma^{'}(\lambda, T, p) + \sigma_B(\lambda, T, p) \tag{4.5}$$

In Figure 4.2 this separation is shown for both the light intensity and the absorption cross section. Equation 4.4 can now be written as:

$$\begin{aligned} I(\lambda, L) &= I_0(\lambda) \cdot exp(-\int_{l=0}^{l=L} (\sum_i ((\sigma_i^{'}(\lambda, T, p) + \sigma_{B,i}(\lambda, T, p)) \cdot c_i(l) + \epsilon_M(\lambda, l) + \epsilon_R(\lambda, l))\, dl) \\ &= I_0^{'}(\lambda) \cdot exp(-\int_{l=0}^{l=L} \sum_i \sigma_i^{'}(\lambda, T, p) \cdot c_i(l)\, dl) \end{aligned} \tag{4.6}$$

where $I_0^{'}(\lambda)$ is composed of the intensity of the light source (sunlight in this study), broad absorption features of the trace gases, and the Rayleigh- and Mie-extinction, which can be assumed to be only slowly varying with the wavelength.

For the investigation of the trace gases only the differential (i.e. rapidly varying with λ) cross section is of importance. A differential optical density can be defined as:

$$D^{'} = \ln\left(\frac{I_0^{'}(\lambda)}{I(\lambda, L)}\right) \tag{4.7}$$

With $D^{'}$ it is possible to determine the slant column density S_i, of trace gas number i, which is the integrated concentration along the light path:

$$S_i = \int_{l=0}^{l=L} c_i(l)\, dl \tag{4.8}$$

In atmospheric measurements, not only one species i is causing light attenuation. The weakening of light is the sum of the contribution of several trace gases and scattering processes (see equation 4.4 or 4.6). In practice, the number of absorbers i can be limited to those trace gases with absorption features sufficiently strong to be detectable with the DOAS instrument. The strength of the absorption features varies with the wavelength, therefore the number of trace gases to be included in the analysis varies with the observed wavelength interval and the trace gas composition of the investigated air mass. Typically up 10 trace gas absorptions can be identified in a single atmospheric DOAS spectrum [*Platt* 1994]. The SCDs of these trace gases can therefore be measured simultaneously. To retrieve the concentrations, the superimposed absorption features have to be separated numerically. The absorption cross section of many gaseous species are unique like a fingerprint. Some examples of trace gas absorption features are shown in Figure 4.3. The atoms

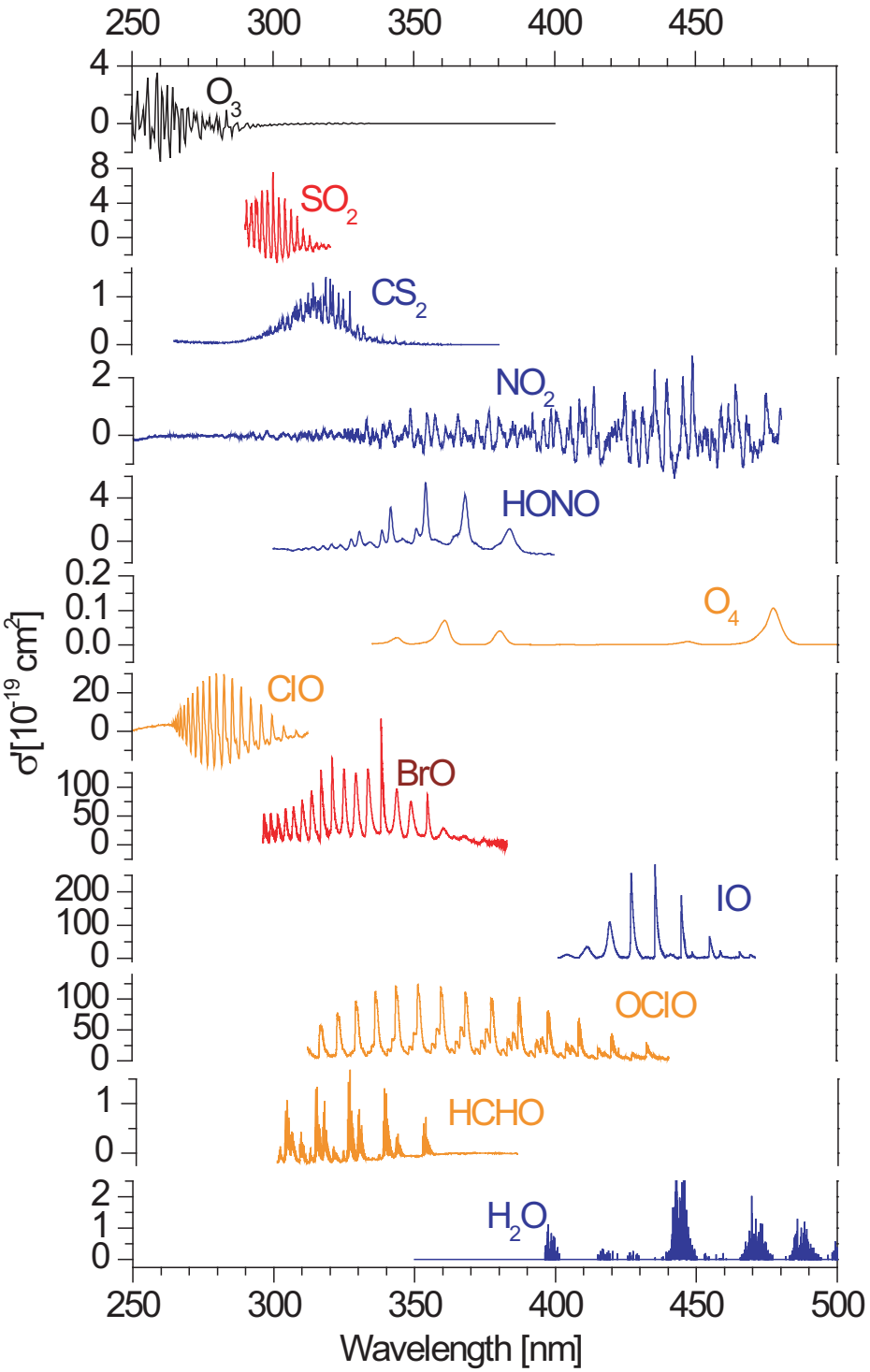

Figure 4.3: *Cross sections in the UV/Vis wavelength range of interest for volcanic gas studies, The cross section of the trace gases, which are the main objects in this thesis are red. Gases represented by the orange colored cross sections were also under investigation while those with the blue colored cross sections are aimed for future research. In black, there is little chance for future research by MAX-DOAS in volcanic plumes.*

and molecules of the different gases in the atmosphere absorb light (electromagnetic radiation), which induces electronic transitions and excites rotational and vibrational levels. Due to the different moments of inertia and different strengths of bonding (dependent on the wavelength of the light), different absorption patterns can be recognized for every trace gas which becomes excited (see e.g. Figure 4.3).

4.4 The Measurement Principle

Figure 4.4 shows simplified the DOAS measurement principle. Starting from the top of Figure 4.4 (a) light source with intensity I_0 is necessary for the measurements. In this study the sun was used as a light source - the so called passive DOAS-technique. Also other light sources, mainly artificial ones for instance halogen or xenon lamps are useable ("active" DOAS-technique). The light passes through the atmosphere and attenuation takes place due to absorption or scattering by air molecules and aerosol particles. Figure 4.4 (a) shows the spectrum of the light with intensity $I(\lambda, L)$ entering the spectrograph under the assumption that the only absorber present in the air mass is formaldehyde (HCHO). The light is collected by a telescope and sent to a spectrograph-detector system through a quartz glass optical fibre. The resolution of the spectrograph is limited, therefore the spectral resolution of the spectrum I(λ, L) is degraded. This process can mathematically be described by a convolution of I(λ, L) with the instrument function H of the spectrograph.

$$I^*(\lambda, L) = I(\lambda, L) * H = \int I(\lambda', L) \cdot H(\lambda - \lambda')\, d\lambda' \tag{4.9}$$

where $I^*(\lambda, L)$ is the convoluted spectrum shown in Figure 4.4 (b). In the case of a multichannel detector (as used in this study) the wavelength range is divided into n discrete pixels, each integrating the light in a wavelength interval $\lambda(i)$ to $\lambda(i+1)$. In Figure 4.4 (c) a discrete spectrum $I'(i)$ is shown as it is recorded and stored with a computer.

$$I'(i) = \int_{\lambda(i)}^{\lambda(i+1)} I^*(\lambda', L)\, d\lambda' \tag{4.10}$$

where the wavelength interval is given by the wavelength-to-pixel mapping Γ_I of the instrument. The spectral width of a pixel $\Delta\lambda(i) = \lambda(i+1) - \lambda(i)$ is constant if the dispersion is linear: $\Gamma_I : \lambda(i) = \lambda(0) + \gamma_0 \cdot i$. In general Γ_I can be approximated by a polynomial:

$$\Gamma_I : \lambda(i) = \sum_{k=0}^{q} \gamma_k \cdot i^k \tag{4.11}$$

The wavelength-to-pixel mapping is determined by the parameter vector (γ_k). While a change in parameter γ_0 causes a spectral shift of the spectrum, changing parameter γ_1 results in a linear stretch or squeeze and changing parameters with higher k values cause

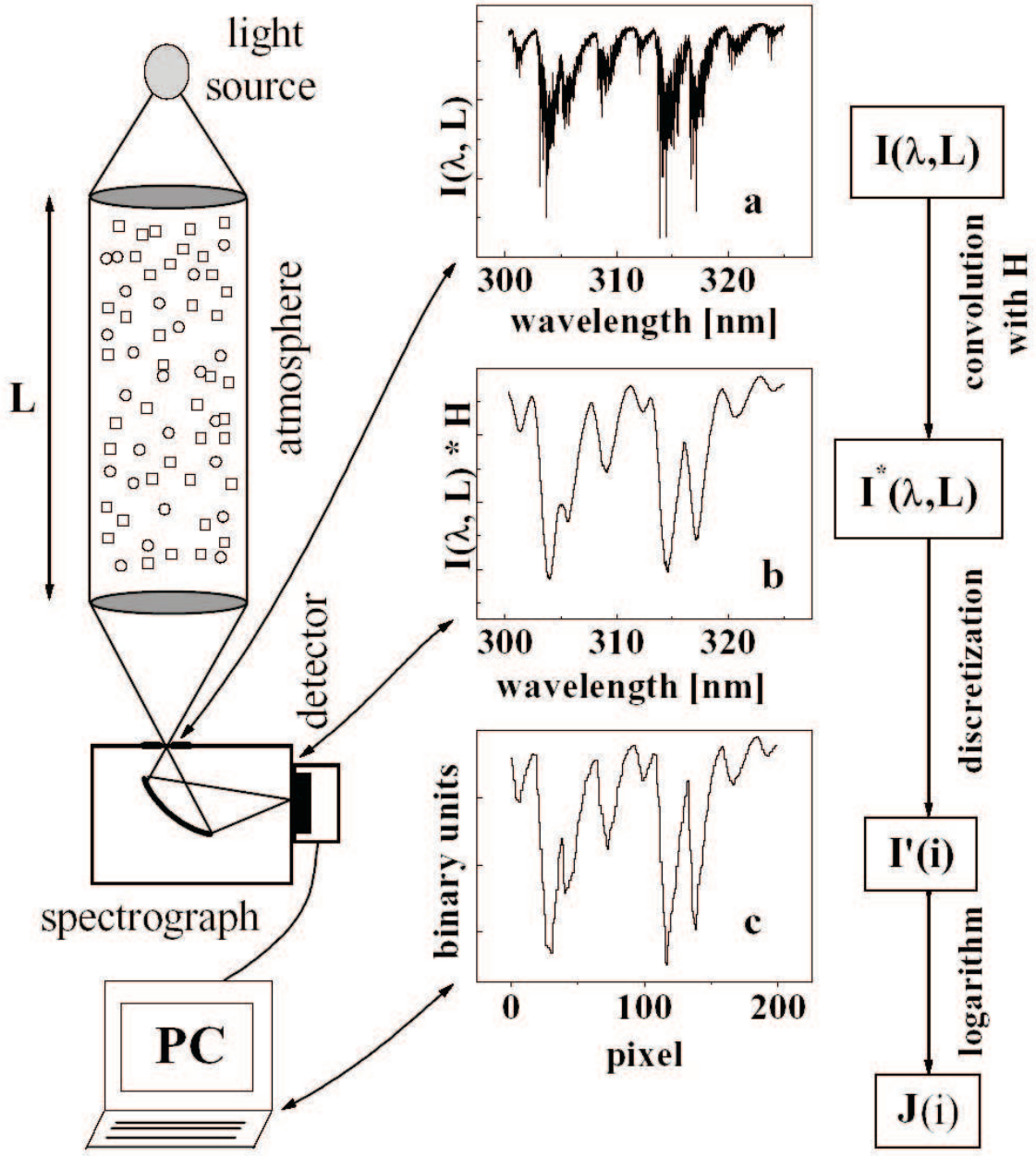

Figure 4.4: *The components of a simplified DOAS set-up used to measure atmospheric trace-gas concentrations. Collimated light undergoes absorption processes on its way through the observed air mass. (a): an example-spectrum of this light entering the spectrograph is shown, assuming only formaldehyde (HCHO) to be present in the observed air mass. This absorption spectrum shows the ro-vibronic structure of HCHO. (b): the same spectrum convolved by the spectrograph's instrumental function is transferred to the detector. (c): the spectrum after it was mapped to discrete pixels by the detector and as it is actually stored to the hard disc of a PC and being ready to be analyzed numerically. Adapted from Stutz [1996].*

distortions of higher order. The grating spectrometers that are used for DOAS measurements usually show a temperature drift when not thermally stabilized. Changes in γ_k can therefore occur and have to be corrected in the analysis procedure.

4.5 The Analysis Procedure

After the measurements have been made, a number of steps are required to derive the concentration of the different trace gases, which absorb light in the range of the measured spectrum (S(λ)).
The analyzed wavelength range of the measured spectrum must contain the absorption features of the trace gases under investigation. If possible, the range should include several absorption bands of the trace gas of interest, since otherwise other trace gases (absorbing at the same wavelength), might interfere. The measured spectrum does not only consist of the solar intensity spectrum: a dark current spectrum D(λ) and an offset O(λ) originate from the electronic detection system (section 4.6) have to be removed.

$$S(\lambda) = I(\lambda) + O(\lambda) + D(\lambda) \tag{4.12}$$

A simple substraction is often enough to remove these effects. In the following text the term 'measured spectrum' refers always to the corrected spectrum I(λ).
The measured intensity $I_0(\lambda)$ has to be converted to the intensity $I_0^{'}(\lambda)$ (see formula 4.7), therefore the broad-band part of the spectrum has to be removed. The negative exponent of Beer-Lambert-Law can be written as:

$$\sum_i (\sigma_{Rayleigh}(\lambda)c_{am}(x) + \sigma_{Mie}(\lambda)c_a(x) + (\sigma_{n_i}(\lambda, l) + \sigma_{b_i}(\lambda, T))c_i(x))L \tag{4.13}$$

$$= \sum_i \sigma_{n_i}(\lambda)c_i L + P(\lambda) \tag{4.14}$$

$$= F(\sigma, \lambda) \tag{4.15}$$

The differential optical density $D^{'}(\lambda)$ represents a linear combination of F(σ_i, λ) depending on the individual cross sections σ_i for the specific trace gas i, and a function, $P(\lambda)$. The function P(λ) is determined by the scattering characteristics. *Platt et al.* [1979] suggests that a polynomial be used to describe the scattering function. The structures, which are to be removed, strongly depend on the order of the polynomial. The polynomial order has to be chosen with care and if necessary changed for every wavelength range and width of the structures to be removed.
The removal of the broad-band structure can mathematically be described by a high-pass filterering process. The division of the measurement spectrum by an adjusted polynomial is one possibility; another is the division by a smoothed spectrum. Techniques such as binomial smoothing or the Savitzky-Golay-method could be used.

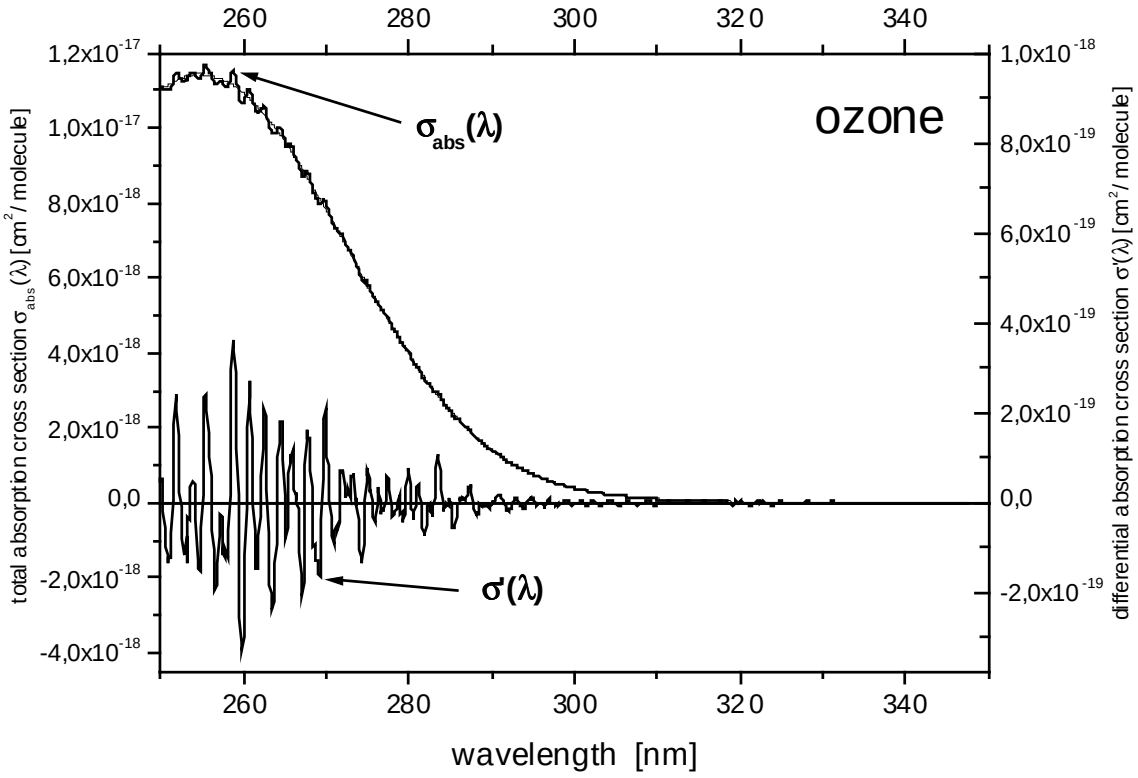

Figure 4.5: *Separation of the broad band absorption part and the narrow band differential absorption cross section is illustrated for the example of ozone.*

If σ is known, a calculation of polynomial coefficients and finally column densities is possible with numerical methods. *Platt and Perner* [1983] introduced the linear modulation of absorption structures by minimizing the square of errors (DOAS-Fit).

4.6 Spectra Corrections

In this section, the spectral corrections that have to be applied in DOAS evaluations are discussed. First, the electronic offset signal and the dark current correction are introduced. When using highly structured light sources (e.g. the sun with strong Fraunhofer absorption), a number of other effects are important. The Ring effect, (filling in of Fraunhofer lines by inelastic Raman scattering) in the atmosphere, is explained. Finally, an overview on the solar I_0-effect caused by interferences of solar Fraunhofer lines with absorption structures of the trace gases to be measured is given.

4.6.1 Dark Current Correction

For the detection of photons reaching the spectrograph, a one dimensional charged coupled device (CCD) is used in the Mini MAX-DOAS systems (For details on the experimental setup see Chapter 5 Instrument). Every discrete pixel can be regarded as a capacitor with a discharge proportional to the number of incoming photons. However, even under dark

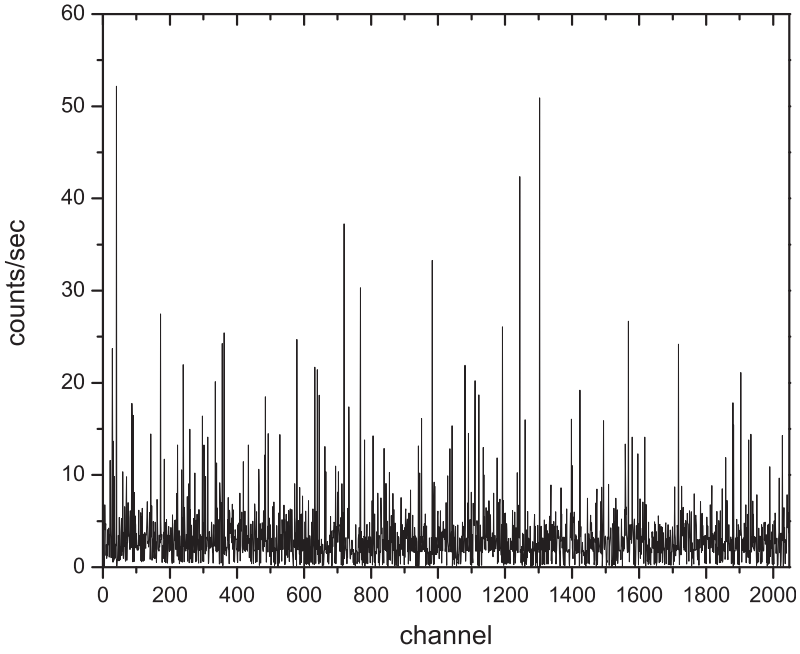

Figure 4.6: *Example of a Dark Current spectrum at 8°C, taken during the measurement campaign in Montserrat, May 2002.*

conditions, (i.e. if the detector is not exposed to light), thermal excitation causes a dark current proportional to the Boltzmann factor: $I_{DC} \propto e^{-\Delta E/kT}$. The dark current signal exponentially decreases with decreasing detector temperature. Therefore, cooling the detector reduces the dark current signal. To digitally correct for remaining dark backgrounds, a dark spectrum is determined by taking one scan with a long integration time (typically 30s for the Mini MAX-DOAS systems) under dark conditions. Afterwards, the corresponding offset signal is subtracted (see section 4.6.2). From every measurement spectrum, a time-weighted dark current signal has to be subtracted during the evaluation procedure:

$$I_{corr}[n] = I[n] - \frac{t_{int,measure}}{t_{int,dc}} \cdot D_{offcorr}[n] \tag{4.16}$$

where $I_{corr}[n]$ is the intensity in channel number n (i.e. photo diode) after dark current correction, $t_{int,measure}$ is the integration time of the measurement spectrum and $t_{int,dc}$ is the integration time of the dark current spectrum. $I[n]$ denotes the intensity in channel n before the dark current correction and $D_{offcorr}[n]$ the intensity of the offset corrected

dark current signal in channel n. A typical dark current spectrum taken at a spectrometer temperature of 8°C is shown in Figure 4.6.

4.6.2 Electronic Offset Correction

For the analysis procedure on a PC, a 12 bit analog to digital converter turns the analog photon generated signal into a digital signal. Detector noise may produce negative analog photo signals that cannot be interpreted by the A/D converter. Therefore, an artificial electronic offset signal is added to each measured scan to avoid this problem. Before the analysis process, the electronic offset weighted by the number of scans has to be subtracted from the measured spectra:

$$I_{offcorr}[n] = I[n] - \frac{numscans_{measure}}{numscans_{offset}} \cdot O[n] \tag{4.17}$$

where $I_{offcorr}[n]$ is the intensity in channel (i.e. photo diode) number n after offset correction, $numscans_{measure}$ is the number of scans of the measurement spectrum and $numscans_{offset}$ is the number of scans of the offset spectrum. $I[n]$ denotes the intensity in

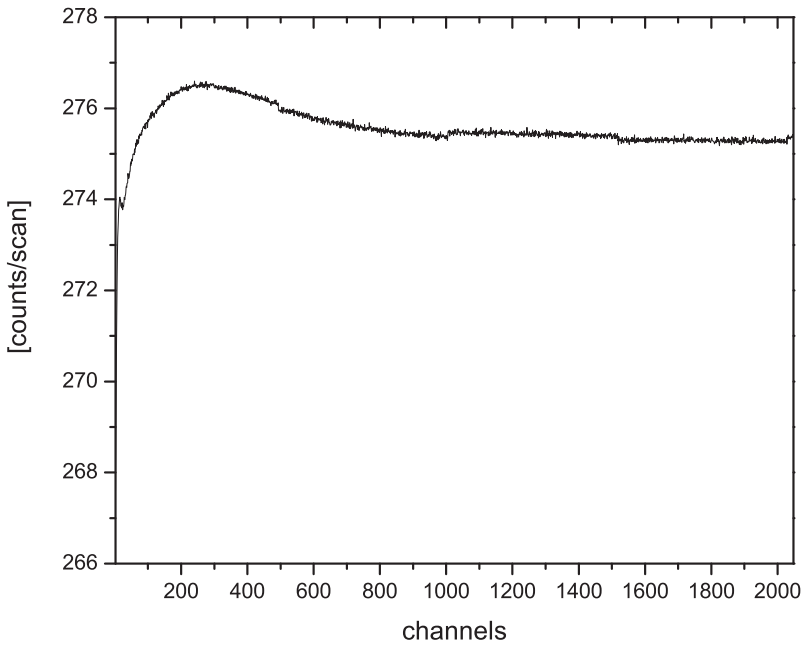

Figure 4.7: *Example of an electronic offset signal at 8°C, taken during the measurement campaign in Montserrat, May 2002.*

channel n before the offset correction and $O[n]$ the intensity of the offset signal in channel n. To determine the electronic offset, a large number of scans (typically 10000) are taken at minimal integration time, which is 3ms for the the CCDs used in the Mini MAX-DOAS systems. The electronic offset signal of the Mini MAX-DOAS is temperature dependant.

In the example shown in Figure 4.7, the temperature was 8°C and the offset signal accounts for about 4 % of the total signal. In reality the fraction of the electronic offset is even higher, because typically only 80% of the maximum saturation degree is used in measurements to avoid saturation effects.

4.6.3 The Ring Effect

In 1962 *Grainger and Ring* [1962] discovered that the depth of the Fraunhofer lines in the solar spectrum decreases when the sunlight is passing through the Earth's atmosphere. Lines observed at large solar azimuth angles seem to be "filled in" compared to the same lines observed at smaller angles. This effect is today known as the *Ring Effect* and most probably caused by inelastic rotational Raman scattering (*Bussemer* [1993]). An inelastic impact of a photon with an air molecule excites a higher or lower rotational and/or vibrational level of the molecule. Since the probability that a photon outside the Fraunhofer line loses or gains energy is higher compared to a photon in the center of the line, more photons are scattered into the line than vice-versa, and the line seems to be filled in. Typical optical density changes caused by the Ring Effect are of the order of a few percent. A very accurate correction of the Ring Effect is important because the atmospheric absorptions in DOAS evaluations are sometimes more than an order of magnitude smaller than changes due to the Ring Effect. Therefore, a Ring spectrum, which can either be calculated or directly measured, should always be included in the fitting process when using passive DOAS.

4.6.4 The Solar I_0-Effect

The intensity of the solar radiation varies strongly with the wavelength due to the high optical density and number of solar Fraunhofer lines. These narrow absorption structures usually cannot be resolved by a typical DOAS spectrometer with a typical resolution ranging from tenths of a nanometer to several nanometers. As a consequence, the observed absorption structures (when measuring direct or scattered sunlight) differ from measurements made using an unstructured (smooth continuum) light source. Narrow absorption lines of the trace gases to be measured and strong solar Fraunhofer lines can overlap. In this case, the standard convolution of the high resolution reference spectra with the instrument function no longer correctly describe the measurements when using a low resolution instrument. This effect is known as the solar I_0-effect because it is caused by the narrow spectral structures of the solar spectrum.([*Johnston* 1996; *Platt et al.* 1997; *Huppert* 2000; *Van Roozendael et al.* 2000]). To account for the solar I_0-effect, "I_0-corrected" reference spectra can be used, which are calculated as follows:
First, the high resolution Fraunhofer spectrum I_0 is convolved with the instrument function

H:

$$I_0^*(\lambda) = I_0(\lambda) * H \tag{4.18}$$

Then a synthetic absorption spectrum is calculated using a high resolution absorption cross section σ and a typical atmospheric concentration c of the trace gas to be investigated. This synthetic absorption spectrum is also convolved with the instrument function:

$$I^*(\lambda) = (I_0(\lambda) \cdot e^{-\sigma \cdot c}) * H \tag{4.19}$$

Finally, the I_0-corrected cross section σ^* can be calculated:

$$\sigma^* = \frac{1}{c} \cdot \ln\left(\frac{I_0^*(\lambda)}{I^*(\lambda)}\right) \tag{4.20}$$

To bring the measured atmospheric spectrum and the I_0-corrected reference spectrum into perfect agreement, the concentration assumed for the calculation and the atmospheric concentration must be the same. For practical purposes however, a typical atmospheric concentration can be used for all spectra.

4.6.5 Error estimation

In principle photo electron shot noise is the theoretical limit, which therefore determines the uncertainty of a DOAS measurement. However, in most cases the realistic error is a sum of a statistical part (due to the numerical fit) and a systematical part. The statistical error (1 σ) is calculated directly by the used evaluation software WinDOAS [*Roozendael and Fayt* 2001] and therefore can be given easily. Systematic errors are caused by a number of different effects, which will only be shortly discussed here. First systematic errors are caused by the noise of the detector, which can be decreased by cooling of the instrument and noise caused by large time differences between spectra and the Fraunhofer Reference Spectrum (FRS), which is accounted for by taken a FRS as often as possible. Other errors are caused by the fact that cross sections of trace gases are often temperature dependent. Especially if a trace gas is distributed over a wide vertical range it can be seldom accounted for. Already the cross sections are probably not free of errors in their absolute values, and are mostly within an estimated error range of 5 %. An incomplete set of references leads to additional residual structures of unknown absorbers. Another critical point is the consistent wavelength description. The quantitative determination of the systematical error are far from being simple and will be mostly neglected in later discussion. The errors on the slant column densities determined in this thesis are based on the numerical fit errors and the size and structure of the residual.

4.7 Passive DOAS

The DOAS principle as outlined above can be applied in a wide variety of light path arrangements and observation modes. To provide a general overview, DOAS techniques can be classified according to their light sources first. One can distinguish between active and passive DOAS. While active DOAS uses artificial light, passive DOAS relies on natural light sources such as solar, lunar, or star light. A large advantage of active DOAS instruments is the independence of daylight and the possibility to do measurements below 300 nm, however, they require a much more sophisticated optical system, more maintenance, and they need one to two orders of magnitude more power than passive instruments [*Platt* 1994]. In the present state active DOAS instruments are not very suitable for investigation in remote areas like volcanoes, where all studies of this thesis took place. Therefore only an overview of the most common passive DOAS experimental setups is given in the following sections.

Most often the sun or the moon are used as light sources, but also starlight represents a possible light source. When using light from the moon or the stars, only direct light can be used because relatively little light reaches the earth from these sources. However, in the case of sunlight, light scattered by air molecules and particles can be employed as well. Thus passive DOAS applications can be subdivided in direct and scattered light measurements. Passive DOAS observation using scattered sunlight are already applied for many years (see Table 4.1). The "Off-Axis" geometry, which are observation to directions that are not the zenith, was first introduced by *Sanders et al.* [1993]. The aim of that investigation was to observe OClO over Antarctica during twilight. During sunrise or sunsets the sky is brighter towards the horizon in the direction of the sun compared to the zenith. With this method *Sanders et al.* [1993] reduced the signal to noise ratio in their measurements and got a better sensitivity for the OClO measurements. They pointed out in this article that the off-axis geometry increases the sensitivity for the lower absorption layers, the tropospheric absorption are highly enhanced whereas the stratospheric absorption for the off-axis and the zenith geometry are comparable. Also for direct moon measurements the off-axis geometry was employed and resulted stratospheric and tropospheric profiles of NO_3 by ground based instruments [*Weaver et al.* 1996; *Smith and Solomon* 1990; *Smith et al.* 1993; *Kaiser* 1997; *von Friedeburg et al.* 2002]. Several applications followed and an overview of the different passive DOAS configurations and their measured quantities is given in Table 4.1.
Just like in active DOAS measurements, Beer-Lambert's law can be applied directly in passive direct light DOAS. The light that is detected by the spectrometer has traversed the entire atmosphere and the first result of the measurement is the slant column density (S) (see equation 4.8). This quantity represents the concentration integrated along the

light path. Conversion of the S into the vertically integrated column density (V) or vertical concentration profiles require radiative transfer calculations. Figure 4.8 shows some examples of direct passive DOAS setups. Plate (1) sketches measurements of direct sun, moon, and starlight from the ground. Determination of vertical profiles of trace gases is possible in balloon borne experiments, when direct light is detected at different altitudes during ascent (Figure 4.8, plate (2), *Ferlemann et al.* [1998]). SCIAMACHY, a space born DOAS instrument, allows for occultation measurements (panel (3) in Figure 4.8).

Scattered sunlight measurements offer an even larger variety of applications. One of the first experiments using scattered light, was the measurement of scattered light from zenith direction (Figure 4.8, plate (4)). Measurements in this viewing geometry are well suited for probing the stratosphere and played an important role in improving our knowledge on stratospheric chemistry (e.g. *Mount et al.* [1987], *Solomon et al.* [1987]). Another application of zenith scattered light is the investigation of the radiative transport in clouds (Figure 4.8, plate (10)). To understand the radiative transport in clouds is essential for climate research (*Pfeilsticker et al.* [1998], *Pfeilsticker et al.* [1999]). Multi-axis DOAS (MAX-DOAS)(Figure 4.8, plate (5)) uses multiple telescope elevations to derive vertical profiles of absorbers in the lower troposphere. A high sensitivity for absorbers located close to the ground is reached, because light detected at low telescope elevation has traversed a significantly longer path through the lower atmosphere compared to light recorded at higher telescope elevations (e.g. *Hönninger et al.* [2004]). This technique is discussed in detail in Section 4.8. AMAX-DOAS is an airborne MAX-DOAS variant, which allows measurements above and below the flight altitude. Furthermore, the derivation of vertical trace gas concentration profiles is possible with this setup (Figure 4.8, plate (6)). An alternative passive DOAS setup is Imaging DOAS which were also applied during this thesis (Figure 4.8, plate (7)). The simultaneous measurement of many viewing elevations allows 2-dimensional visualization of pollution plumes. Satellite borne scattered sunlight measurements have also been conducted during recent years. The DOAS instrument (e.g. Global Ozone Monitoring Experiment - GOME) looks downwards through the atmosphere in the nadir geometry determining global concentration fields of various trace gases (Figure 4.8, plates (8)). In order to determine vertical profiles of atmospheric absorbers at high resolution, the SCanning Imaging Absorption SpectroMeter for Atmospheric CHartographY (SCIAMACHY) instrument also measures in limb geometry (Figure 4.8, plates (9)).

The passive DOAS applications share the advantage of a relatively simple experimental setup. Compared to active DOAS systems, the optical setup is simplistic and no artificial light sources are required resulting in low power consumption. Passive DOAS applications are well suited for measurements in remote areas (e.g. the study of volcanic plumes, or measurements in Arctic regions). However, unlike the artificial light sources in active

DOAS measurements, the spectra of natural light sources are highly structured. The strong Fraunhofer lines in the solar spectrum have to be accurately removed in order to detect the much weaker absorptions due to trace gases in the atmosphere. Because the light source structure contains narrow and deep absorptions, care has to be taken in the application of the DOAS technique (see Sections 4.2 - 4.5). The largest challenge in the interpretation of passive DOAS measurements is the determination of the light path. This information is essential for the conversion of the slant column densities (S) to vertical column densities (V) and concentrations and can only be obtained by accurate radiative transfer calculation (see for more details section 4.8).

4.8 Multi-AXis-DOAS (MAX-DOAS) technique

The MAX-DOAS technique is used in this thesis with a ground based instrument, that collects scattered sunlight using a single telescope and transferring the light to a spectrograph. By changing the telescope pointing direction, light can be received from different directions, thus allowing spatial information to be derived about the absorbing molecules. Table **??** gives an overview of the history of the different scattered light passive DOAS applications.

4.8.1 Scattered Light

For the analysis and interpretation of DOAS measurements using scattered sunlight it is important to correctly describe the radiative transfer in the atmosphere. For trace gases with distinct vertical profiles (O_3, NO_2, BrO, etc.) or in plumes (SO_2, BrO, NO_2, etc) the apparent absorption measured by a ground based spectrograph depends strongly on the distribution of the light paths taken by the registered photons on their way through the atmosphere.
As described in Sections 4.2. and 4.3 the analysis procedure of DOAS leads to slant column densities (S), defined as the trace gas concentration integrated along the light path:

$$S = \int c(x)\ ds \tag{4.21}$$

For a single S measurement the individual photons registered in the detector may have travelled different paths through the atmosphere before being scattered into the DOAS telescope. Therefore equation 4.22 can only give a result for the most probable path defined by the statistics of the registered photon ensemble. Since the S depends on the observation geometry and the occurring meteorological conditions, it is usually converted to the vertical column density (V), which is defined as the trace gas concentration $c(z)$ integrated along

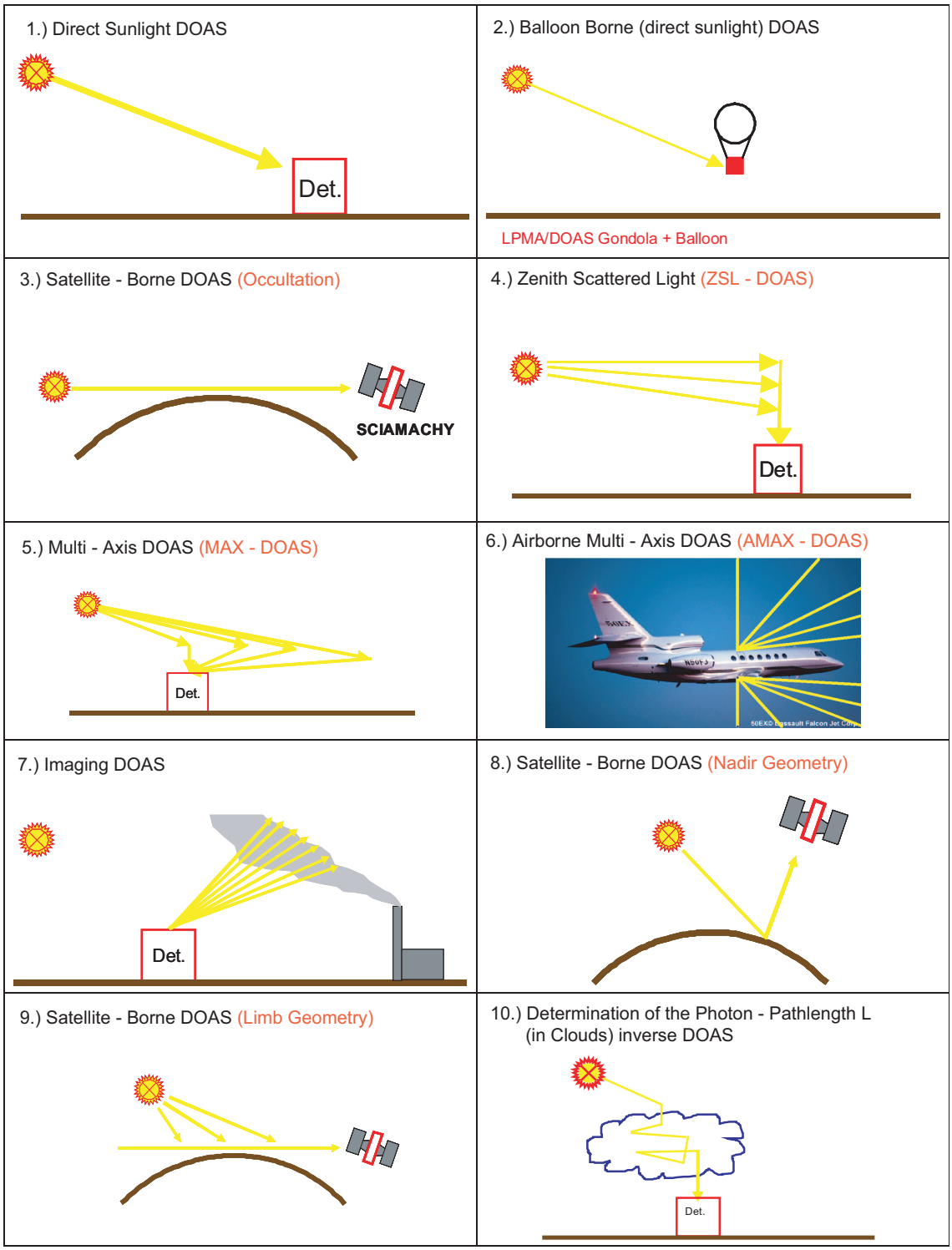

Figure 4.8: *Different passive DOAS setups. Passive DOAS offers a large variety of possible applications. In general, one distinguishes between direct and scattered light measurements. (Adapted from Platt and Stutz 2005).*

Table 4.1: *Overview and history of the different scattered light passive DOAS applications,# Axis indicates the number of different viewing directions combined. (M - spectra are taken simultaneously in different axis, S - scanning of different viewing directions.) Adapted from Hönninger et al. [2004].*

Method	Measured quantity	No. of axes	References technique
COSPEC	NO_2, SO_2, I_2	1,(S)	Millan et al.(1969),Davis(1970),Hoff and Millan(1981),Stoiber and Jepsen (1973),Hoff et al.(1992)
Zenith scattered light DOAS	Stratospheric NO_2,O_3, OClO, BrO, IO	1	Noxon(1975),Noxon et al.(1979),Harrison(1979),McKenzie and Johnston (1982), Solomon et al.(1987a,b, 1988, 1989, 1993),McKenzie et al. (1991), Fiedler et al.(1993),Pommereau and Piquard(1994),Aliwell et al. (1997), Eisinger et al.(1997), Kreher et al.(1997), Richter et al. (1999),Wittrock et al.(2000)
Zenith sky + Off-Axis DOAS	Stratospheric OCIO	2	Sanders et al.(1993)
Off-Axis DOAS	Stratospheric BrO profile	1	Arpaq et al.(1994)
Zenith scattered light DOAS	Tropospheric IO, BrO	1	Kreher et al.(1997),Friess et al.(2001, 2003),Wittrock et al.(2000)
Off axis DOAS	Tropospheric BrO	1	Miller et al.(1997)
Sunrise Off-Axis DOAS + direct moonlight	NO_3 profiles	2,S	Weaver et al.(1996), Smith and Solomon(1990),Smith et al.(1993)
Sunrise Off Axis DOAS	Tropospheric NO_3 profiles	1	Kaiser(1997),von Friedeburg et al.(2002)
Aircraft-DOAS	Stratospheric NO_2	1	Wahner et al.(1989)
Aircraft-DOAS	Tropospheric BrO	2	McElroy et al.(1999)
Aircraft zenith sky + Off-axis DOAS	"near in-situ" Stratospheric O_3	3	Petritoli et al.(2002)
AMAX-DOAS	Trace gas profiles	8+,M	Wagner et al.(2002),Wang et al.(2003), Heue et al.(2003)
Multi-Axis-DOAS	Tropospheric BrO profiles	4,S	Hönninger and Platt(2002),Hönninger et al.(2004a)
Multi-Axis-DOAS	Trace gas profiles	2-4,M	Löwe et al.(2002), Oetjen(2002), Heckel (2003), Wittrock et al.(2003)
Multi-Axis-DOAS	NO_2 plume	8.M	von Friedberg(2003)
Multi-Axis-DOAS	BrO in the marine boundary layer	6,S/M	Leser et al.(2003), Bossmeyer(2002)
Multi-Axis-DOAS	BrO and SO_2 fluxes from Volcanoes	10,S	Bobrowski et al.(2003)
Multi-Axis-DOAS	BrO emissions from Salt Lake Salt Lake	4,S	Hönninger et al.(2004b)

the vertical path through the atmosphere:

$$V = \int c(z)\ dz \tag{4.22}$$

V is independent of the light paths and viewing geometry and can therefore serve as a result for comparing different measurements. An air mass factor (AMF) is defined as the

ratio of S and V (see figure 4.9)

$$AMF(\lambda, \vartheta, \alpha, \phi) = \frac{S(\lambda, \vartheta, \alpha, \phi)}{V} \tag{4.23}$$

with:
λ - wavelength
ϑ - angle between zenith and the direction of the sun (solar zenith angle (SZA))
α - angle between the horizontal direction and the viewing direction of telescope (telescope elevation angle)
ϕ - the relative azimuth angle between the telescope direction and the sun (it was shown in *Hönninger* [2002] and *Hönninger et al.* [2004] that the dependence of the AMF on ϕ is small)

The AMF depends on the radiative transfer in the atmosphere and is therefore determined by factors such as the trace gas profile, pressure, temperature, ozone and aerosol profiles, clouds, surface albedo etc. To determine the relationship between S and V, the optical density D of solar radiation passing through a concentration field $c(x)$ assuming that the temperature and pressure dependency of the absorption cross section σ is small:

$$D(\lambda) = -\ln\left(\frac{I(\lambda)}{I_0(\lambda)}\right) = \sigma(\lambda) \cdot \int_0^L c(\vec{x})\ ds = \sigma(\lambda) \cdot S(\lambda) \tag{4.24}$$

Here, $I_0(\lambda)$ is the intensity observed in absence of the absorber in the atmosphere. This equation is only valid for a well defined light path between the position of the sun and the observer. This is for example the case for the observation of direct sunlight (or moonlight) in a plane parallel to the atmosphere with a trace gas layer. It is also a good approximation of the situation sketched in Figure 4.9, as long as the indicated photon path is representative for the ensemble of photons received in the detector. For the case sketched in Figure 4.9 A (e.g. a stratospheric absorption layer), the path integral in equation 4.24 is calculated along a straight line between the sun and the position of the scattering process (if refraction is neglected). Along the path between the scattering process and the detector no additional absorption is considered. The line element for a given solar zenith angle ϑ is $ds = dz/\cos(\vartheta)$ with dz being the vertical line element. Therefore, the slant column density S_{strat} can be calculated as follows:

$$S_{strat}(\vartheta) = \int c(x)ds = \int c(z)\ \frac{dz}{\cos(\vartheta)} = \frac{V}{\cos(\vartheta)} \tag{4.25}$$

Hence, by neglecting refraction, the air mass factor for this approximation can be written as:

$$AMF_{strat}(\vartheta) = \frac{S_{strat}(\vartheta)}{V} = \frac{1}{\cos(\vartheta)} \tag{4.26}$$

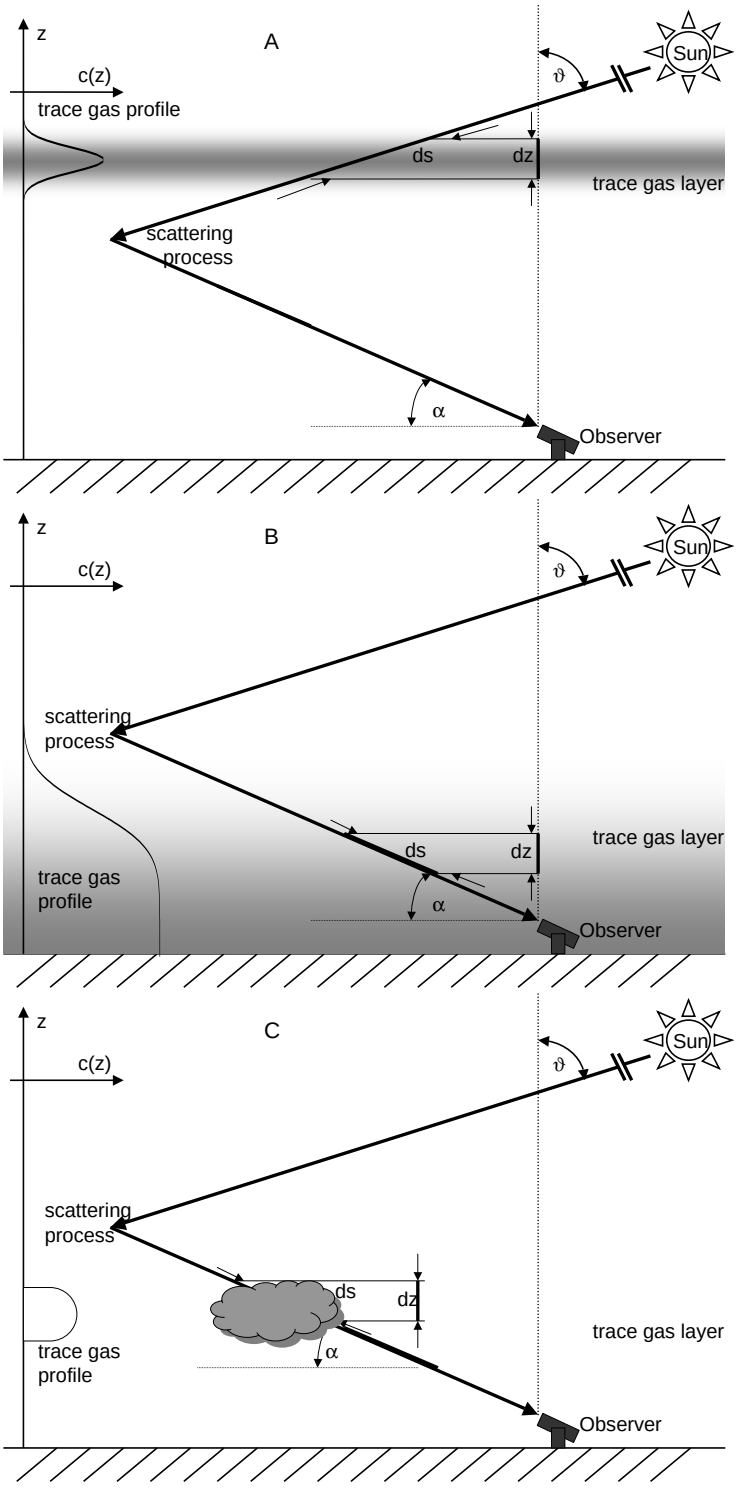

Figure 4.9: *Observation geometry for a ground based DOAS using scattered sunlight. Light enters the atmosphere at the solar zenith angle ϑ. For the single scattering approximation light received by the observer is scattered exactly once into the telescope viewing direction defined by the elevation angle α. The observed SCD (integral along ds) is larger than the VCD (integral along dz), with AMF being the conversion factor. Part A represents the situation for a high altitude trace gas layer, part B is representative for a trace gas layer at the surface, part C shows the situation for a trace gas within a plume (Part A and part B adapted from Hönninger [2002]).*

Here AMF_{strat} is only a function of the solar zenith angle ϑ. This is a good approximation for the air mass factor for zenith scattered sunlight measurements of stratospheric absorbers, as shown by Frank [*Frank* 1991].
The situation changes for a trace gas layer close to the ground as sketched in Figure 4.9 B (e.g. an absorber confined to the boundary layer). In this case the scattering process occurs above the absorption layer and therefore the path integral is calculated along a straight line between the detector and the position of the scattering process. Along the path between the scattering process and the sun no absorption is possible. The line element can now be expressed for a given telescope elevation angle α as $ds = dz/\sin(\alpha)$. The slant column density S_{bl} is calculated as follows:

$$S_{bl}(\alpha) = \int c(x)ds = \int c(z)\ \frac{dz}{\sin(\alpha)} = \frac{V}{\sin(\alpha)} \tag{4.27}$$

The airmass factor for the surface absorption layer,

$$AMF_{bl}(\alpha) = \frac{S_{bl}(\alpha)}{V} = \frac{1}{\sin(\alpha)} \tag{4.28}$$

is simply a function of the telescope elevation angle. These approximations for AMF_{strat} and AMF_{bl} are valid for small solar zenith angles ($\vartheta \lessapprox 70°$) and telescope elevation angles smaller than $\alpha \approx 20°$. It was shown by *Hönninger* [2002] and [2004] that AMF_{bl} is a reasonable approximation as long as multiple scattering can be neglected, which is in reality only possible for a low aerosol content, which means considering only Rayleigh scattering and neglecting Mie scattering. The determination of the SCD of the oxygen dimer (and/or other species with known atmospheric distribution, e.g. O_2) provide an opportunity for the determination of the aerosol load of the investigated atmosphere. The concentration profile of O_4 in our atmosphere is well known. O_4 is a collision's complex of two oxygen molecules and its absorption bands occur at several wavelengths in the UV/Vis spectral range [*Perner and Platt* 1980]. The O_4 reference spectra [*Greenblatt et al.* 1990; *Hermans et al.* 1999] has often to be included in the DOAS analysis. Therefore the measured O_4 slant column densities for a series of elevation angles can be compared to a series of calculated O_4 S's from the temperature and pressure profile on the measurement location and then used to quantify Mie scattering and aerosols. This has been done in [*Hönninger et al.* 2004; *Sinreich* 2003; *Wagner et al.* 2004]
The situation illustrated in Figure 4.9 C, corresponds to the measurement situation in this thesis and will be quantitatively discussed in Chapter 8.
However, for plume studies, the extremely high temporal and spatial variability of the trace gas and aerosol concentration makes the AMF calculation quite complex. Some first examples and ideas of the radiative transfer processes in plumes will be given later in chapter 8.5., Photon-Path-Length inside the Plume. Otherwise SCD and concentration are mainly estimated by geometric approximation in this thesis. (see Chapter 7 Measurements and Chapter 8 Results)

4.8.2 MAX-DOAS as the Successor of COSPEC

In the late 1960's, the correlation spectrograph (COSPEC) instrument [Barringer Research Inc., Canada] was developed [*Millán et al.* 1969; *Davies* 1970] and a strategy for measurements of total SO_2 and NO_2 emissions from various sources, e.g. industrial exhaust plumes [*Hoff and Millán* 1981] and volcanic plumes [*Stoiber and Jepsen* 1973a], was successfully applied. For more than 30 years, the COSPEC instrument was until recently, the principal tool for the remote surveillance of volcanic plumes and is still frequently used. The COSPEC system, employing an early and simple form of DOAS, was very innovative at the time, but has several disadvantages:

- Only certain species, where masks are available, can be measured. In particular the instrument is not very flexible since masks have to be specifically made for each species
- It is difficult to deduce a trace gas concentration from the data
- Light scattered by clouds or aerosols can lead to large errors in the determination of the column densities

Technological developments have given sensitive and fast multichannel array detectors, powerful computers, and algorithms for the analysis of differential absorption spectra. Additionally, during the past decade significant improvements in radiative transfer modelling and understanding of multiple scattering processes in clouds have been achieved. Thus the first flux measurements of volcanic gas emissions using a mini-DOAS instrument were made in Nicaragua in April 2001 by Galle and Oppenheimer. Subsequently, the first time-resolved measurements with a scanning mini-DOAS instrument were made on Montserrat in January 2002 by Galle and Edmonds. In May 2002 the first measurements of BrO in a volcanic plume was made by Bobrowski, and the first measurements of volcanic plume velocity using a double-beam mini-DOAS was made in Nicaragua in November 2002 by Galle and Hansteen. All these developments constitute major improvements in volcanic gas monitoring, and the techniques have been implemented and further developed also by other scientists in Europe, USA, Canada and Japan. The demonstrated capability of these instrument to provide gas flux measurements with high time resolution, plume speed and height measurements, 2- dimensional plume tomography and simultaneous measurements of SO_2 and BrO has given new possibilities to investigate and maybe predict in the future complicated geophysical phenomena.
In addition, the measurement of oxygen dimers (O_4) allows correction for possible errors due to multiple scattering in dense aerosol plumes.
Some possible instrumental set-ups for MAX-DOAS instruments studying volcanic or other emission plumes are sketched in Figures 4.10 - 4.13.

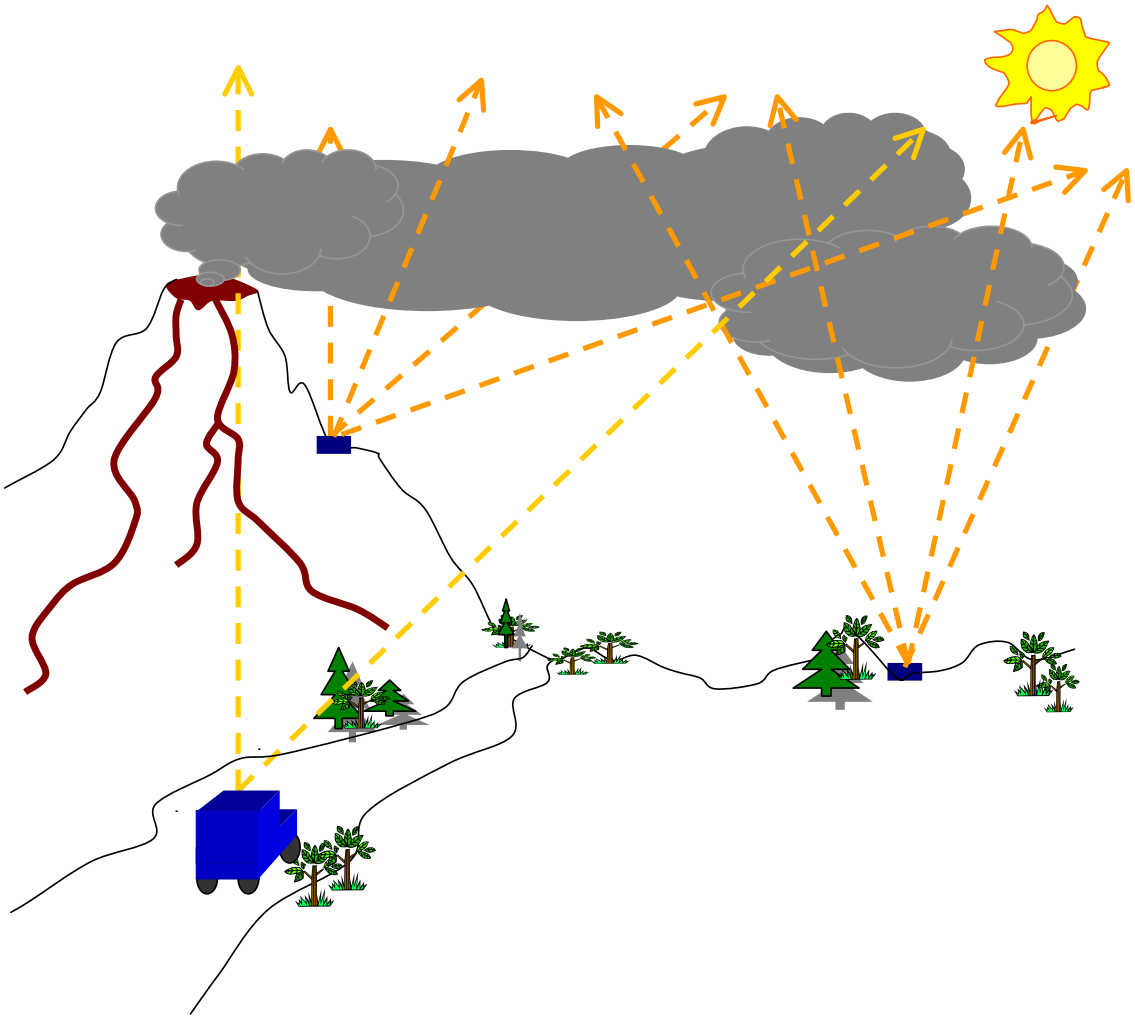

Figure 4.10: *MAX-DOAS at volcano: Several instruments or several different viewing directions are applied to probe the plume at various positions.*

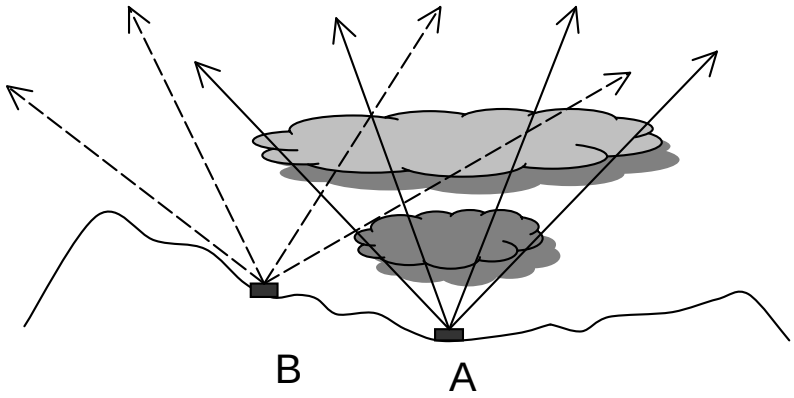

Figure 4.11: *Possible viewing geometries using static MAX-DOAS instruments. By combination of two or more systems the vertical distribution of the plume can be determined.*

The MAX-DOAS system can be applied in static mode (shown in Figure 4.10, 4.11, 4.13) and then sequentially scan spectra from different geometries (Figure 4.10, 4.11) or do simultaneous measurements (Figure 4.13) using several spectrographs.
By scanning from horizon to horizon (Figure 4.11), the integrated number of molecules in a cross section can be obtained from a fixed position. Only with instrument A, the vertical distribution still remains unclear. It is illustrated that the instrument at position A receives the same signal from both plumes. One way to obtain vertical information about the plume would be additional meteorological measurements and modelling. Another possibility is to use a second instrument. The combination of different elevation angles and two instruments at different locations (Figure 4.11) allows the determination of two dimensional information about the plume, derivation of the plume density and also the height by triangulation.
Another approach is mobile monitoring of the trace gas columns (especially that of SO_2) inside a volcanic plume along different transects by taking a series of measurements from different locations. The height of the plume can be obtained by operating the instrument on a mobile platform (Figure 4.12) taking a car, ship or helicopter. The classical COSPEC mode of operation uses a single telescope pointing at zenith. This leads to a good determination of the integrated number of molecules in the plume.
By adding a second viewing direction at 60° declination, the height of the plume can be obtained. In addition, by being positioned under the plume, and pointing the second telescope in a direction upwind, the plume speed may be obtained (from a fixed position).
An alternative approach to the sequentially scanning DOAS system is to use a line of individual spectrographs and telescopes with zenith viewing directions (Figure 4.13). An advantage of this concept is that it is not very sensitive to errors in the plume height and the radiation transfer modelling is relatively easy. In addition to the spectroscopic data the wind speed of the plume can be determined.

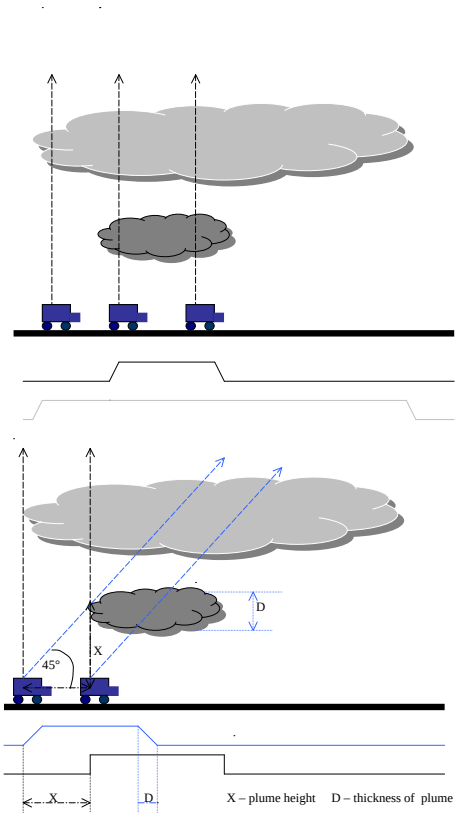

Figure 4.12: *Using a mobile dual-spectrograph scattered light DOAS system (2 telescopes pointing at 90° and 45° elevation), the plume height can be determined.*

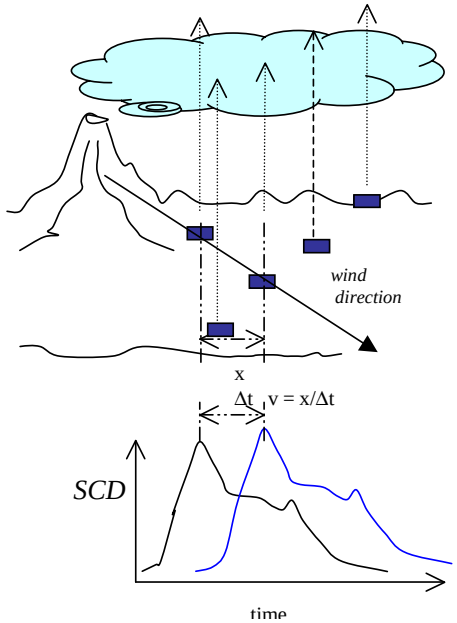

Figure 4.13: *Setup of a static multi-spectrograph DOAS system for plume observation. The wind speed of the plume can be determined by the time delay between two time series of the column density.*

Chapter 5

Instrumental Set-ups

Two types of DOAS instruments were applied during the investigations described in this thesis. A description of the DOAS technique is given in chapter 4 therefore only the technical part of the Mini-MAX-DOAS instruments and the IDOAS will be described in this chapter.

5.1 The Mini-MAX-DOAS Instrument

The MAX-DOAS system, like all DOAS instruments, is highly sensitive and allows specific detection of many trace gases at the same time; for instance SO_2, NO_2, O_4, HCHO, CS_2, halogen oxides (ClO, BrO, IO) and ozone (for details see Chapter 4). MAX-DOAS belongs to the passive DOAS instrument family and uses scattered sunlight as light source. The instrument provides the possibility for a better understanding of atmospheric chemistry and transport processes in a plume.
The first version of the Mini-MAX-DOAS instrument was built by *Hönninger* [2002] and used in the Indian Ocean [*Hönninger* 2002]. It was later used by Frank Weidner [2003] in Kiruna. A scetch of the set-up is given in 5.1. The OceanOptics spectrometer (described below) was only placed in a metal box and surrounded by silica gel to keep it dry. A peltier-cooling system was used to stabilize the temperature and the whole unit was isolated by styrofoam. Unfortunately the styrofoam box that surrounded the peltier elements and the cooling box was not air tight and water condensation inside the box did not allow a stable temperature control.
The second version had major improvements for air-tightness and temperature stabilization and can be transported in a suitcase while travelling. The suitcase also serves as a protection box during measurements on rough places like volcanoes. The OceanOptics spectrograph is placed in a metal dewar, which is filled with argon and a small pack of silica gel. A Peltier cascade is used and it is possible to cool it to around 35-40°C below ambient temperature. The temperature controller unit allows the user to select a tempera-

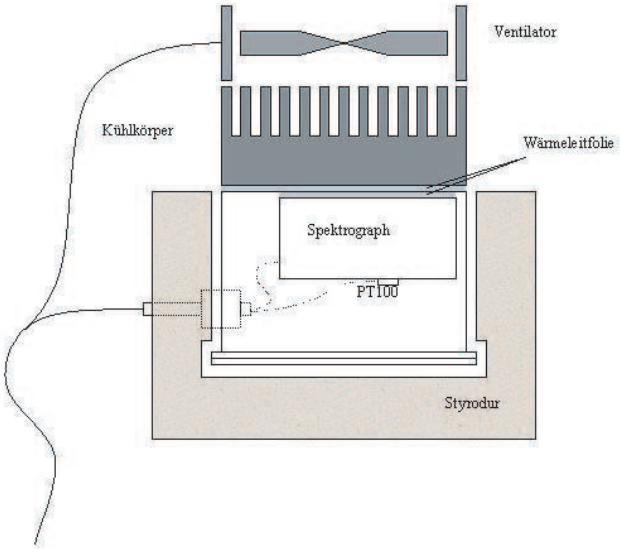

Figure 5.1: *Sketch of the first Mini-DOAS built by Hönninger [2002].*

ture by a set-screw and also to limit the current, depending on the available power supply. The telescope consists of a quartz lens with a focal length of 40 mm and a diameter of 22 mm, as well as of an UG5 Hoya-filter to block light with wavelengths longer than 400 nm (to reduce spectrometer straylight). The entrance optics has a field of view of approximately 0.4°. The telescope is connected to a stepper-motor which is placed in a separate box. The scattered sunlight is transmitted from the telescope to the spectrometer by a quartz fiber-bundle which is 4 m long and consists of 4 individual fibers, each with a core diameter of 200 μm. The 4 fibers are arranged in a rectangular configuration at the focal point of the quartz lens and in a linear configuration at the spectrometer entrance slit (width 50 μm, height 1 mm). The quartz fiber is protected by a Teflon tube. A second suitcase can be used as a protection box for a notebook computer and the motor controller. However, if transport of the instruments in rough terrain was required, suitcases are still not portable enough (for further details see [*Bobrowski* 2002]): therefore further developments were necessary.

The third version of the Mini-MAX-DOAS-system, used during this study, is an improved version of the second version, developed and applied during the author's Diploma thesis [Bobrowski, 2002]. The Mini-MAX-DOAS instrument consists of a small entrance optic (quartz lens, f = 40 mm, d = 20 mm) coupled to a quartz fibre bundle, which transmits the light into a commercial miniature fibre optic spectrometer (OceanOptics Inc., USB2000). The simple telescope unit is not separated anymore, all parts of the set-up are now in-

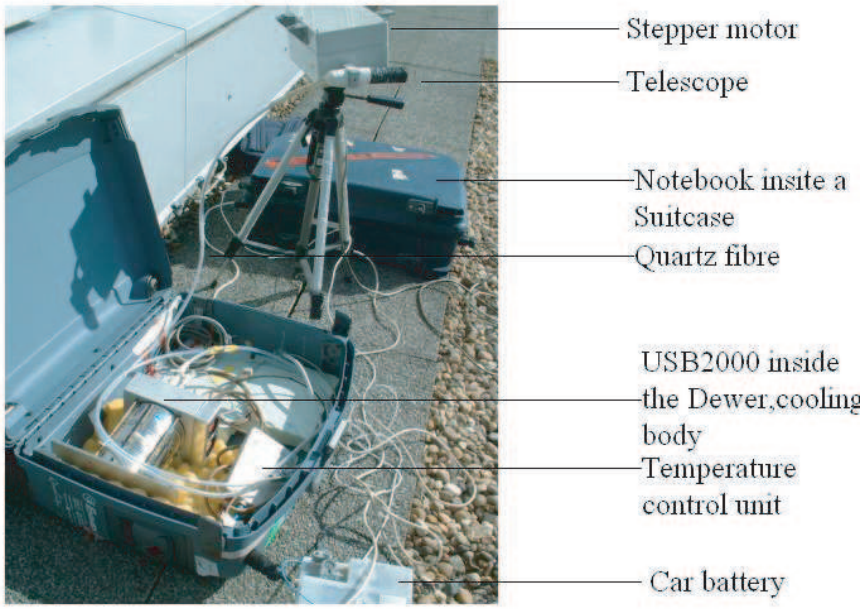

Figure 5.2: *Photograph of the second version of the cooled Mini-MAX-DOAS instrument, taken on the roof of the Institut für Umweltphysik.*

cluded in one aluminium box.

The spectrometer-telescope unit attached to a stepper motor can be mounted on a tripod (see Figure 5.3). The unit could be moved to point at elevation angles between 0° and 180° above the horizon using a stepper motor drive. The approximately 1 m long quartz fibre bundle, which is coiled inside the unit, consisted of four individual 200 μm core diameter fibres, arranged in rectangular configuration in the focal point of a quartz lens and linear configuration at the spectrograph entrance slit (width 50 μm, length 1000 μm). An UG5 Schott filter blocks the visible light longer than 400 nm to reduce the stray light in the spectrograph and to provide a more uniformly distributed light intensity over the spectral range of the spectrograph. To prevent direct sun light from being scattered into the fibre (and as a protection from acid rain) a tubular black sun shield is attached in front of the entrance optics (22 mm diameter, 80 mm length). The field of view of the entrance is approximately 0.6°. The USB2000 device is a crossed Czerny-Turner spectrograph (Aperture ratio = f/2.2, UV grating 2400 grooves/mm) with a CCD detector (2048 elements at 14 μm centre - centre spacing and a height of 200 μm) coupled to a 12-bit ADC and USB interface. Figure 5.4 shows the main components of the spectrograph. The optics, detector and electronics (for read out of the CCD array, A/D conversion and spectral averaging) of the spectrograph is a compact unit (89 mm x 64 mm x 34 mm, 0.2 kg). The quartz fibre transmits the light to the entrance slit (width = 50 μm), which guarantees a spectral

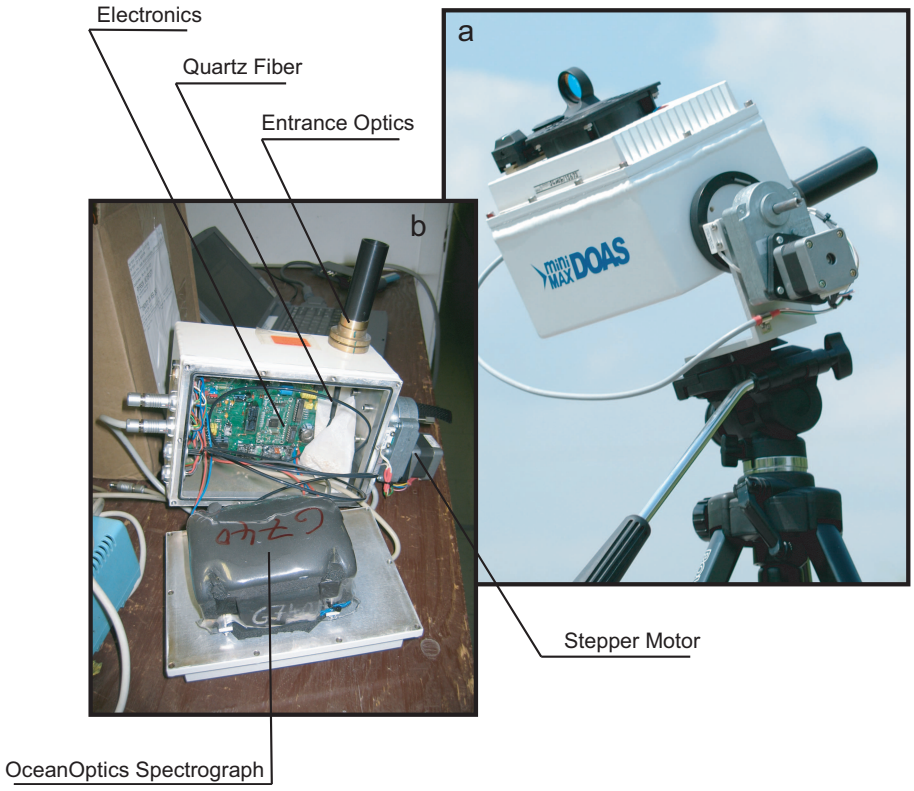

Figure 5.3: *Photograph of the third cooled Mini-MAX-DOAS version (a) One Mini MAX-DOAS instruments during measurements. (b) The main components of the Mini MAX-DOAS system. Adapted from Bobrowski and Filsinger [2005].*

resolution of about 0.7 nm FWHM for an instrument temperature of about 10°C. The entrance slit is mounted in the focal point of the collimating mirror (f = 42 mm). From this mirror the light is reflected in a parallel beam and dispersed by a plane diffraction grating (OceanOptics Grating #7, 2400l/mm holographic, for efficiency curve, see Figure 5.5). The dispersed light is imaged onto the CCD detector with a focussing mirror (f = 68 mm). The wavelength region observed by the detector is set from about 290 to 420 nm by adjusting the grating position. The wavelength to pixel mapping in a first evaluation run as well as the instrumental line shape is determined by taking a spectrum of a low-pressure mercury emission lamp and using the known mercury line positions to calculate a polynomial fit for the wavelength to pixel mapping. Figure 5.6 shows the wavelength as a function of detector pixel number. The linear and the second order fit result are shown. Each of the 2048 pixels is 14 μm x 200 μm in size and represents a potential well, which collects the energy dissipated on light exposure as electrical charge, which is proportional to the light intensity (e.g. [*Papp* 2004]). The full potential well depth corresponds to 160000 photo electrons. Thermally activated electrons also produce a signal, which is called dark current (see chapter 4). In order to reduce the dark current of the CCD and stabilize the

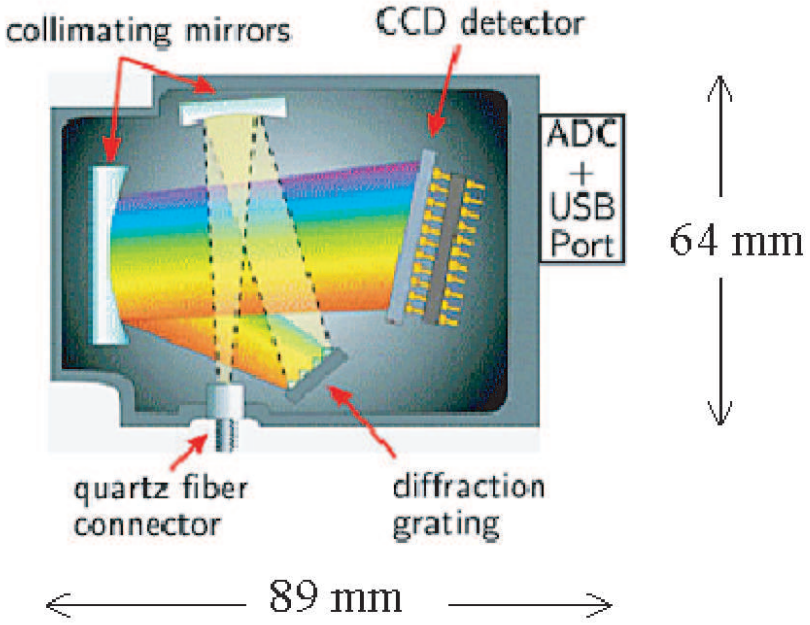

Figure 5.4: *Main components of the OceanOptics USB2000 spectrograph.*

optical bench the complete USB2000 spectrograph was cooled to a temperature around 10°C for most of the applications using Peltier elements controlled by a temperature control unit. During the readout process the charges are shifted to a buffer and after addition of an electronic offset signal (see chapter 4), it is transferred to the ADC (12 bit, operating at 1 MHz). The fact that the electronic offset signal depends on the temperature of the USB2000 device is also accounted for by stabilizing the device temperature. In order to protect it from moisture and for better temperature stabilization the whole unit is sealed in an airtight metal box. Silica gel is added to keep the interior dry in case of leakage. The cooling system is able to sustain a temperature difference of up to 35 K. The cooling system is regulated by a temperature control unit [Hoffmann Messtechnik, Rauenberg] which is included in the same metal box as the spectrometer in a separate circuit box. This control unit needs a temperature sensor on the 'cold-side' of the peltier cascade and a second temperature sensor is placed at the 'warm-side' of the Peltier cascade, which is used for temperature monitoring purposes only. The Peltier current is turned off if T_{warm} is ≥ 65°C. Both temperature sensors are of the PT-1000 type. The fan for efficient cooling is controlled by its current. T_{set} can be changed in this version by software (DOASIS). A problem observed is the non-optimized transient response (especially in the starting phase)

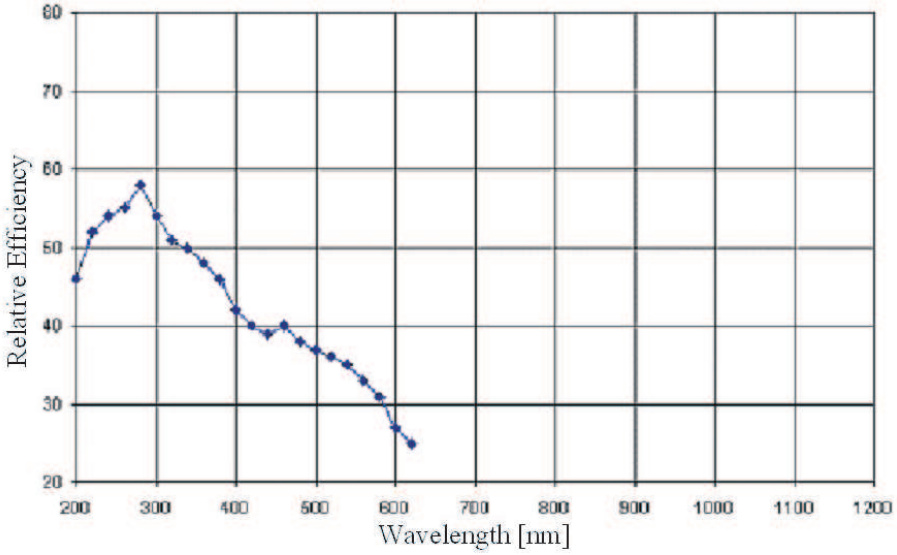

Figure 5.5: *Grating efficiency curve of the 2400 l/mm holographic grating used for this study.*

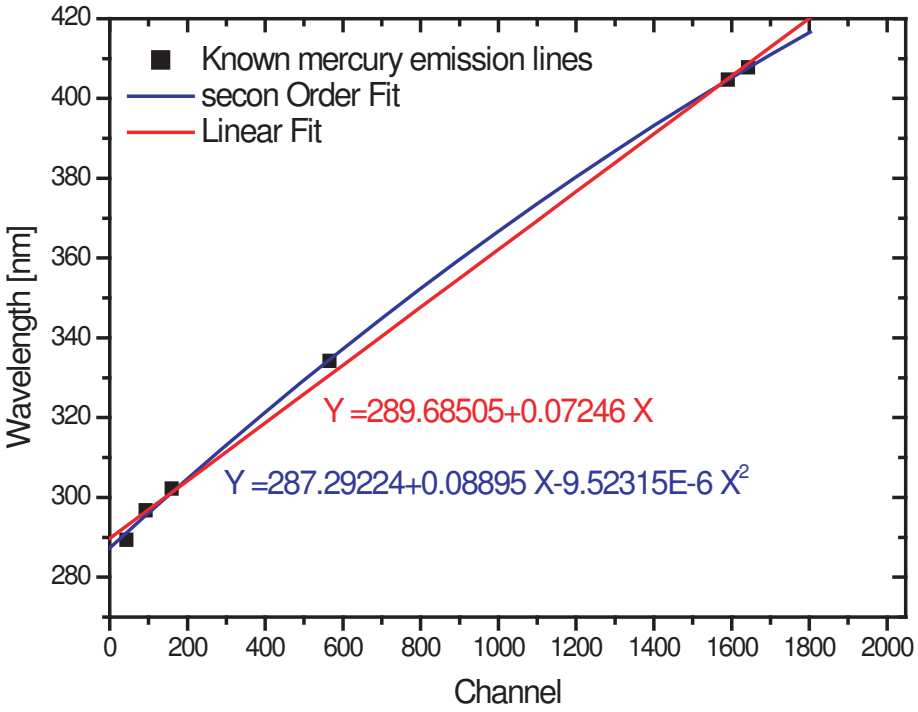

Figure 5.6: *Wavelength to pixel mapping of the USB2000 spectrograph.*

of the system, but it is much improved in comparison to former versions. It was observed that the T_{set} changed during the cooling process in this state and had to be re-adjusted after some minutes. When the desired temperature is reached it is stable to ± 0.1 K. The

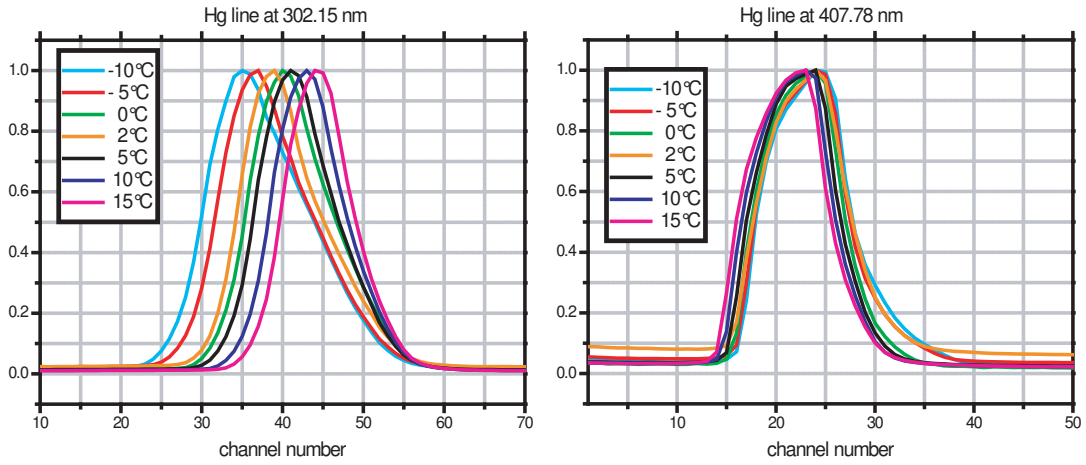

Figure 5.7: *Wavelength and temperature dependent mercury line profiles for an USB2000 of the 302.15 nm, 407.78 nm line, respectively.*

optical bench is best adjusted for 15°C. 10°C was chosen in most of the application, as it is an acceptable compromise for the given environment. At 10°C, the dark current noise is sufficiently small and the line-profile for the spectrometer (which is strongly dependent on temperature - see Figure 5.7) is still nearly gaussian.
Investigations of instrumental line-profile were carried out for different temperatures and wavelengths during this thesis. Five instruments were tested and similar temperature dependency was observed for all of them. The variation of the instrument function over the CCD detector was also investigated, (see an example in Figure 5.7), showing two mercury lines of 302.15 nm, 407.78 nm respectively for temperatures between + 15°C and -10°C . The asymmetric property of the line-profile increases and the spectroscopic resolution decreases with decreasing temperatures due to optical misalignment when cooling the optical bench. For all 5 instruments this effect was stronger in the (300 nm) UV range of the CCD, than in the visible range of the spectrum. The figures illustrate that the lines are not only shifted with temperature - they also show a significant change of the line profile. The data acquisition is performed by a notebook computer, or alternatively by an handheld PC, which controls the entire unit, including the stepper motor drive which periodically change the viewing direction. The entire system (notebook PC, cooling system, spectrometer and stepper motor) operates on 12 V for about 24 hours from a standard car battery (capacity of 60 Ah) or for several hours with a small lead battery (7.2 Ah) by using a Pocket PC instead of a notebook. The power consumption is < 20 W. The total instrument has a weight of 4.5 kg.

5.2 The Imaging DOAS (I-DOAS) Instrument

The imaging spectroscopy method employs a spectrometer with a 2 dimensional CCD detector. One dimension is used to measure the spectral intensities of incident light, while the second dimension contains the spatial information of one direction in space. The second spatial direction is obtained by scanning the field of view using the pushroom method. The spectra contain narrow band (of the order of one to a few nm) wavelength dependent absorption structures. These can be analyzed by the DOAS technique to yield slant column densities (SCD) of the respective absorbers for each pixel. Colour coding of the column density values results in a complete I-DOAS image of the gas distribution. Combination of imaging spectroscopy and DOAS measurement results in a three-dimensional set of data, which could be called a 'super colour' or 'hyperspectral' image in contrast to an ordinary colour image containing intensity information of only three wavelength ranges [*Lohberger et al.* 2004; *Lohberger* 2003] Figure 5.8 shows an outline of the measurement principle used

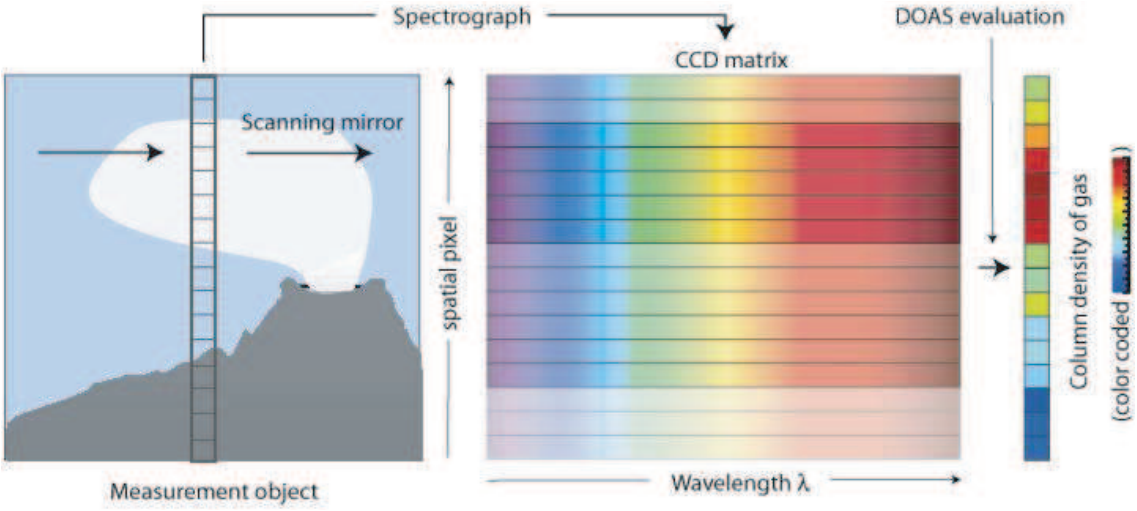

Figure 5.8: *Measurement principle: A column (one spatial dimension - a column of pixels) is spectrally imaged by the I-DOAS instrument. The resulting two-dimensional set of data is analyzed to retrieve the column densities of trace gases for each pixel of the measured column. The second spatial dimension is scanned using a mirror. The two spatial dimensions can be combined to achieve a color-coded image of the trace gas distribution (see text for details).*

to retrieve two-dimensional trace gas information from I-DOAS observations. Figure 5.9 depicts the observation geometry of an I-DOAS measurement. The instrument is set-up at a safe distance (typically 500 m to several km) from the volcanic emission source and the field of view is aimed at the volcanic summit or where sources are suspected. The mean elevation angle α (vertical viewing direction of the instrument) is adjusted so that the vertical extent of the plume is within the vertical field of view of the I-DOAS instrument. From radiation

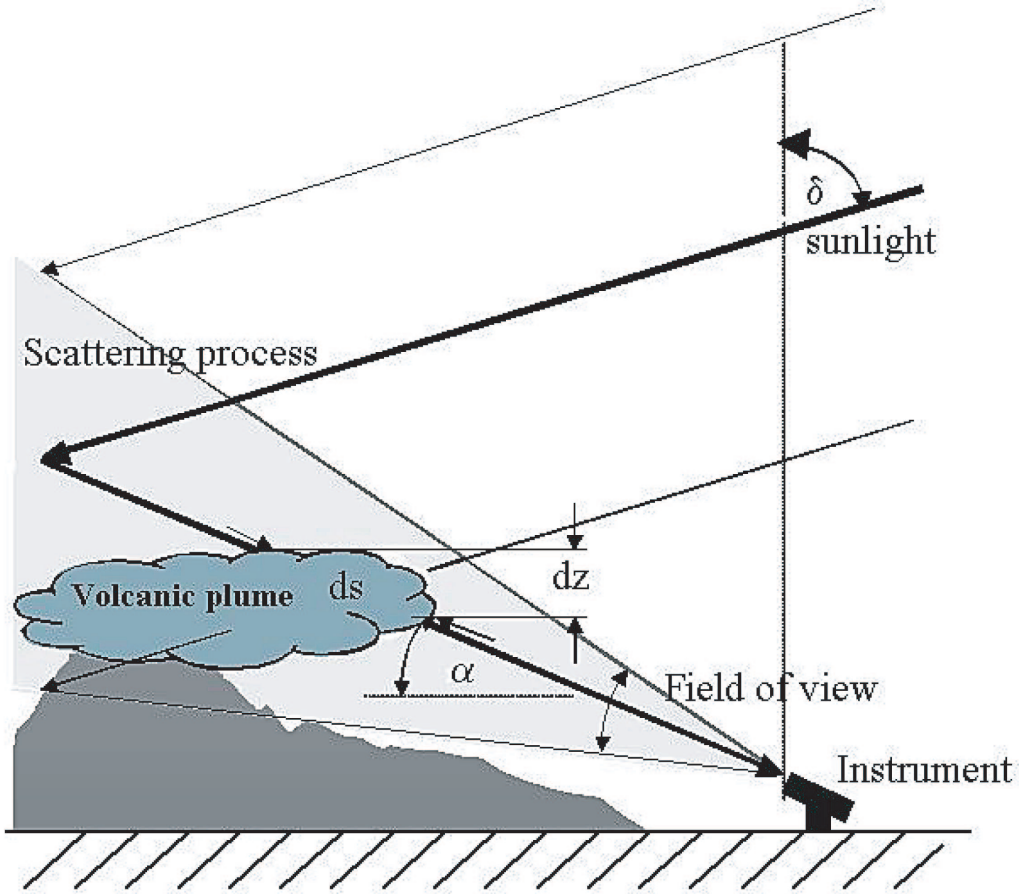

Figure 5.9: *Observation geometry of ground based I-DOAS instrument. Sunlight is being scattered in the atmosphere before passing the plume.*

transfer modelling of similar geometries [*Hönninger et al.* 2004]. It can be assumed that for distances of less than 10 km, sunlight received by the instrument is most likely scattered beyond the volcanic plume and is thus subject to absorption by gases while transecting the plume. In order to eliminate the unwanted background gas concentration and to account for the strongly wavelength dependent Fraunhofer structures of the sunlight, it is necessary to obtain a Fraunhofer reference spectrum (FRS). The evaluated quantity is then the difference in slant column density, i.e. the trace gas concentration integrated along the path ds in the plume only. The FRS can be measured while looking far away from the plume, thus eliminating a possible stratospheric or tropospheric trace gas background. In practise, either a row of the measured image located outside the plume is chosen, or an additional image of only one row is recorded in a direction looking away from the plume. Plumes can be identified very easily with this method - their extent perpendicular to the propagation direction can be measured, and spatial inhomogeneities are immediately discovered in the image as long as they appear on a larger timescale than the scanning

time of the I-DOAS, which is in the order of minutes.

Instrument Description

The instrument is described in detail by *Lohberger et al.* [2004] and *Lohberger* [2003], thus only a brief description is given here. The main elements of the instrument are shown in 5.10. Light is received by the entrance optics (quartz lens, f=30 mm, d = 20 mm,

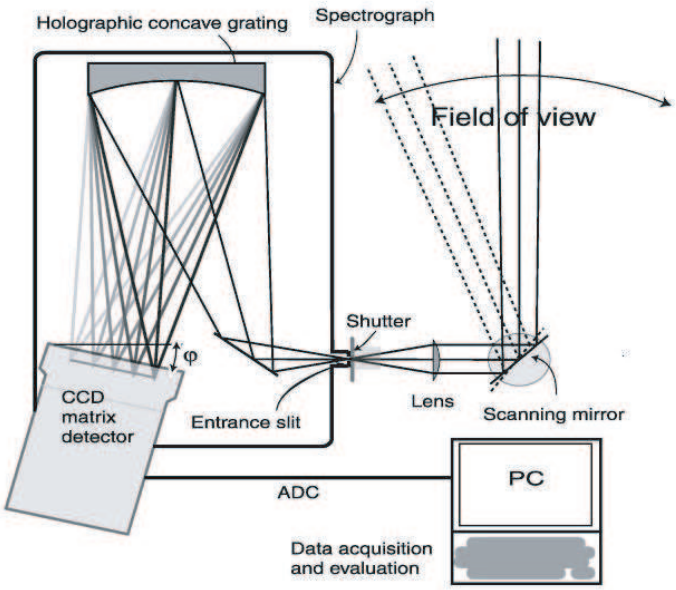

Figure 5.10: *Sketch of the instrument: Main components are the scanning mirror, imaging lens and imaging spectrograph with a two dimensional CCD detector allowing push-broom imaging spectroscopy. Adapted from Lohberger et al. [2004]*

field of view 13.1° vertical; minimum spatial resolution 0.026° vertically) which focusses the incident scattered sunlight originating from the direction of the investigated object onto the entrance slit (height = 6.9 mm, width = 46 μm) of the spectrograph via a moving mirror. The spectrograph (JobinYvon UFS200, f/# = 3.2, holographic flat-field aberration corrected concave grating, f=21 cm, grating efficiency 30-40%, 273.70 - 385.06 nm spectral range) images the vertical direction of the entrance slit on one dimension of a two-dimensional CCD detector (Andor DU440UV, (spectral) 2048 x (spatial) 512 pixels) while the spectrum is dispersed in the perpendicular (horizontal) CCD dimension. The spectral resolution of the spectrometer/detector assembly is 0.3 nm FWHM within the spectral range that is used for data evaluation. Scanning in the second spatial (horizontal) direction is implemented by a plane mirror, which scans the field of view using a stepper motor driven by computer control. The minimum step size of the stepper motor is 1.8°, but including the gear unit with a 279:1 reduction ratio steps as small as 0.0065° can be achieved. However, due to the limitation of the slit, (which has a width of 46 μm),

the best horizontal resolution is 0.087°. A portable PC controls the entire instrument set-up using a custom software package. The simple and relatively compact design of the Imaging DOAS instrument (ca. 50 x 50 x 20 cm^3, 10 kg without the PC) allows easy transport and set-up in the field. If necessary, temperature stabilization of the optical bench could be added in the future in order to eliminate the influence of ambient temperature changes. This could be built from a light-weight foam around a heated spectrometer. The heater would probably require 10 W of additional electrical power. However, for fast measurements (< 20 min), temperature stabilization was found to be non-essential. For the alignment of our spectrometer, the best compromise between best spectral and best spatial resolution was chosen [*Lohberger et al.* 2004; *Bobrowski et al.* 2005]. The aberration in the dispersion direction is accounted for by an averaged instrument function (measured as mercury emission line profile of negligible line width compared to the instrument's spectral resolution), with which the high-resolution reference spectra are convolved. The resolution of the spectrometer perpendicular to the dispersion direction (vertical) is degraded due to 'cross talk'. It was determined by *Lohberger et al.* [2004] that the point spread function (PSF) of the spectrometer in vertical direction has a width of about 2-3 detector pixels. In the evaluation, eight detector lines were binned, thus decreasing the spatial resolution in the vertical direction to 64 rows at an angular resolution of 0.208 ° each. Therefore, the degradation of image quality due to the PSF should be negligible. In the future, the line shape change over the full spectral range of the detector can be accounted for by fitting a high resolution solar spectrum, and possibly determining a wavelength dependency of the line shape to perform more accurate measurements. This can be achieved by using an implementation of an automated calibration of each spectrum by a fit to the high-resolution solar spectrum using line shape and wavelength shifts as fit parameters.

Chapter 6

Evaluation of DOAS Data

In this chapter the evaluation for the different species measured by the Mini-MAX-DOAS (and IDOAS - only SO_2) instrument for this thesis will be described exemplary for each investigated species. Possible error sources will be discussed. All data described in the following chapters is evaluated in the same way. Problems regarding individual measurement sites are considered in the chapter on field sites. The exemplary data set was taken at the 5^{th} August 2004 at Mt. Etna. For HCHO data from the 25^{th} March 2003 at Masaya has been taken, because HCHO could not be detected in the data set of Mt. Etna on the 5^{th} August 2004.
For the DOAS fit the software WinDoas V2.10 from IASB (Belgium Institute for Space Aeronomy, [*Roozendael and Fayt* 2001] was used to derive the SCD from the recorded spectra. In the case of scattered sunlight as light source the solar Fraunhofer lines (modulating $I_0(\lambda)$) had to be removed carefully in order to allow sensitive measurements of trace species. As Fraunhofer reference spectrum (FRS, $I_0(\lambda)$) an actual background spectrum taken after each volcanic plume scan was chosen and care was taken that the FRS did not contain any absorption by the volcanic plume.
All spectra were corrected for dark current and offset, weighted by the respective integration time and the number of scans before the DOAS fit was applied.

6.1 Evaluation of Sulphur Dioxide

SO_2 was evaluated with a variety of available cross sections of *Vandaele et al.* [1994] and of *Bogumil et al.* [2003] for 293 K, 273 K, 243 K, 223 K in order to optimize the fit results - as these results depend strongly on the quality and the resolution of available literature spectra. It was investigated if there is a significant temperature dependence for which care has to be taken when evaluating spectra, which are collected in different environmental conditions. Except the different SO_2 references, the fit scenarios were all equal in all of the described studies. Due to the huge amounts of SO_2 and not always sunny conditions

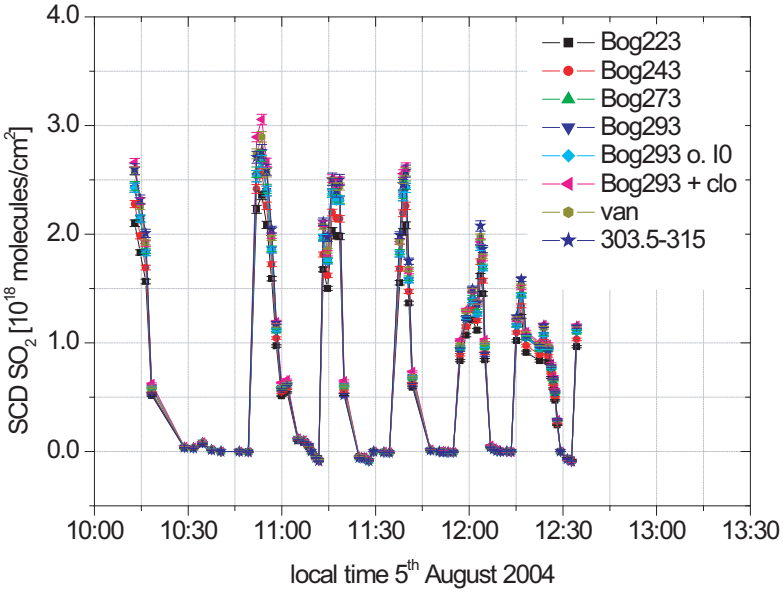

Figure 6.1: *Time series of SCDs of SO_2, for different evaluation settings*
Black, red, green, purple, are evaluations carried out with the SO_2 reference of Bogumil et al. [2003] for 223 K, 243K, 273 K and 293 K, repectively.
Light blue use the Bogumil et al. [2003] reference of 293 K without an I_0 correction
Pink - fit scenario with an additionally trace gas (ClO).
Dark yellow - fit scenario with the SO_2reference of Vandaele et al. [1994].
Violet - fit scenario with an enlarged evaluation range (to 303.5 -315nm).

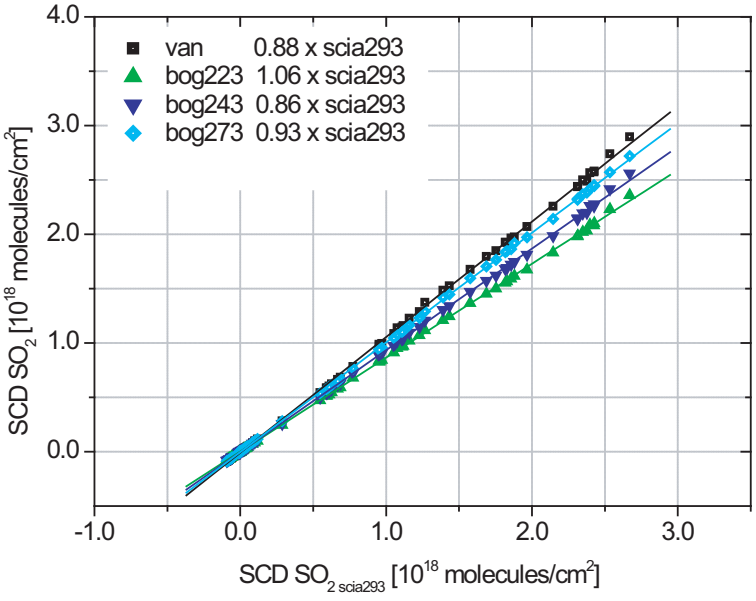

Figure 6.2: *All SO_2 SCDs are plotted as a function of the evaluation with the SO_2 reference at 293 K of Bogumil et al. [2003] in a wavelength range 306 - 315 nm. Correlation of SO_2 SCDs for the cross sections of different temperatures. (black - Vandaele cross section 295 K, green - Bogumil 223 K, blue - Bogumil 243 K, light blue - Bogumil 273 K)*

(higher UV intensity) an evaluation range from 307.5 to 315 nm was chosen to provide the possibility of an equal evaluation for all sites and therefore better comparability. Besides the SO_2, an O_3 reference [*Bass and Paur* 1985] and a Ring-spectrum (calculated with DOASIS [*Kraus* 2001]) were included in the fit. To remove broadband structures a polynomial of the second order was applied. Additionally the option of a pre-logarithm offset was used to take account for the amount of spectrometer stray light.
As a Fraunhofer reference spectrum (FRS) always the closest spectrum (regarding the time) was applied to the DOAS fit. In general the results of the scenarios with different SO_2 cross setions are comparable in their 2 σ fitting error range. But nevertheless there

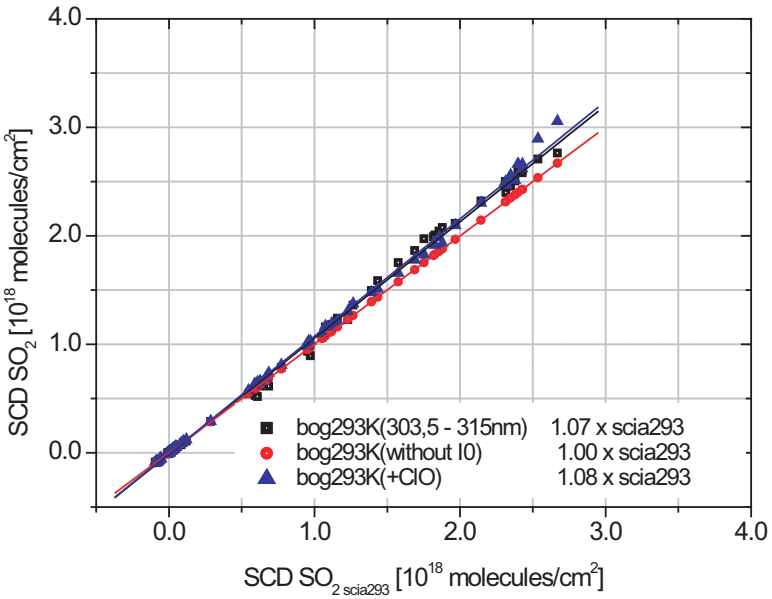

Figure 6.3: *All SO_2 SCDs are plotted as a function of the evaluation with the SO_2 reference at 293 K of Bogumil et al. [2003] in a wavelength range 306 - 315 nm. Correlation of SO_2 SCDs for changes of the fitting scenario: black evaluation in an enhanced wavelength range (303.5 - 315 nm), red evaluation with a I_0 corrected SO_2 reference, blue fit scenario with an additionally trace gas (ClO).*

is also a clear trend visible in the results: Smaller SCD values for lower temperatures.
Surprisingly the *Vandaele et al.* [1994] reference is in the best agreement with the *Bogumil et al.* [2003] reference of 273 K and not with the cross section at 293 K as it would be expected since the Vandaele reference spectra [*Vandaele et al.* 1994] was taken at 295 K. Up to 20 % difference can be found between the references for the different temperatures in a range of 70 K. It should be recommended to choose always the closest temperature possible to the measurement conditions to get accurate fit results. In case of measurements with the Mini-MAX-DOAS instruments (or other spectrometers with the same or lower spectral resolution (0.7nm)) the resolution of the cross section of [*Bogumil et al.* 2003] (0.2

nm) is sufficient.

The scenario applying the SO_2 reference at 293 K by *Bogumil et al.* [2003] was additionally

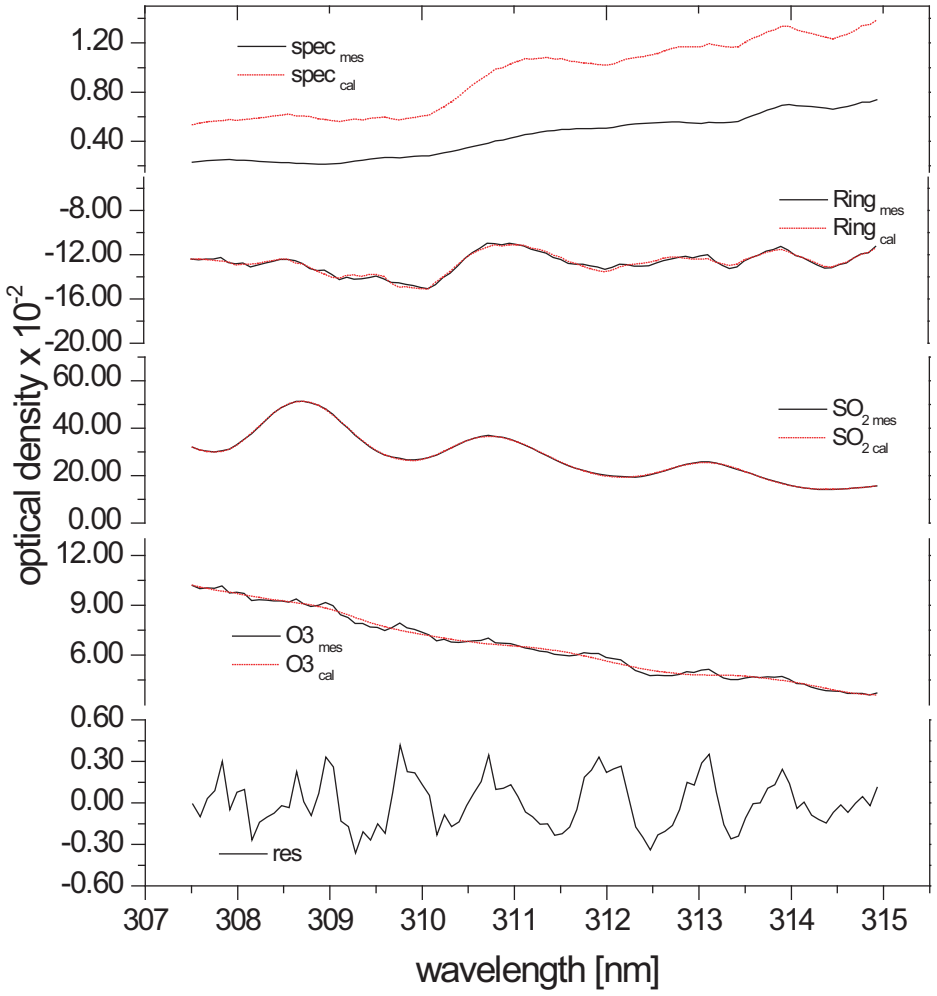

Figure 6.4: *Example of the DOAS SO_2-Fit. Black lines: measured spectra, red lines: reference spectra, the atmospheric spectrum was taken at plume center at Mt. Etna on 5^{th} of August 2004.*

tested for the comparability of the fit results by fitting an additional reference (in this case chlorine monoxide (ClO) [*Burrows et al.* 1999]), which could have been present as well, which was at several volcanic sites later shown to be true. ClO shows absorption features in the same evaluation range chosen for the SO_2 evaluation, but does not influence the SO_2 result significantly. The difference for the SO_2 SCD's are inside an 1 σ fitting range. The effect of an applied I_0 correction for the SO_2 cross section and the change (enhancement) of the evaluation range were tested as well. The results are shown in Figure 6.3 on

the left side. The differences of the SCD results here are in the range of the fitting errors. The I_0 correction for the SO_2 convolution shows nearly no change in the resulting SCDs. For the result of the studies in this thesis the SCDs of SO_2 are results by applying the cross section of *Bogumil et al.* [2003] at 293 K (because it was assumed that the investigated volcanic plumes had a temperature above zero) and applying the fit scenario as described above. A shift and a squeeze of 1^{st} order were allowed for the measurement spectra to overcome e.g. slight temperature changes. An example for one evaluated spectra is given in Figure 6.4

6.2 Evaluation of Bromine Monoxide

The BrO-fit, like it is displayed for exemplary in Figure 6.6, was applied for all analysis procedures during this study. BrO was evaluated in a wavelength range from 332 to 352 nm, which includes 4 strong absorption bands of the BrO cross section. As suggested in *Aliwell et al.* [2002] 2 ozone [*Voigt et al.* 1999] references for 223 K and 246 K, a O_4 [*Hermans et al.* 1999] reference and NO_2 [*Voigt et al.* 1999] at 246 K were fitted beside the BrO at 298 K [*Wilmouth et al.* 1999]. Additionally to the recommended cross sections of *Aliwell et al.* [2002] a SO_2 [*Bogumil et al.* 2003] at 293 K reference was applied. Because of the high SO_2 SCDs even the very small cross section in that region might disturb the detection of BrO. A Ring spectrum calculated with DOASIS [*Kraus* 2001] and a Fraunhofer reference spectrum (the closest spectra (regarding the time) outside the plume) was fitted. A polynomial of the 3^{rd} order was applied to remove the broad band structure and a 2^{nd} order pre-logarithm offset was applied to overcome the high amount of spectrometer stray-light due to the small size of the instrument. A shift and 1^{st} order squeeze were allowed for the measured spectra. An example for this evaluation is given in Figure 6.6
Sensitivity studies on two further wavelength ranges were carried out for each spectrum as already described in *Bobrowski* [2002]. The same cross sections were fitted in a wavelength range from 320 - 358 nm, which includes 8 absorption bands of the BrO and in the "standard" BrO evaluation range 346 - 358 nm, including only 2 absorption bands, as suggested from *Aliwell et al.* [2002]. For the wide range of 8 bands a polynomial of 5^{th} order and in the case of the narrow range of 2 bands a polynomial of 2^{nd} order were applied. Comparison for the evaluation of the spectra set of 5^{th} August 2004 are presented in Figure 6.5. No significant differences can be seen on the left panel of Figure 6.5, all three evaluations are in agreement inside the 2 σ error range. By looking in the correlation plot on the right panel in general higher values for the narrow and lower values for the wide evaluation range can be observed. This behavior was found in other investigated data sets, too.

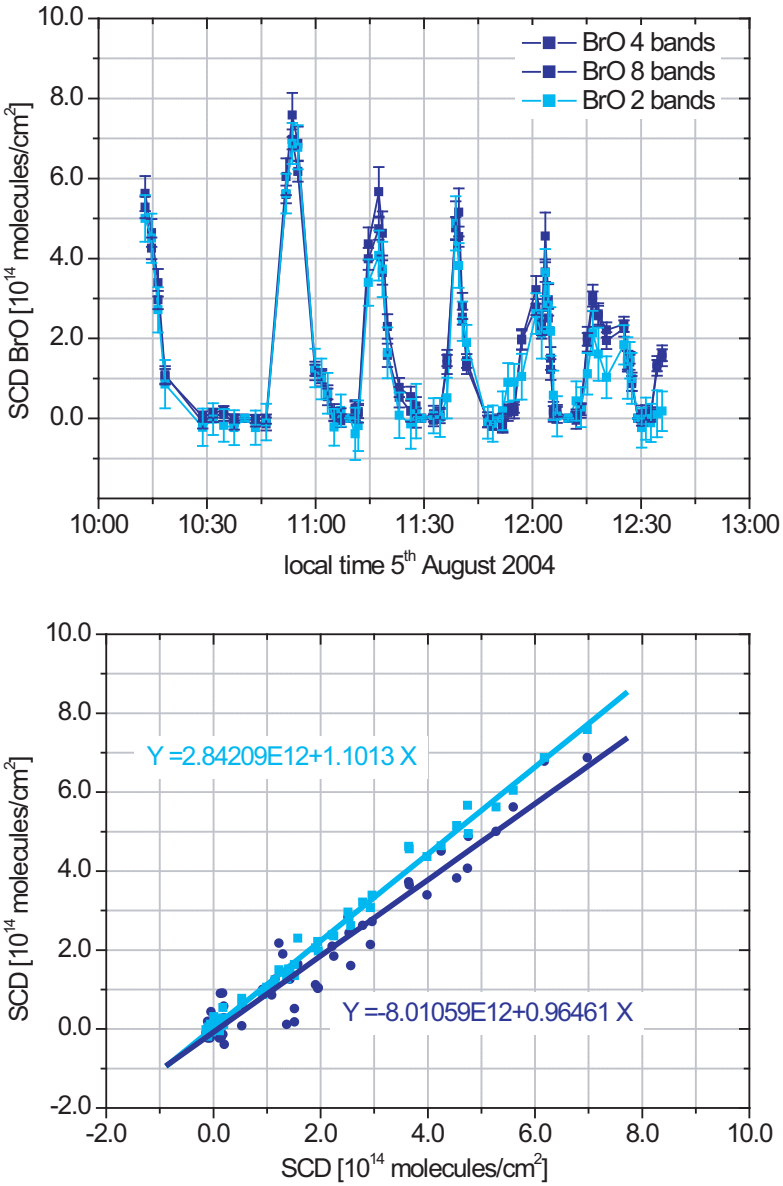

Figure 6.5: *BrO Fit results for evaluation in different wavelength ranges are shown as a function of time. Blue displays the evaluation of 4 bands used during this study. Light blue color shows the result of the "standard" BrO evaluation [Aliwell et al. 2002]. The dark blue presents the evaluation in the very wide range of 8 absorption band (320-358 nm). The lower part of the Figure shows the correlation of the 2 and 8 BrO absorption bands evaluation to the 4 BrO absorption band evaluation.*

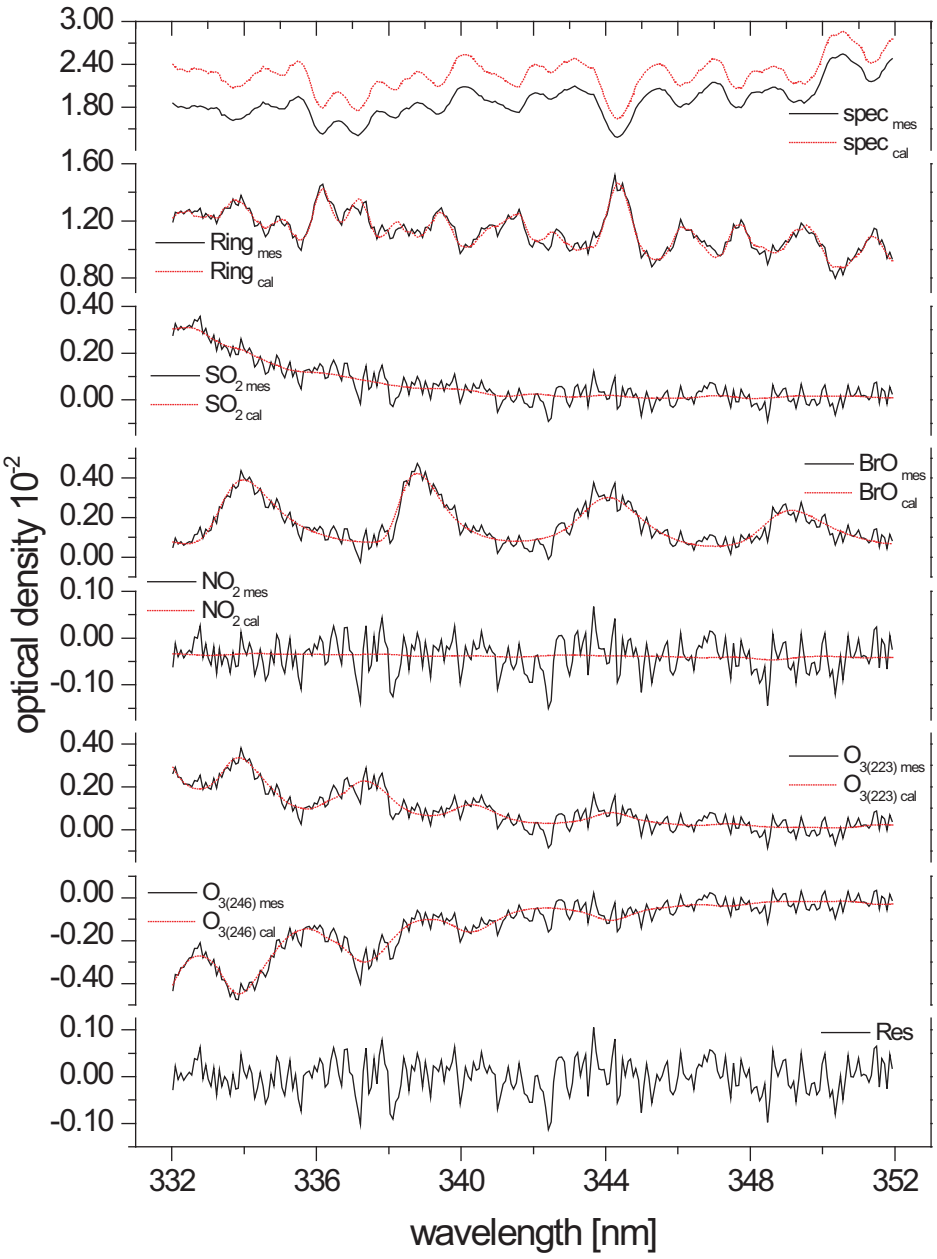

Figure 6.6: *Example of the DOAS BrO-Fit. Black lines: measured spectra, red lines: reference spectra, the atmospheric spectrum was taken at the plume center at Mt. Etna on 5th of August 2004.*

6.3 Evaluation of Chlorine Monoxide

The evaluation in this low wavelength range is not unproblematic. Strong absorption bands of ClO are located at $\lambda \leq 308$nm. At this wavelength the solar intensity is quite low (O_3 absorption), thus the photon statistic is relatively poor. The photon noise is already a quite limiting factor for a good quality evaluation. The other problem is the possible interference of other cross section of the trace gases. Several evaluation settings were investigated and

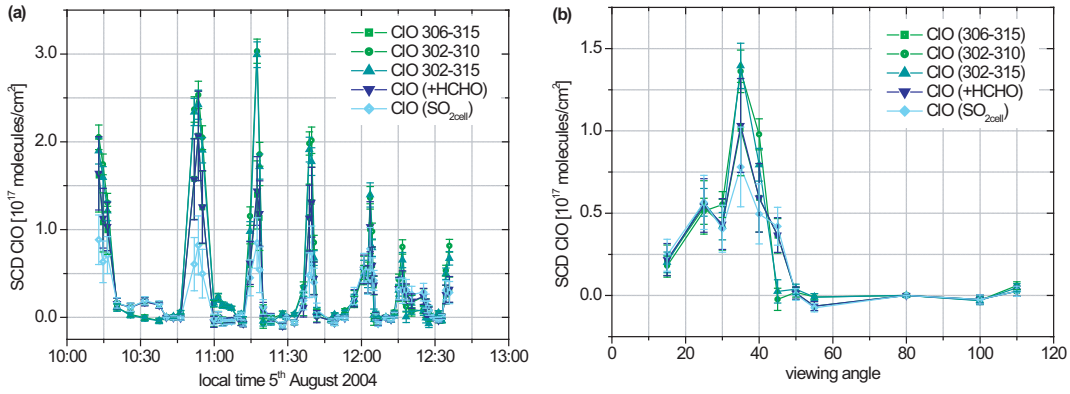

Figure 6.7: *Time series of ClO SCDs for different fitting scenarios (a) SCDs of different ClO evaluation settings coded by different colors for all data of 5th August 2004 (b) One plume scan is zoomed out.*

the results are presented in the following. They clearly show that care has to be taken to obtain information about this further halogen compound in volcanic plumes. In this study only the data for sunny days (with high UV radiation) were used for interpretation. Further research and improvements are necessary, like a better Ring spectrum, where beside N_2 and O_2 also the Raman-scattering regarding the O_3 is considered. Measurements of an active DOAS system compared to a MAX-DOAS system are desirable and highly recommended for the future.

The 5^{th} August 2004, a very sunny day was used to do different case studies for the ClO evaluation. ClO was analyzed in 3 different wavelength regions 306 - 315 nm, 302.7 - 310 nm, 302.7 - 315 nm. Beside ClO [*Burrows et al.* 1999], one ozone (243K) [*Bass and Paur* 1985] and a SO_2 (293K) [*Bogumil et al.* 2003] reference spectrum were applied to the fit scenario. Also a Ring spectrum calculated with DOASIS [*Kraus* 2001] and a Fraunhofer reference spectrum (the closest spectra (regarding the time) outside the plume) was fitted. A 2^{nd} order polynomial (for the range 302.7 - 315 of 3^{rd} order) was applied to remove the broad band structure and a second order pre-logarithm offset was applied to overcome the high amount of spectrometer stray-light due to the small size of the instrument. A shift and 1^{st} order squeeze were allowed for the measured spectra. Further sensitivity studies were made by adding another reference (HCHO) and by using a SO_2 spectrum gained by

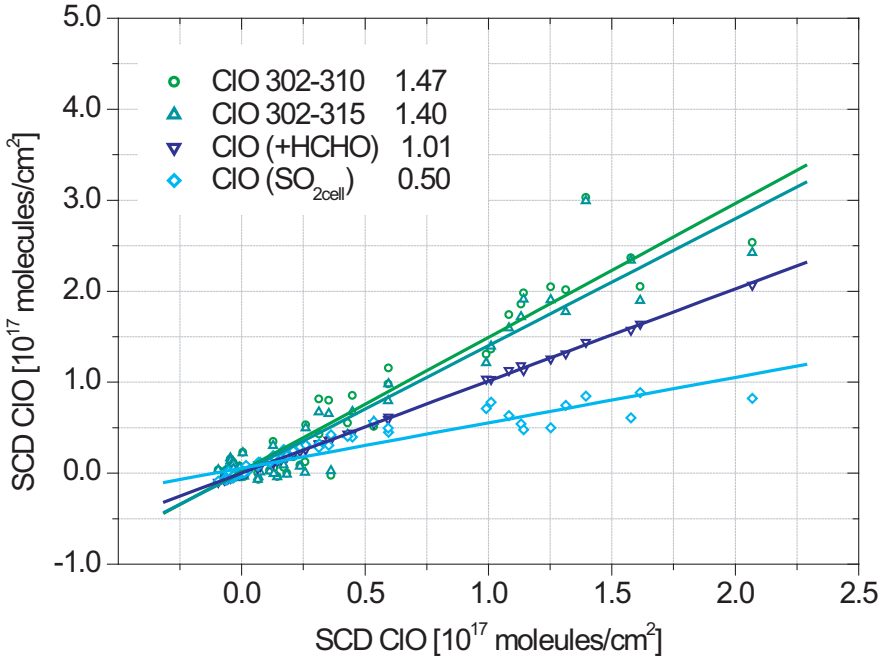

Figure 6.8: *Comparison of different ClO fit-scenarios. ClO SCDs are plotted as a function of the ClO SCDs for an evaluation range of 306 - 315 nm (used in this thesis).*
Green: Evaluation with a shifted evaluation range (302.7 - 310 nm)
Dark Cyan: Evaluation with an extended wavelength range (302.7 - 315 nm)
Navy Blue : Evaluation by applying an additional cross section (HCHO)
Cyan: Evaluation by using a SO_2 reference taken with the same instrument by cell measurements

measurements with a SO_2 cell.
All results for the ClO SCDs follow the same trend, increasing at elevation angles near the plume center and decreasing by leaving the plume (Figure 6.7). But the SCD values scatter up to a factor of 2 (Figure 6.8), which shows the high uncertainty of this values later in this study. Nevertheless it is worth to gain a value within at least an order of magnitude for this new discovered species in a volcanic plume.

6.4 Evaluation of Chlorine Dioxide

OClO was analyzed between 341 and 390 nm, where 6 strong absorption bands of OClO can be found. Beside OClO, 2 ozone [*Voigt et al.* 1999] references for 223 and 246 K, a O_4 [*Hermans et al.* 1999] reference, NO_2 [*Voigt et al.* 1999] at 246 K were fitted and BrO [*Wilmouth et al.* 1999] at 298 K and an additionally SO_2 [*Bogumil et al.* 2003] at 293 K reference. Because of the high SO_2 slant column densities even the very small cross

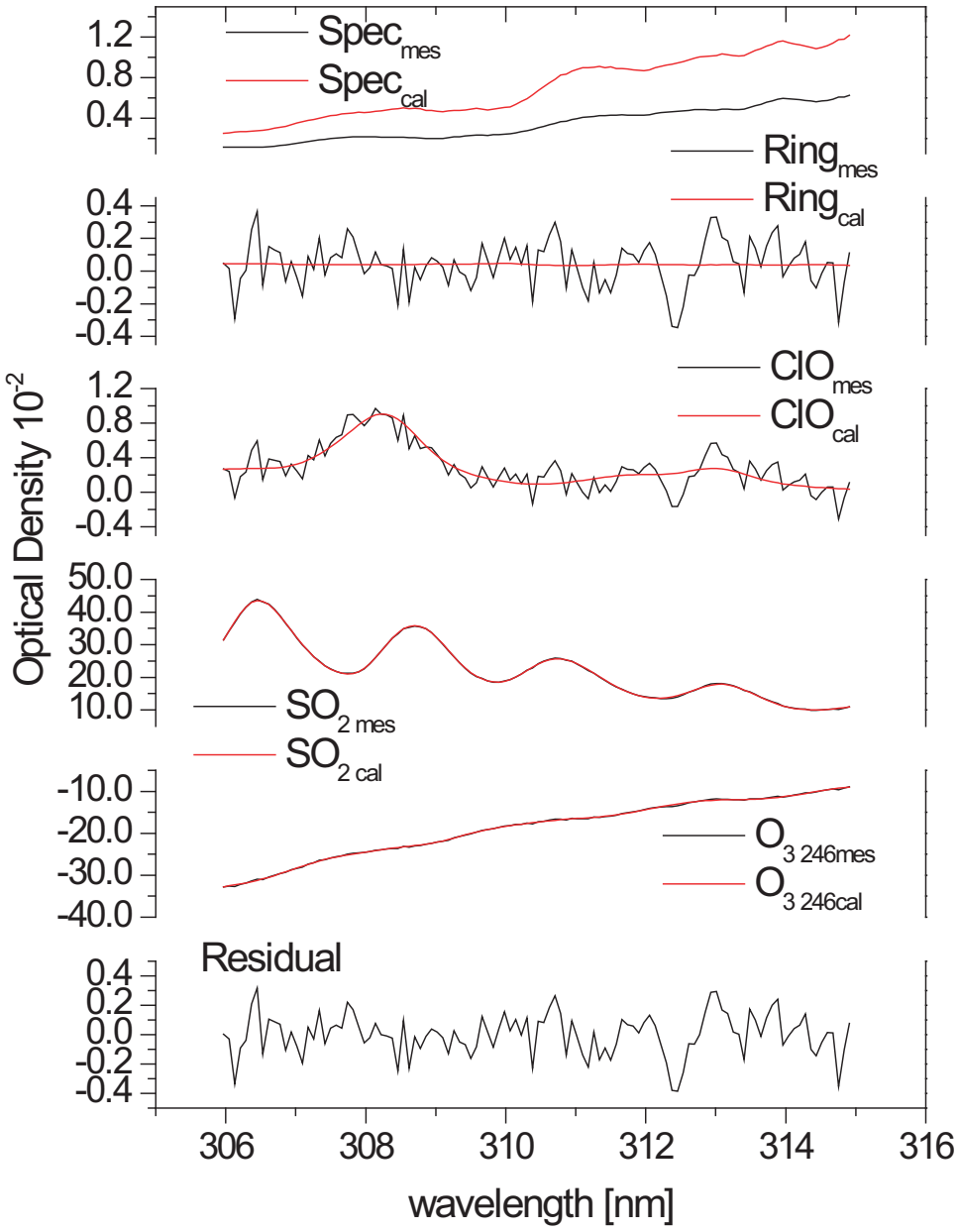

Figure 6.9: *Example of the DOAS ClO-Fit. black lines: measured spectra, red lines: reference spectra, the atmospheric spectrum was taken at plume center at Mt. Etna on the 5th of August 2004.*

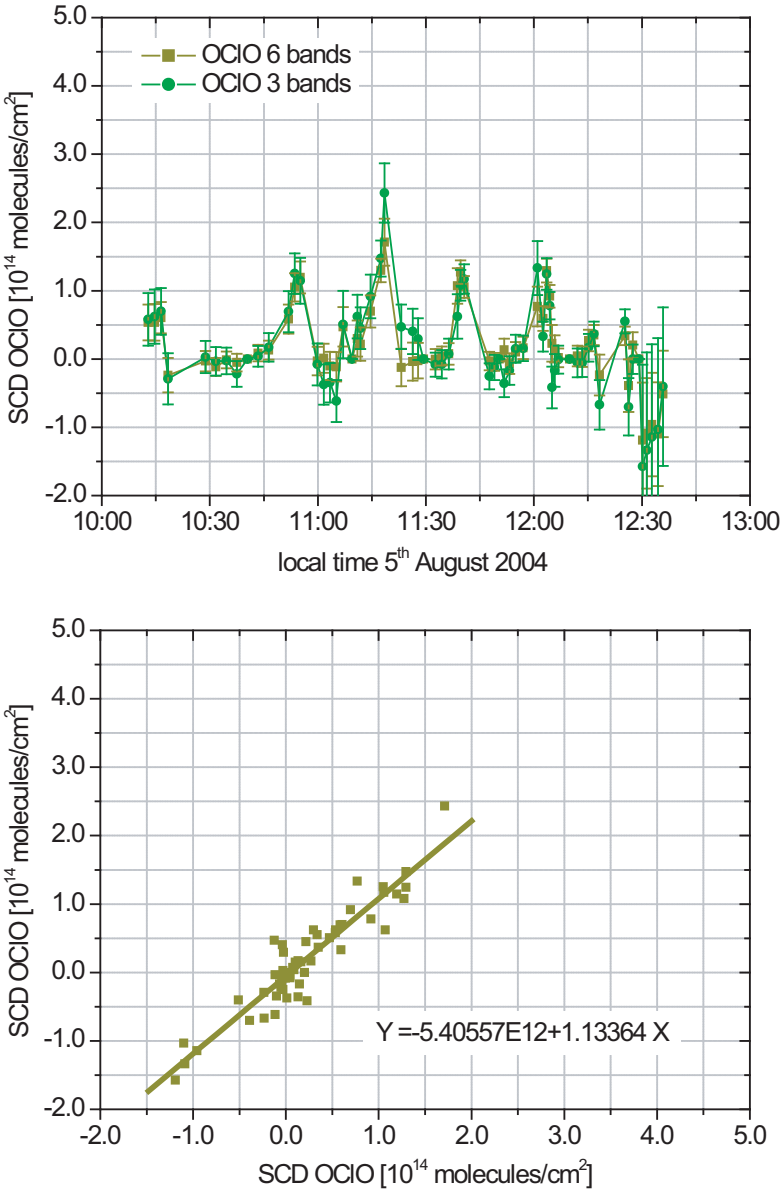

Figure 6.10: *OClO-Fit comparison for two wavelength ranges. The wide fitting range from 241 to 390 nm is presented in dark yellow. The smaller wavelength range of three OClO absorption bands (362 to 390) nm is presented in green. The same SCD results within a two σ error range can be observed, again the shorter evaluation range shows enhanced SCD values, similar to the feature seen in the analysis of other trace species (e.g. BrO).*

section in that wavelength region might otherwise disturb the detection of OClO. Also a Ring spectrum calculated with DOASIS [*Kraus* 2001] and a Fraunhofer reference spectrum (the closest spectrum (regarding the time) outside the plume) was fitted. A polynomial of the 5^{th} order was applied to remove the broad band structure and a second order pre-logarithm offset was applied to overcome the high amount of spectrometer stray-light due to the small size of the instrument. A shift and 1^{st} order squeeze were allowed for the measured spectra. A second evaluation for OClO in the same evaluation range as

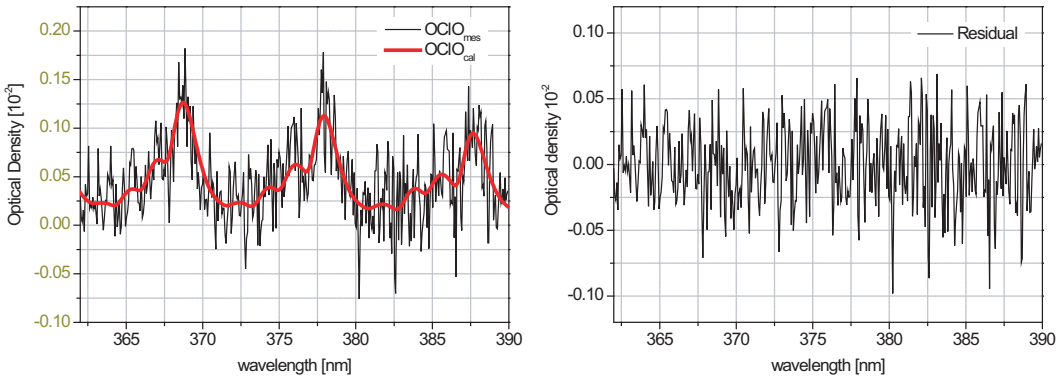

Figure 6.11: *OClO-Fit for an evaluation range of 362 - 390 nm. The WinDOAS fit result for one example of OClO detection. On the left side the OClO absorption bands in red, the measured spectrum in black. In the right panel the residual for this fit is shown, with a peak to peak of 1.5 %.*

performed by *Kühl* [2005] was done. An example of the detected OClO absorption is given in Figure 6.11. A comparison for the data set for both evaluations is presented in Figure 6.10. Similar to the BrO evaluation both results are in agreement regarding a 2 σ fitting error. Again the SCDs of the shorter evaluation range are enhanced in comparison to the evaluation of the wide range of 6 absorption bands.

6.5 Evaluation of Formaldehyde

HCHO was evaluated between 324 and 347 nm, where 2 double band absorption features of HCHO can be found. HCHO [*Meller and Moortgat* 2000], 2 ozone [*Voigt et al.* 1999] references for 223 and 246 K, a O_4 [*Hermans et al.* 1999] reference, NO_2 [*Voigt et al.* 1999] at 246 K were fitted and BrO [*Wilmouth et al.* 1999] as well as additionally a SO_2 [*Bogumil et al.* 2003] reference were applied to the fit scenario. Also a Ring spectrum calculated with DOASIS [*Kraus* 2001] and a Fraunhofer reference spectrum (the closest spectrum (regarding the time) outside the plume) was fitted. A polynomial of the 3^{rd} order was applied to remove the broadband structure and a second order pre-logarithm offset

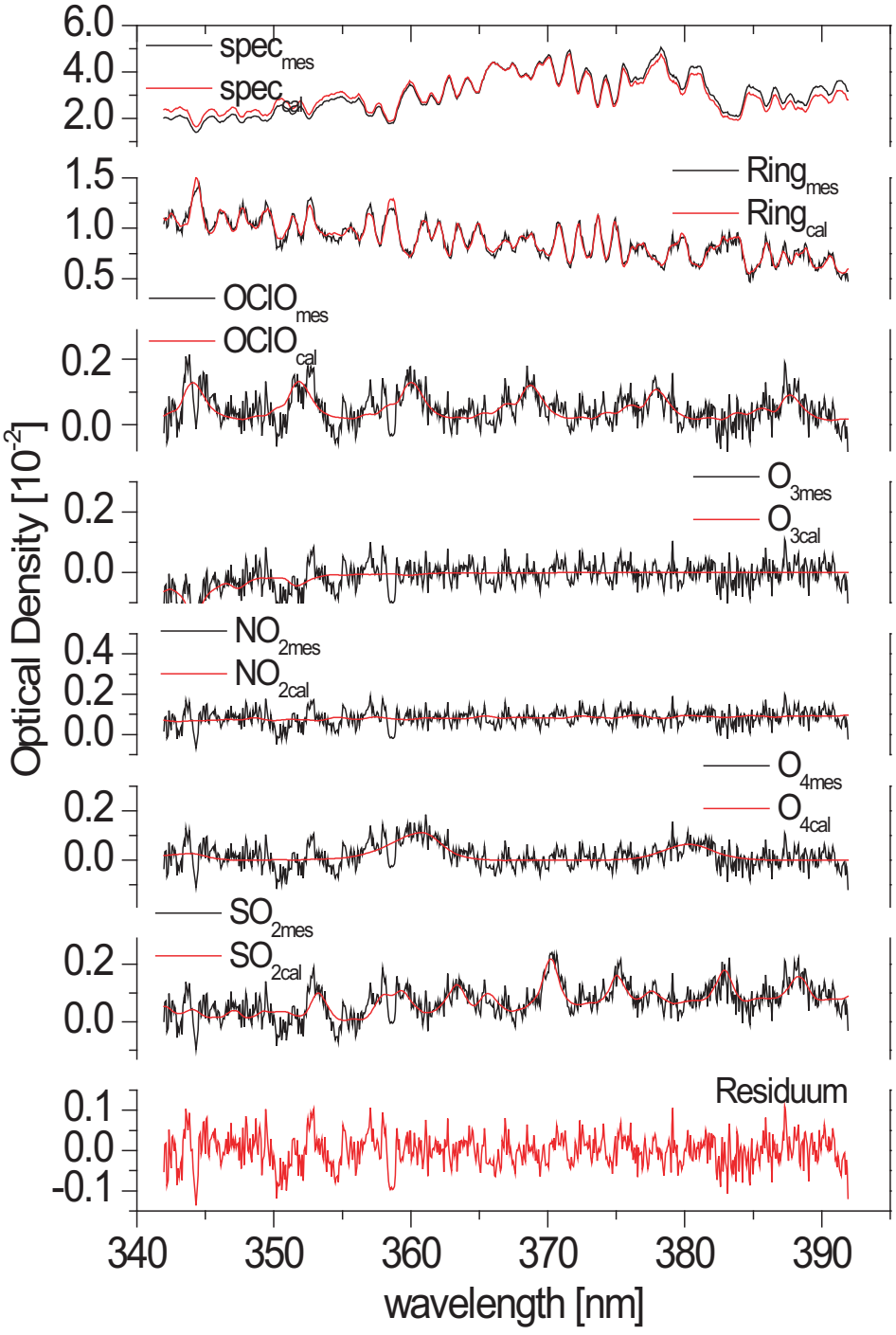

Figure 6.12: *Example of the DOAS OClO-Fit. black lines: measured spectra, red lines: reference spectra, the atmospheric spectrum was taken at plume centre at Mt. Etna on the* 5^{th} *of August 2004.*

was applied to overcome the high amount of spectrometer stray-light due to the small size of the instrument. A shift and 1^{st} order squeeze were allowed for the measured spectra.

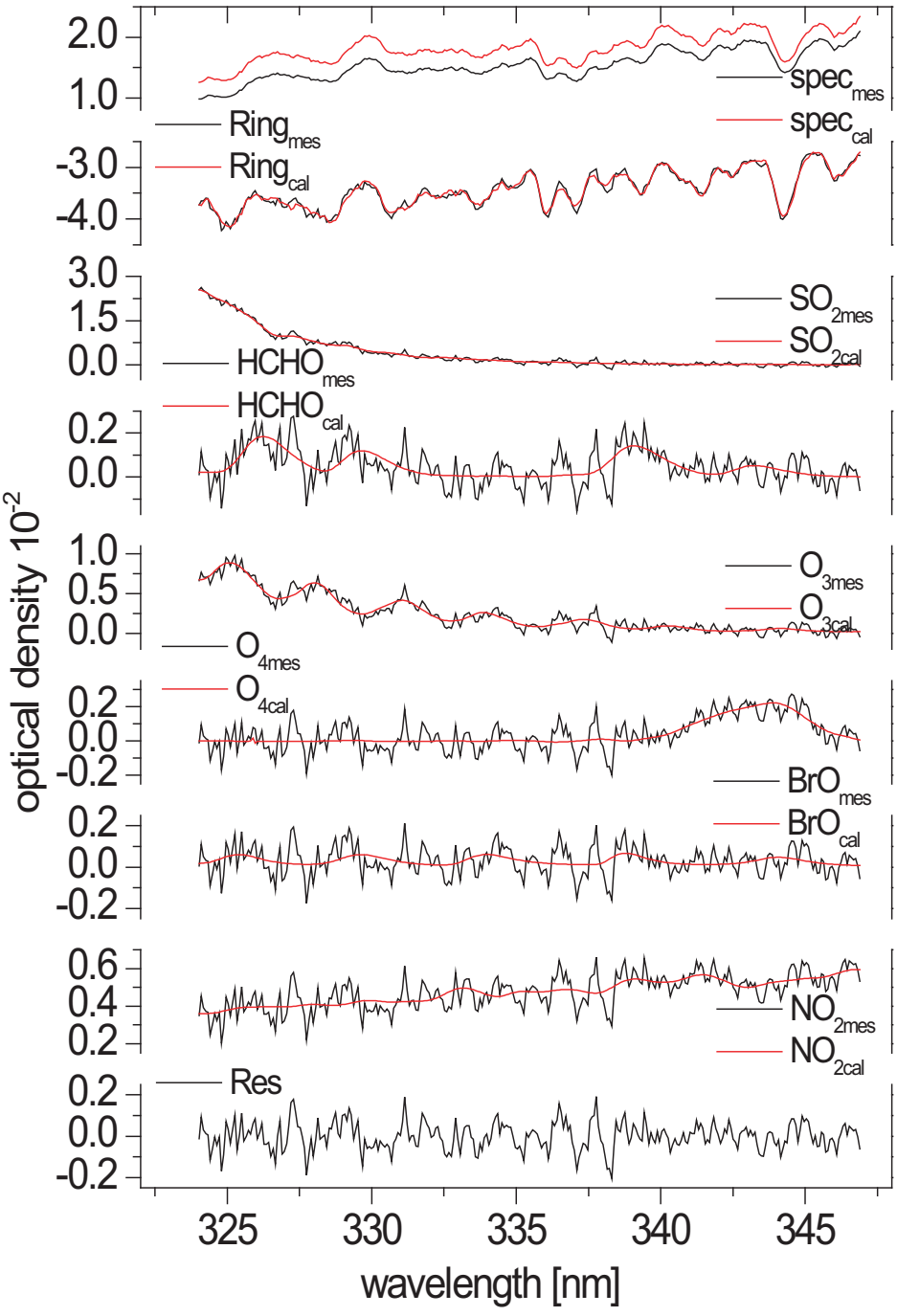

Figure 6.13: *Example of the DOAS HCHO-Fit. black lines: measured spectra, red lines: reference spectra, the atmospheric spectrum was taken above the crater of Masaya on 25th of March 2003.*

Chapter 7

Fieldwork

7.1 Description of Field Sites and Measurements

Measurements were carried out on three continents (Central America, South America, Europe). In Figure 7.1 a world map with marks for each measurement location is shown. All sites are subduction zone volcanoes, but the volcanoes differed in their individual magma composition and their volcanic activity during the time of measurements. A full description of every measurement site and campaign will be given in this section. The results are described in detail for each location and campaign. Throughout this thesis, every species is assigned its own specific color. BrO is presented in blue. ClO is displayed in green, OClO in dark yellow, HCHO in purple, O_4 in black and SO_2 in red.

Overview of the measurement sites

- Nicaragua and Costa Rica (Central America) - March 2003
- Italy (Europe)
  - September/October 2003
  - August 2004
  - September/October 2004
  - May 2005
- Chile and Bolivia (South America) - November/December 2004

7.2 Nicaragua and Costa Rica

Within the scope of the 8^{th} Gas field workshop of IAVCEI (International Association of Volcanic Chemistry and Earth Interior) measurements were carried out at three volcanoes, namely Masaya, Momotombo and Poas.

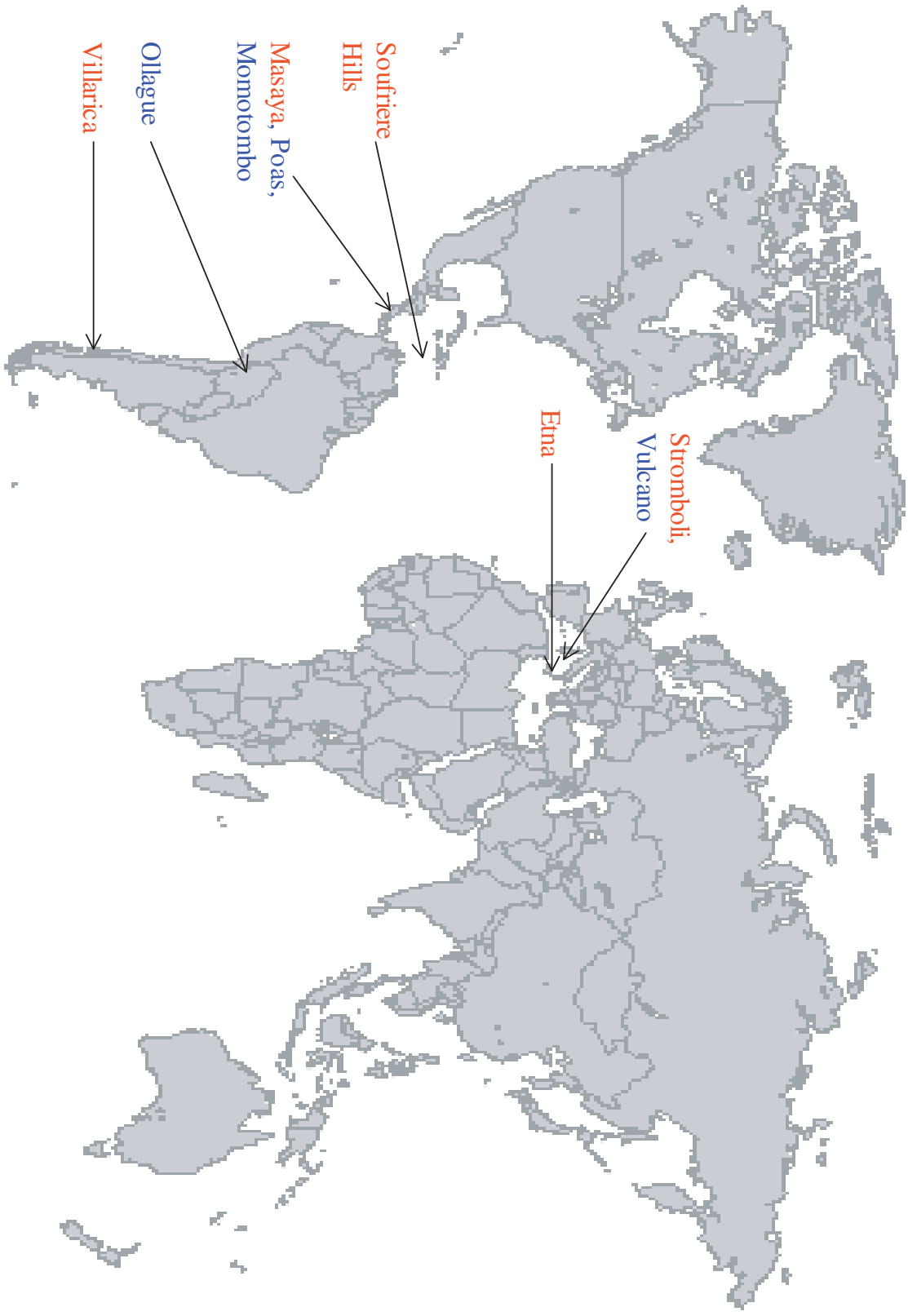

Figure 7.1: *Overview of measurement sites investigated in this study. Those volcanoes where bromine monoxide has been detected are shown in red*

7.2.1 Masaya

Masaya(12.0 N, 86.2 W) is located in Nicaragua about 25 km southwest of Managua, the capital of Nicaragua. It is the most active volcano in this region, with an altitude of 635 m above sea level. From 1965 to 1979 Masaya contained an active lava lake. The most recent eruption was in 2003, with white steam and gas emissions, but nearly without any ash. The eruption column rose about 4.5 km into the atmosphere and could be detected by satellite observations. Despite Masaya being a basaltic volcano, explosive eruptions have been observed in the past. The eruption in 4550 B.C. was one of the largest worldwide in the last 10000 years. Today Masaya consists of a caldera (approximately 6 x 11.5 km in size) with several vents. Most activity at these vents has consisted of effusions of basaltic lava. Pyroclastic eruptions have built three main cones: Masaya, Nindiri, and Santiago. Santiago was formed from 1850 to 1853. Spatter and scoria deposits indicate fire fountaining at Masaya, the only known occurrence of this type of eruption in Central America [*Williams* 1983]. The volcano Masaya has a shield-like morphology. Today Masaya emits several hundreds of tons of sulphur dioxide gas per day. It has an approximately 25 year cycle of non eruptive degassing crises [*Stoiber et al.* 1986]. The volcano affects human health in an area of about 900 km^2 downwind [*Delmelle et al.* 1999].

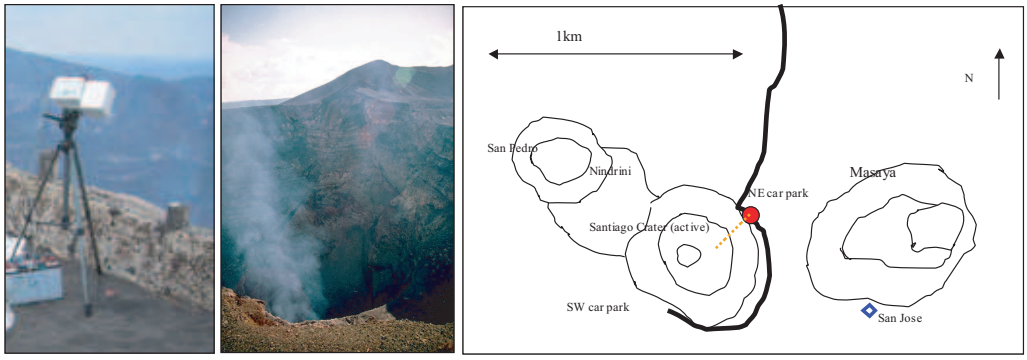

Figure 7.2: *Photo and map of the measurement location at Masaya during 25th and 28th March 2003. The measurement site is marked by a red point and the viewing direction is illustrated by the yellow dots.*

Field Measurements at Masaya 2003

On March 25th, 28th and 29th 2003 measurements with a Mini-MAX-DOAS instrument were carried out in the vicinity of Masaya. The first measurements took place in the parking lot North East (NE) of the Santiago crater. The Mini-MAX-DOAS was first pointed into the Santiago crater and then above the rim, scanning elevation angles of 0, 5, 10, 20, 30, 40, 50, 60 degrees on the first (March 25th 2003) and also on the second day (March 28th 2003). On the third day of the campaign the measurements were carried out on the

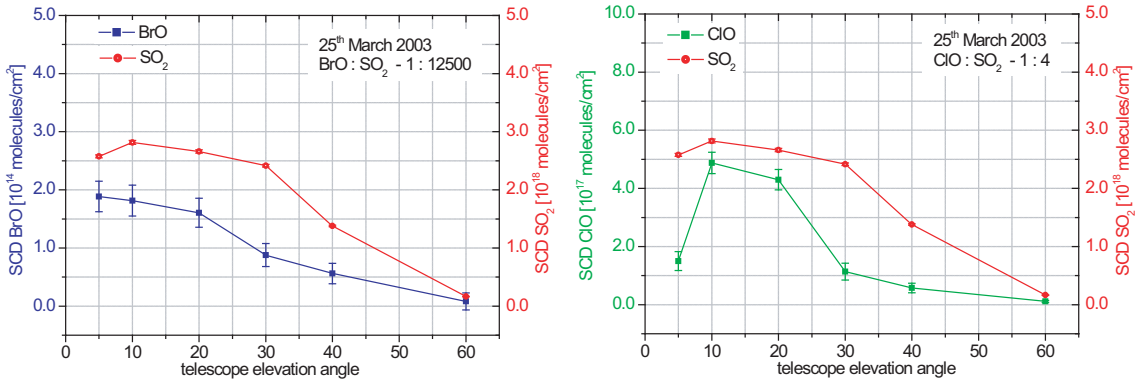

Figure 7.3: *BrO and ClO results of Masaya on 25th March 2003 by scanning a vertical angle up to 60° above the crater.*

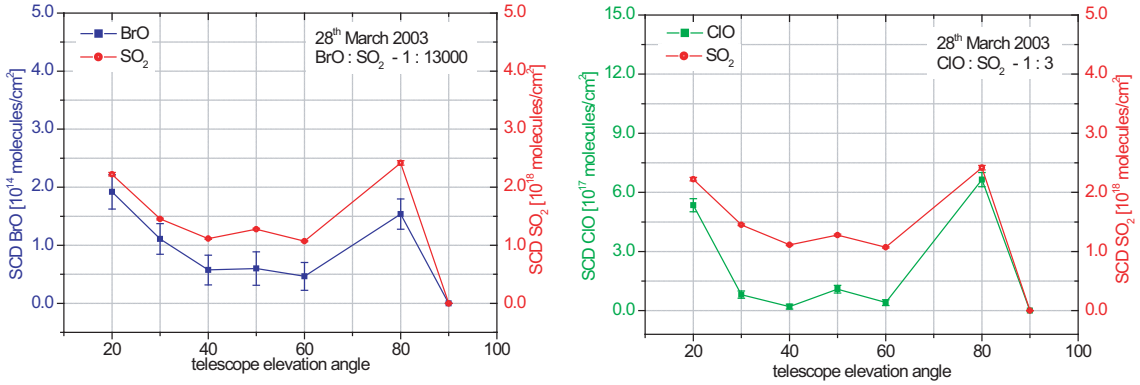

Figure 7.4: *BrO and ClO results of Masaya on 28th March 2003 by scanning a vertical angle of up to 60° above the crater.*

flank of Masaya in a place were only soil degassing (CO_2) was expected, and very little fumarolic degassing could be observed. During the 8th Gas field workshop all measurement were carried out without an UG5 filter in front of the entrance optic (because the UG5 filter broke in transport), which led to a higher amount of stray light inside the spectrometer and therefore to more difficulties in the data analysis, especially regarding trace gases in very low concentrations.

On March 25th 2003, SO_2 could clearly be detected, as well as BrO and ClO. In Figure 7.3 an example for the distribution of the SCDs of BrO and ClO compared to the SCDs of SO_2 are presented as a function of the telescope elevation angle. For the complete data set see Appendix (Figure A.1 and A.2). The correlation of BrO and ClO with SO_2 can be seen in the single plume example as well as in the complete time series. The results for March 28th 2003 are exemplary presented in Figure 7.4 for one set of elevation angles. Due to instrumental problems, especially temperature sta-

bilization, data collection was interrupted on the second measurement day. In general, both days show comparable results, except for a slightly higher BrO/SO_2 ratio on the first measurement day ($8 \cdot 10^{-5}$ on March 25^{th} 2003 in comparison to $7.6 \cdot 10^{-5}$ on March 28^{th} 2003), but this is in the magnitude of uncertainty and within the errors. On March 29^{th} 2003 the SCD of SO_2 is slightly above zero at times, but mainly scatters around zero as expected. One of the clear SO_2 detections (above 2 σ) is displayed in Figure 7.5. The complete time series for this day is presented in the Appendix (Figure A.4). Mostly the SCDs are scattered around zero.

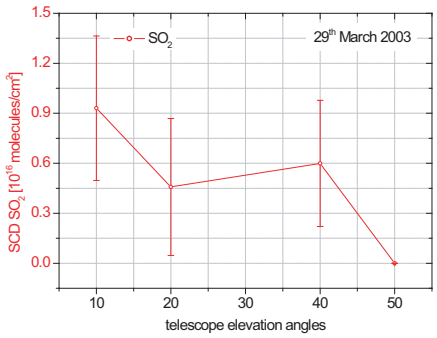

Figure 7.5: *One of the few plume scans where SO_2 could be detected above the 2 σ error on 29^{th} March 2003.*

Not only halogen oxides and SO_2, but also the possibility of the existence of other absorbers was studied on the first two measurement days. The works of *Schwandner et al.* [2004] and several others (see *Jordan* [2003] and references therein) - their measurement results - give strong indications for volcanic emission of organic compounds. One of these is formaldehyde (HCHO) and since it has absorption lines in the wavelength ranges of the applied Mini-MAX-DOAS instrument, it was separately evaluated. In the Masaya plume it was detected for the first time at a volcanic site by a DOAS instrument. Figure 7.6 shows the HCHO trend in purple color for a single scan of the Masaya plume. An analysis example can be found in Chapter 6. For summary and better comparison SO_2, BrO, ClO, OClO and HCHO are plotted together for a single scan through the plume as a function of the telescope elevation angle (Figure 7.7). The HCHO follows within the 2 σ error bars the plume shape indicated by the SO_2 signal like ClO and BrO. As can be seen for all trace gases, there

Table 7.1: *Flux estimation of ClO, BrO and HCHO for the Mini-MAX-DOAS results by applying the ratio to SO_2 and an average SO_2 flux of 11 kg/s (950.40 t/d) and flux estimation for HCl and HBr [Wardell et al. 2004] from active Filter-pack measurements using the same method.*

	BrO [t/d]	ClO [t/d]	HCl [t/d]	HBr [t/d]	HCHO [t/d]
25.03.2003	0.11	189.30	-	-	2.97
28.03.2003	0.11	252.50	492.50	0.56	6.85

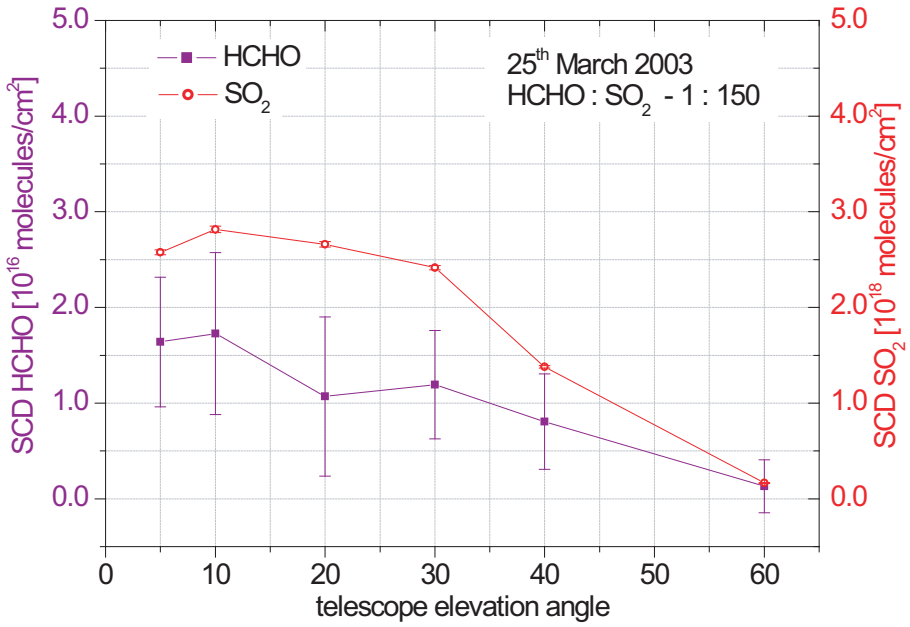

Figure 7.6: *HCHO results of Masaya on 25th March 2003 by scanning a vertical angle of 60° above the crater for one single plume scan, exemplary. For the entire data set see Appendix A.3.*

was no match for a total plume, since the plume could not be identified in a proper shape. Therefore the viewing geometry applied was just a scan starting from above the crater and then increasing the viewing angle above the crater up to 60° and not perpendicular to the plume. An estimation of the fluxes is therefore not possible. During the workshop numerous traverses below the plume with mini-DOAS and COSPEC instruments took place. An average result was applied to calculate the fluxes of the individual trace gases BrO, ClO, HCHO by using the X/SO_2 ratio and then compared with filter measurements from *Wardell et al.* [2004], who used the same SO_2 flux assumption for calculating the fluxes of HCl and HBr. The comparison of the two data sets is shown in Table 7.1. Using filter packs delivers the amount of bromine and chlorine, which are believed to originate only from HBr and HCl respectively. BrO and ClO cannot be detected with this method. Surprisingly, a quite high amount (about 10 %) of the bromine content seems to be in the form of BrO, assuming that no significant other bromine species than HBr and BrO are abundant. By a similar assumption ClO would even account for 40% of the chlorine abundance in the plume.

Both, Mini-MAX-DOAS and Filter-pack measurements were carried out next to each other on the 28th of March 2003.

The chemistry of halogens inside volcanic plumes is poorly understood (see Chapter 3 and 8). These measurements might help to shed some light in this insufficiently understodd

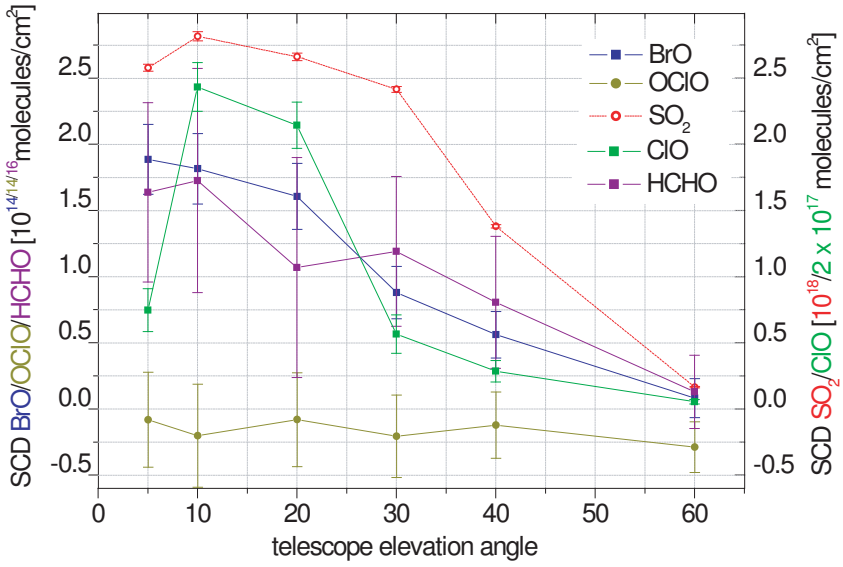

Figure 7.7: *Plume scan of Masaya, SCDs of SO_2, BrO, ClO, OClO and HCHO are plotted as a function of the telescope elevation angle on 25^{th} March 2003.*

area of atmosphereic chemistry and are therefore very interesting. Since there were no parallel measurements of HCHO by another method, a direct comparison is unfortunately not possible.

7.2.2 Momotombo

Momotombo is a young stratovolcano north west of lake Managua. It lies near the center of the volcanic arc that passes through western Nicaragua. It is situated at 12.4 N, 86.5 W. Momotombo rises 1297 m above sea level. The volcano started growing about 4500 years ago. Momotombo shows a long record of strombolian eruptions and rare larger explosive eruptions. Its history includes strong Plinian eruptions with catastrophic consequences. Today Momotombo consists of a somma from an older edifice that is surmounted by a symmetrical younger cone with a 150 m x 250 m wide summit. Leon, the former capital of Nicaragua was destroyed by an eruption of Momotombo in 1605 and 1606. Since 1524, 15 eruptions have been observed at Momotombo, most recently in 1905, when basaltic lava flows on the north-eastern flank reached the foot of the volcano. Presently Momotombo's activity is characterized by fumarolic degassing.

Field Measurements at Momotombo 2003

On March 27^{th}, an expedition started to the top of Momotombo and took many gas samples from the hot fumaroles. The results are summarized in Table 7.2. Gas samples

Table 7.2: *Overview of measurement results of samples from different groups taken on March 27th 2003 for Momotombo volcano and on March 31th for Poas volcano. The values are all given in mmol/mol. Table adapted from Delmelle, 2004.*

	C	H_2O	CO_2	S_t	SO_2	H_2S	HCl	HF	He	Ne	H_2	Ar	O_2	N_2	CH_4	CO
Momotombo P-7																
Firence (FR)	614	741.82	197.61		43.246	9.829	0.300	0.031	0.00035	0.000029	3.17968	0.03789	0.3101	3.56520	0.00001	0.07010
GEOMAR (GE)		861.88	105.00		24.467	4.866	0.557	0.057	0.00013	0.000009	1.47017	0.01808	0.0768	1.58346	0.00001	0.01702
GSJ (GS)	614	928.56	54.50	12.117	4.596	7.521	2.681	0.190	0.00023		1.37888			0.63772		
GSJ (GS)	614	918.50	58.48	18.140	12.357	5.783	2.687	0.185	0.00024		1.38293			0.61803		
Palermo (PL)	630	899.01	74.94	20.445			0.609	0.100	0.00043				0.0000	1.91031	0.00007	0.04866
TIT (TI)	614	919.10	58.23		13.398	3.698	3.314	0.260			1.09979		0.0522	0.79240		0.05464
UNAM (UA)	614	914.00	63.20	17.500			3.800	0.320	0.00071		0.60000	0.00150		0.57000	nd	0.11000
UNM (UN)	614	942.79	43.26	9.958	3.344	6.614	2.419	0.182			0.80959	0.00090		0.54351		0.03759
Momotombo P-9																
Firence (FR)	741	631.65	274.95		83.427	5.820	3.152	0.190	0.000002	0.57345	0.00271	0.0237	1.84005		0.02473	
GEOMAR (GE)		873.83	89.47		26.749	4.804	0.306	0.018	0.00022	0.000005	4.01763	0.00712	0.0324	0.75434	0.00001	0.01042
GSJ (GS)	746	919.03	57.27	15.727	9.884	5.844	2.782	0.147	0.00032		4.35511			0.69387		
GSJ (GS)	746	915.17	60.07	15.902	9.782	6.120	3.427	0.191	0.00035		4.50972			0.72645		
Palermo (PL)	746	897.19	70.21	19.521			4.323	0.326	0.00015		6.11298			2.14031		0.17975
TIT (TI)	746	874.83	89.25		19.603	4.399	4.178	0.453			5.46149		0.1131	1.31829		0.40160
UNAM (U)	748	883.00	81.20	27.000			4.200	0.310	0.00024		3.30000	0.00510		0.78000	0.00095	0.19000
UNM (UN)	748	788.57	160.26	39.010	26.825	12.185	1.447	0.058			8.19052	0.00289		1.94292		0.51938
Poas																
Firence (FR)	97	930.65	42.94		24.321	0.357	1.576	0.000	0.00005	0.000003	0.00040	0.00335	0.0105	0.14874	0.00002	0.00009
Firence (FR)	97	908.24	56.91		33.873	0.493	0.300	0.000	0.00010	0.000003	0.00084	0.00306	0.0039	0.17299	0.00012	0.00017
GEOMAR (GE)	97	922.09	39.92		35.797	1.182	0.886	0.000	0.00010	0.000000	0.00095	0.00060	0.0009	0.11830	0.00001	0.00002
GSJ (GS)	97	968.64	18.09	11.834	11.423	0.411	1.005	0.007	0.00011		0.36311		0.0013	0.05778	0.00008	
GSJ (GS)	97	964.07	18.65	14.077	13.636	0.441	3.083		0.00022		0.00161		0.0067	0.10816		
Palermo (PL)	97	964.18	21.13	13.312			0.647	0.000		0.00017	0.37732		0.0046	0.35328	0.00015	0.00005
TIT (TI)	97	946.64	35.13		15.792	0.164	2.204	0.000	0.0000		0.00030	0.0067	0.05524	0.00000	0.00000	
UNAM (UA)	97	944.00	35.20	18.600			2.000	0.000	0.00011		0.27000	0.00120		0.07000	0.00090	0.00040
UNM (UN)	97	976.28	15.20	6.215	6.024	0.191	2.234	0.004	0.00014		0.00079	0.00056	0.0000	0.06488	0.00001	0.00009

Figure 7.8: *Photograph from the top of Momotombo inside the crater. Sulphur deposits around the fumaroles can be identified by the yellow color. The Mini-MAX-DOAS instrument is pointed towards the fumaroles.*

with Giggenbach-flasks were collected at "Punto 9" by several groups. Punto 9 is a fumarole inside the crater at the top of Momotombo and had a temperature of about 750°C on this day. Participants also collected additional samples at lower temperature spots, (like the presented data in Table 7.2 of P-7) with a temperature of about 614°C. The results in Table 7.2 show a very broad range of values. Some results of the different groups for the individual gas species differ in an order of magnitude, e. g. the values for SO_2 at "Punto 9" scatter between 3.344 mmol/mol and 43.246 mmol/mol. These large uncertainties illustrate today's situation and the difficulties of such measurements and their interpretation (see also chapter 3 and 8). The HCl to SO_2 ratio for example spans two orders of magnitude, from $7 \cdot 10^{-3}$ to $7 \cdot 10^{-1}$ without any significant visible difference between the two sample sites.

Also measurements with the Mini-MAX-DOAS at a distance of about 150 m from the fumaroles were conducted for about 1 hour at midday. The Mini-MAX-DOAS scanned an elevation angle of 60° starting at 10° with a step width of 10° up to 70°. The instrument was cooled to a temperature of 10°C and was pointed to the largest fumarole visible (the fumarole with 750°C temperature), but probably a mixture of several fumaroles was in the path of photons collected by the telescope of the Mini-MAX-DOAS. Similar to the Masaya data, no optical filter (UG5) was applied to the entrance optic, therefore the amount of

stray-light inside the spectrometer was higher than normal and a higher residual limited the quality of the data. The clear detection of small trace gas concentrations like BrO became an even greater challenge. Nevertheless SO_2 could be clearly detected and also an attempt to evaluate BrO, OClO and ClO was undertaken. The results are presented in Figure 7.9 for one elevation angle series. A BrO evaluation was attempted in all scenarios

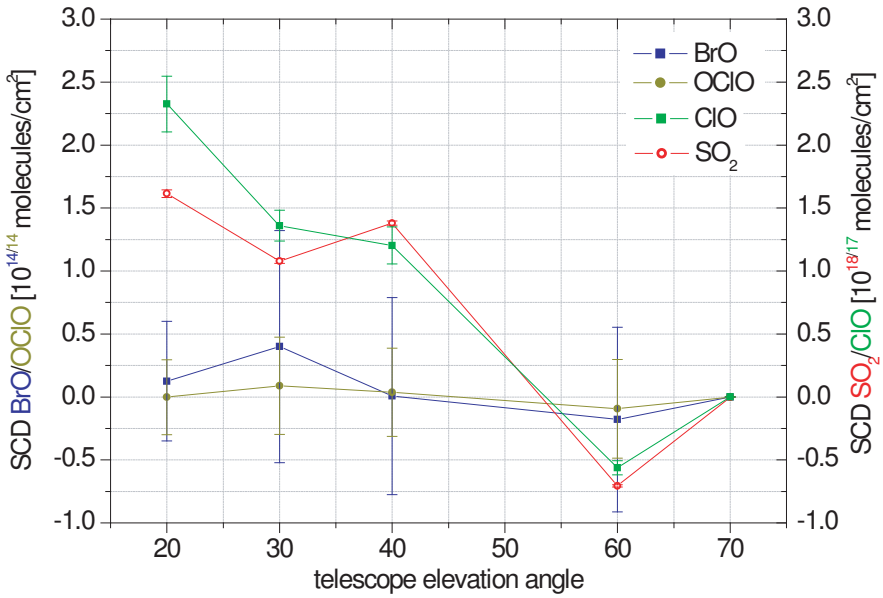

Figure 7.9: *Plume scan of Momotombo, SCDs of SO_2, BrO ClO, OClO plotted as a function of the elevation angle. Measurements were taken on 27th March 2003.*

described in Chapter 6. Within the 2 σ fitting error the SCD of BrO is scattering around zero. Only the results of the "standard" BrO evaluation, as suggested after a comparison campaign in 1996 [*Aliwell et al.* 2002] are shown here. All calculated BrO SCDs are plotted as a function of time together with the SO_2 values and are found in the Appendix in Figure A.5. The OClO SCDs are also zero by considering a 2 σ fitting error. This is not an unexpected result, since BrO is a necessary educt of the OClO formation, but no BrO could be clearly identified here. On the other hand the ClO shows SCDs clearly above zero and a very good correlation to SO_2 (about the limitation for the ClO evaluation see Chapter 6).
Since no defined plume was observed, no attempt was undertaken to calculate the total SO_2 flux.

7.2.3 Poas

Poas Volcano is close to the capital of Costa Rica - San Jose. Numerous explosion craters can be found on the summit, one of them contains a small turquoise lake of sulphurous

Figure 7.10: *The Poas volcano. The photo shows a view of the active crater lake of POAS volcano and the measurement set-up.*

steaming water. The high sulphur and acid content reduces the pH value of the water nearly to zero. Poas is one of the main tourist attractions of Costa Rica, even though violent explosions occasionally occur here. There is almost no vegetation and the entire surrounding area is covered with ash. The diameter of the active crater is about 800 m and it is situated 2300 m above sea level.
The eruption activity is known since at least 1747. The most violent eruption took place in 1910 and emitted ash up to a height of 8000 m. The last eruption of Poas took place between 1952 and 1954.

Field Measurements at Poas 2003

On March 31^{th} 2003 a field campaign took place at the Poas crater. The instrument was set-up inside the crater near the lake. It was difficult to gain a reference spectrum for this day, since the entire crater area is surrounded by fumaroles, as can be seen in Figure 7.10. The upper part shows a view taken at the crater rim above the lake. The picture below shows the experimental site to give an impression of the surroundings.
Due to instrumental problems at the beginning of the measurement period and the limited time for a stay inside the Poas crater, just a few spectra could be recorded. Elevation angles from 10° up to 80° were scanned in 10° steps. The data on BrO and ClO in comparison to SO_2 for one vertical scan is presented in Figure 7.11. The spectra were evaluated as

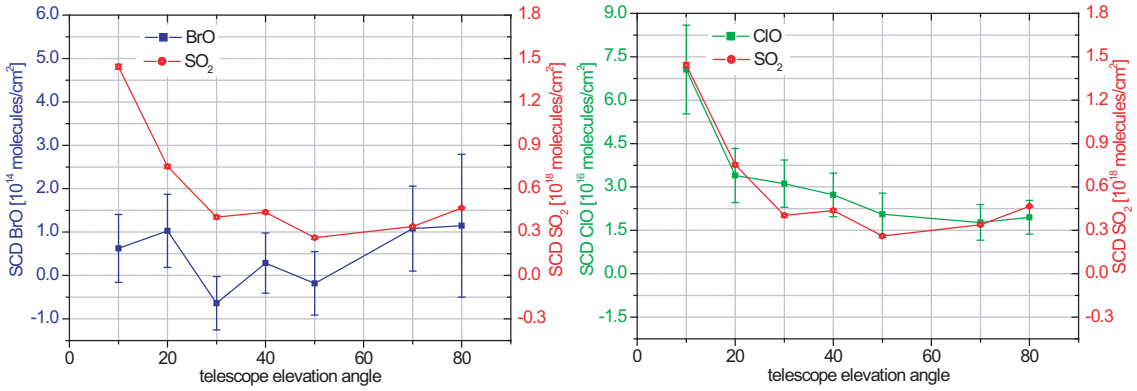

Figure 7.11: *(a) BrO measurement results of Poas - evaluated according to the suggestion of Aliwell et al. [2002] (b) evaluation result of ClO, one scan above the fumaroles starting at 10 degree moving the telescope up to 80 degree, for the complete data set see Appendix.*

described in Chapter 6. Since it was impossible to record a clean reference spectrum (in the absence of trace gases from the fumaroles), the reference was taken from measurement data recorded at Momotombo (four days before) and applied for the evaluation. The results are similar to the results of Momotombo, where no BrO signal could be detected, but ClO seems to be abundant. A SCD of ClO up to $(1.3 \pm 0.3) \cdot 10^{17}$ molecules/cm^2 could be detected and a ratio of ClO/SO_2 of $5 \cdot 10^{-2}$ was calculated. The fact that no BrO could be detected near the source, but ClO could, might be surprising at first. It will be discussed in Chapter 8 in more detail.

7.3 Italy

The most detailed studies for this thesis were carried out in southern Italy with the focus on Mt. Etna. Mt. Etna is the largest active volcano in Europe and one of the most active volcanoes worldwide. In total four measurement campaigns took place in Italy within the scope of this study. The first one in September/October 2003, the second in August 2004, the third within the DORSIVA project in September/October 2004 and the last in May 2005.

7.3.1 Vulcano

Vulcano is the southernmost of the seven Aeolian Islands in the north of Sicily. It is located at 38°24' N and 14°58'E in the Tyrrhenian Sea and has a maximum altitude of 499 m. The word "volcano" has its origin in the Roman name for this island: "Vulcano". The volcanic activity in this region is a result of the collision between the Eurasian and the

African plates. Vulcano Island has three volcanic centers. The oldest one comprises some partially collapsed stratovolcanic cones. The youngest centre is Vulcanello in the north which was active until 1550. The Gran Cratere has been most active recently and lies at the top of the Fossa cone. 7 major eruptions have occurred here in the last 6,000 years, the last eruption taking place between 1888 and 1890. The activity during this eruption was characterized by the style of vulcanian eruptions (see Chapter 2). Today Vulcano shows constant fumarolic activity, which is concentrated in the Gran Cratere.

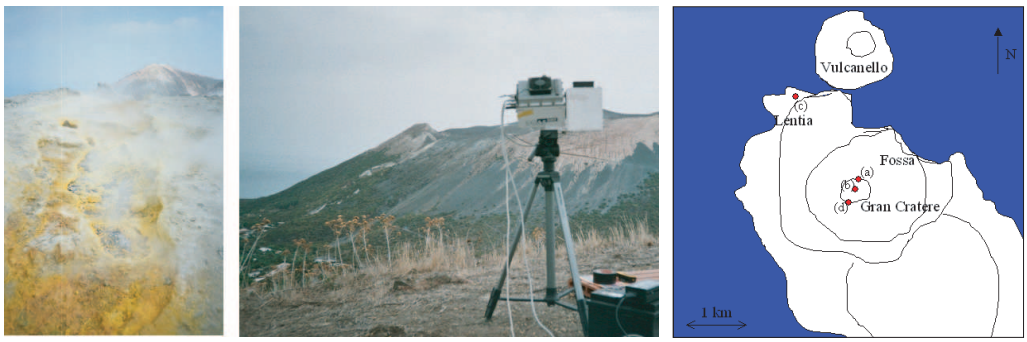

Figure 7.12: *Photograph and map of Vulcano Island. The first picture shows the fumarolic field on the crater rim of the Gran Cratere, the second the Mini-MAX-DOAS set-up at Lentia, the active crater in the background. The map shows the location of the measurement sides, indicated by red dots (a, b c and d).*

Field Measurements at Vulcano 2003

The measurements at Vulcano were carried out on the 23^{rd} and 24^{th} of September and the 4^{th}, 5^{th} and 6^{th} of October 2003. During the first two days the Mini-MAX-DOAS system was set up on the rim of the Gran Cratere at the heliport (see Figure 7.12, map point (a)) with the telescope aiming in a south-easterly direction at the main fumarolic field and scanning elevation angles from 0 to 90 degrees. In September, 1,000 scans were added for each spectrum, in October only 200 were used to aim for a better time resolution. During noon of September 24^{th} 2003 the measurements were undertaken at a second place inside the crater below the fumarolic field (see map point (b)) to have a longer light path through the volcanic gases. On the October 4^{th} the spectra were again taken at location (a). On the October 5^{th} and 6^{th} 2003 the measurements were carried out north-westerly of the crater, the instrument was set up at Lentia (see Figure 7.12 map point (c)). In the afternoon of the 6^{th} of October the measurements were carried out at the southern rim of the crater (point (d) in Figure 7.12).

SO_2 was detected during all measurements. During the first days the weather was very sunny, in October it was hazy and slightly cloudy in the morning, and for the whole period nearly no wind was blowing.

The results of all days are shown in the Appendix (Figure A.7 and A.8). One example from

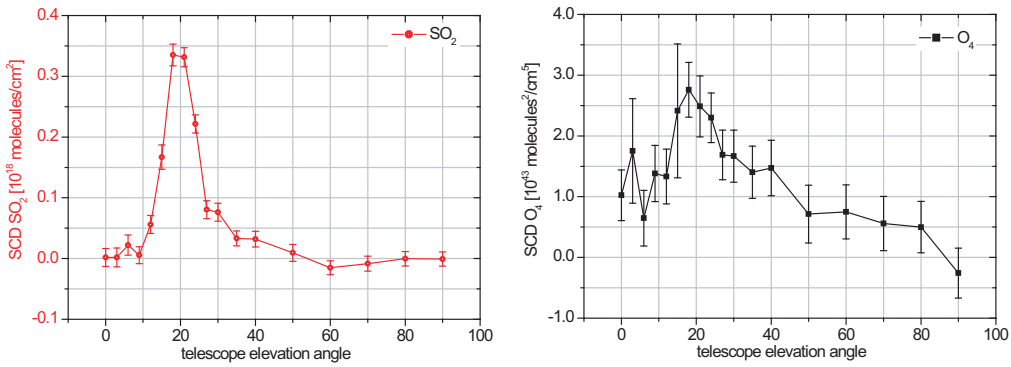

Figure 7.13: *SCDs of SO_2 and O_4 at Vulcano. One plume scan of measurements taken at Lentia (point (c)) on the 5^{th} October 2003. O_4 is enhanced in the center of the plume.*

the October 5^{th} 2003 where the plume was well scanned was chosen to illustrate the main outcome and is displayed in Figure 7.13. The plume was not visible. The wind direction (and therefore the angle under which the plume was scanned) and velocity are unknown and therefore no fluxes were estimated from these results. Beside the SO_2 evaluation, attempts were undertaken to detect halogen oxides and HCHO, but none of them could be identified in the spectra. Studies on the oxygen dimer (O_4) were carried out as well and are displayed next to the SO_2 plots. An increase of the SCDs of O_4 in the center of the plume could be observed (see Figure 7.13), indicating that the light is scattered inside the fumarolic degassing and the light path is elongated. Detailed discussions on the eventual light path elongations in volcanic plumes can be found in Chapter 8.5.

7.3.2 Stromboli

Stromboli Island also belongs to the Aeolian Islands, which are located in the north of Sicily in the Mediterranean Sea (38.8 N, 15.2 E). The small volcanic island measures about 2 km in diameter and has a height of 920 m above sea level. Stromboli is classified as a basaltic stratovolcano. It is one of the most active volcanoes on Earth, and has been continuously active for at least 2000 years, maybe even longer. Most of the present cone was built 15,000 years ago. The eruptions at Stromboli are mostly small gas explosions that throw incandescent blobs of lava above the crater rim. Several explosions occur each hour. Larger eruptions and lava flows are less frequent. From a distance Stromboli looks like a classical stratovolcano, with its active crater lying about 150 m below the summit.

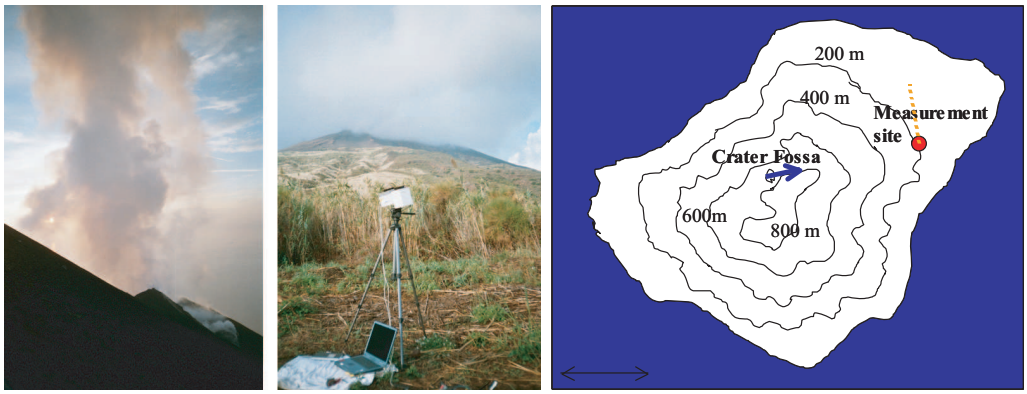

Figure 7.14: *Photographs of Stromboli and the measurement site on the left side, map of Stromboli Island on the right side. The red point is marking the measurement location, the blue arrow the wind direction, and the yellow dots indicate the viewing direction.*

Field Measurements at Stromboli 2003

At Stromboli, measurements were carried out on September 27^{th} 2003. The system was set up near the volcanic observatory and the instrument was scanning perpendicular to the plume. The wind was blowing from the south-west on this partly cloudy day (see Figure 7.14). Angles between 0° and 120° were scanned using steps of 10 degrees. BrO, ClO, OClO and SO_2 were measured and SCDs of these trace gases are displayed in Figure 7.15. The gases are highly correlated. The complete time series of each trace gas is found in the Appendix (Figure A.9). Fluxes of all three species were estimated by assuming a wind velocity of 5 m/s and a distance of 1 km from the instrument to the plume and are displayed in Table 7.3. The plume seemed to be split up into two parts, which is a quite interesting

Table 7.3: *Flux estimation of ClO, OClO, BrO and SO_2 for Mini-MAX-DOAS results by applying the ratio to SO_2, neglecting the second part of the plume and assuming a wind velocity of 5 m/s.*

SO_2 [t/d]	$\frac{ClO}{SO_2}$	ClO [t/d]	$\frac{OClO}{SO_2}$	OClO [t/d]	$\frac{BrO}{SO_2}$	BrO [t/d]
103.7	$7.1 \cdot 10^{-2}$	6.1	$4.2 \cdot 10^{-4}$	$5.7 \cdot 10^{-3}$	$2.1 \cdot 10^{-4}$	$3.2 \cdot 10^{-2}$

feature. For the calculated fluxes the second part of the plume was neglected. Hence, the calculated values are probably just a lower estimate. Possible scattering processes inside the plume were not taken into account and the plume diameter was geometrically determined to 440 m.

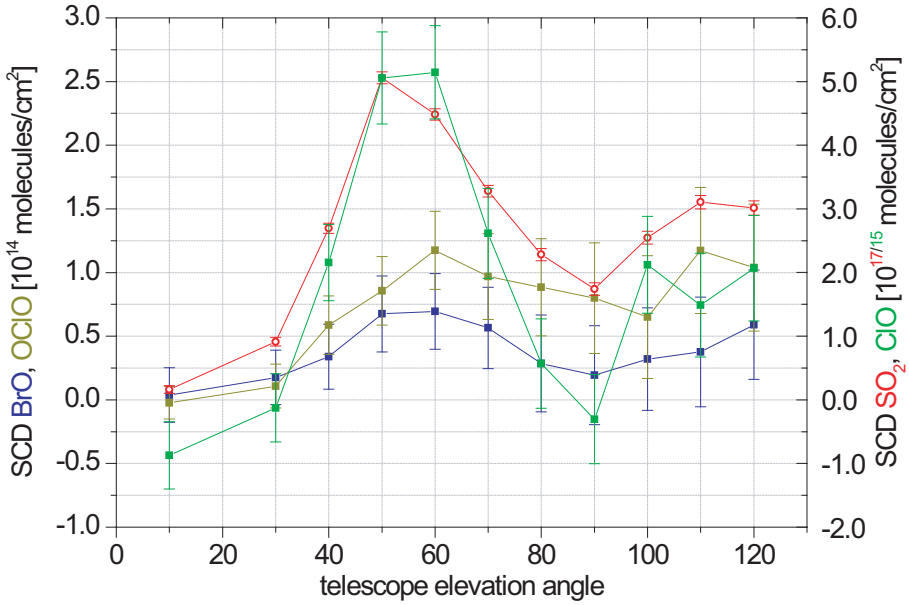

Figure 7.15: *A single plume scan is presented illustratively by plotting the SCDs of BrO, SO_2, ClO and OClO as a function of the telescope elevation angle. The measurements were carried out near the volcanic observatory on the 27^{th} of September 2003. The complete data set is found in the Appendix.*

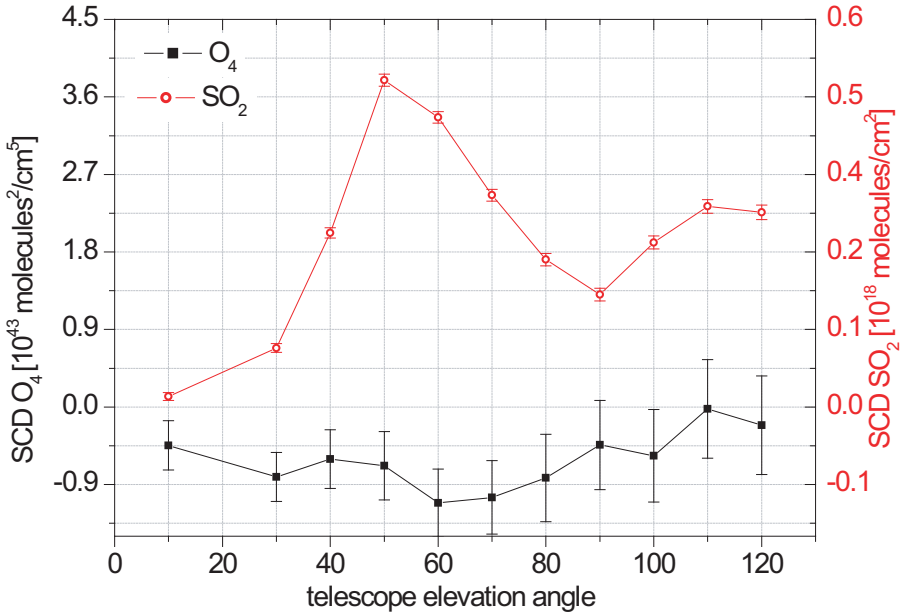

Figure 7.16: *A single plume scan is presented illustratively by plotting the SCDs of O_4 and SO_2 as a function of telescope elevation angle. The measurement was carried out near the volcanic observatory on the 27^{th} of September 2003.*

Typical HCl/SO_2 ratios of Stromboli are 1 [*Aiuppa and Frederico* 2004]. When this is compared to the ClO/SO_2 ratio of this study ($7.1 \cdot 10^{-2}$) and assuming that HCl and ClO are the only or at least the major chlorine species in the plume, the chlorine monoxide abundance seems to account for ∼7% of the emitted chlorine amount. This is much smaller compared to the measurements of Masaya, presented above.
Figure 7.16 shows a plume scan example for the SCDs of O_4. Nearly constant O_4 values can be observed over the entire range of measured elevation angles. The interpretation of this result is not straightforward. Due to the not fully sunny and clear sky conditions during this measurement example the difficulties in analyzing the radiative transfer are further increased. Therefore Figure 7.16 only illustrates the complexity of radiative transfer processes and our insufficient understanding. Both will be discussed in Chapter 8.5 in this thesis.

7.3.3 Etna

Since Mt. Etna was the main volcano studied in this work, some additional details and a short historical overview of this volcano , which might help with the interpretation of the observed data, are presented here.
Etna is located on Sicily, which is located in the south of Italy in the Mediterranean Sea (37.7N, 15.0E). Today, Etna dominates the eastern coastline of Sicily and its activity has been ongoing for over 500,000 years. Etna is one of the largest and most active continental volcanoes worldwide. Its base measures about 60 x 40 km and its summit rises to more than 3300 m above sea level. Mt. Etna's structure is quite complex: below an altitude of 1700 m it shows clear features of a shield volcano. Above that altitude, Etna is a stratovolcano made of several coalesced vents. Much of the surface of the volcano is covered by historical lava flows and most eruptive products consist of basalt.
The history of Etna can be divided into 5 main periods: the volcanism on the Hyblean Plate, the pre-Etnean phase, the Ancient Etna, The Trifoglietto II, and the Mongibello. Since the middle Triassic (230 million years ago), volcanism has occurred in the eastern part of Sicily. At that time, voluminous and silica poor lava was emitted on the Hyblean Plateau (Monti Iblei), mostly below sea level. This phase of volcanism lasted until the early Pleistocene, (about 1.4 million years ago), and showed a shift of the eruptive centers to the north. The pre-Etnean phase started around half a million years ago. Its lavas were mainly submarine. The common belief is that these volcanic activities took place in a vast marine gulf and extended over the area were Etna is located at present. About 300,000 years ago an increase in the frequency of eruptive activity occurred mainly in the south-western part of Etna. This phase did not produce much lava in comparison to the entire edifice of Etna, but lasted for more than half of Etna's life-time. During the ancient phase of Etna, the first large stratovolcano presumably started building up in this area

and its eruptive products changed to alkali basalts and hawaiites. During the following phase of Trifoglietto, which started around 80,000 years ago, volcanic activity became more explosive and the emitted lava became more differentiated. Several stratovolcanoes built up and each one ended its life with caldera collapse. The last phase of activity in the Etna area started about 35,000 years ago and continues up to the present day. This phase belongs to the so called Mongibello and can be divided into 3 parts: the Ancient, Recent and Modern Mongibello. In the beginning the Mongibello eruptions were explosive and the erupted volcanics showed the most differentiated composition in the history of Etna. Afterwards, Etna changed to more effusive eruptions and the erupted products had a higher Fe and Mg content, but less silica. During a major caldera collapse, several thousands years ago, the Valle de Bove was formed. The last of these collapses took place about 3500 years ago and led to the present form of the Valle de Bove. During the last few thousand years Etna's eruptions have been mainly characterized by Strombolian activity and lava emissions, however sometimes more explosive episodes occurred, mainly from the summit craters. In particular, an unusually explosive (Plinian) eruption occurred in the year 122 B.C..

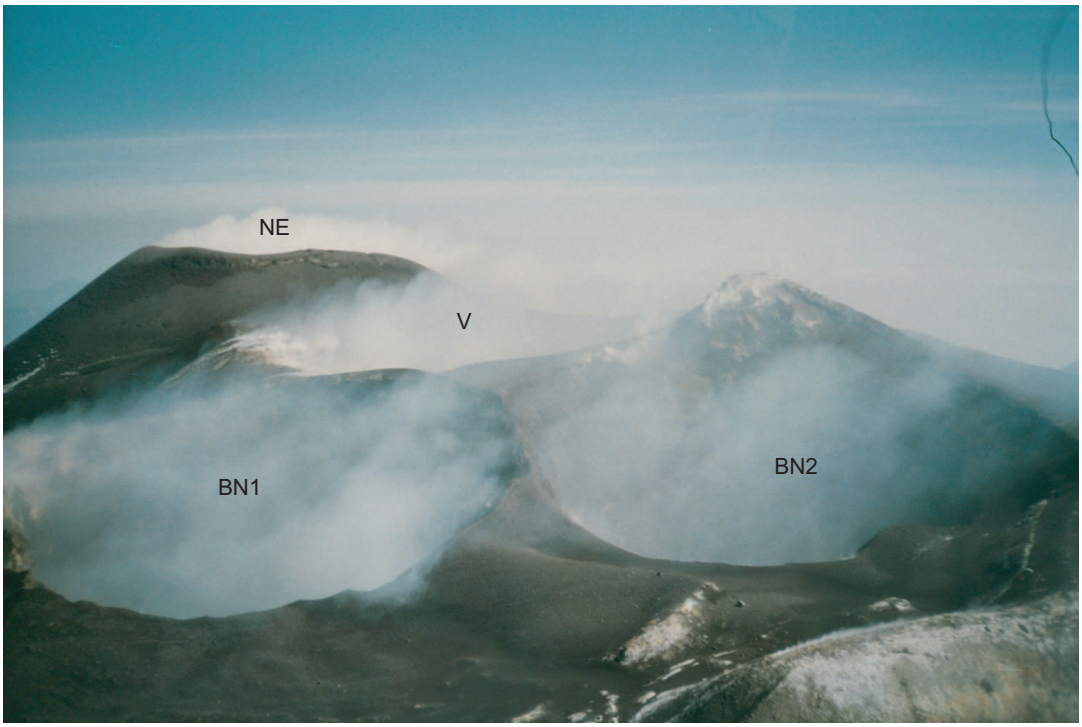

Figure 7.17: *Photo of the summit area of Mt. Etna. North east crater (NE) and the crater Centrale (V - Voragine, BN1 - Bocca Nova 1, BN2 - Bocca Nova 2).*

Field Measurements at Etna 2003

The first measurements at Etna within the scope of this thesis were carried out on the morning of September 30^{th}, 2003 and parallel measurements were done with a FTIR instrument by M. Burton from the INGV Catania. The measurements took place on the eastern flank of Mt. Etna at an altitude of 1030m, near the town of Fornazzo (see Figure 7.18). On October 1^{st} 2003 COSPEC measurements took place. These measurements have been conducted routinely since 1987 using the Correlation Spectrometer (COSPEC) instrument [*Caltabiano et al.* 1994] and aim at measuring the emitted SO_2 flux. The results of these complementary measurements are used to calculate the fluxes of the different species

The COSPEC instrument measures the SO_2 column density. The instrument is normally

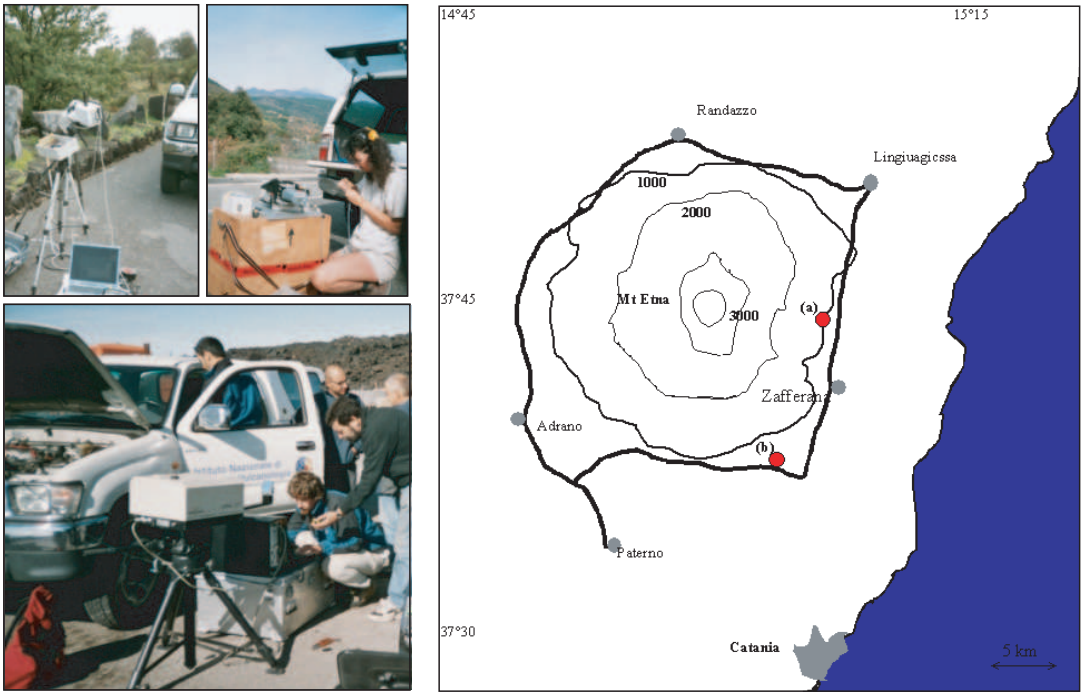

Figure 7.18: *Map of Mt. Etna with the location of the measurement site for (a) the 30^{th} of September (mini-MAX-DOAS) and (b) the 9^{th} of October (IDOAS).*

mounted in a car, which is driven on a road below the volcanic plume while the instrument simultaneously records the SO_2 column density combining this data with the output from a GPS receiver to calculate the cross-sectional burden. A total integrated concentration cross section of the plumes can be obtained, and after multiplication with the concentration weighted wind component perpendicular to the cross section, the flux of SO_2 can be calculated. For further details on this technique see [*Hoff and Millán* 1981]. OP-FTIR spectroscopy is a powerful remote sensing tool that is widely used in environ-

mental and, increasingly, in volcanic monitoring [*Francis et al.* 1998; *Edmonds et al.* 2002]. The heart of the instrument is an interferometer that allows the intensity of radiation at all detectable wavelengths to be measured simultaneously. OP-FTIR instruments working at high spectral resolution are commonly used in the "Network for the Detection of Stratospheric Change (NDSC)" to measure column amounts of trace gases in the stratosphere. Over the last ten years portable instruments with lower resolution have been increasingly used to measure gas emissions from volcanoes. The main advantage of this approach for volcano monitoring is that many volcanic species can be detected while performing measurements at a safe distance.

Since May 2000 a Bruker Open Path Gas Analyzer-22 (OPAG-22) FTIR spectrometer has been used by the remote sensing group of INGV Catania for routine measurements of the proportions of SO_2, HCl and HF in the volcanic plume produced by Mt. Etna, Sicily [*Burton et al.* 2003]. These measurements are complementary to the SO_2 flux monitoring performed with the COSPEC instrument, because by using both instruments together the fluxes of SO_2, HCl and HF can be determined. The OPAG-22 has a maximum optical path difference of 1.78 cm, allowing a spectral resolution of 0.5 cm^{-1}. The field of view of the instrument is 30 mrad, and it uses a ZnSe beam-splitter, a non-hygroscopic material that allows measurement throughout the mid-infrared. Sunlight is used as radiation source and by using a plane first-surface mirror mounted 70 cm from the input aperture, it is hand-steered into the spectrometer. The solar radiation was attenuated using a metal wire mesh, mounted in front of the ZnSe aperture window. The spectrometer was controlled by a portable computer and powered by a 12 V car battery.

The Spectra were analyzed by fitting a simulated spectrum to the observed one, dynamically adjusting the amounts of volcanic and atmospheric species as well as a frequency shift and a polynomial function until the measurement was accurately reproduced. This approach obviates the need for radiometric calibration or a clear-sky reference spectrum. The non-linear least square fitting program is based on *Rodgers* [1976] optimal estimation algorithm and the simulated spectra are produced using the RFM forward model [*Dudhia et al.* 2003] and the HITRAN '96 [*Rothman et al.* 1996] spectral line database.

A total number of 289 spectra were collected with the Mini-MAX-DOAS instrument on September 30^{th}, 2003 from 9:00 to 12:20 GMT. The plume was scanned several times and it can be clearly observed that the plume was not stable over this time period as can be seen in Figure 7.19. The measurement was interrupted between 11:00 and 11:30. SCDs up to $1.78 \cdot 10^{14}$ molecules/cm^2 and $4.40 \cdot 10^{17}$ molecules/cm^2 for BrO and SO_2 respectively were determined with the highest values measured at the beginning of the measurement period. The SCD's decreased with time and during the last hour of measurement the peak amounts were $6.00 \cdot 10^{13}$ molecules/cm^2 for BrO and $2.2 \cdot 10^{17}$ molecules/cm^2 for SO_2. As can be seen in Figure 7.20 a good correlation between BrO and SO_2 was found in the data collected before 11:00. A ratio of BrO to SO_2 of 1/2200 was observed. SCD's

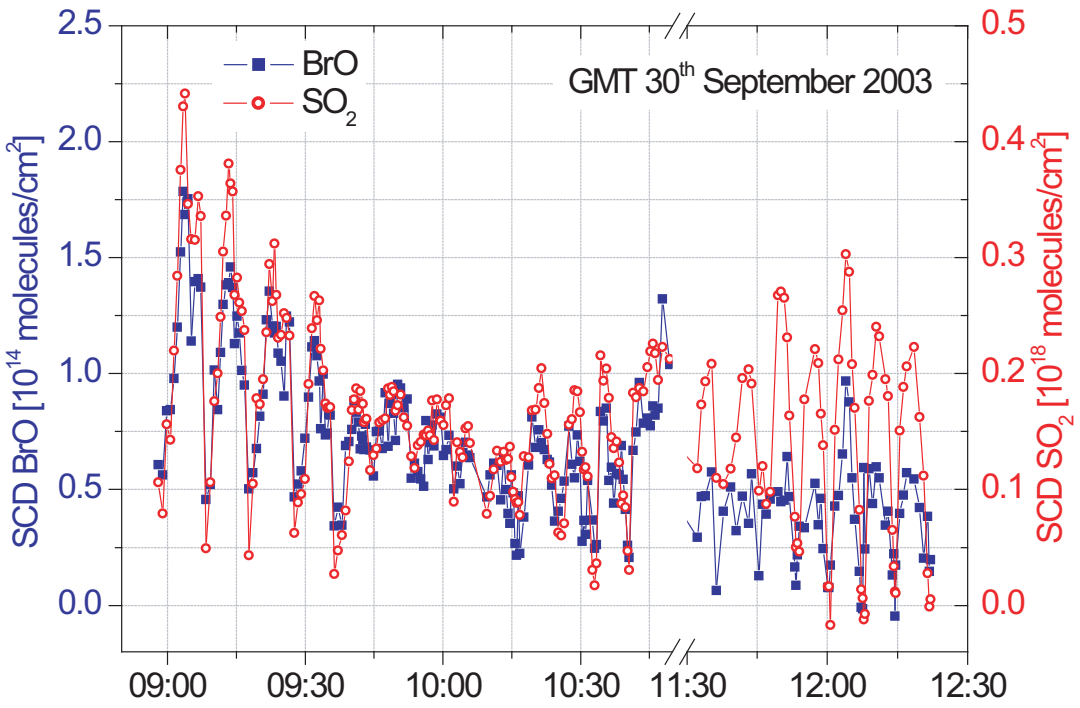

Figure 7.19: *Temporal variations in the SCDs of SO_2 and BrO observed in a series of scans through the plume with Mini-MAX DOAS. The spectrometer performed 22 scans of the sky viewing from one horizon to the other, orthogonal to the plume direction, producing peaks in SO_2 and BrO amounts when the plume was observed overhead.*

determined after 11:30 indicate a higher BrO/SO_2 ratio of 3300.

72 FTIR spectra were collected using the Bruker OPAG-22 spectrometer from 8:33 to 8:50 GMT on the 30^{th} of September. The amount of volcanic SO_2, HCl and HF were determined from each spectrum. Assuming a homogenous composition during the measurement period, a scatter plot of retrieved SO_2 against retrieved HCl and HF should be highly correlated over a range of concentrations, as the varying geometry of the measurement (produced by movement of the Sun and plume movement) entails sampling of varying concentrations of volcanic gas. These plots are shown in 7.20, together with a linear fit to the data. The gradients of the fits are the ratios of SO_2/HCl and HF/HCl, and calculated to be 1.94 and 0.45, see Figure 7.20. The scatter of the HF plot is much higher than the one of SO_2, primarily because at the higher frequency of the HF absorption small variations in the solar alignment produce changes to the apparent instrument line-shape, due to under-filling of the field of view of the instrument by the sun. The retrieval of HBr from the FTIR spectra was also attempted, but this species was found to be below

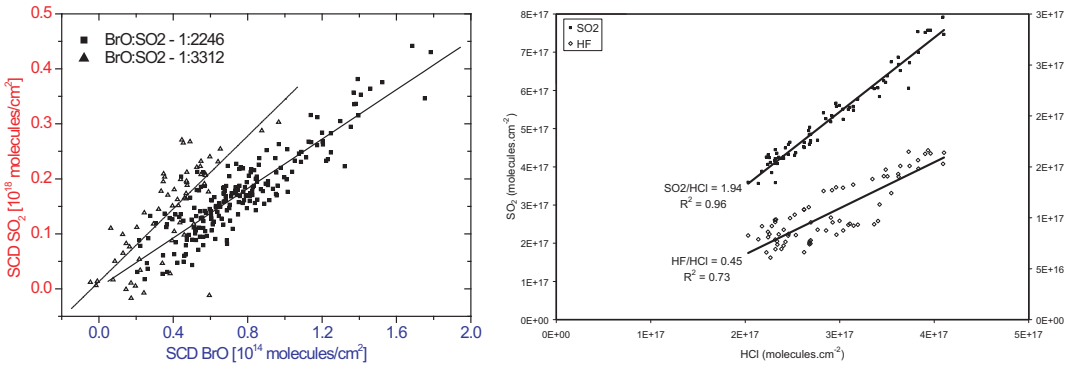

Figure 7.20: *BrO, HCl, HF and SO_2 results at Etna on 30^{th} September 2003. (a) Scatter plot of SO_2 against BrO retrieved from Mini-MAX DOAS spectra (b) Scatter plots of SO_2 and HF against HCl retrieved from FTIR spectra.*

the detection limit of this measurement technique. The residual of the retrieval of HBr was 0.5 % for the spectrum with strongest SO_2 absorption ($7.92 \cdot 10^{17}$ molecules/cm^2). No significant HBr absorption has been found, and therefore it can may be placed an upper limit of $3 \cdot 10^{16}$ molecules/cm^2 HBr can be assumed, as this SCD would produce an absorption of 0.5 % in the retrieval window, which was centered on a wavelength of 2620 cm^{-1}.

COSPEC measurements of the SO_2 flux from Mt. Etna were performed on the 1^{st} of October, with an average flux of 1600 t/d resulting from two traverses underneath the volcanic plume. This flux is in agreement with the average flux seen during September and October 2003.

Combining the COSPEC flux measurements with Mini-MAX DOAS and FTIR com-

Table 7.4: *Flux estimation of BrO for Mini-MAX-DOAS results and HCl and HF by FTIR by applying the ratio to SO_2. SO_2 flux of COSPEC measurements carried out a day after the Mini-MAX-DOAS and FTIR measurements.*

SO_2 [t/d]	$\frac{BrO}{SO_2}$	BrO [t/d]	HCl [t/d]	HF [t/d]
1600	$4.8 \cdot 10^{-4}$	0.9	470	110

position data allows us to calculate the flux of HF, HCl and BrO. Table 7.4 present a summary of the calculated halogen and SO_2 fluxes for Mt. Etna. The upper HBr limit of $3 \cdot 10^{16}$ molecules/cm^2 in a spectrum that contains $7.92 \cdot 10^{17}$ molecules/cm^2 of SO_2

places a lower limit of $3.8 \cdot 10^{-2}$ on the HBr/SO_2 ratio, which is significantly higher than the BrO/SO_2 ratio of $4.5 \cdot 10^{-4}$ observed with Mini-MAX DOAS. It therefore cannot be excluded the possibility that Br partitioning strongly favors HBr; the HBr/BrO ratio may be as high as 86, based on the upper limit for HBr/SO_2 derived from OP-FTIR. The strong variability of BrO observed during the measurement period suggests either that its emission from the volcano is highly variable, which may suggest that its variations are related to interesting volcanic phenomena, or that plume chemistry and photochemistry plays an important role in controlling its abundance. In this case, BrO would be of limited use for volcano monitoring. For further discussion on this issue see Chapter 8.

During the measurement campaign at Mt. Etna in September/October 2003 the IDOAS instrument was applied for the first time at a volcanic site. The instrument was set up on a road at a distance of around 7 km from the summit (see Figure 7.18 (b)).
The CCD of the IDOAS was cooled to - 30°C in order to minimize noise due to the dark current of the CCD-detector (see section 5.2). The light conditions at the measurement site made for an integration time of 6.5 s per CCD exposure. Each exposure results in one vertical column of the image. To monitor a complete image, a scan time of around 15 minutes was necessary.
On this day the wind direction was variable and thus several attempts were necessary to take an image of the entire plume. An image of the SO_2 distribution of the plume was derived from an IDOAS measurement between 12:59 local time and 13:14 local time. The result is shown in Figure 7.21. The image of Figure 7.21 b was taken between 12:12 and 12:29. 64 vertical pixels and 100 horizontal pixels comprise the IDOAS image. With a plume distance of 7 km the angular spatial resolution of one pixel can be converted to spatial resolution in the plume of about 25 m (vertical) x 55 m (horizontal). The entire picture therefore includes an area of 1600 m x 5500 m. The maximum values for the SO_2 SCDs are up to $5 \cdot 10^{17}$ molecules/cm^2. Isolated blue pixels indicate that the DOAS fit for these pixels did not yield a valid result because of an insufficient signal to noise ratio. This is one problem in the automatic evaluation routine that has to be improved in the future. The plume was well captured in Figure 7.21, which also indicates the outline of the hill in the foreground (left side). The IDOAS image shows the largest amounts of SO_2 in the center of the plume (dark red area). The maximum SCDs in the center of the image, compared to lower values just above the crater emission source could indicate that the plume was first rising vertically for some distance and then was blown in the direction of the measurement site, resulting in a longer absorption path at the center of the image.
The photo of Mt. Etna, upper panel, was taken during the IDOAS scan shown directly below as SO_2 SCDs. The wind was blowing towards the instrument. Figure 7.21 (right side) shows a second (partial) scan of the plume from the same day, just about one hour earlier (compared to the measurement shown in Figure 7.21 (left side)).

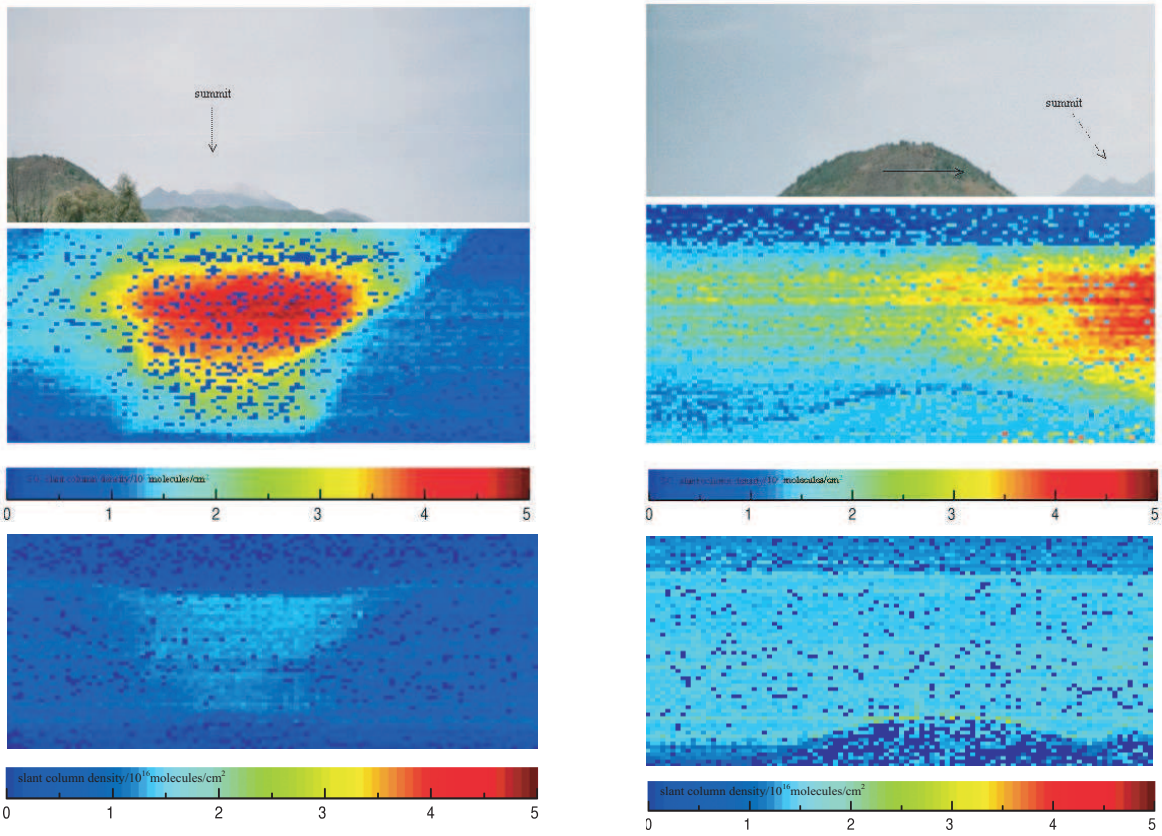

Figure 7.21: *Visualization of the SO_2 distribution in the plume of Etna derived from the I-DOAS scan (bottom), which is invisible in the RGB colour picture taken with a digital camera (top).*

In Figure 7.21 (right side) the instrument was aiming in another direction (more to the left compared to Figure 7.21 (left side) - meaning a more westerly direction). As in the previous image, the SO_2 SCDs reaches a maximum at $5 \cdot 10^{17}$ molecules/cm^2. The left part of the plume is nicely captured in this image and decreasing SCDs are seen to the left of Etna's summit visible in the digital picture in the lower right corner. The plume above the summit appears to consist of two distinct vertical layers; lower SO_2 SCDs can be seen in the center between two horizontal plumes (arrow). Due to the variable wind conditions on this day the plume seemed to be smeared out over the measurement time.

The IDOAS provides the possibility to study two-dimensional trace gas distributions and can be used to study the chemical variation, transport and turbulent mixing processes as well as the plume morphology of volcanoes. This makes it very useful for volcanic applications. Therefore further measurements were conducted during the period of this thesis [*Louban* 2005]. Although only the results for one gas - SO_2 are shown here,

other trace gases like NO_2 and BrO can simultaneously be measured with the same technique [*Lohberger et al.* 2004; *Louban* 2005]. It provides the possibility of new insights into volcanic processes, since plume chemical processes are hardly understood to date. A permanently installed system could give at least one two dimensional image of the trace gases distributions every quarter of an hour. From those images a change in plume chemistry of relatively stable degassing systems could be observed. This additional data could help to improve the forecast of volcanic eruptions. New information about trace gas distributions could be a big step forward in the field of volcanic gas emission studies. Until now, essentially all studies of volcanic trace gases were only one-dimensional. The ground-based measurements presented here can also be made at low degassing sites, because of their much higher sensitivity. Also multiple vent systems can be conveniently characterized (see [*Louban* 2005]). With improved time resolution and further enhanced evaluation algorithms it will also be possible to determine the wind speed by comparing the temporal evolution of SO_2 SCDs. Thus, the source strength of the plume can be determined.

On the October 11^{th} plume traversing measurements were carried out by using a helicopter. It was a relatively sunny day and the pilot tried to fly quite near to the summit. A double plume could be identified. The plume was crossed 3 times, but during the second plume traverse the telescope was blocked at times. During the first traverse, the pilot attempted to stay under the volcanic plume as long as possible, to aim for the possibility of adding of spectra afterwards. The Mini-MAX-DOAS was held out of the helicopter in a near zenith looking position. Only 30 scans were added for a single

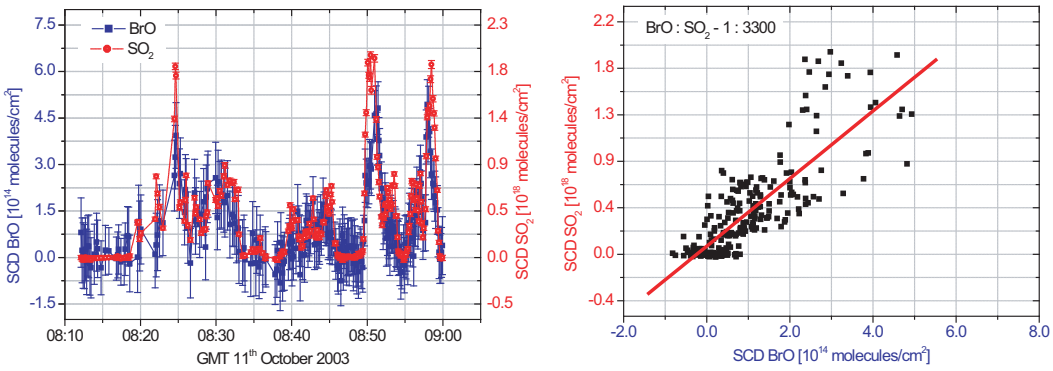

Figure 7.22: *The measurements taken during a helicopter-flight on 11^{th} October 2003(a) SCD's of BrO (blue) and SO_2 (red) as a function of time. (b) SCDs of SO_2 as a function of SCDs of BrO.*

spectrum, therefore the results are relatively noisy and show a quite high error especially for the SCDs of BrO. Nevertheless a good correlation between SO_2 and BrO could still be

found. The values scatter around a ratio of 1/3300 BrO/SO_2, which is not an untypical value, as can be seen in the data of the following campaigns in 2004 and 2005, which are described below.

Field Measurements at Etna, August 2004

In August 2004, the second measurement campaign at Etna within the scope of this thesis took place. DOAS measurements were conducted on 4 consecutive days. On three days the measurements were carried out at Pizzi Deneri - the volcanological observatory at a height of 2800 m (see Figure 7.23 left side). In the same time period filter-pack measurements at the summit region were undertaken and aerosol distribution and chemical composition was measured [*Allen et al.* 2005]. The days were very sunny and the plume always clearly

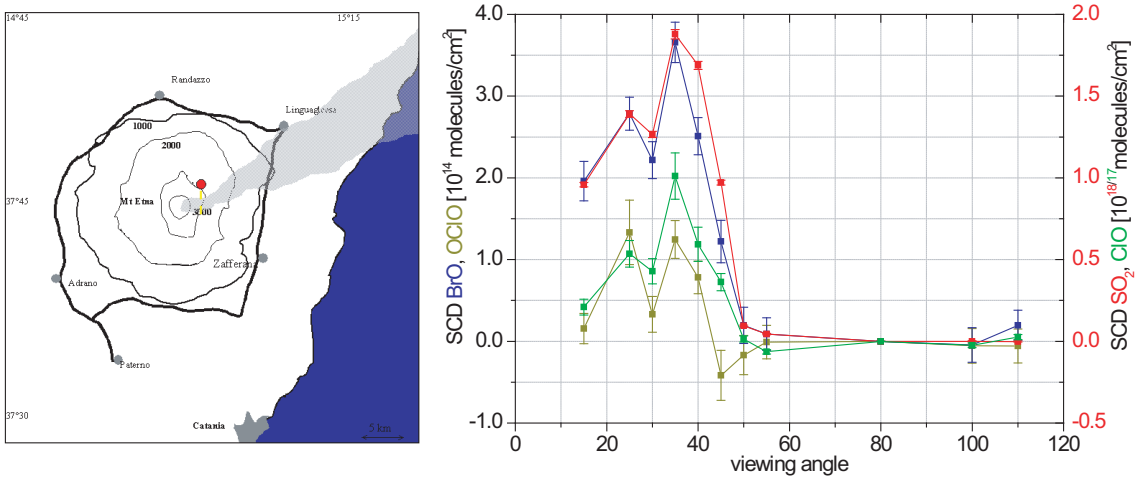

Figure 7.23: *SCDs of ClO, OClO, BrO and SO_2 with a 2 σ fitting error are displayed for one example of a plume scan taken at Pizzi Deneri on the 5^{th} August 2004.*

visible. The measurements were always carried out during midday.

The SCDs of SO_2, BrO and ClO for all four days as time series and their correlations are presented in the Appendix Figure A.10 and the results are summarized in Table 7.5. BrO, ClO and SO_2 could be identified above the detection limit each day. Over this short time the BrO/SO_2 ratio scatters between $1.6 \cdot 10^{-4}$ and $3.1 \cdot 10^{-4}$, ClO/SO_2 between $6.3 \cdot 10^{-2}$ and $1.0 \cdot 10^{-1}$. This may have several reasons. Although the measurement location was the same for three out of four days, the telescope might not have been pointed perfectly in the same direction every day. Thus the measurements can be expected to have a slightly different distance downwind. Another cause could be the variability of the wind speed, which leads to a different plume age at a fixed point downwind. Another likely cause is that the volcanic behavior is rarely stable. Due to the not negligible and up to now not fully understood meteorological influences on the data, it is difficult to study the

Table 7.5: *Summary of measurement results of August 2004. Ratios of BrO/SO_2, ClO/SO_2 and $OClO/SO_2$ and the daily fluxes of BrO, ClO, OClO estimated for the four days of measurements with a similar procedure as at Masaya, by using the ratios to SO_2. SO_2 flux measurement of the 4^{th} of August 2004 were averaged to 1380 t/d [Allen et al. 2005].*

	BrO/SO_2 10^{-4}	ClO/SO_2 10^{-2}	BrO flux [t/d]	ClO flux [t/d]
02.08.2004	1.6	6.6	0.3	73.3
03.08.2004	3.1	10.0	0.6	110.0
04.08.2004	2.0	8.3	0.4	91.6
05.08.2004	2.1	6.3	0.4	69

links between the changes in gas composition and volcanic activity, especially in small data sets, where statistics cannot be effectively be applied. After all, the differences in the ratios from the data taken at Pizzi Deneri is not even of a factor of 2, which is a relatively small difference when considering volcanological data.

The August 5^{th} 2004 was a very sunny day during the morning hours and measurements

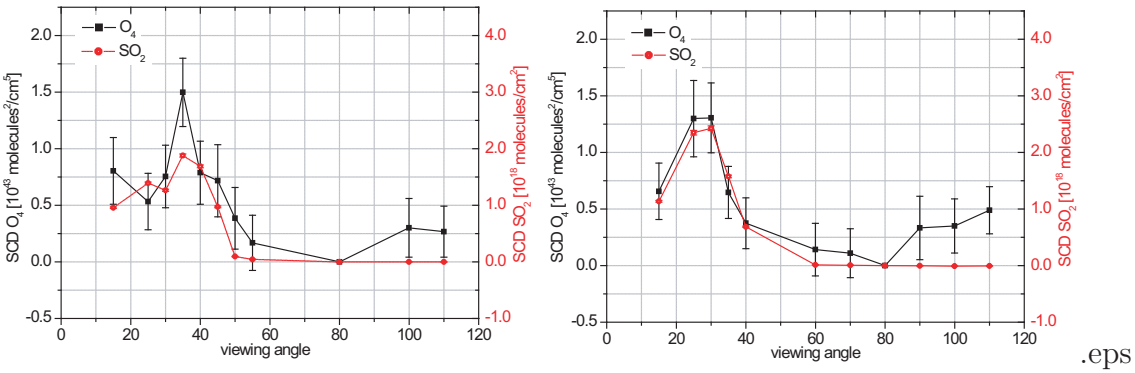

.eps

Figure 7.24: *Measurements at Pizzi Deneri, 5^{th} August 2004, two examples of single plume scans, SO_2 (in red) indicating Mt. Etnas plume and O_4(in black), a clear correlation can be observed.*

took place at Pizzi Deneri. The plume was studied under several viewing angles and the SCDs were quite high on this day, since the plume was not widely dispersed 3 km downwind. This day is shown as an example to display the additional studies of OClO and ClO, besides the ones of BrO and SO_2, as can be seen in Figure 7.23. OClO could be detected on this day as well as ClO, BrO and SO_2. It correlates nicely with the other trace gases in the plume. Due to difficulties in the ClO evaluation (see Chapter 6), it is very desirable to have a further indication (OClO) of the abundance of ClO. During this study OClO was detected in a volcanic plume for the first time. The SCDs of OClO are comparable with

the SCDs of BrO and they are about 4700 times smaller than the SCDs of SO_2. ClO is about 16 times less abundant in the plume than SO_2.
In this data set O_4 was studied too. An interpretation of the data of O_4 is not straightforward (see chapter 8.5), since the plume of Mt. Etna was very near the horizon during these days. Therefore, a possible increase of O_4 absorption in the plume could have been overseen, because the O_4 signal rapidly decreases with larger elevation angles, due to higher O_4 concentrations in the lower atmosphere and the elongated light path in it. On the other hand, the weather conditions were perfect. Very few clouds were present aside from the volcanic plume. Figure 7.24 shows two examples of single plume scans. O_4 and SO_2 are plotted as a function of the telescope elevation angle (the other plume scans can be found in the Appendix A.11). The data seems to give a clear indication on an elongated light path due to the volcanic plume on this day. This is in contradiction to other first studies of light pathes inside the plume [*Louban* 2005; *Kritten* 2004]. A high influence of the weather condition (condensing of the water inside the plume) and volcanic activity is probable. The transparency of the plume depends on several factors, e.g. emitted aerosols, ash content and relative humidity.

Field Measurements at Etna September/October 2004

The third field campaign at Etna was carried out in September/October 2004. It was the most intensive campaign and took place within the frame of the European project DORSIVA. Beside the measurements of the Mini-MAX-DOAS from Heidelberg, Cambridge and Gothenburg, measurements with a COSPEC instrument from the group of CEAM (Valencia), and FTIR measurements from Cambridge and Gothenburg were carried out in parallel.
Already from the beginning of this campaign, Etna's activity was above its normal level. The SO_2 fluxes had decreased over several weeks, but a fracture had opened and a flow of lava had started which did not stop until the end of the campaign. The lava flow finally stopped in March 2005. This provided unique and interesting possibilities for studies comparing gas emissions above the fracture. It was a quiet eruption without any risk for humans and the lava only spread over a desert zone (the Valle de Bove). Unfortunately the weather conditions were not ideal for the measurements. Figure 7.25 shows a schematic map of the beginning of the eruption. The blue line with number 1 shows the place of the fracture, which opened on 7^{th} September 2004 for only a few hours. The red arrows in this figure indicate the locations of the first lava flows. In the days following September 7^{th} the field of fractures expanded slowly. In the afternoon of September 9^{th} the start of fumarolic activity could be observed at the field of fractures [INGV-Catania]. In the early morning of September 10^{th} a new effusive vent opened in a height of 2650 m on the western flank of the Valle de Bove, (number 3 in Figure 7.25). Lava started to flow out very quietly, with some phreatic explosions at the contact points

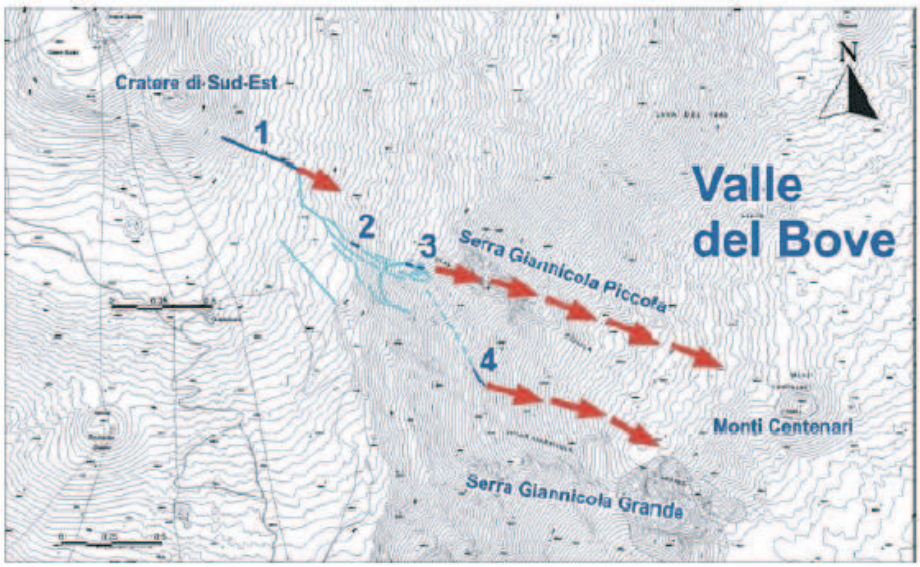

Figure 7.25: *Schematic map of the fracture (blue = eruptive fracture; cyan = dry fracture) 1) bocca of active eruption on 7th September 2004 2) bocca characterized by discontinued degassing 3) open bocca on 10th of September 2004 4) bocca dry eruptive starting on the 13 th September, the red arrows show the zones of the lava flows. Adapted by INGV Catania.*

with a snow layer. The lava flow split into two pathes between Sierra Giannicola Piccola and Sierra Giannicola Grande.

The first measurements of this campaign were carried out with a Mini-MAX-DOAS instrument during midday of September 9th 2004, two days after the first fracture had opened. The Mini-MAX-DOAS was also collecting data during the afternoon when the fumarolic activity started and on the afternoon of the 10th of September after the first lava flow had found its way into the upper part of the Valle de Bove. At this time no direct observations at the fumarole or above the new lava flow were conducted, just the main plume of Etna was observed. The results are shown in Figure 7.26. During those two days the weather was sunny with not more than 50% white cloud cover. The weather was fairly stable. At first glance the results seem to show a significant increase for the BrO/SO_2 ratio from $2.8 \cdot 10^{-4}$ to $7.7 \cdot 10^{-4}$, nearly a factor of three. But care has to be taken since the measurement location was different for every presented plot. Therefore the various distances, which have a strong influence on the BrO/SO_2 ratio - see Chapter 8.1., have to be considered as well. The different location of the measurements of September 9th and 10th are shown in the left upper part of Figure 7.26. As shown on the map, the difference in distances between the various measurement locations is unfortunately also increasing for the first two measurements, but can probably not explain the total increase

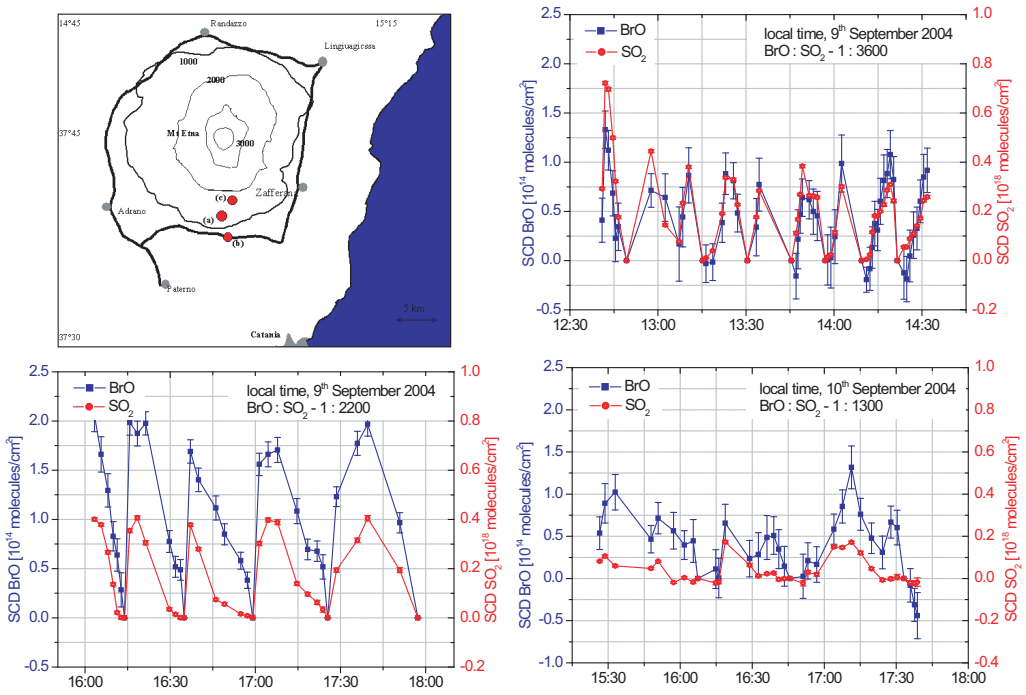

Figure 7.26: *SCDs of SO_2(red) and BrO(blue) data from September 9^{th} and 10^{th} 2004. Time of fracture opening and start of lava flow, for a detailed description see text.*

in the BrO/SO_2 ratio, especially considering the steep slope here and on the September 10^{th}, when the distance to the summit was even smaller, so that after the studies for the BrO/SO_2 dependence on distance the values are normally expected to be smaller ([*Bobrowski et al.* 2005] and Chapter 8.2.)

Normally an increase in volcanic activity is often accompanied by a rise in the sulphur dioxide flux, which should lead to a decrease in the BrO/SO_2 ratio. This could not be observed here. Neither in the COSPEC measurements nor in the mini-DOAS traverses and scanning mode a significant increase of the SO_2 flux was seen [INGV Catania]. Investigation of the erupted lava showed that this lava consist priorly of degassed material. The solubility of sulphur and halogens is different (Chapter 3) in a manner that sulphur tends to be degassed first, followed in a second step by the more soluble halogens. This could explain the increasing BrO/SO_2 ratio, since the gas of the fracture field was mixed with (and therefore somewhat diluted) the main plume of Mt. Etna. A more detailed discussion of the data will be given in Chapter 8.3, were the Mini-MAX-DOAS data will also be discussed in context with halogen data from filter-pack measurements during these days.

During the following weeks the lava flowed out quietly. A second fracture with lava flowing out opened on September 13^{th} at a height of 2350 m (see number 4 in Figure

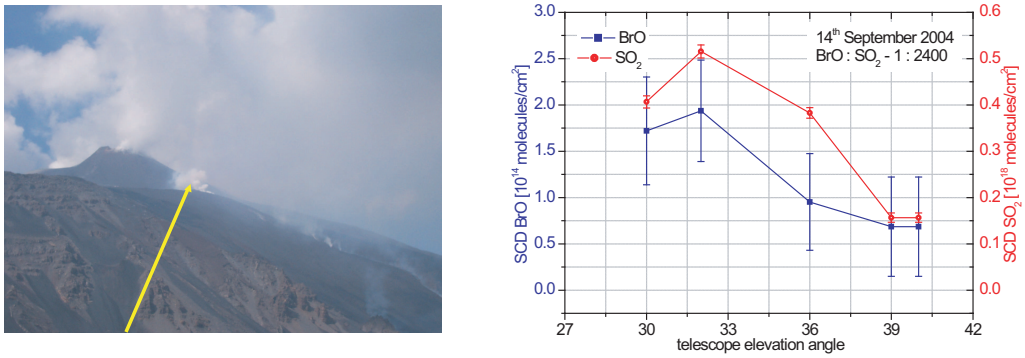

Figure 7.27: *(a) Photograph of the telescope viewing direction. (b) SCDs of SO_2(red) and SCDs of BrO(blue) as a function of telescope elevation angle. One example for measurements over the entrance of the lava flow.*

7.25). On the September 14^{th} measurements from the south-western site of the Valle de Bove across the Lava flows were carried out. In the morning the weather was very sunny, but soon after the beginning of the measurements grey and cloudy conditions prevailed. The telescope was pointed to the visible whitish looking fumarolic emission at the origin of the lava flow. In Figure 7.27 a photograph is given, the viewing direction is indicated by a yellow arrow. Next to this photograph a scan through the fumarole is displayed by plotting the SCDs of BrO and SO_2, respectively as a function of the viewing angle of the telescope. The BrO/SO_2 ratio is comparable to one of the highest measured ratios in the plume of the main craters of Etna during the first two measurement on September 9^{th} and 10^{th} 2004. This result fits to the observation that the lava flow was already highly degassed, meaning that the halogen to sulphur ratio is usually increased, because of the solubility differences.

One main focus in this campaign was to carry out various measurements with the Mini-MAX-DOAS at different locations to investigate the SO_2/BrO ratio in dependence of the distance to the source (dependence of the plume age). Because of the limitation on instruments most of the time, there was no possibility of to measure simultaneously. To compensate the fluctuations in the ratio caused by unstable activity of the volcano and the possible influences of different meteorology, several measurements at the same distance were done to average the values later on.

Figure 7.28 presents a single plume scan illustratively for each of the three measurement days taken at about 4 km from the summit. For a better orientation a small map of Etna with the measurement site marked by a red point is given in this figure. The BrO/SO_2 ratios have a maximal difference of 15%. The weather conditions were sunny in the mornings, but quickly changed to very cloudy conditions with fog. On September 11^{th} the measurements started already under foggy conditions. The average BrO/SO_2

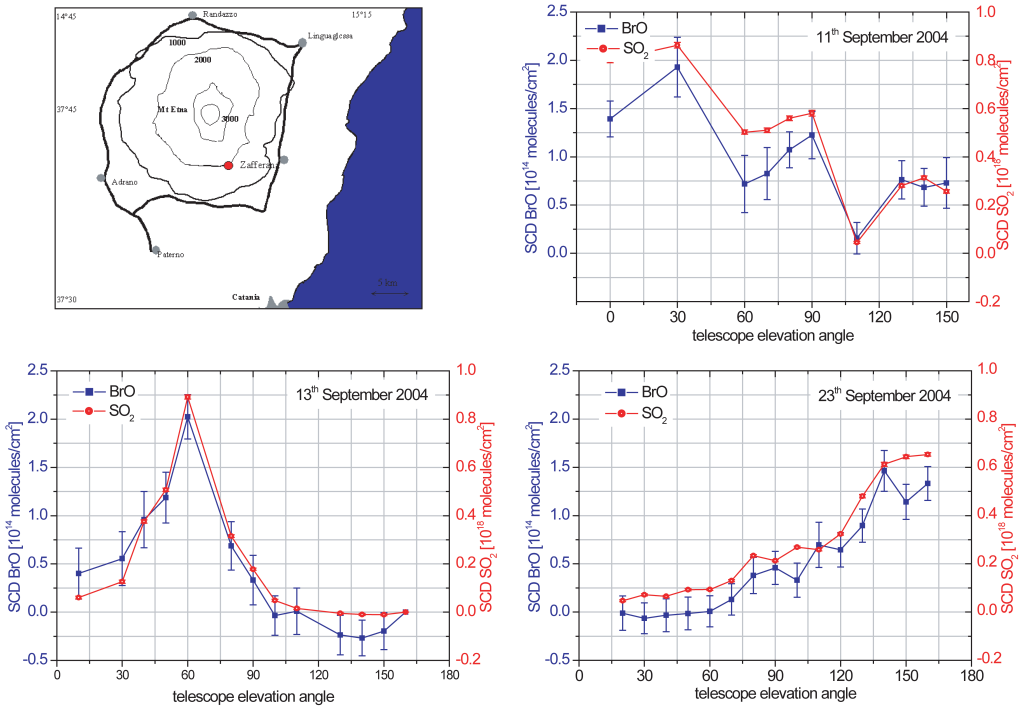

Figure 7.28: *Single plume examples for three measurements carried out about 4 km downwind (see map upper left corner). SCDs of SO_2 (red) and SCDs of BrO (blue) as a function of telescope elevation angles.*

ratio of these three days was taken as the BrO/SO_2 value for the 4 km distance 2004 in the later discussion (Chapter 8.2). The weather conditions did not allow evaluation for ClO, because of the fact that its absorption cross section mainly lies below 308 nm (see Chapter 6) where little light was available.

On September 22^{th} 2003 investigations were carried out on the high pressure degassing vent at 2830 m. In the morning hours the weather was very sunny and upon reaching Torre de Filosofo shortly after 10 am the South East (SE) crater was clearly visible, which unfortunately changed after midday. The degassing vent had shown continuous high pressure gas emission mostly in the absence of explosive activity for several days already. But a week there had been no observable smell at the edge of the emitted gaseous plume, the mainly emitted gas had probably been water vapor (an upcoming thunderstorm had prevented measurements at this time). On the 22^{nd} it was not possible to breathe without a gas mask when entering the gases. A strong SO_2 smell could be recognized in the vicinity of this vent. FTIR and DOAS instruments were set-up near the fumarole entrance. Measurements with the Mini-MAX-DOAS took place from two different viewing directions at the fumarole. First the Mini-MAX-DOAS was situated just below the degassing fumarole, looking along the gaseous plume. The risk of scanning

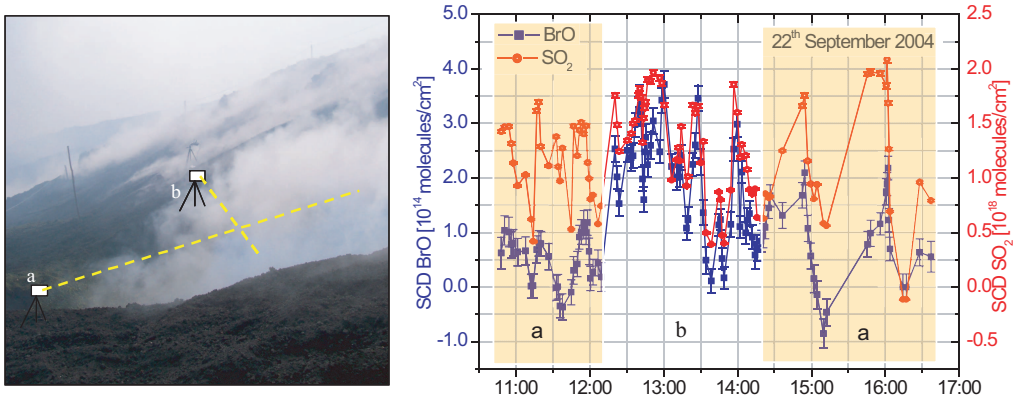

Figure 7.29: *Measurements carried out on the new fumarole scanning the fumarole from two sites (orange (a) and white (b)). SCDs of SO_2(red) and SCDs of BrO (blue) as a function of time.*

the plume of the SE crater in the background could not be totally ruled out, even though attempts were made to avoid looking into the visible part of this plume. After a little more than an hour of measurements the Mini-MAX-DOAS was moved to a point to the east of the fumarole and more perpendicular scans were conducted, but with a higher risk of having the 'main' plume of Etna in the background, due to the unfavorable wind direction on this day. After two more hours the instrument was changed back to the first location. In figure 7.29 on the left panel a photo including the measurement locations is shown. The right panel shows the SCDs of SO_2 and BrO both as a function of time. The data from the location below the fumarole (observation direction along the gaseous emission of the vent (a)) are underlined with an orange colored rectangle.
It can be seen that the BrO/SO_2 ratio is enhanced in the second measurement geometry (figure 7.29(b)). Due to the open question, to which amount the gas of the main craters might be imaged, the data is very difficult to interpret. It is very surprising that even in the measurements at such a near distance the BrO/SO_2 ratio is relatively high (see Chapter 9.2, 9.4). Assuming BrO is not directly emitted, the observations could be explained by two reasons, either the emitted gas could very quickly mix with the ambient air and the described chemical conversion take place even faster than assumed for a volcanic plume. This is possible, since the fumarolic plume has a much smaller size and is therefore mixed more quickly with the ambient air. But it is also possible that the measurements are dominated by a signal originating in the main plumes. An argument against the second explication is, that DOAS measurements were additionally carried out in parallel by the Cambridge group who pointed their telescope just above the entrance of the fumarole, which resulted in a very similar value for the BrO/SO_2 ratio [DORSIVA - Annual Report 2004]. In the days ensuing, the high pressure emissions decreased, but

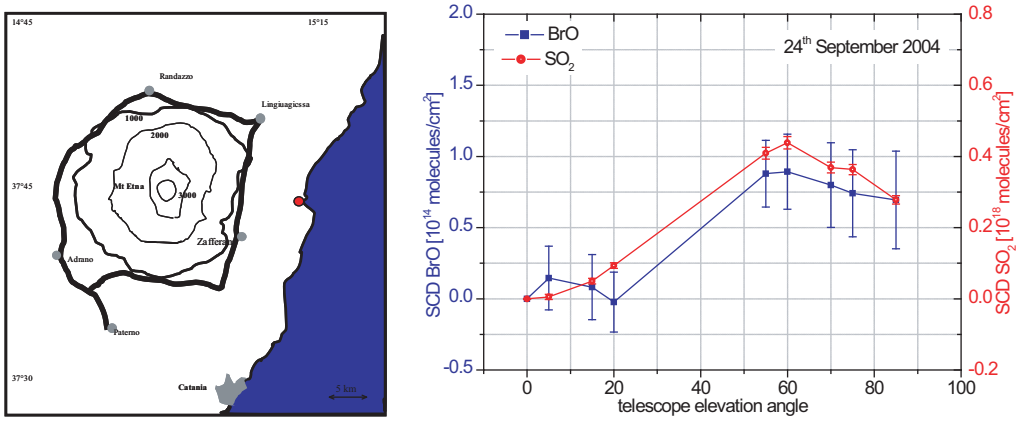

Figure 7.30: *Measurements undertaken 19 km downwind of the summit, near Riposto, at the coast on 24th September 2004. SCDs of SO_2(red) and SCDs of BrO (blue) as one example of a plume cross-section.*

no further measurements at this location were undertaken.

On the 24th of September measurements at a nearly maximal distance to the summit of Etna were carried out, beside the sea near the town Riposto. At this distance, the plume is already highly diluted and often very wide, which results in very small SCD's for BrO and therefore a higher relative error. Several attempts to repeat these measurements were hindered by bad weather conditions. Therefore, this data could only be used for discussion of the BrO formation processes in volcanic plumes. Figure 7.30 shows a map and one plume scan example with SCDs of BrO and SO_2, respectively, as a function of the telescope elevation angle.

Figure 7.31 and 7.32 are results of measurements from the upper part of Etna above

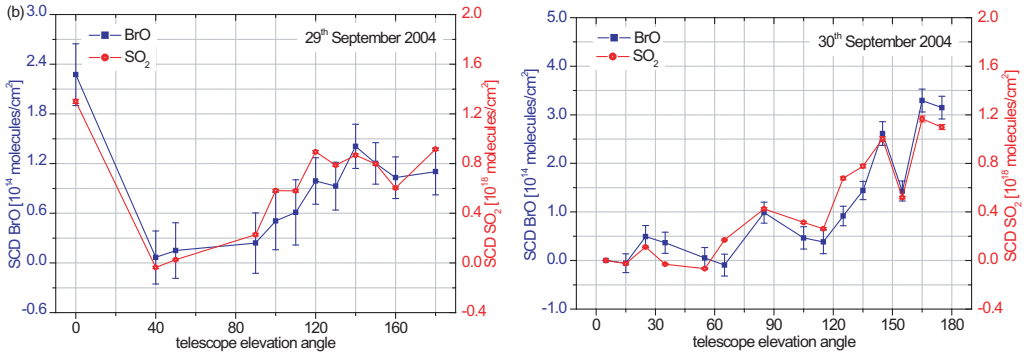

Figure 7.31: *Measurements carried out in the upper part of Mt. Etna, above 2800m (near the summit), 29th September 2004 and 30th September 2004. SCDs of SO_2 (red) and SCDs of BrO (blue) as a function of telescope elevation angle.*

2800 m, just below the direct crater region. Measurements were carried out at slightly different locations near the Torre de Filosofo during three days, September 29^{th}, 30^{th} and October 1^{st} 2004. On the 29^{th} of September 2004 the instrument was set up near the new fumarole, where the gas now was steaming out less pressurized than a few days earlier. The visibility was fairly low, because Etnas upper part was inside the clouds on this day. The plumes of the different main craters of Etna (SE, Bocca Nova, Voragine and NE) seem to be still at least partly separated at this point, but unfortunately due to geometrical limitations of the measurement site it was impossible to collect sufficient data to discuss the differences in the gas emissions of the different craters. The separated part on the western side (left side in Figure 7.31) consists of only one data bpoint. The BrO/SO_2 ratio of $1.7 \cdot 10^{-4}$ was significantly lower than the measured ratios at Etna the days before, but it was also the first direct investigation of the plume from the main crater at this close distance. A second measurement was conducted on the following day. The ambient conditions on the 30^{th} of September were even worse, not only was the visibility very low, but a sulphur smell could be recognized during the measurements, indicating that the instrument was situated inside the plume of Mt. Etna. A reference

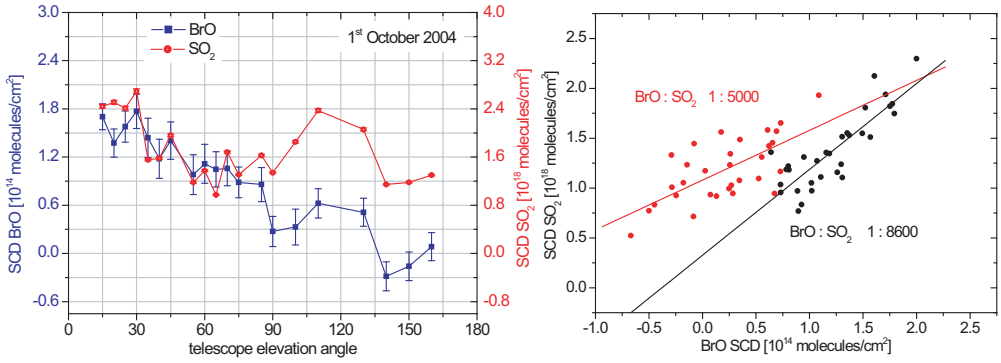

Figure 7.32: *(a) One example of a plume scan of Mt. Etna 1^{st} October 2004. Measurements were carried out in a height of 2900 m at the southern side. The SCDs of BrO (blue) and SO_2 (red) are plotted over the elevation angle of the telescope. Two plumes with different BrO/SO_2 ratios are observed. (b) All data of 1^{st} October 2004 for SO_2 as a function of BrO are plotted, 15° to 70° elevation angle in red 80° to 160° elevation angle in black.*

spectrum from the lowest possible elevation angle was taken to evaluate the spectra as well as possible, but nevertheless the true total column densities were probably not obtained for this day. The ratio of BrO/SO_2 of $2.5 \cdot 10^{-4}$ is enhanced compared to the day before. There is a wide range of speculation on the reason. As could be seen already, the ratio could be correlated to activity changes and even though there were no clear seismic signals, the activity of Etna in these days was not assumed to be very stable. The measurement locations were actually not exactly identical and it is possible that small

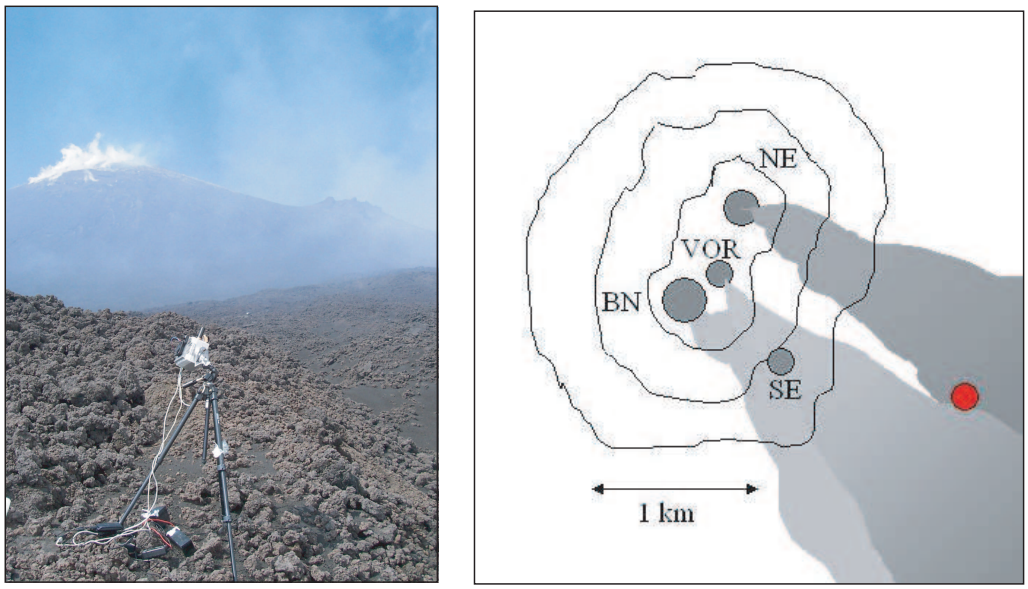

Figure 7.33: *Measurement set up is illustrated by a photo. The measurement location is marked by a red dot on the map, 1st October 2004*
NE - North East crater, SE - South East crater, BN - Bocca Nova, VOR - Voragine.

variations in the distance (plume age) may have large effects, as fast chemical reactions may take place in the first minutes or seconds (also see Chapter 8). In addition to the distance change, the measurements on this day took place a bit more to the west. It is possible that a plume originating from a crater with a different chemical composition, was observed (see also Figure 7.32 and discussion below and in Chapter 8.2.). To a minor part an error in measurements and evaluation might play a role, but cannot explain the difference of about 30 %.

The aim on the 1^{st} of October 2004 was to find a location in the upper part of Mt. Etna, where the instrument could be placed between the plumes of different craters. It was a very sunny day in contrast to the two days before and the clouds appearing at midday were fortunately below the measurement site. Figure 7.32 presents an example of a total scan from 15° to 160° (north-easterly to south-westerly direction) on the left panel. The entire data set (see Appendix Figure A.15 and right panel of Figure 7.32) shows that the BrO/SO_2 ratio is higher in the right(east) than in the left(west) side of this figure. Assuming that the eastern side is more affected by the NE crater and the western side by the Crater Centrale (Voragine and Bocca Nove) due to geometrical considerations (see Figure 7.33), this can be interpreted as an enrichment of halogens (or a lower sulphur emission) at the NE crater compared to the Crater Centrale (Bocca Nova and Voragine) as well as the SE crater. This assumption is supported by Filter pack measurements by *Aiuppa et al.* [2005]. That also illustrates the complex system of a volcano like Mt. Etna.

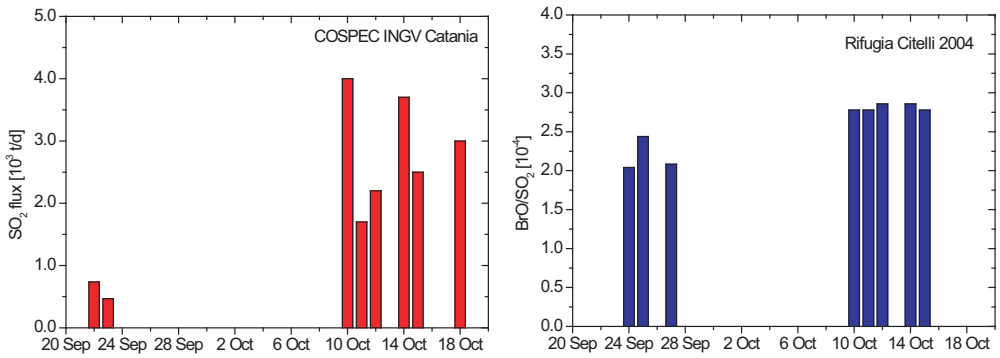

Figure 7.34: *Measurements at Rifugio Citelli September - October 2004. BrO/SO_2 ratio as a function of time and measured SO_2 fluxes by COSPEC [INGV Catania] in the same time period.*

The measurement site, where most of the measurements were carried out in this study, was Rifugio Citelli, which is about 6 km from the summit on the eastern flank of Mt. Etna. The main wind direction is westerly and therefore a plume overpass in this direction is highly probable. This makes Rifugio Citelli an ideal place for a higher frequency of measurements, and gives a good chance to investigate temporal variations. The BrO/SO_2 ratio seems to be quite stable during the measurements in mid October and slightly higher in average than the ones taken on three days in September. An average for these eight days was taken for the later discussion on the BrO/SO_2 dependency on the plume age.

On October 18^{th} an expedition was carried out to reach the crater area of Mt. Etna. It was a very sunny day and measurements with a Mini-MAX-DOAS instrument took place for two hours near the Voragine crater. The very young plume was studied at a distance of about 100 m from the crater. Filter pack measurements were conducted simultaneously. No BrO could

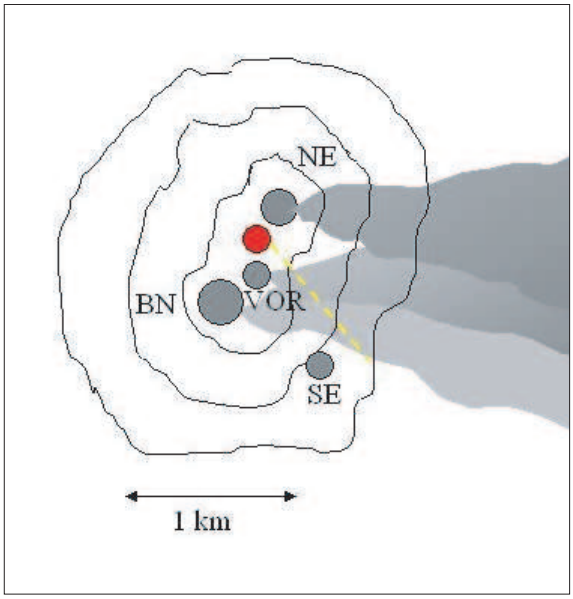

Figure 7.35: *The measurement location is marked by a red dot on the map, the viewing direction is illustrated by a dashed yellow line, 18^{th} October 2004.*
NE - North East crater, SE - South East crater, BN - Bocca Nova, VOR - Voragine.

be detected in the plume, even though the
SCDs of SO_2 were quite high and also ClO
was clearly recognized in the spectra with a ClO/SO_2 ratio of 1/30. The filter pack measurement resulted in an increased sulphur to bromine ratio of about 6,000 on this day, but no significant change was observed in Etna's sulphur flux.

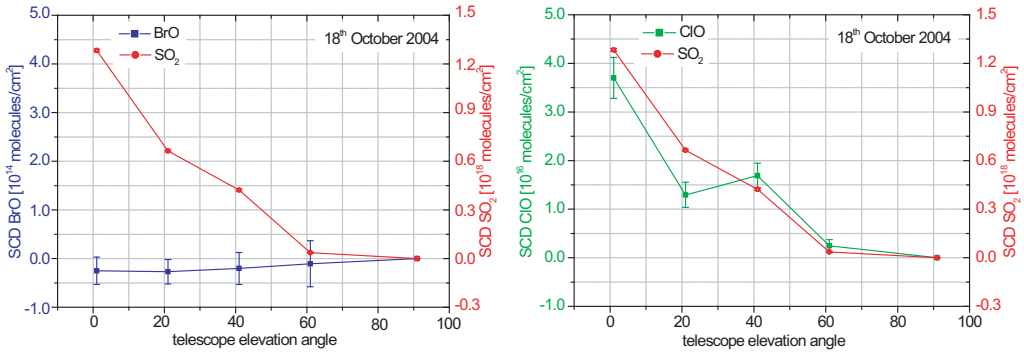

Figure 7.36: *Measurements at the NE crater, October 18th 2004. SCDs of SO_2 (red) SCDs of BrO (blue) and SCDs of ClO (green). No BrO could be detected, but ClO is already abundant and correlates well with SO_2.*

Field Measurements at Etna May 2005

The last campaign during this study was carried out during and after the IAVCEI Gas-workshop 2005. The seismic activity of Etna was very low at this time [INGV-Catania]. The campaign's focus was on further studies of the dependencies of the BrO/SO_2 ratio on plume age. Investigations were carried out with up to three Mini-MAX-DOAS instruments, set up at different distances from the sources.

The first measurements of this campaign in May 2005 were carried out at Rifugio

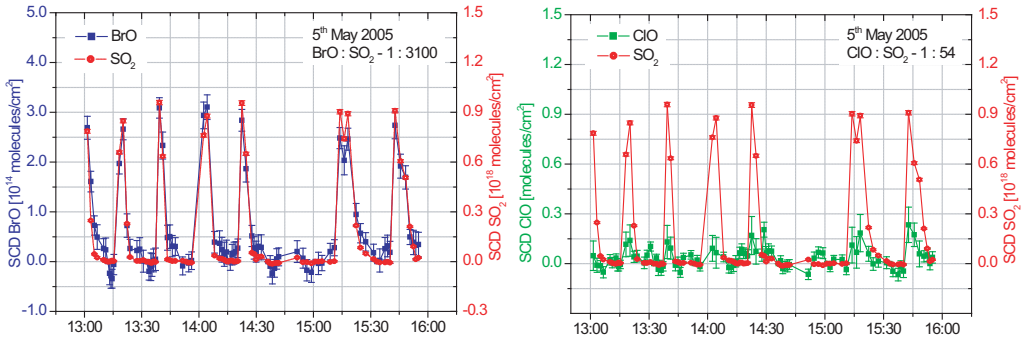

Figure 7.37: *Measurement at Rifugio Citelli 5th May 2005 as example for BrO and ClO detection in Mt. Etnas plume always plotted in comparison to SO_2.*

Citelli (about 6 km downwind of the summit) on the 5^{th} of May 2005. Afterwards, Mini-MAX-DOAS measurements took place every day at Rifugio Citelli until the 18^{th} of May 2005, except for May 6^{th}, 12^{th} and 16^{th}, when the plume was not observable from this point. An example of these daily measurements is given by Figure 7.37 (all other days are presented in the Appendix - A.20).

Figure 7.37 shows the time series of plume scans for the 5^{th} of May 2005. High SCDs indicate measurements inside the plume. Measurements around zero are taken while looking in directions outside the plume. Again BrO and SO_2 SCD correlate very well with each other.

The ClO SCDs for the entire campaign were close to zero, except for the measurements in the crater region on May 7^{th}.

On this day, an excursion took place to the summit area. It was a sunny day with very strong wind velocities $>$ 10 m/s. Just below the summit, Mt. Etna was still partly covered with ice flowers, but the temperature was about 3°C.

In the summit region only the emission of the NE crater was investigated with the Mini-MAX-DOAS instrument. The distance to the plume was several hundred meters. The plume had an age of about 30 s assuming a wind speed of 10 m/s and a 300 m distance from the crater.

Unfortunately results of parallel Filter pack measurements are only available for the Voragine crater for this day (carried out by A. Aiuppa) and showed a (HBr+Br)/SO_2 ratio of 1/2950, which is in the same range as measured last year (see *Aiuppa et al.* [2005]). The next Filter pack measurement carried out on the NE crater was carried out on the 20^{th} of May and shows a quite typical HBr+Br/SO_2 ratio of 1/1230 [A. Aiuppa, personal communication]. The BrO/SO_2 ratio is quite high, in comparison to earlier measurements [October 2004 this study, *Oppenheimer et al.* [2005] as well as the ClO/SO_2 ratio. There is nothing known about any signs of exceptional activity of Etna on this day. The difference to the earlier

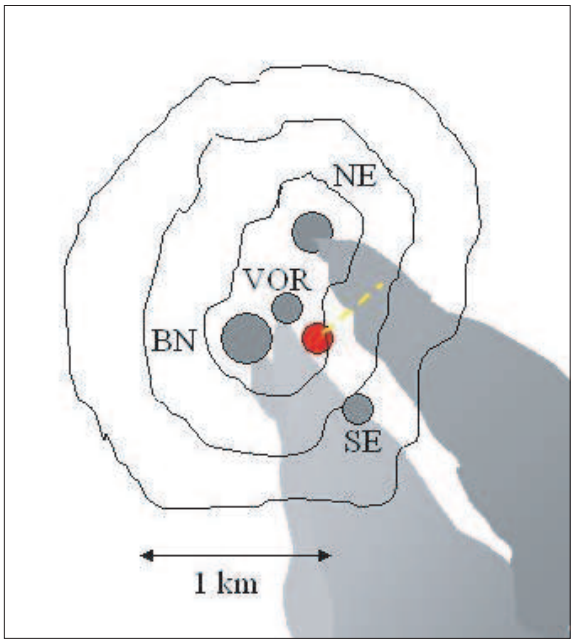

Figure 7.38: *The measurement location is marked by a red dot on the map, the viewing direction is illustrated by a dashed yellow line, 7^{th} May 2005.*
NE - North East crater, SE - South East crater, BN - Bocca Nova, VOR - Voragine

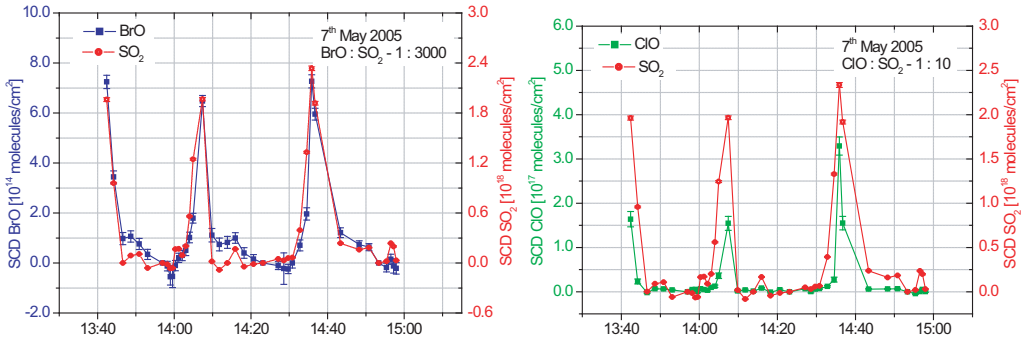

Figure 7.39: *Measurement at the summit, 7th May 2005 as example for BrO and ClO detection in Mt. Etnas plume. Both plotted in comparison to SO_2.*

measurements is the choice of crater plume. In the Filter pack measurements, a significant difference between both craters is visible, too. The NE crater shows a higher halogen to sulphur ratio than Voragine [*Aiuppa et al.* 2005], which seems to be indicated by the DOAS measurements, too. This is an important result. These measurements also indicate that BrO is formed even faster than earlier measurements and first model calculation suggest.

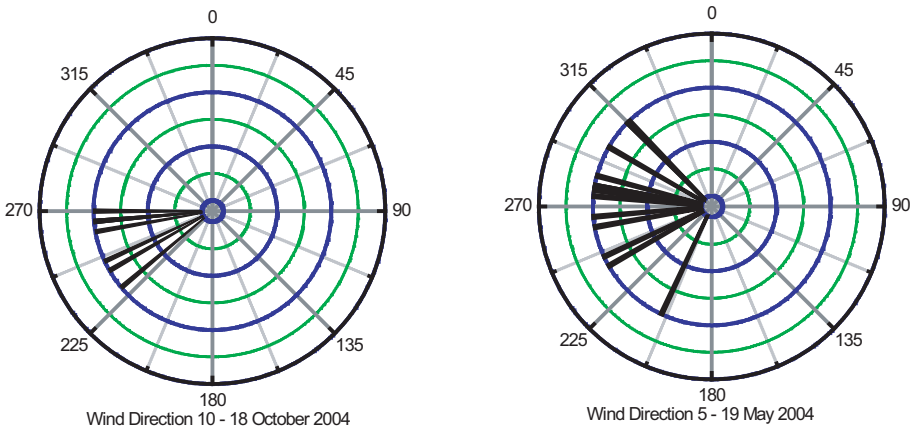

Figure 7.40: *Wind directions for October 10th - 18th 2004 and May 5th - 19th 2005.*

Measurements further downwind at Rifugio Citelli and north of Milo during this day nevertheless show the increase of the BrO/SO_2 ratio already observed in autumn 2004 and later in this campaign. The BrO/SO_2 ratios are unusually high on this day.

From May 7th to 18th 2005 (1.5 weeks), almost daily MAX-DOAS measurements at Rifugio Citelli were carried out. This short time series can at least give hints and indications on the distance dependencies of SO_2/BrO ratios. Although there was no exceptional activity at Mt. Etna recorded in May 2005, the ratio of the SCD values of SO_2 to BrO scatter far more than they do in the time series (of about a week) at the same location during the eruption in October 2004. The weather of both time series changed during the period of

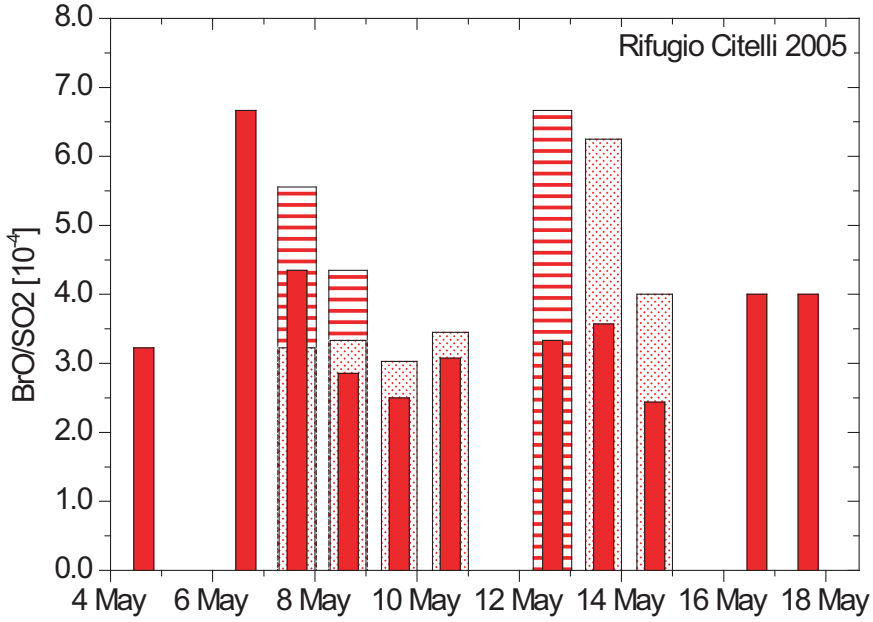

Figure 7.41: *Measurements at Rifugio Citelli, May 2005. Time series of the BrO/SO_2 ratio. A high variation could be observed.*

measurements from very sunny to very cloudy, even to rain. The BrO/SO_2 ratio in average was found to be higher in May 2005 than in September/October 2004. The main difference between both periods is the activity of Etna, which had an effusive eruption in autumn 2004. This eruption had stopped about 1.5 months before the measurements in May 2005 took place. Another difference is the wind direction, which could have an influence on the results, especially because just the edge of the plume could often be measured from Rifugio Citelli. It is possible that even in a distance of 6 km the plumes are not fully mixed and that the observed difference in the BrO/SO_2 ratio is caused by the different parts of the plume.

The main wind directions in the course of these two periods are shown in Figure 7.40. Indeed more scattering in the wind directions is observed in May. It also seems possible that the plume of the NE crater influenced the May measurements more than the measurements carried out in 2004. Furthermore, it should be taken into account that the SE crater showed enhanced activity during the eruption which could have diluted the plume with more SO_2 and would explain the slightly lower BrO/SO_2 ratio during the measurements in 2004 to 2005.

Beside the studies carried out from the measurement site Rifugio Citelli, measurements further downwind at distances of up to 19 km from the summit were again carried out

simultaneously and showed similar results to the measurements in autumn 2004 (see chapter 8.2).

7.4 Chile and Bolivia

During and after the IAVCEI workshop in Pucon 2004, measurements were carried out on two volcanoes in the Andes, volcano Villarica and volcano Ollague.

7.4.1 Villarica

Villarica is situated in the southern Andes in Chile (39.3 S, 71.4 W). It is characterized by an open vent system. Villarica is a basaltic-andesitic stratovolcano with a height of 2847 m above sea level and with a long historic record that includes fatal eruptions. A very large (Volcanic Eruption Index VEI = 5) eruption was dated to ca. 1810 B.C. by using the carbon-14 method. The first historic eruption was recorded in 1558. Since then, there have been numerous small gas explosions that throw incan-descent blobs of lava above the crater rim. Today several explosions occur each hour. Larger eruptions and lava flows are less frequent. Since the end of the last eruption in 1985, an active lava lake has been present in the summit crater and the volcano has been continuously degassing. [http://volcano.und.nodak.edu/vwdocs/volc_images/south_america/chile/Villarrica.html]

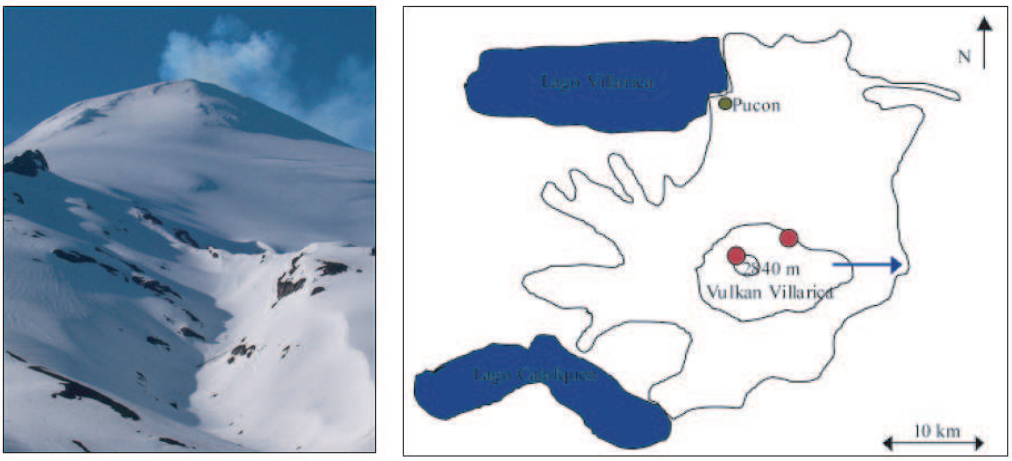

Figure 7.42: *Photo and Map of Villarica Volcano, the red dots mark the measurement locations for the two days (November 17th and 24th 2004).*

Field Measurements at Villarica 2004

Measurements at Villarica were successfully carried out on November 17^{th} and 24^{th} 2004. November 17^{th} 2004 was a very sunny day without any cloud cover, except for the volcanic plume. The observations lasted about 4.5 hours at the north eastern side of the volcanic edifice in a distance of around 3 km from the summit. The instrument was pointed to elevation angles of 21, 24, 27, 30, 33, 36, 39, 50, 60, 70, 90 degrees above the horizon.

On two days, attempts were undertaken to reach the top of Villarica and to do measurements beside the crater. Due to bad weather conditions, the measurements failed on November 20^{th}. But on November 24^{th} 2004 a field trip to the top of the volcano was successfully carried out and measurements near the crater rim took place for 1 hour. A white cloud layer could be seen below the measurement site. Discontinuous emissions were observed, probably caused by rising and falling of the lava lake inside the crater. From

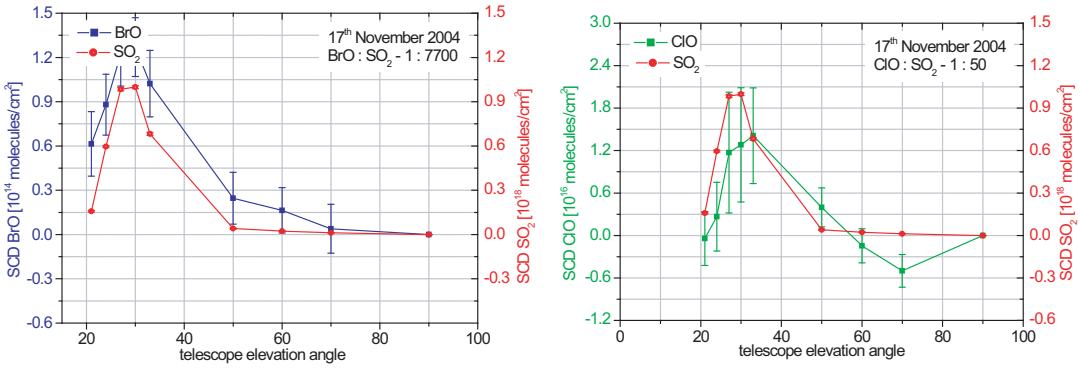

Figure 7.43: *SO_2, BrO and ClO SCDs at Mt. Villarica. The plume was scanned about three km downwind, on the 17^{th} November 2004. A single plume scan is displayed. For the complete data set see Appendix A.22.*

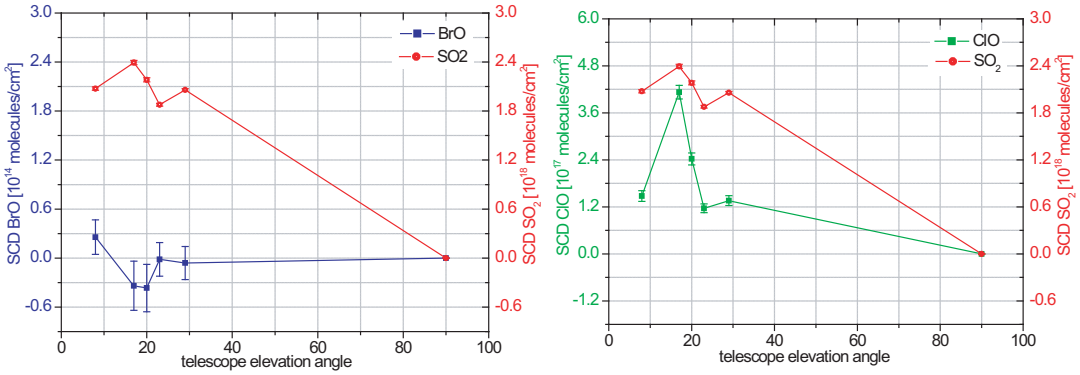

Figure 7.44: *SO_2, BrO and ClO SCDs from the top of Mt. Villarica, carried out on 24^{th} November 2004. A single plume scan is displayed. For the complete data set see Appendix A.23.*

5° to 30°, measurements were performed with steps of 3°, above 30° to 90° the increment was 10°. After each plume scan one reference spectrum was taken by pointing away from the crater at 150° elevation.
For the 17^{th} as well as for the 24^{th} of November 2004, SO_2 and ClO could be clearly recognized in the evaluated spectra as can be seen from the SCD values of both species displayed in Figure 7.43 and 7.44. BrO could only be identified in the spectra taken further downwind. This will be discussed in more detail in Chapter 8.2, section "BrO Formation in Volcanic Plumes".

7.4.2 Ollague

Ollague is situated on the border between Bolivia and Chile (at 21°18' S and 68°11' W). It is a composite cone volcano and the summit reaches an altitude of 5,863 m. It has a long history of activity, which covers at least 10,000 years. The summit region contains an eroded crater with a diameter of about 1.2 km and has fumarolic activity. Sulphur is mined at several locations in the summit region. A persistent fumarolic steam plume can be seen on the southern flank of the volcano and appears to come from a single vent, that is located on a summit dacite dome. The youngest lava has a basaltic andesitic composition. [*Shanaka and Francis* 1991]

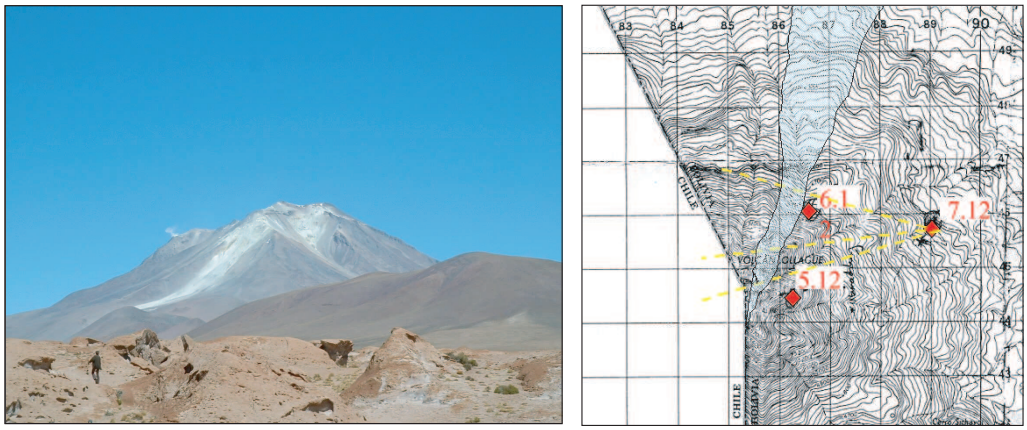

Figure 7.45: *Photo and Map of Ollague Volcano. The red dots mark the measurement locations for the three days (December 5-7th 2004).*

Field Measurements at Ollague 2004

Three days of measurements on December 5^{th}, 6^{th} and 7^{th} 2004 were performed on the Ollague volcano. The measurement site was changed every day to get data from different distances from the source. The highest and also closest measurement site to the source was in a height of around 5400 m a.s.l. The lowest measurement point was about 4400 m

a.s.l. The different measurement points are shown on the map in Figure 7.45.
The usual wind pattern during these days were north easterly during the morning hours and south westerly s after noon. Because all measurement sites were on the north-eastern flank of Ollague, they were carried out after midday. Most of the time the degassing of Ollague could be only recognized by a very weak light whitish looking "cloud". The emission did not seem to be continues but rather like a "puffing" system.
The spectra were only evaluated for SO_2 and the total data set can be found in the Appendix A.24. The timescale on the x-axis in Figure A.24 is only a relative time, since due to instrumental and power problems in the beginning, the time information from the hand-held PC was lost and no clock was available during the time of the measurement campaign.
Figure 7.46 presents single plume scans for the 3^{rd} measurement day. In the upper left

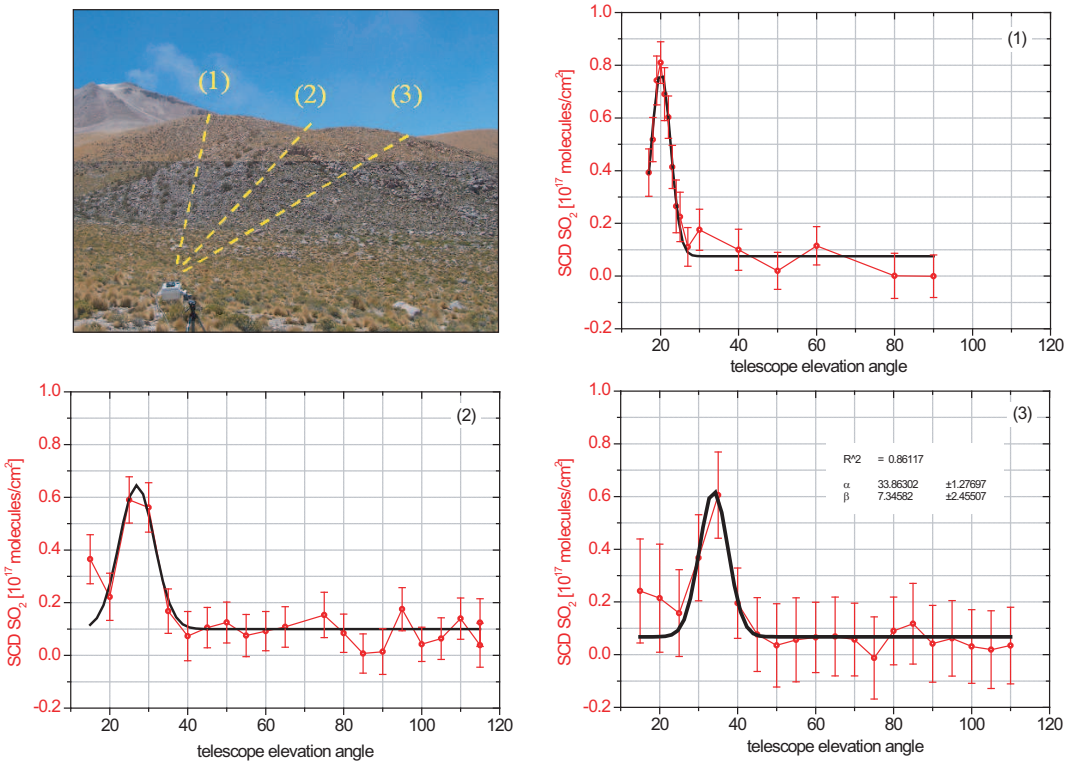

Figure 7.46: *SO_2 measurements at Ollague on December 7^{th} 2004. The measurement situation is displayed in the upper left panel, the different azimuth viewing directions applied during this day are marked by yellow dashed lines and one plume example for every direction is given beside, with an overlayed Gaussian fit.*

panel a photo of the measurement situation is shown. During this day, measurements in different azimuth angles (different plume distances) were carried out. For each direction one single scan example is presented. The SO_2 SCDs are plotted as a function of elevation

angle. The highest SO_2 SCDs can be seen at the closest distance to the emission source where the plume is less diluted.
The angle to the plume in viewing direction 2 was nearly perpendicular and therefore will be taken for an estimation of the SO_2 flux. Since no gas measurements at Ollague are available today, this might be the first estimation for this volcano.
The flux was calculated similar to *Bobrowski* [2002] (for a detailed description also see Chapter 8.5). It was assumed that no additional light scattering took place in the plume of Ollague and therefore the light path through the plume was equal to the diameter of the plume. The wind velocity was estimated by measuring the time (2 min), which one of the visible structures in the plume took to move from the summit to a characteristic location $\sim$ 600 m from the summit. The calculated plume diameter (d) is about 310 m (by estimating the distance from the instrument to the plume to about 2000 m and using $d = 2\ \sigma = \tan(\frac{\beta}{2}) \cdot \frac{2000m}{cos\alpha}$ see Chapter 8.5 or [*Bobrowski* 2002] and use values displayed in Figure 7.46). This leads to an SO_2 concentration of about $2 \cdot 10^{12}$ molecules/cm^3 and with the estimated wind velocity of 5 m/s to a flux of 2.2 t/d.

Chapter 8

Discussion of the Measurement Results

8.1 BrO Emissions of Volcanoes

Within the study of this thesis, BrO was detected at five volcanic sites. The measurements and results presented in Chapter 7 will be summarized and discussed here. In 2004 two other volcanoes were investigated as well (Nyiragongo in Congo [*Galle et al.* 2005] and Sakurajima in Japan [*Lee et al.* 2005]) in respect to the emission of BrO. An estimation of the BrO emission from the volcanoes examined in this study will be compiled and an "upscaling" for a global flux estimation computed, even though high uncertainties are imminent, because the data set is small in comparison to the number of active volcanoes today (about 500).

The BrO and SO_2 SCDs in this study range from close to zero up to several 10^{14} molecules/cm^2 and several 10^{17} or 10^{18} molecules/cm^2, respectively, for the investigated volcanoes. An example of BrO and SO_2 SCDs as a function of telescope elevation during a single scan across the plume for each of the volcanoes, where BrO was detected is given in Figure 8.1 (a) Montserrat, (b) Masaya, (c) Stromboli, (d) Etna 2003, (e) Etna 2004, (f) Villarica.

The SO_2 SCD was plotted as a function of the elevation angle (α) and the FWHM ($\Delta\alpha$) was taken to calculate the plume diameter Δd by using an assumed distance (L) between the plume and the telescope, taking into account the viewing direction and the main wind direction during the time of measurements.

$$\Delta d = L \cdot tan(\Delta\alpha) \tag{8.1}$$

The results of this estimation on the plume diameter, the maximum BrO and SO_2 SCDs for all sites and the average BrO and SO_2 concentrations calculated by assuming a light path equal to the plume diameter are summarized in Table 8.1.

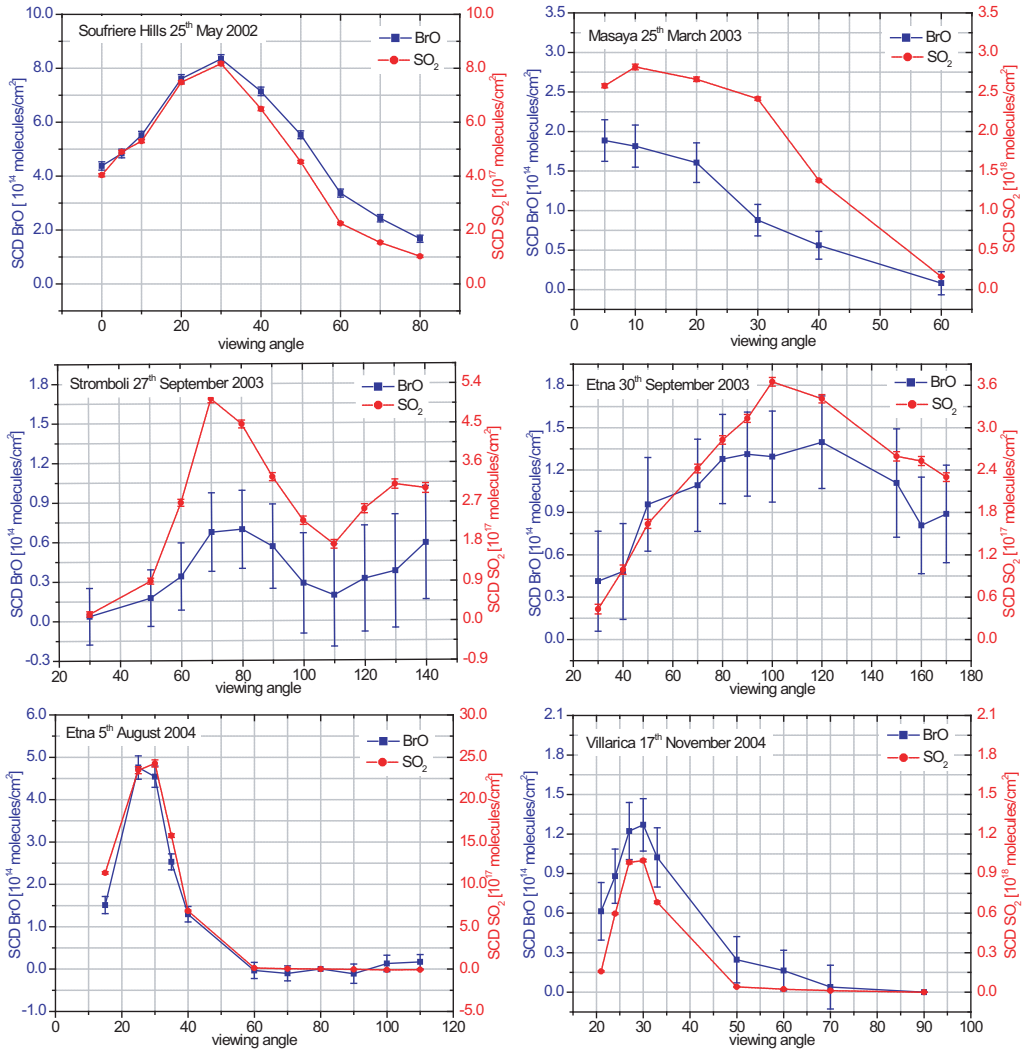

Figure 8.1: *One example of a plume scan for each volcano, the SCDs of BrO (blue) and SO_2 (red) are plotted as a function of the elevation angle of the telescope.*

SO_2 was generally closely correlated to BrO (see also Figure 8.2). The BrO/SO_2 ratios were smaller by a factor of 2.1, 4.8 and 7.7 at Etna 2003, Stromboli and Villarica, respectively compared to the observations at Soufriere Hills where $BrO/SO_2 = 1 \cdot 10^{-3}$ was found [*Bobrowski* 2002]. In 2004 the BrO/SO_2 ratio shown in the example for Etna in Figure 8.2 decreased significantly (to around $2.1 \cdot 10^{-4}$) in comparison to the measurements of 2003 ($BrO/SO_2 \approx 4.8 \cdot 10^{-4}$). The value presented for 2005 lies between the presented measurements of 2003 and 2004.

The SCDs which are shown for Etna in 2004 in Figure 8.1 and A.10 are higher than the ones analyzed from the data taken in 2003, because they were measured at a shorter distance from the source, - at Pizzi Deneri in August 2004. Therefore the plume is less

Table 8.1: *Summary of the BrO and SO_2 SCDs, estimated concentration (c) for BrO and SO_2 and plume width for the 5 volcanic sites. At Masaya the plume was not well scanned, since the start of the plume scan took place inside the crater (the plume was not at all perpendicular scanned), therefore the diameter of the plume could not be determined.*

Volcano	Date of measure-ments	Distance downwind from crater [m]	BrO SCD_{max} 10^{14} $[\frac{molec}{cm^2}]$	SO_2 SCD_{max} 10^{17} $[\frac{molec}{cm^2}]$	Plume Δ d [m]	c_{BrO} [ppb]	c_{SO_2} [ppm]
Soufriere Hills	25.05.02	4000	8.4	8.1	630	0.5	0.5
Masaya	25.03.03	600	1.9	28	-	-	-
Etna(2003)	30.09.03	7000	1.1	3.3	(4000)	0.01	0.03
Etna(2004)	05.08.04	2500	4.8	24	900	0.2	1.0
Etna(2005)	09.05.04	6000	3.4	12	520	0.3	1.0
Stromboli	27.09.04	2000	6.9	5.1	440	0.06	0.4
Villarica	17.11.04	3000	1.3	10	520	0.1	0.74

dispersed. Masaya has the smallest BrO/SO_2 ratio. However, the BrO to SO_2 ratios of all other volcanoes are in the same order of magnitude, (except the one of Masaya). At first glance, the signal to noise ratios in the results for the different measurement sites shown in Chapter 7 and the Appendix as well as in Figure 8.1 are quite different. This can have several explanations. The time resolution, for example, is highly dependent on the amount of available sunlight. In regions near the equator and during sunny days in summer there will be far more UV radiation, because the sun is almost in the zenith at noon, than in autumn or at higher latitudes, where the sky is often cloudy at this time of year. For this reason. the data from Masaya is not as good as some of the other volcanoes. Furthermore, there was no Hoya UG5 filter available for these measurements and several problems with the temperature stabilization degraded the instrument's performance during the measurements resulting in higher errors. Nevertheless BrO and SO_2 could be clearly detected. The measurements in Italy in 2003 also show higher errors compared to the measurements of Soufriere Hills, Etna 2004 and Villarica. This is caused by the poorer statistics, because just half of the measurement time (500 scans co-added) was used for one spectrum in comparison to the other measurements (1000 scans). This clearly results in higher errors for the individual measurements. Figure 8.2 shows the range of the BrO/SO_2 ratios for the different measurement sites. The cause for the variations between the measurement sites is a highly interesting topic from both, the volcanological and the atmospheric chemistry point of view.

One reason for the different BrO/SO_2 ratios could be a different magma composition at the various volcanic sites, which also makes itself visible in other species studied in volcanic emissions [*Oppenheimer et al.* 2003]. Another reason could be the variations in

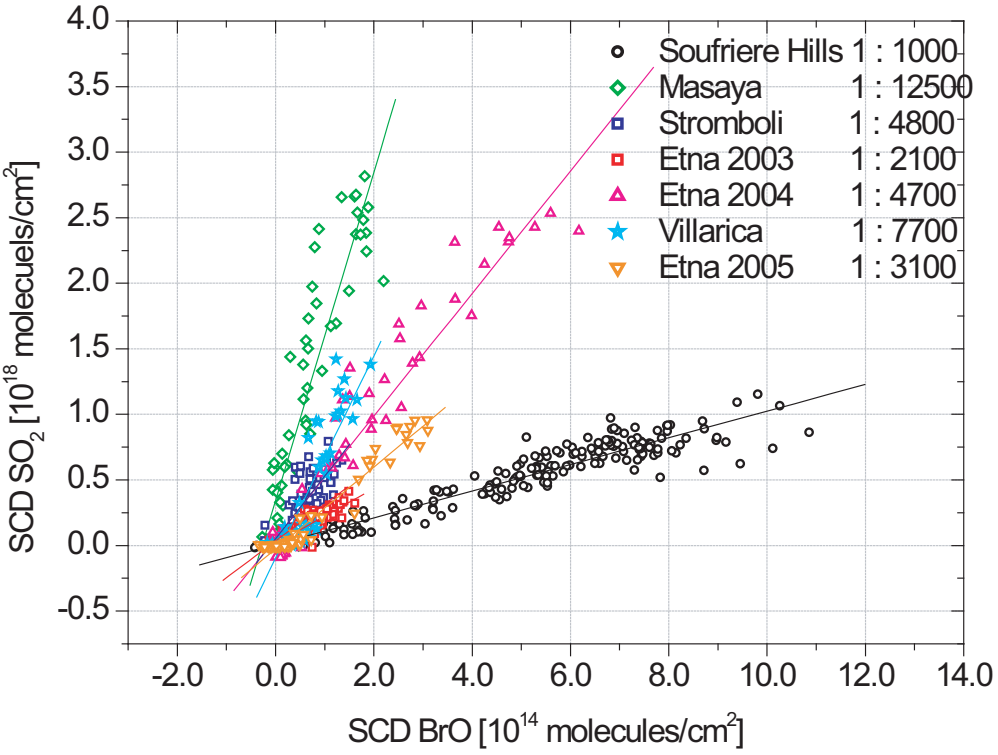

Figure 8.2: *SO_2 as a function of BrO is plotted for the 5 volcanic sites; the species are well correlated for every location, but show different correlation factors for the different sites.*

the distances of the measurement sites to the sources. If BrO is formed inside the plume and not directly emitted [*Gerlach* 2004; *Bobrowski et al.* 2005; *Oppenheimer et al.* 2005] its concentration should increase in downwind direction. BrO could form from HBr (see Chapter 3 and Chapter 8.1.2 below) and also by the mechanisms discussed in Section 1.3 from HOBr, which can liberate bromine molecules from particle surfaces. These will subsequently photolyze and then be oxidized by ozone, which is mixed into the plume from the ambient air. Also hydrogen halides (in particular HBr) can dissolve in the liquid layer of the particles, which are emitted from volcanoes as well, and then be liberated. The ratio of BrO to SO_2 at Masaya, which was measured very close to the source (so that ambient air is not yet well mixed with the volcanic plume), might not be comparable with the ratio some km downwind, where the other measurements took place. Studies regarding this point were carried out at Etna and Villarica and it could be shown that BrO cannot be detected in the first few hundred meters from the source (see Chapter 8.1.2 below). At distances of more than 2 km the BrO signal clearly exceeds the detection limit above the error range (see next section 8.1.2 and [*Bobrowski et al.* 2005]).

A third point could also be the state of volcanic activity. As already mentioned in the

introduction, there are strong hints that the sulphur-halogen ratios change with the level of activity [*Aiuppa and Frederico* 2004; *Aiuppa et al.* 2005], which can be explained for instance by the different solubility of the compounds.
A further point could be, even though it may only play a minor role, that the radiative transfer is somewhat different for the different spectral ranges where SO_2 and BrO are evaluated. The examination of volcanic BrO regarding its global significance by satellites is also very interesting - a first attempt on this issue was performed by *Afe et al.* [2004] who found the ratio of BrO/SO_2 on average a factor of at least 5 to 20 smaller than the one measured by our ground based study at Soufriere Hills. These values are inside the variation for the ground-based measurements from the different sites. For the data on Mt. Etna published by *Afe et al.* [2004] one derives a BrO/SO_2 ratio of $3 \cdot 10^{-4}$ by dividing the maximum SCDs of BrO and SO_2 detected by SCIAMACHY on the 31^{st} of October 2002. This value lies between the measurements of 2003, 2004 and 2005. Difficulties for satellite measurements arise due the low spatial resolution of 320 x 40 km (east-west x north-south) of a GOME pixel or 60 x 30 km for a single SCIAMACHY pixel. If one assumes that a volcano is situated in the center of a GOME pixel with the wind blowing the plume along the long side of this pixel, a volcanic plume of 160 km length and an assumed diameter of 0.5 km would fill 1/160 of the GOME pixel. Taking an upper value of the ground based SO_2 SCD of 2 x 10^{18} molecules/cm^2 for the avarage concentration of the plume and an SCD BrO/SCD SO_2/ ratio of $3 \cdot 10^{-4}$ would result in a SCD BrO value of $< 5 \cdot 10^{12}$ molecules/cm^2 which is an order of magnitude below the detection limit ($5 \cdot 10^{13}$ molecules/cm^2) given by *Afe et al.* [2004]. Note that this consideration is independent of plume dispersion as long as the number of BrO molecules per unit length of the plume stays constant. In addition to this fact, the data presented by *Afe et al.* [2004] unfortunately contains only two volcanic sites for possible direct comparison (Soufriere Hills and Etna) and only considers eruption events, when SO_2 concentrations lie well above their average value. None of the data presented in this study of ground-based measurements was recorded during major eruptions. An enhancement of SO_2 also does not automatically mean that BrO will be enhanced (e.g. [*Aiuppa and Frederico* 2004]).
Aiuppa and Frederico [2004] investigated the changes in the ratio of HCl to SO_2 during the Stromboli eruption. While this was only a case study on chlorine, chlorine and bromine could react quite similarly in volcanic processes as pointed out by *Villemant and Boudon* [1999] and *Bureau et al.* [2000]. Therefore BrO may not increase during an eruption, which would implicate an decreasing ratio of BrO to SO_2. The fact that the Cl/S ratio was found to decrease by a factor of 10 during the eruption of Stromboli in 2003 seems to support this theory. The most detailed satellite study to date [*Afe et al.* 2004] dealt with Nyamuragira, a Rift volcano, whose feeding system differs greatly from that of subduction zone volcanoes, which are the most common volcanoes on Earth and were under investigation in this study. Ground based measurements showed a BrO/SO_2 ratio of about $6 \cdot 10^{-5}$ at Nya-

muragira [*Galle et al.* 2005], which would make the detection of bromine monoxide by the present day satellites difficult. In summary it can be said, that the satellite observations of volcanic BrO and SO_2 are not in contradiction to the results of this work.
The first reactive halogen measurements in volcanic plumes were made during the Montserrat measurement campaign in May 2002 and resulted in unexpectedly high mixing ratios of about 1 ppb of BrO. Also at Masaya, Mt. Etna, Stromboli and Villarica, BrO could be detected and the ratio BrO/SO_2 was of the same order of magnitude as on Soufriere Hills for all, except for Masaya. This shows that Soufriere Hills on Montserrat is not an exceptional volcano regarding its bromine emission, although its BrO/SO_2 ratio currently appears to be somewhat higher than that of the other volcanoes studied in this thesis, but at Sakurajima an even higher BrO/SO_2 ratio of $1.0 \cdot 10^{-3}$ was observed.
Therefore it can be concluded that volcanic sources of reactive bromine could have dramatic effects on the earth's atmosphere. Table 8.2 summarizes the measured BrO/SO_2 ratios, the SO_2 fluxes and the resulting BrO fluxes. The sum of the BrO fluxes from these seven volcanoes is already 1.2 kt/yr. If we use the global SO_2 emission of 14,000 kt/yr

Table 8.2: *SO_2 fluxes cited from the literature and summary of the so far known BrO/SO_2 ratios for 7 volcanic sites. The BrO fluxes were calculated by using the refereed SO_2 flux and the measured BrO/SO_2 ratio.*

Volcano	SO_2 flux [t/yr]	SO_2 flux reference	BrO/SO_2 $[10^{-4}]$	BrO flux [t/yr]
Soufriere Hills	$3.7 \cdot 10^5$	*Bobrowski et al.* [2003]	8.3	460
Masaya	$3.5 \cdot 10^5$	*Wardell et al.* [2004]	0.8	42
Etna(2003)	$3.4 \cdot 10^5$	*McGonigle et al.* [2003]	4.8	240
Stromboli	$1.0 \cdot 10^5$	*McGonigle et al.* [2003]	2.1	31
Villarica	$9.5 \cdot 10^4$	*Witter et al.* [2001]	1.3	19
Nyiragongo	$2.4 \cdot 10^6$	*Galle et al.* [2005]	0.6	215
Sakurajima	$1.4 \cdot 10^5$	*Lee et al.* [2005]	10	210

as suggested by *Andres and Kasgnoc* [1998], these seven volcanoes would already account for about 30 % of the worldwide volcanic SO_2 emissions. By further assuming that our volcanic set would be representative for the bromine monoxide emissions, one could scale the flux to about 3.6 Gg/yr globally (3 Gg reactive Br/yr). This would be on the lower end of the global estimation by *Bobrowski et al.* [2003]. However uncertainties remain quite high.
Another method for reaching a global estimate would be to divide the volcanoes in characteristic groups, for example recording the different style of activity similar to the work of *Pyle and Mather* [2003], who calculated a global volcanic mercury flux. The classification in four volcanic categories can be found in Table 8.3. The BrO fluxes were calculated by using the refereed SO_2 flux and the measured BrO/SO_2 ratio. The above estimated BrO

Table 8.3: *Time averaged SO_2 emission from volcanoes divided in different styles of volcanic activity. Adapted by Pyle and Mather [2003] and references therein. The BrO fluxes were calculated by using the refereed SO_2 flux and the measured BrO/SO_2 ratio.*

	Time-averaged SO_2 [Tg/yr]	volcanoes of this thesis	BrO/SO_2 $[10^{-4}\ \frac{mol}{mol}]$	BrO flux [Gg/yr]
Continuous emission from 'passively degassing' volcanoes	6 - 9	Soufriere Hills, Villarica, Etna, Masaya	0.8 - 8.0	0.7 - 10.8
Sporadic emission from non-explosive eruptions (1-2 eruptions/yr)	2	Nyiragongo	0.6	0.2
Sporadic emission from smaller explosive eruptions ($< 10^{13}$ kg tephra) (20-30 eruptions/yr)	6 - 8	Stromboli, Sakurajima	2.1 - 10.0	0.3 - 3
Sporadic emission from larger explosive eruptions ($> 10^{13}$ kg tephra) (1-2 eruptions/century)		-	-	
Total time-averaged annual emission from degassing and erupting volcanoes	15 - 21			1.2 - 14

flux (3.6 Gg/yr) lies with in the limits of this second global estimate of 1.2 -14 Gg/yr (11.7 Gg/yr reactive bromine).
In these estimations we neglected that HBr is probably the main volcanic species, that the BrO/SO_2 ratios were not always measured at a distance were the BrO formation process (see next section) was terminated, and that beside HBr and BrO probably other bromine species are also abundant in the volcanic plume.
A global bromine flux estimated by HBr emission measurements near the summit by *Aiuppa et al.* [2005] was calculated to 13 Gg/yr. This is close to the upper value of the estimated BrO (11.7 Gg/yr reactive bromine) flux. Assuming that no BrO is emitted directly from the volcano (see next section 8.2), that would mean that a high amount of the emitted HBr reacts to BrO.

8.2 BrO Formation in the Volcanic Plume

Villarica and Etna are two case studies carried out within the scope of this thesis to investigate the chemical behavior of bromine monoxide alongside the plume. Section 8.1 deals with the detection of bromine monoxide at five different volcanic sites and gives a

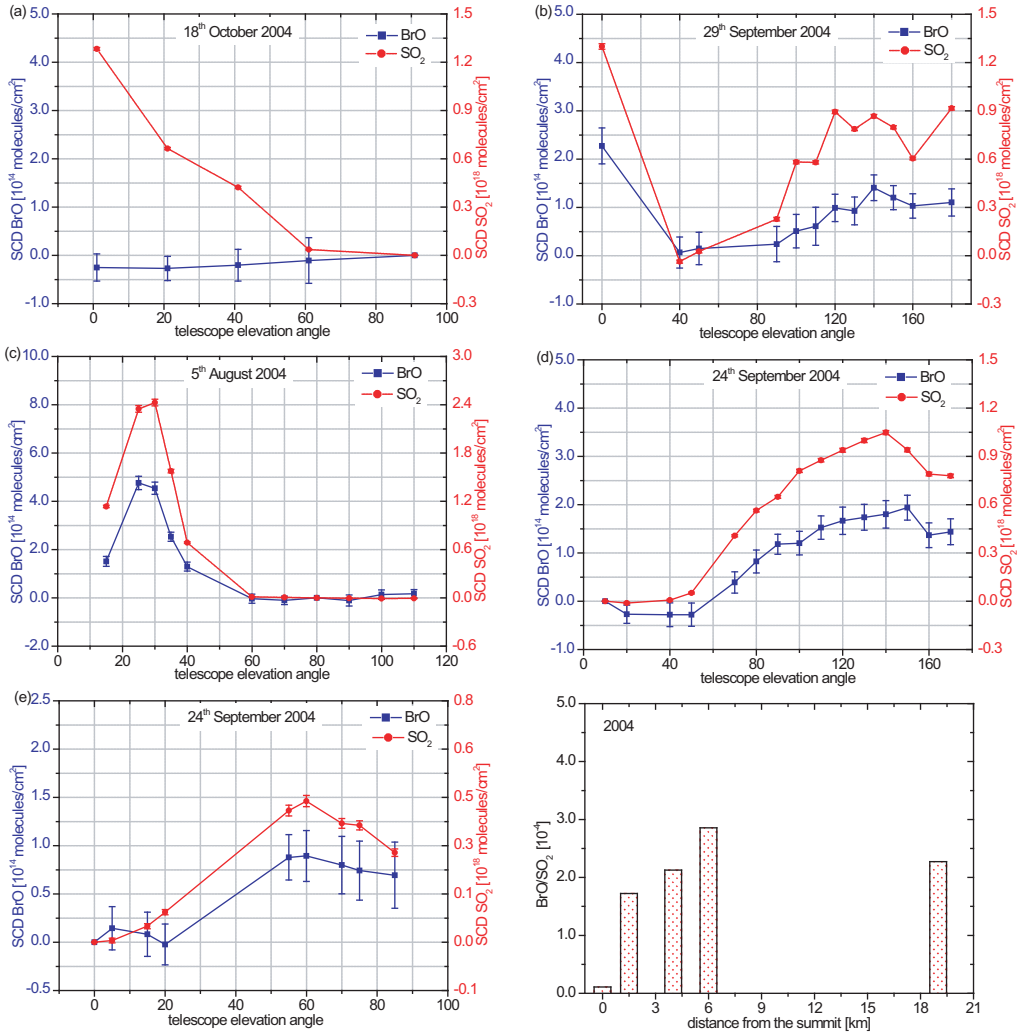

Figure 8.3: *One example of a plume scan for every distance measured at Etna in 2004. The SCDs of BrO (blue) and SO_2 (red) are plotted as a function of the elevation angle of the telescope. For details see text.*

first explanation for the different BrO/SO_2 ratios.

One cause could be the variation in the distance of the measurement location from the source. This will be discussed in detail in this section.

Momotombo and Poas are two volcanic sites, which were also studied in course of this thesis and which are not known as poor of halogens. Nevertheless, BrO could not be detected at either site. One reason could be the location of the instrument, which was limited to positions inside the craters of these volcanoes. As shown in Figures 8.3 and 8.4, both at Etna and Villarica, no BrO could be detected at the summits. Therefore it is suggested, that BrO is not directly emitted from volcanoes. Figure 8.3 shows measurements of the

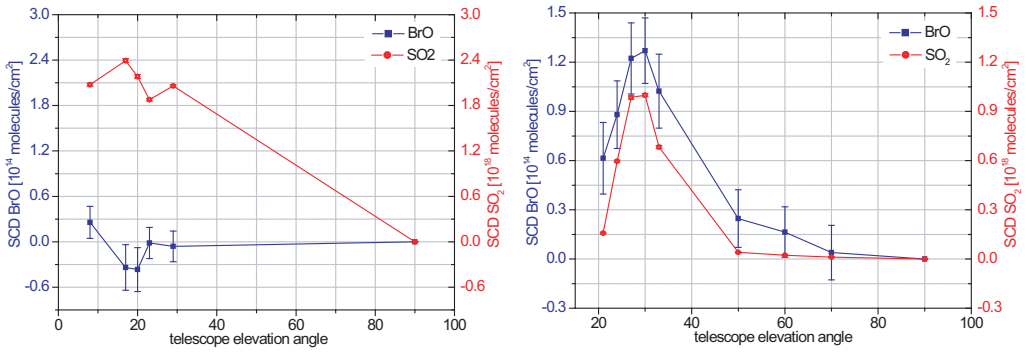

Figure 8.4: *One example of a plume scan for of Villarica plume at the summit and 3 km further downwind, respectively. The SCDs of BrO (blue) and SO_2 (red) are plotted over the elevation angle of the telescope.*

Etna campaigns of August 2004 and September/October 2004.
In Figure 8.3 (a) the results of spectra taken directly beside the Voragine crater show no BrO signal. At a distance of 1.5 km (Figure 8.3 (b)), which represents a plume age of around 300 s, assuming a wind velocity of 5m/s, the abundance of BrO in the plume

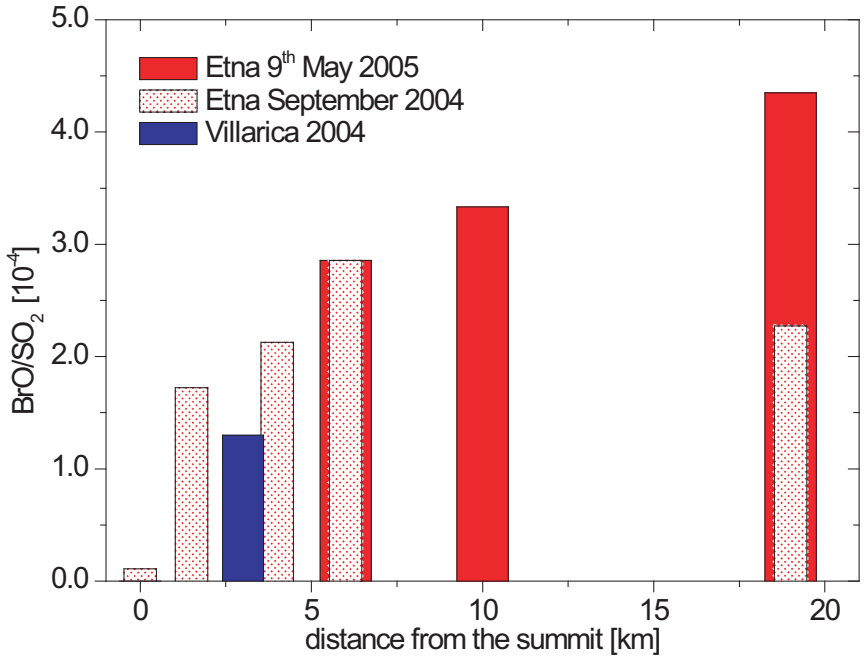

Figure 8.5: *The BrO/SO_2 ratios for the different measurements at distances up to 19 km from the summit in 2004 (red pointed columns) and May 9^{th} 2005 (red columns) for Mt. Etna. Mt. Villarica is displayed in blue.*

can already be clearly detected. Due to the dispersion of the plume, the SCDs decrease significantly after a certain distance which leads to higher relative errors further downwind for BrO as well as for SO_2 (Figure 8.3 (e)).
During the field campaigns in August 2004 and September/October 2004, the data for different distances could not be collected simultaneously on one day, due to the limited number of instruments. It could be argued, that the ratio changed with time and not with distance, especially because Etna was not in a stable activity phase during the measurement period, which additionally took place over a long time. However, there are several

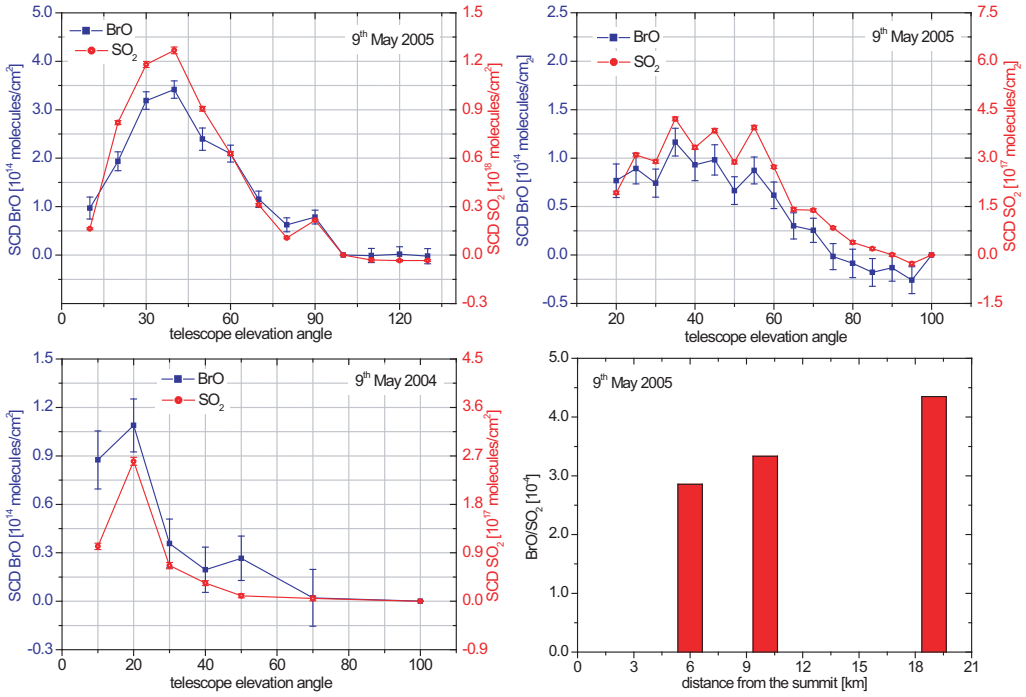

Figure 8.6: *One example of a plume scan for every distance simultaneously measured at the eastern flank of Mt. Etna May 9th 2005. The SCDs of BrO (blue) and SO_2 (red) are plotted as a function of the elevation angle of the telescope.*

arguments that rebut this hypothesis.
Figure 8.5 (a) illustrates the increasing BrO/SO_2 ratio as a function of distance from the summit. Every column, except the first and the last, represents an average value for at least three measurement days on the specific locations. Unfortunately only very little data could be collected for the point nearest to the source and the point 19 km away. Nevertheless this figure shows a clear trend.
On the other hand, the same kind of experiment was repeated in May 2005. This time, three instruments were available and therefore simultaneous measurements at three different distances could be carried out. The result is qualitatively the same, as can be seen

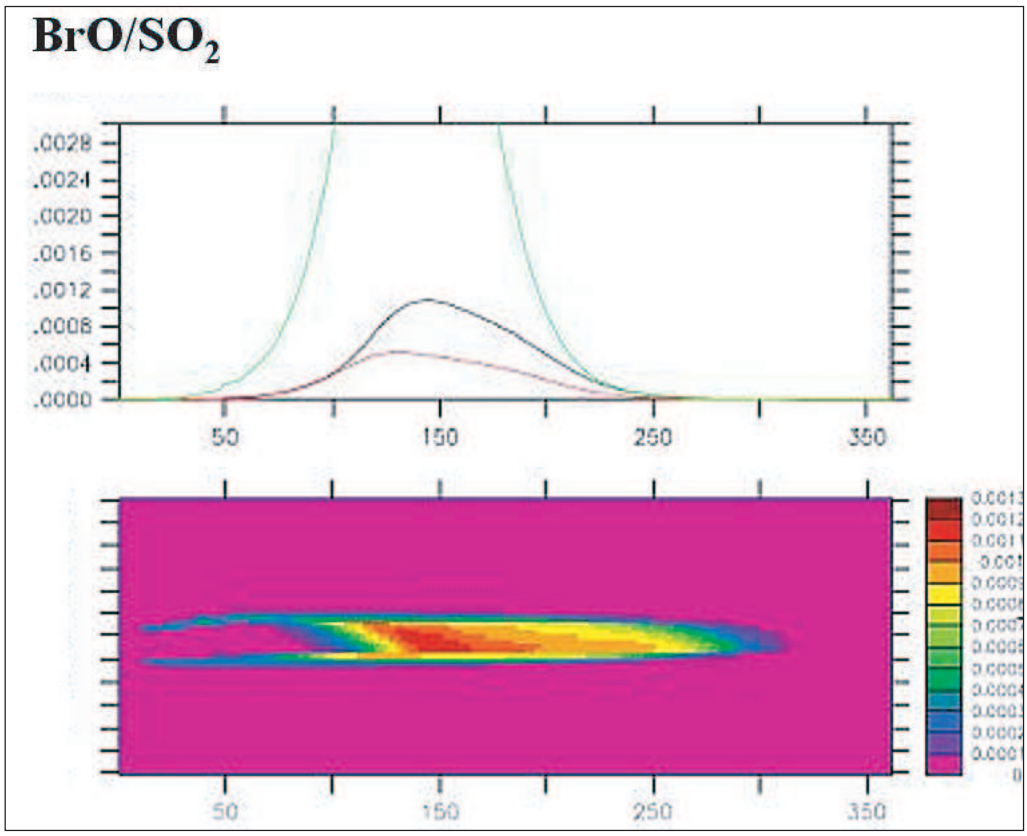

Figure 8.7: *First model studies on the BrO formation processes inside volcanic plumes. The ratio of BrO/SO_2 is displayed as a function of plume age. The highest values are displayed in red, the lowest one in purple. Courtesy to R. Von Glasow.*

in Figure 8.5 (b), where measurements from the 9^{th} of May 2005 are presented. Figure 8.6 presents one single plume scan, exemplary for each of the three distances used on the May 9^{th} 2005.

Likewise, the studies of *Oppenheimer et al.* [2005] are not negligible. They studied the changes of the BrO content at Mt. Etna in the region near the summit and came to the same result.

Fourth a second volcano, Villarica in Chile, was examined under the same aspect. This study led to the same results as shown in Figure 8.4.

Assuming that the SO_2 content does not change in the first km of a volcanic plume (e.g. *McGonigle et al.* [2004]) it can be concluded that BrO must be formed alongside the plume.

Also, first model studies carried out by Von Glasow [personal communication] show a similar result. The BrO/SO_2 ratio increases with increasing plume age (larger distance from the summit) and reaches values in the same order of magnitude as measured. One difference is that the timescale of the BrO formation in the model is significantly slower

than the measured increase of BrO. This might be caused by an insufficient understanding of the chemistry and by too large uncertainties of the input parameters.

8.3 BrO/SO_2 - Volcanic Activity Dependence

Besides their very important influence on atmospheric composition, volcanic gases can also provide valuable information for the understanding of volcanic processes. Recently it has been shown that ratios between halogens and sulphur in volcanic plumes might serve as an indicator of changes in volcanic activity [*Aiuppa and Frederico* 2004; *Oppenheimer et al.* 2003], which, in turn, has implications for the prediction of volcanic activity.
During the measurements of this thesis, a small eruption of Mt. Etna occured. As already described in Chapter 7, unfortunately no data was recorded directly prior to the eruption, and the influence of distances from the summit on the BrO/SO_2 ratio was only discovered a short time afterwards. Therefore no care was taken when choosing the location regarding the distance (plume age) of the measurement sites for the first measurements of the September/October 2004 campaign. Because the data was collected unaware of the influence of the distance, the interpretation of the small data set is very difficult. Nevertheless it was a first study on the BrO/SO_2 ratio behavior during an activity change of a volcano. This makes it a very interesting and valuable data set, although it can only give small hints for further studies.

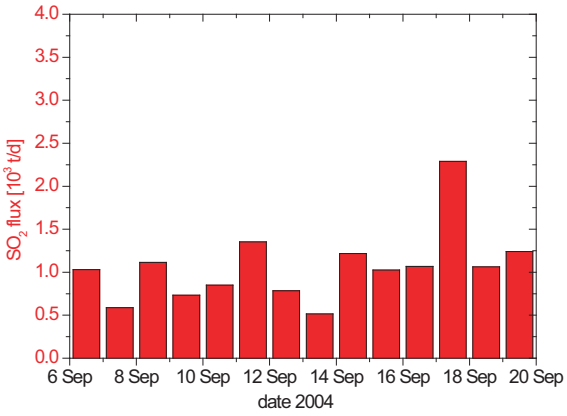

Figure 8.8: *SO_2 flux measurements in September 2004, carried out by mini-DOAS traverses. Courtesy to B. Galle.*

As already mentioned in Chapter 7 the Etna eruption 2004/2005 was a very quite one with no seismic activity in advance. The SO_2 flux during the first days of September did not show significant increases above the normal noise level (see Figure 8.8). Beside the Mini-MAX-DOAS measurements, Filter-pack measurements by *Aiuppa et al.* [2005] were also undertaken before, during and after this interesting period and fortunately before the eruption (in August 2004), even in a higher time resolution than usual (two times a month). This data set, which also shows the halogen to sulphur ratios, is presented in Figure 8.9. A clear drop in the sulphur to bromine as well as in the sulphur to chlorine, sulphur to fluorine and sulphur to iodine ratios can be seen just before the eruption.

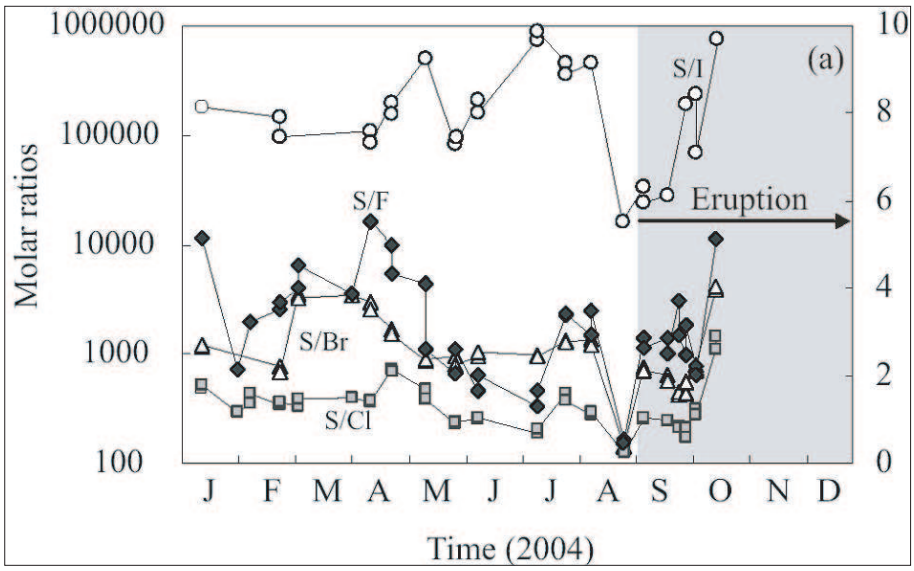

Figure 8.9: *Variations in sulphur to halogen molar ratios in Etnas North-East crater plume between January and October 2004. The primary y-axis corresponds to the S/I and S/Br ratios, the secondary y-axis, to the S/Cl and S/F ratios. The gray shaded area indicates an eruption, which commenced on September 7, consisting of persistent lava effusion from a fracture on Etnas eastern flank.*

Unfortunately, no Filter-pack data was taken on the 9^{th} or 10^{th} of September. Nevertheless, it seems that the same pattern, the initial decrease of the S/Br ratio, can also be observed in the DOAS measurements, where the BrO/SO_2 ratio increase (which is equivalent to a decrease in SO_2/BrO ratio) within the first two days when the lava flow started to pull out.
That this increase has a steeper slope than given by the distance dependency of the BrO/SO_2 ratio, is shown in Figure 8.10. On the left side the BrO/SO_2 ratio is presented as a function of time, on the right side of (Figure 8.10) as a function of distance. The values of the BrO/SO_2 ratio in the beginning of September 2004 are significantly enhanced, even if one takes into account that the data was taken at different distances, the change in the results of these two days is exceptionally high.
The strong variability of BrO observed in these measurements suggests that its emission from the volcano is variable, which may suggest that its variations could be related to interesting volcanic phenomena and should be studied in detail in the future.

Most of the measurements for this study were carried out at Rifugio Citelli, which is about 6 km from the summit on the eastern flank of Mt. Etna. The main wind direction at Mt. Etna are westerly winds and therefore a plume overpass in this direction is highly probable. This means Rifugio Citelli is an ideal place to allow a higher frequency of

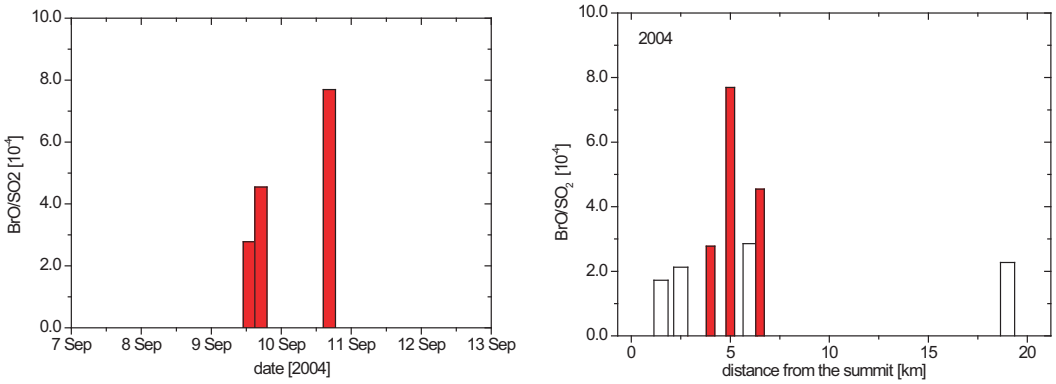

Figure 8.10: *BrO/SO_2 ratios on the left panel as a function of time on the right panel as a function of distance. Red columns are measured during the start of Mt. Etna's eruption 2004, white columns the averaged results of BrO/SO_2 ratios for various distances in autumn 2004. The BrO/SO_2 values are significantly enhanced.*

measurements, which gives a good possibility to investigate temporal variations. The BrO/SO_2 ratio seems to be quite stable during mid October and slightly higher in average than the one measured on three days in the second part of September. The results of the measurements in May are more scattered than the ones from the field campaign during September-October 2004. Their average value exceeds the one from 2004. An explanation could be found in the meteorological influence of different wind directions and therefore in the scanning of different parts of the volcanic plume (different crater plumes) which

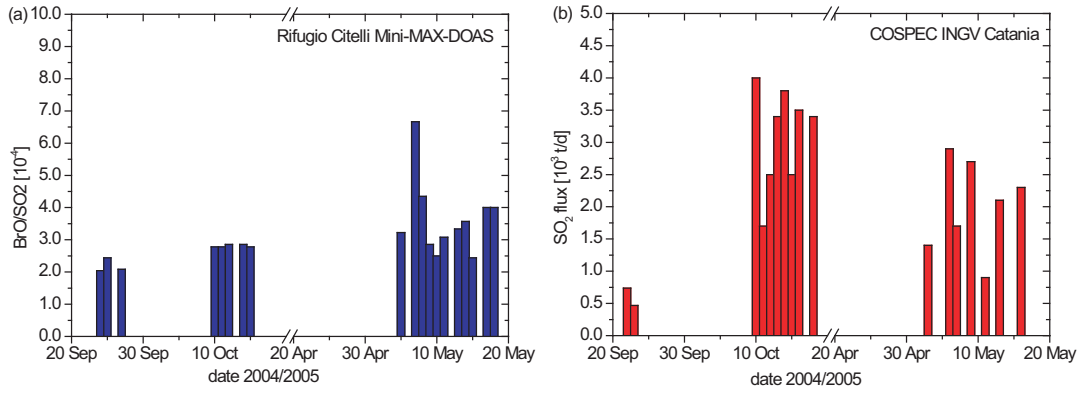

Figure 8.11: *The calculated BrO/SO_2 ratio for all measurements carried out at Rifugio Citelli, situated about 6 km downwind on the eastern flank of Mt. Etna. Temporal variation are visible on short and 'longer' timescale. A general trend show an increase in the BrO/SO_2 value which can be explained by the different main crater activities (see text).*

might not be fully mixed even in distance of 6 km downwind, or in a change in the different activity of the different vents. As shown in *Aiuppa et al.* [2005] the NE crater is richer in halogen compounds than for instance Voragine.
The main plume during May 2005 could be determined to be mainly from the NE crater, whereas Etna's main plume in autumn 2004 could have been influenced more by additional emission from the SE crater and emission by the Central crater (Bocca Nova and Voragine).
The regular SO_2 flux measurements carried out by INGV Catania show slightly higher values in autumn 2004 than in spring 2005. This supports the interpretation of a relation of the BrO/SO_2 ratio to volcanic activity changes, even if the ratio could be influenced by meteorological parameters as well.

These measurements give an indication for possible future applications to support investigation of the activity changes and the volcanic feeding system by DOAS measurements, which is of high interest from the volcanological point of view and should be an aim of future research.

8.4 Halogen Chemistry in Volcanic Plumes

The common picture of halogen species in the atmosphere is that inorganic halogen species (X, X_2, XY, XO, HOX, $XONO_2$, HX, where X, Y = Cl, Br, I) are produced in the lower atmosphere either by degradation of organic halogen compounds or by oxidation of halogenides (X^-) e.g. from sea salt (see Chapter 3). This section will concentrate on the possible application of the known chemistry of these environments to a third possibly very important source of halogens: volcanic emissions. In comparison to the average atmospheric environment there are very unique environmental conditions to be found in volcanic plumes.
A huge amount of particles is available - solid, fluid and also in gaseous form. These particles provide a larger surface area for chemical reactions than normally found in the atmosphere. Besides other gases, a high amount of acids such as HCl, H_2SO_4 and HNO_3 is typically emitted. Therefore a very low pH-value is often observed in the vicinity of volcanic emissions.
Since water vapor is one of the main constituents of gaseous volcanic emissions, the humidity can be assumed to be high and the temperature in the initial plume will probably be at least a few degrees higher than the ambient air.
The emission of halogens, including bromine, from volcanoes was already shown by several studies with different techniques (e.g. [*Sugiura and Y. Mizutani* 1963; *Schwandner et al.* 2004; *Aiuppa and Frederico* 2004], but were mostly carried out by gas condensate samples. The global data set of bromine emission from volcanoes is still very limited and

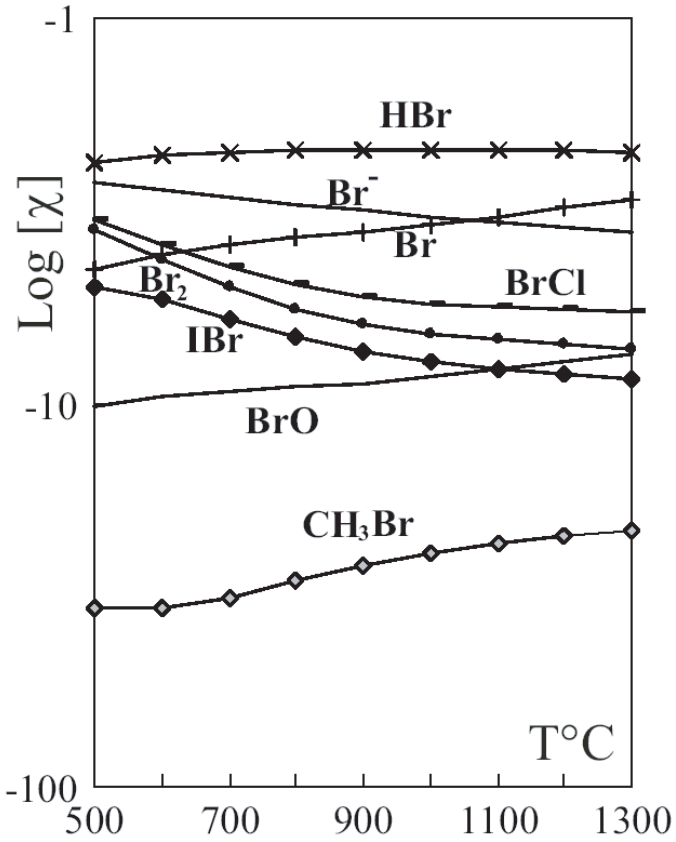

Figure 8.12: *Equilibrium mixing ratios (as mole fraction in %) of bromine species versus temperature, for p = 1 bar. The data was determined by solving a set of mass balance and mass action relations, using a Gibbs free energy minimization algorithm, with HSC software (v. 2.1). The mass balance equations were parameterized using the H-O-C-S-Cl-I-Br composition of Etnas magmatic gases, derived from the H2O-CO2-SO2 data of Allard et al. [1991], and S/Cl, S/Br and S/I ratios from Aiuppa et al. [2005]. Figure adapted by Aiuppa et al. [2005].*

the question as to which bromine compounds are directly emitted and which formed in subsequent reactions is not yet solved.

Recently, first studies regarding this topic were carried out with thermodynamical equilibrium models [*Gerlach* 2004; *Aiuppa et al.* 2005; *Oppenheimer et al.* 2005]. It can be assumed that the largest fraction of bromine is emitted in the form of HBr. In Figure 8.12 model results of *Aiuppa et al.* [2005] are presented, which were carried out with a thermodynamical equilibrium model which was specially parameterized with the conditions at Mt. Etna, where most investigations in this thesis were carried out. The mixing ratios of the different bromine species are plotted as a function of temperature. For all temperatures HBr is the main species, as already observed by *Gerlach* [2004].

In *Oppenheimer et al.* [2005] the thermodynamic partitioning of HBr into the gaseous and the aerosol phase as a function of relative humidity was studied for the case with and without the abundance of HCl, because the abundance of HCl and the amount of relative humidity are the critical factors for the HBr partitioning into the gas and aerosol phase (condensed phase). If HCl is present, the partitioning of HBr into the gas and the aerosol phase is more discrete and about 50 % for each phase at 40 % relative humidity.

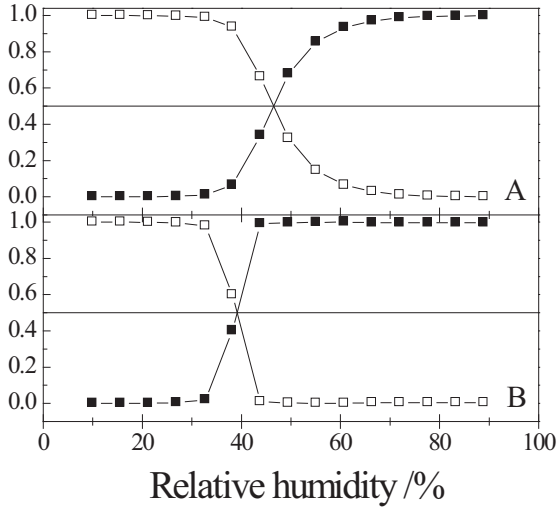

Figure 8.13: *Partitioning of 30 nmol/mol HBr (=1.339 · 10^{-4} mol m^{-3}) at 283 K between the aqueous (open squares) and gas phases (solid squares) as a function of relative humidity for A: 1 mg m^{-3} (1.04 · 10^{-5} mol m^{-3}) H_2SO_4; B: 1 mg m^{-3} H_2SO_4 + 10 mmol/mol (= 4.44 · 10^{-2} mol m^{-3}) HCl.*

In the following we will take these assumptions, which have been made and motivated above, for the suggestion of possible formation of BrO in a volcanic plume.
During daytime O_3 is photolyzed:

$$O_3 + h\nu \longrightarrow O_2 + O1D \tag{8.2}$$

The formation of excited oxygen atoms leads to the formation of OH radicals. Under typical ambient conditions (20°C, 50 % relative humidity) roughly 10 % of the oxygen atoms in the 1D state react with H_2O, while the majority is quenched to the 3P ground state:

$$O1D + H_2O \longrightarrow OH + OH \tag{8.3}$$

The fraction reacting with water vapor in a plume can probably reach much more than 10 %, because amount of H_2O in the initial plume is very high (see above).

Besides 8.3, the production of OH could also be a possible without air mixing from outside the plume by taking into account that CH_4 is emitted by volcanoes as well as Cl, which could lead to the following reaction:

$$CH_4 + Cl \longrightarrow CH_3 + HCl \tag{8.4}$$
$$CH_3 + O_2 \longrightarrow CH_2O + OH \tag{8.5}$$

This cycle might also produce a sufficient amount of OH and excited oxygen atoms which can react with the halogens to build XO. The reaction of CH_3 with O_2 can lead also to HO_2, which could finally result in a production of OH as well:

$$CH_3 + O_2 \longrightarrow CH_3O_2 \tag{8.6}$$
$$CH_3O_2 + O_2 \longrightarrow CH_2O + HO_2 \tag{8.7}$$
$$CH_2O + h\nu \longrightarrow CO + H_2 \tag{8.8}$$
$$\longrightarrow H + CHO \tag{8.9}$$
$$HO_2 + NO \longrightarrow OH \tag{8.10}$$

Hydroxyl radicals can undergo many reactions. Another important one in volcanic plumes can be SO_2-oxidation:

$$SO_2 + OH + M \longrightarrow HSO_3 + M \tag{8.11}$$
$$HSO_3 + O_2 \longrightarrow HO_2 + SO_3 \tag{8.12}$$

which leads to the formation of HO_2 radicals.

As described above, HBr seems to be the main emitted bromine species. HBr is thermodynamically stable in magma as well as in the atmosphere and will be either oxidized by OH in the gas phase or partitioned into the condensed phase (aerosol). Both reactions are possible in volcanic plumes (see above)

$$HBr + OH \longrightarrow Br + H_2O \tag{8.13}$$
$$Br + O_3 \longrightarrow BrO + O_2 \tag{8.14}$$
$$BrO + HO_2 \longrightarrow HOBr + O_2 \tag{8.15}$$

The reaction 8.13 is very slow, but may nevertheless be relevant to start the formation of BrO. The partition of HBr into the condensed phase forms Br^- ions. Together with Cl^- ions they are oxidized to BrCl or Br_2 by HOBr. Br_2 and BrCl molecules will be released

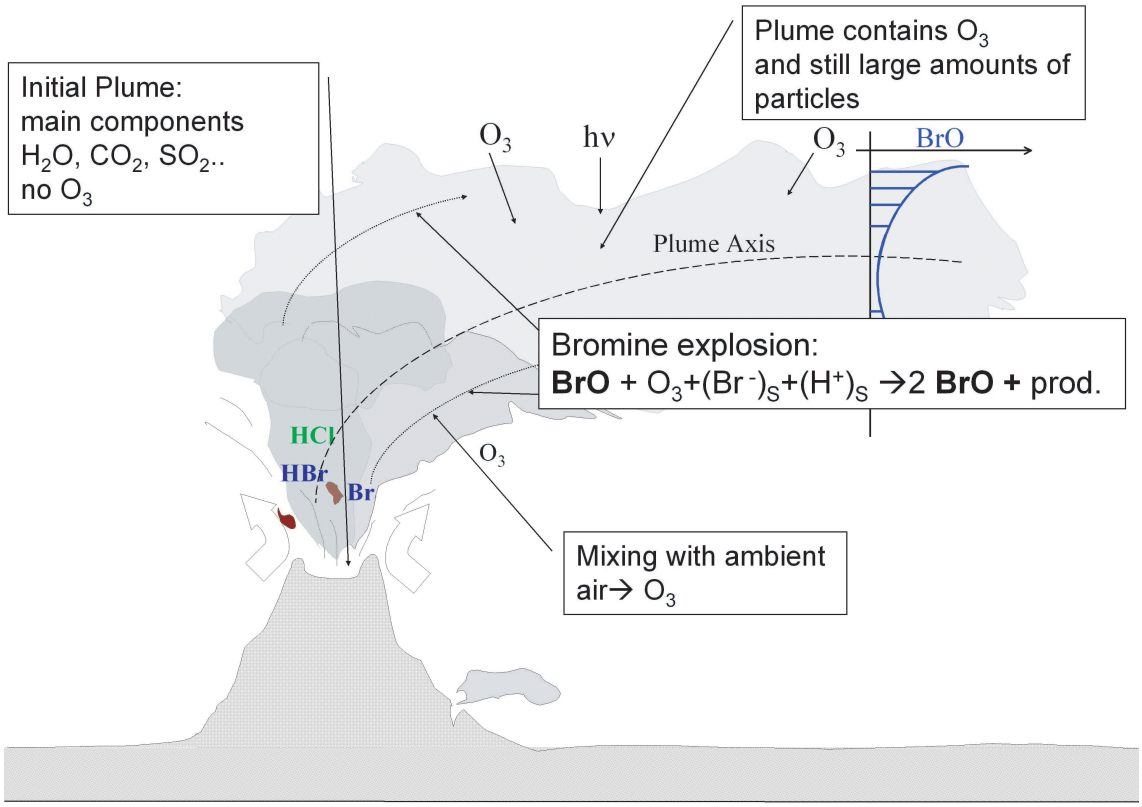

Figure 8.14: *Sketch of processes in a volcanic plume: after emission the plume mixes with ambient air, thus ozone becomes available and radical chemistry starts (see text). As a consequence the initial hydrogen halides are heterogeneously converted to halogen oxides.*

back into the gas phase and are photolyzed to Br atoms (in an order of minutes)

$$HOBr + (Br^-)Surface + H+ \longrightarrow Br_2 + H_2O \tag{8.16}$$

$$Br_2 + h\nu \longrightarrow 2Br \tag{8.17}$$

$$HOBr + (Cl^-)Surface + H+ \longrightarrow BrCl + H_2O \tag{8.18}$$

$$BrCl + h\nu \longrightarrow Br + Cl \tag{8.19}$$

This process produces two halogen radicals from a single bromine atom. A chain reaction starts, which accelerates with time (Bromine Explosion, see Chapter 3). As long as O_3 is available it is most likely that Br and Cl react rapidly with O_3 (reaction 3.18)
Typical conversion time constants ($O_3 \sim 30$ ppb) via 8.17 for e.g. X = Br are around 1 s. Bromine atoms are regenerated by photolysis of BrO, which, however, is offset by Reaction 8.17:

$$BrO + h\nu \longrightarrow Br + O \tag{8.20}$$

thus leading to a photo-stationary state between Br and BrO with BrO/Br of the order of 100. In summary reaction 8.16 followed by photolysis of Br_2, 8.14 and 8.15 leads to a cycle with the net result:

$$BrO + O_3 + (Br^-)Surface + (H^+)Surface \longrightarrow 2BrO + products \tag{8.21}$$

Effectively one BrO molecule is converted into two, at the expense of bromide in the particles, by oxidizing bromide at particle surfaces (for the conditions see *Oppenheimer et al.* [2005]). This process leads to an exponential growth of the gas-phase BrO concentration in the atmosphere (as long as there is ozone available), which led to the term 'Bromine Explosion' [Platt and Lehrer 1997, Wennberg 1999]. In addition Cl atoms (and ClO) could be produced via 8.18 followed by the photolysis of BrCl and the reaction with ozone.
The suggested chemistry is sketched in Figure 8.14. The processes in the plume could occur in the following steps:

- Emission of the warm initial plume containing large amounts of CO_2 and water vapor as well as gaseous hydrogen halides (HCl and HBr) and particles.
- Upon mixing with ambient air the plume cools, water condenses on particles, ozone enters the plume starting radical chemistry as described above. Also hydrogen halides (in particular HBr) dissolve in the liquid layer of the particles.
- Once OH and HO_2 radicals are available, there are good conditions (large specific surface area, acidity, humidity) for autocatalytic release of reactive halogen species (BrO, ClO) from the halides.

Further investigation by laboratory and field measurements are necessary as well as model studies to prove the suggested chemical processes.

8.5 Photon Path Length Inside Volcanic Plumes

The trace gas fluxes in this thesis were mainly scaled to SO_2 fluxes of COSPEC measurements carried out in parallel or were calculated very roughly by using geometrical considerations. The later one is a commonly applied method today, but can result in high errors, which will be illustrated for one example. In this section, a description of the problematic, today's understanding and first studies of light paths in volcanic plumes will be discussed. It will be shown that even the direction of the error cannot simply be

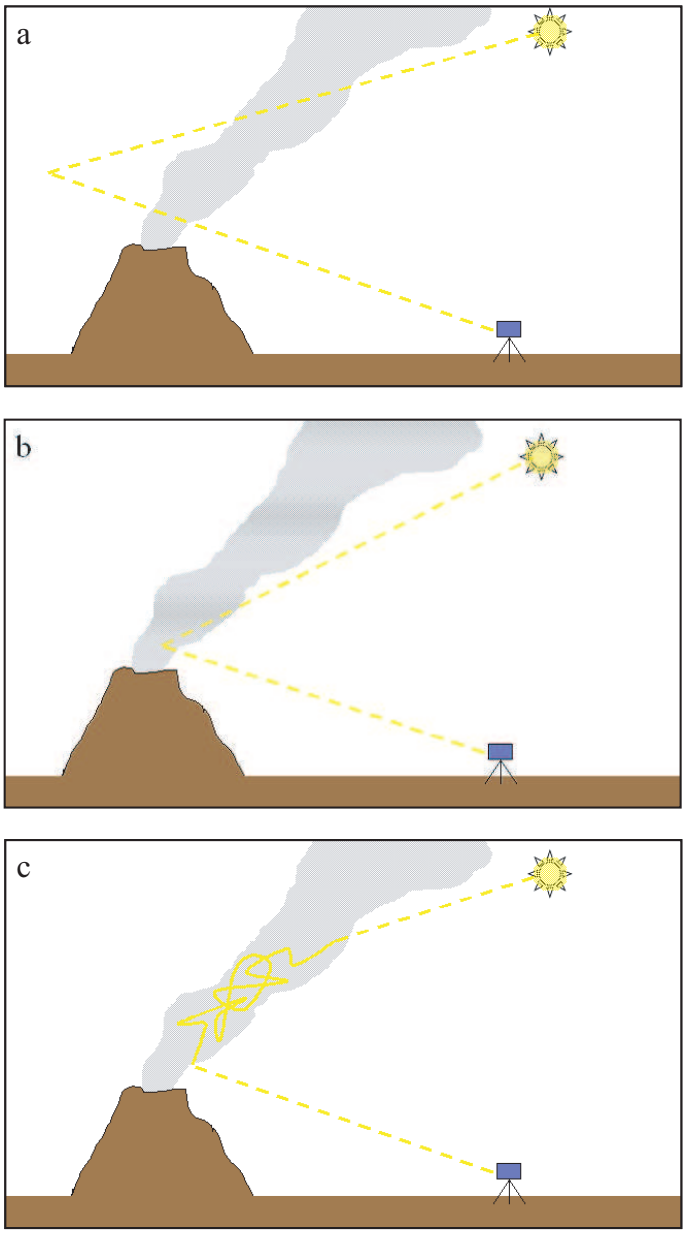

Figure 8.15: *The three figures show different possible scenarios for a light path during volcanic plume measurements.*
(a) The light is not influenced by the volcanic plume, single scattering takes place.
(b) The light is scattered at the edge of the plume and the mean light path is shortened.
(c) Multiple scattering takes place in the volcanic plume; the light path might be longer than without the disturbtion in the plume.

assumed. The complexity of a volcanic plume and the Earth's atmosphere makes a simple rule for a correction of the geometrical approach impossible. An underestimation as well as an overestimation of the flux of a volcanic plume is possible if simple geometrical calculations are used.

The oxygen dimer (O_4) is a well known and during the last years increasingly applied indicator for the radiative transport and therefore also for the length of light paths (see Chapter 4). The concentration of O_4 is proportional to the square of the O_2 concentration [*Janssen* 1986] and therefore dependent on the air density. Only very small variations in the atmospheric column exist.
In contrary to O_2, the absorption bands of O_4 are several nm in width [*Greenblatt et al.* 1990] and lie between 340 to 630 nm. O_4 can therefore be resolved by a typical DOAS instrument [*Platt* 1994]. The concentration of O_4 can be calculated with the ideal gas law:

$$[O_4] \approx a^2 \cdot (\frac{p}{kT})^2 \tag{8.22}$$

k – Boltzmann constant

p – pressure

T – temperature

a – oxygen fraction in air 0.21

During measurements with low telescope elevation angles, the O_4 column density will be enhanced in comparison to higher telescope elevation angles (assuming horizontally homogeneous conditions) due to the enhanced light path through the atmosphere and a higher concentration of O_4 near the ground. If a change of this behavior can be observed by pointing to a volcanic plume, then this is an indication of a change in the light path due to the volcanic plume. Depending on the composition and thickness of the plume and the solar zenith angle an enhancement or decrease of the light path is possible.
For the following the simplification is made that only single scattering takes place in an atmosphere without clouds. In Figure 8.15, different situations are outlined. Figure 8.15 (a) shows the simplest case. The light is not influenced by the volcanic plume, no additional scattering takes place and therefore geometrical consideration (see *Bobrowski* [2002], *Bobrowski et al.* [2003]) would lead to a relatively good light path estimation. Figure 8.15 (b) illustrates a case where the assumption of the light path being equal to the plume width would not be correct. The flux calculation would in this case lead to an underestimated flux, since the photons would only partially cross the plume on average. The SO_2 SCDs would show lower results compared to Figure 8.15 (a). Figure 8.15 (c) is a more complex situation. In contrary to case (b) the results present a light path enhancement which would result in higher SO_2 SCDs and in an overestimation of

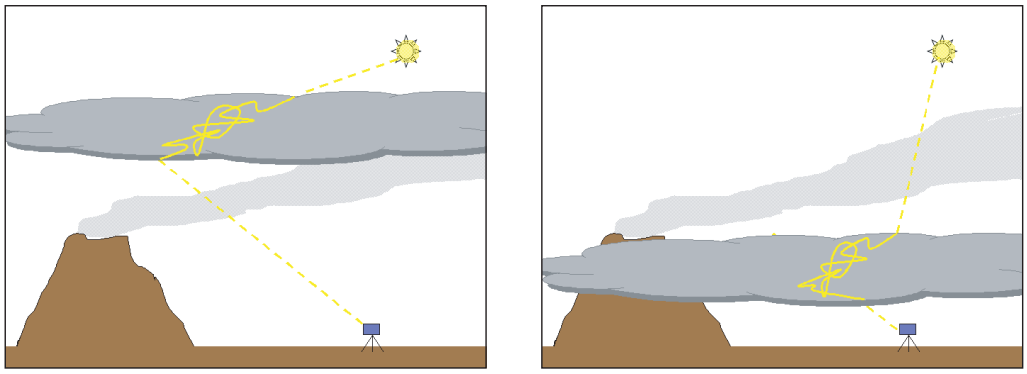

Figure 8.16: *The two figures show different possible scenarios for a mean light path during volcanic plume measurements with a Mini-MAX-DOAS under cloudy conditions. (a) The cloud layer is located above the volcanic plume. Changes in the O_4 SCDs result from the changes in the light path due to the cloud and can cover the changes caused by a volcanic plume.*
(b) The cloud layer is located below the volcanic plume. Due to a higher sensitivity of changes in the light path, because of higher O_4 concentration in lower altitudes (where multiple scattering has a greater influence), the SO_2 SCDs will be lower than in case (a) the same situation, except for the cloud, is assumed.

the flux.
Figure 8.16 attempts to illustrates some possibilities for the even more complex situations in case of a cloudy sky, where the O_4 information might not be sufficient or even helpful in trying to calculate the trace gas flux of a volcano. In Figure 8.16 (a) the clouds are above the volcanic plume, which could lead to larger or smaller SCDs of O_4 before the influence of scattering events inside the volcanic plume (on the light path) are considered. In Figure 8.16 (b) the clouds are below the volcanic plume. This could result in values of SO_2 SCDs similar to a more diluted plume, if a lot of photons, which did not cross the plume would be collected by the spectrometer. Also higher SCDs of O_4 would be seen, because the light path was elongated by the cloud below the plume.
Calculating an atmospheric light path in the case of a cloud covered sky is already a challenge without a volcanic plume and a problem which is not fully resolved to date. This strongly indicates that the O_4 method might have limited application in the case of light path determination in volcanic plumes, but nevertheless could make a good tracer for the length of the light path for at least for especially chosen meteorological conditions (sunny day, blue sky, low relative humidity, etc).

The photon light path also shows a wavelength dependence [*Wagner et al.* 2004], which opens the question, if besides the error for the flux calculation the variation of the

trace gas ratios is also strongly influenced by meteorological variations. This cannot be totally ruled out, but nearly excluded, if we assume that the Mie scattering in volcanic plumes plays a significant role. This assumption is possible because of a high aerosol content and aerosol sizes of about 2 μm normally found in volcanic plumes.

During this study, there were at least few times meteorological circumstances that

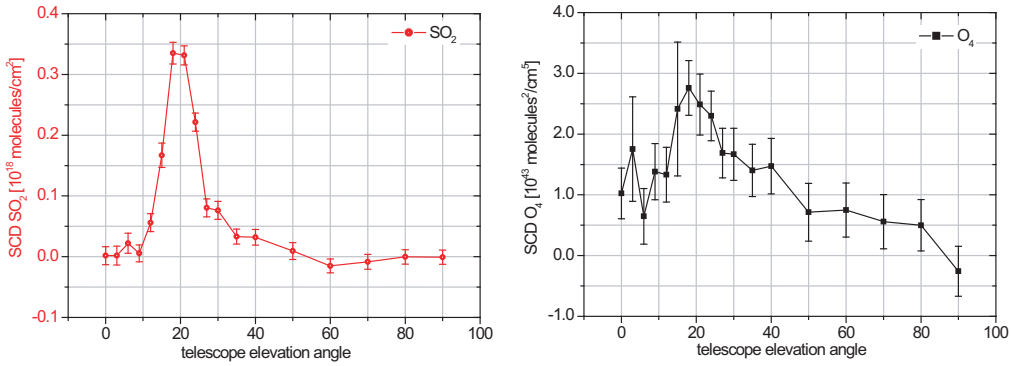

Figure 8.17: *SCDs of SO_2 and O_4 at Vulcano. One plume scan of measurements taken at Lentia (point (c) in Figure 7.12) on the 5^{th} of October 2003. O_4 is enhanced in the center of the plume.*

allowed to study a volcanic plume as the only "cloud" in the sky. The measurements at Vulcano 2003 serve as a good example. These measurements already introduced in Chapter 7 are shown once again in Figure 8.17.

In the following, an example of a comparison between the flux calculated by only geometrical considerations and the flux calculated by taking account the light path enhancement through the plume by using the O_4 results is given.

Flux calculation neglecting scattering processes in the plume

The SCDs of SO_2 can be used to calculate a flux. For this example some simplifications are made. First it is assumed that the telescope was pointed perpendicular to the plume and that the plume cross section was a circle. Furthermore a wind velocity of 2 m/s is assumed. The distance between the instrument and the volcanic gas was about 2 km (see the map in Figure 7.12., Chapter 7). In Figure 8.18 the calculation of the plume diameter (D) is illustrated, it results in a value of D = 2 σ = 312 m.
If a homogeneous SO_2 concentration in the plume is further assumed, one can calculate:

$$c = SCD/D = \frac{3.5 \cdot 10^{17} molecules/cm^2}{31200 cm} = 1.1 \cdot 10^{13} molecules/cm^3 \quad (8.23)$$

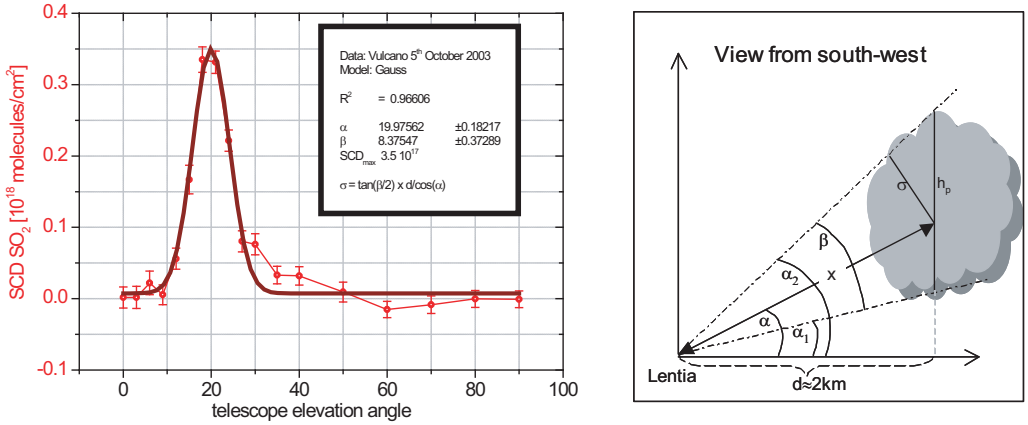

Figure 8.18: *SCDs of SO_2. One plume scan of measurements taken at Lentia (point (c) on the 5^{th} October 2003. A Gaussian curve is fitted through the plume. A sketch for the calculation of the plume diameter adapted from [Bobrowski et al. 2003].*

The cross section (A) of the plume is 76500 m^2. A wind velocity (v) of 2 m/s gives a flux (f) of:

$$f = c \cdot A \cdot v \cdot \frac{64g}{6 \cdot 10^{23}} \tag{8.24}$$
$$= 15t/d$$

This result lies in the same order of magnitude as other flux measurements at Vulcano carried out in the last two years (e.g 13 - 17 t/d [*McGonigle et al.* 2003]).

Flux calculation by using O_4 as an indicator of the photon light path

Figure 8.17 shows the SCDs of O_4 for one single plume scan. The concentration for O_4 was calculated by assuming $a_{air} = 0.21$ and using equation 8.22. A homogenous distribution of O_4 is assumed for the altitude of the plume. From the maximal O_4 SCD value ($2.76 \cdot 10^{43}$ molecules^2/cm^5) belonging to the center of the plume (18°), the O_4 SCD ($1.38 \cdot 10^{43}$ molecules^2/cm^5) at an elevation angle of 9° (just below the plume) was subtracted and the resulting values divided by the calculated O_4 concentration to gain the length of the light path inside the plume. This is a lower limit of the light path. The O_4 SCD at 18° without a volcanic plume in a "single scattering scenario" would be smaller than the one of 9° one used here, but since no measurements outside the plume were taken, it is the best possible estimation in this case.

$$L = \frac{SCD}{[O_4]} \tag{8.25}$$
$$\approx 5100m$$

This light path (L) leads to a concentration of SO_2 of $6.9 \cdot 10^{11}$ molecules/cm^3. Calculating the flux using the light path regarding O_4 leads to an emission of only about 1 t/d. This value is expected to be at the upper range and illustrates, that the flux calculated above from only geometrical considerations seems to be overestimated by several factors, even more than an order of magnitude.

One of the larger problems of flux calculation from volcanic emissions today is the uncertainty of the light path inside a volcanic plume. This uncertainty may result in large errors which can be in the same order of magnitude as the errors caused by the uncertainty of wind speed (>100 % [*McGonigle et al.* 2005]).
Great effort should be spend in the next years to overcome this problem and probably the only solution will be complex radiative transfer models like TRACY [*von Friedeburg* 2003] which include the modelling of clouds.

Chapter 9

Summary and Outlook

9.1 Summary

The first reactive halogen measurements in volcanic plumes were made during the Soufriere Hills measurement campaign in May 2002 and revealed unexpectedly high BrO emissions of 460 t/d [*Bobrowski et al.* 2003].
In this work, further reactive halogen and sulphur dioxide measurements in volcanic plumes were conducted during six measurement campaigns in Italy, Nicaragua, Costa Rica, Chile and Bolivia. All measurements were carried out with the new Mini-MAX-DOAS instrument combined with a Pocket PC. This greatly enhanced the possibilities and was indispensable for some measurements in remote areas, where the instrument had to be carried. The main results obtained in this work are:

- BrO could be detected at Masaya, Mt. Etna, Stromboli and Villarica. BrO/SO_2 ratios of $0.8 \cdot 10^{-4}$, $4.8 \cdot 10^{-4}$, $2.1 \cdot 10^{-4}$, $2.1 \cdot 10^{-4}$, $1.3 \cdot 10^{-4}$ were found in the plumes of Masaya, Etna 2003, Etna 2004, Stromboli, Villarica respectively, compared to $10.0 \cdot 10^{-4}$ measured at Soufrire Hills, 2002. These BrO/SO_2 ratios are of the same order of magnitude as on Soufriere Hills except Masaya. Daily BrO fluxes of 42 t/d, 240 t/d, 31 t/d and 19 t/d were estimated for Masaya, Mt. Etna, Stromboli and Villarica, respectively.
  This shows that Soufriere Hills on Montserrat is not an exceptional volcano regarding its bromine emission, although its BrO/SO_2 ratio currently appears to be somewhat higher than the various volcanoes studied in this thesis. Nevertheless it can be concluded that volcanic sources of reactive bromine could effect the Earth's atmosphere, at least locally.

- BrO is formed downwind, although it is not yet clear by what chemical processes. Experimental studies at two volcanic sites, Mt. Etna and Mt. Villarica, were

carried out and showed similar results. At Mt. Etna, measurements took place from the summit up to a distance of 19 km in downwind direction. Simultaneous measurements of BrO/SO_2 ratios in May 2005 showed an increase of 16 % from 6 km to 10 km and and 52 % from 6 km to 19 km downwind. The results were qualitatively comparable to first model studies of Von Glasow [personal communication].

- ClO and OClO were detected for the first time as further active halogen compounds in volcanic plumes. ClO was already detected next to the source (in contrast to BrO), and shows no significant increase in the ClO/SO_2 ratio in the aging plume. The ClO/SO_2 ratio even seems to decrease by measuring further downwind. Near the summit craters a ClO/SO_2 ratio of 0.16 at Mt. Villarica, 2004 and 0.10 at Mt. Etna, 2005 was observed. In a distance of 3 km further downwind at Mt. Villarica the measured ClO/SO_2 ratio decreased to $2 \cdot 10^{-2}$. The ClO/SO_2 ratio at 6 km downwind from the summit of Mt. Etna decreased to $1.9 \cdot 10^{-2}$. An explanation for this behavior could not be given in this thesis and more systematic studies of this phenomenon are necessary.

- The BrO/SO_2 variations were studied during and after the Mt. Etna eruption 2004. They were compared with filter pack measurements and SO_2 flux variations. The meteorological influence on the data set could not be fully explored. However, the measurements indicated that the use of BrO to gain additional information about volcanic processes is feasible. This is also supported by measurements of the different feeding systems of Mt. Etna (the North East Crater and Voragine). The North East Crater showed larger BrO/SO_2 ratios than Voragine. Filter pack measurements show also larger halogen to sulphur ratios at North East crater.

- A first approach to shed some light on the halogen chemistry processes inside volcanic plumes was made. A suggestion similar to the processes found in Polar regions and at salt lakes is made regarding the BrO formation. The initial conditions are motivated by summarizing results of different thermodynamical studies from recent literature.

- Studies regarding the still insufficiently investigated topic of radiative transfer in volcanic plumes and its difficulties were discussed. This discussion shows the strong need of radiative transfer models and better determination of light paths and the limitation of the use of O_4 SCDs for the determination of light paths in volcanic plumes, especially in the case of a cloud covered sky. An example of light path

elongation, which illustrates the possible overestimation of an order of magnitude for SO_2 flux measurements with the scanning MAX-DOAS-sytem was given.

- Imaging Differential Optical Absorption Spectroscopy (IDOAS) combines a "push-broom" imaging spectrometer with the DOAS technique and thus allows recording two-dimensional trace gas distributions, e.g. in volcanic plumes. The IDOAS system presented here allows taking two-dimensional images of the trace gas distribution in a volcanic plume with a spatial resolution of 100 pixels horizontally times 64 pixels vertically, each with a field of view of 0.087° in horizontal and 0.208° in vertical direction. Thereby IDOAS provides useful information about the chemical composition and chemical variability in a volcanic plume. This allows studying plume dispersal and chemical transformations. The technique was applied to visualize the SO_2 distribution in the plume of Mt. Etna for the first time in October 2003.

9.2 Outlook

The Mini-MAX-DOAS system is a very simple and low cost instrument which has the potential to be used for long-time monitoring measurements at many volcanic sites. This will be started in an upcoming project.
The extension of the data set will open the possibility of a better estimation of the volcanic reactive bromine source and therefore the influence on the Earth's atmosphere. It also allows the investigation of the relation of changes in the BrO/SO_2 ratio with volcanic activity. This might allow to improve the forecast of volcanic eruptions which is highly desirable.
To overcome the distortion of the results by meteorological variations, detailed and systematic studies under different weather conditions have to be performed and the change in the BrO/SO_2 ratio observed. Since the activity of volcanoes is rarely stable, a distinction between meteorological and activity influences will likely only be possible through a large data set and statistical considerations.
Another very important issue is the investigation of light paths inside volcanic plumes. Therefore, a better knowledge of the aerosol composition and distribution in volcanic plumes will be necessary. The development of three dimensional radiative transfer models, which can deal with the multi-scattering in different cloud layers is a difficult but worthwhile task for the future.
The DOAS technique provides the possibility to study further trace gases, besides BrO and SO_2, like ClO, OClO, HCHO, NO_2, CS_2 etc., which are also abundant in volcanic plumes. Today the data set of these species is scarce for volcanic plumes, though very important to improve the knowledge about the chemical processes inside the volcanic plumes, which

are still widely unknown.
Effort should for example, be put into improving the evaluation of ClO by an enhanced Ring spectra where, besides N_2 and O_2, Raman-scattering regarding O_3 is considered. Measurements using an active DOAS system in comparison with a MAX-DOAS system are highly recommended for the future. Measurements with an active DOAS system would also provide the possibility to investigate nighttime chemistry in a volcanic plume, about which next to nothing is known to date.
Model studies and laboratory measurements are necessary to examine whether the suggested chemical processes can explain the observations, and ways have to be found to determine the O_3 and OH content inside the volcanic plume, as these are critical parameters.
The IDOAS has the potential to become a powerful tool for volcanic research in the future. New information about the two-dimensional gas distributions could be a step forward in the field of volcanic gas emission studies and could help to explain the chemical processes inside the plume. The two-dimensional visualization of different trace gas distributions and their ratios often simplifies the recognition of otherwise hidden structures and processes, as for example the discovery of a non-homogenous BrO distribution over a volcanic plume cross section [*Louban* 2005].

Appendix A

Data

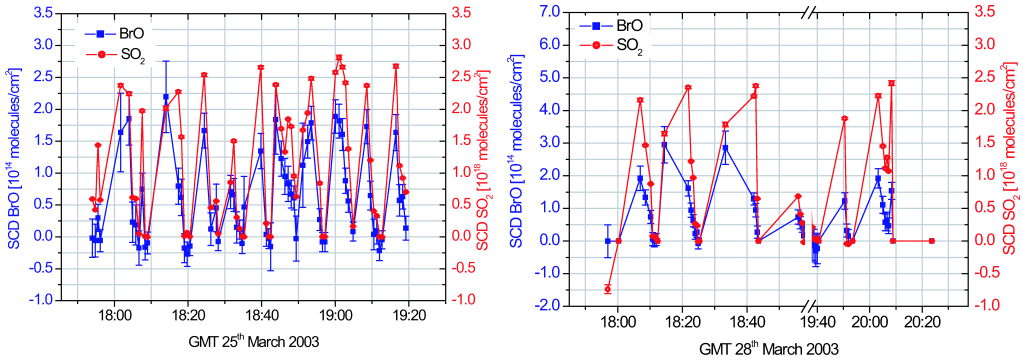

Figure A.1: *BrO SCDs of Masaya on the 25th and 28 th March 2003 by scanning an vertical angle of 60° above the crater.*

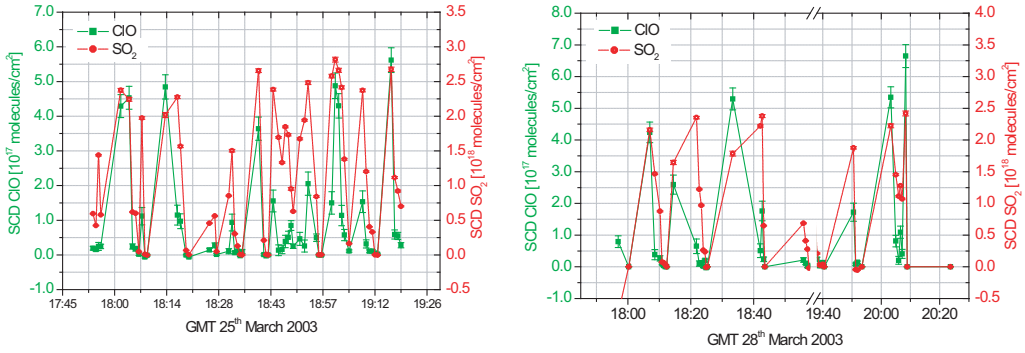

Figure A.2: *ClO results of Masaya on the 25th and 28 th March 2003 by scanning an vertical angle of 90° above the crater.*

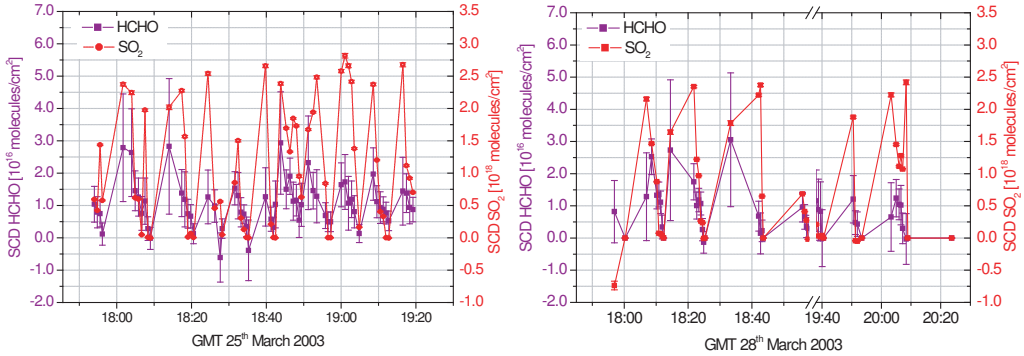

Figure A.3: *HCHO results of Masaya on the 25th and 28 th March 2003 by scanning an vertical angle of 60° above the crater.*

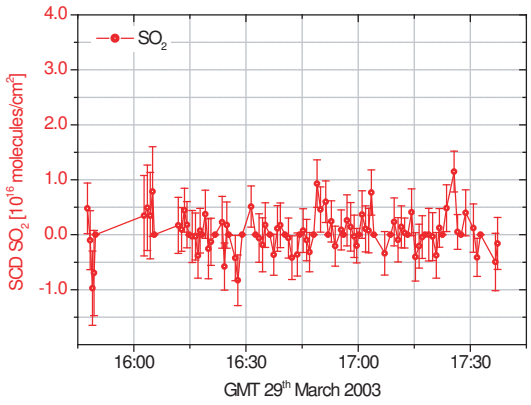

Figure A.4: *SO_2 SCDs of Masaya on March 29th 2003.*

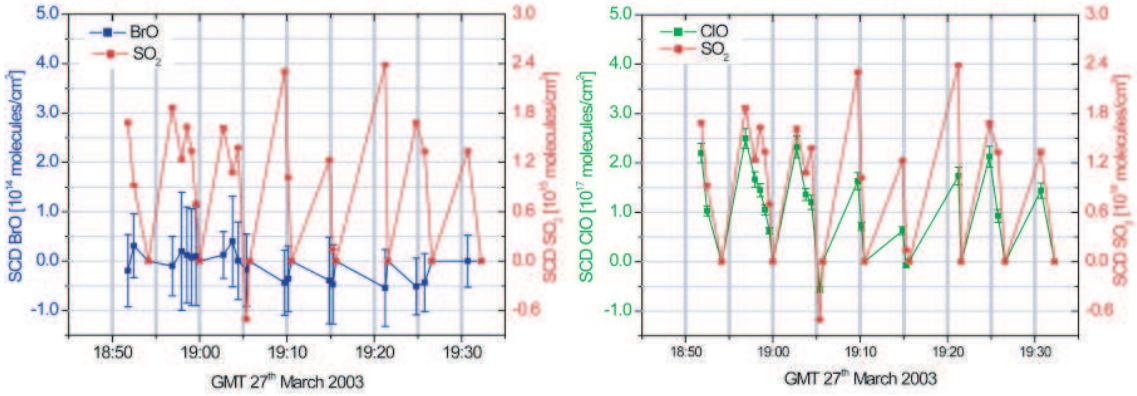

Figure A.5: *(a) BrO measurement results of Momotombo - evaluated for the suggestion of Aliwell et al., 2001 (b) evaluation result of ClO*

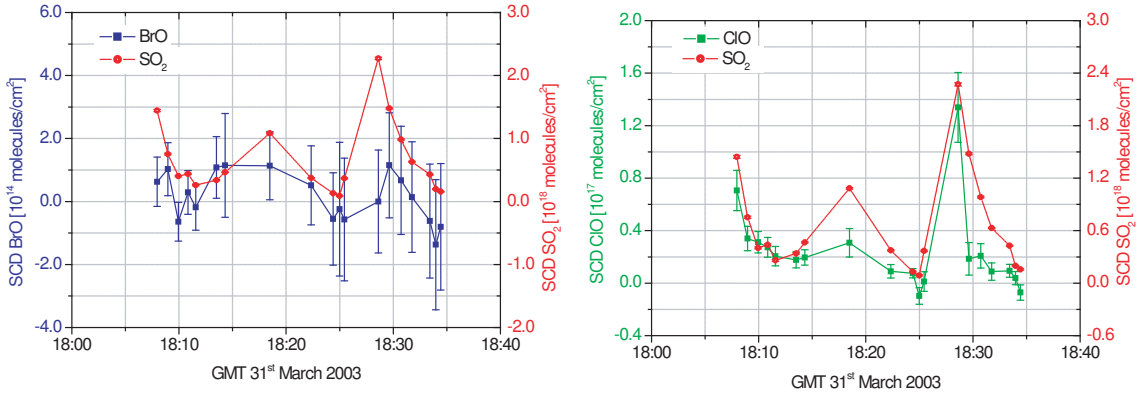

Figure A.6: *(a) BrO measurement results of POAS - evaluated for the suggestion of Aliwell et al., 2001 (b) evaluation result of ClO*

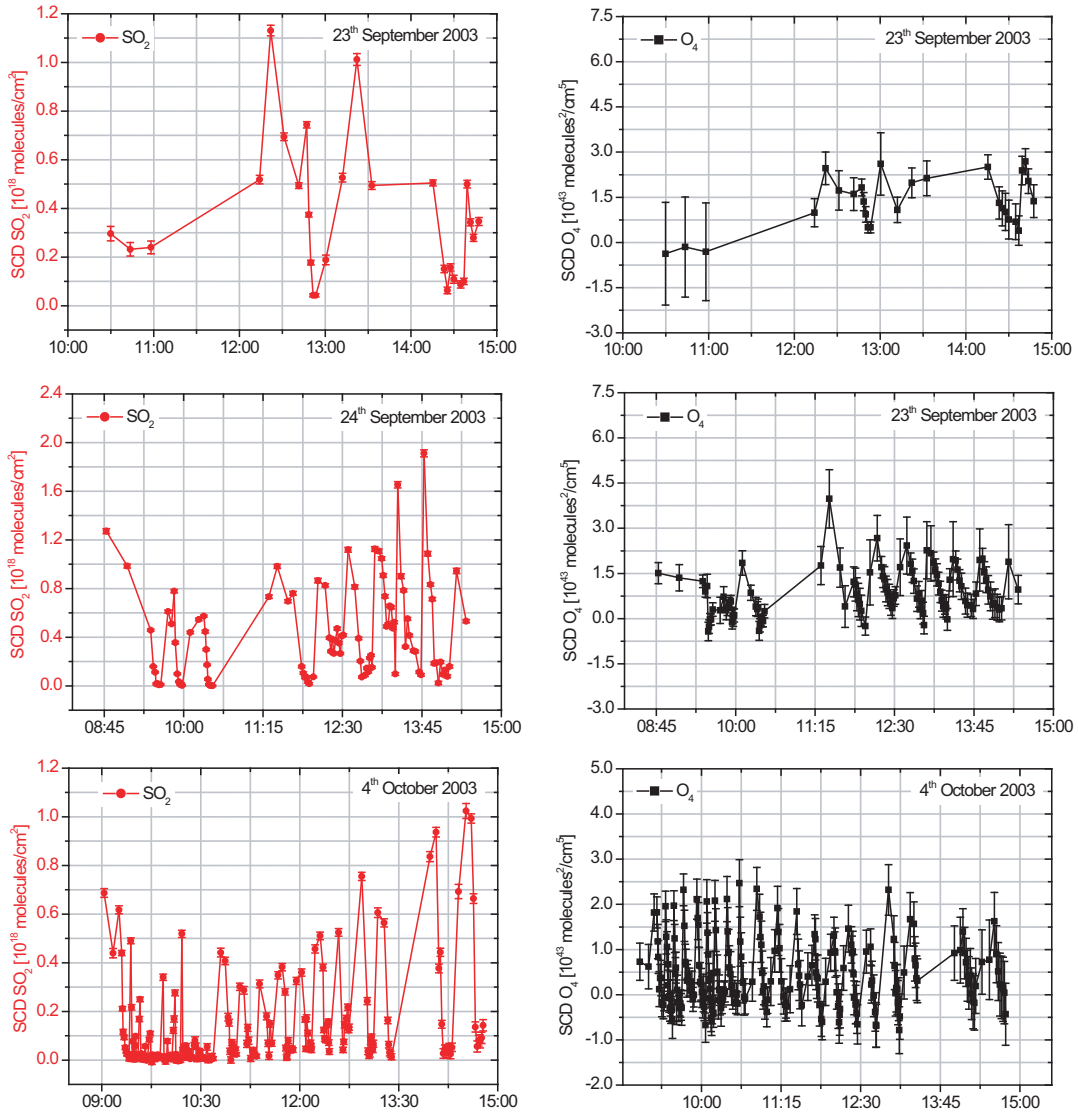

Figure A.7: *SCDs of SO_2 and O_4 are displayed for 23^{th}, 24^{th} September and 4^{th} October 2003. Data was taken at Vulcano Island.*

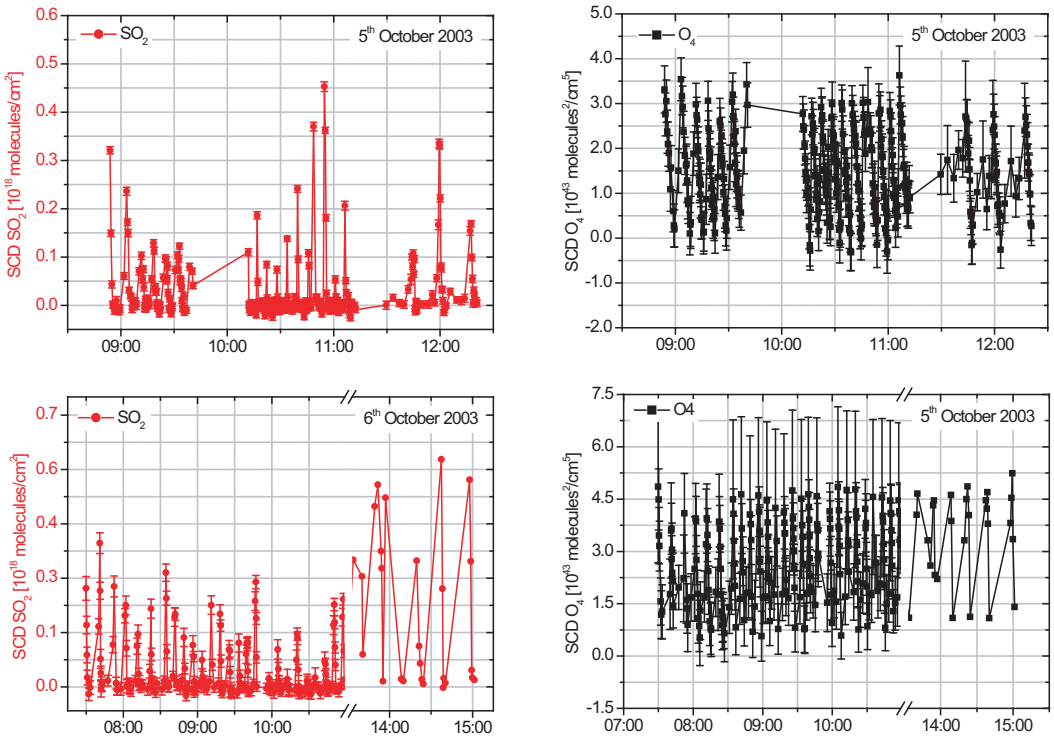

Figure A.8: *SCDs of SO_2 and O_4 are displayed for 5^{th} and 6^{th} October 2003. Data was taken at Vulcano Island.*

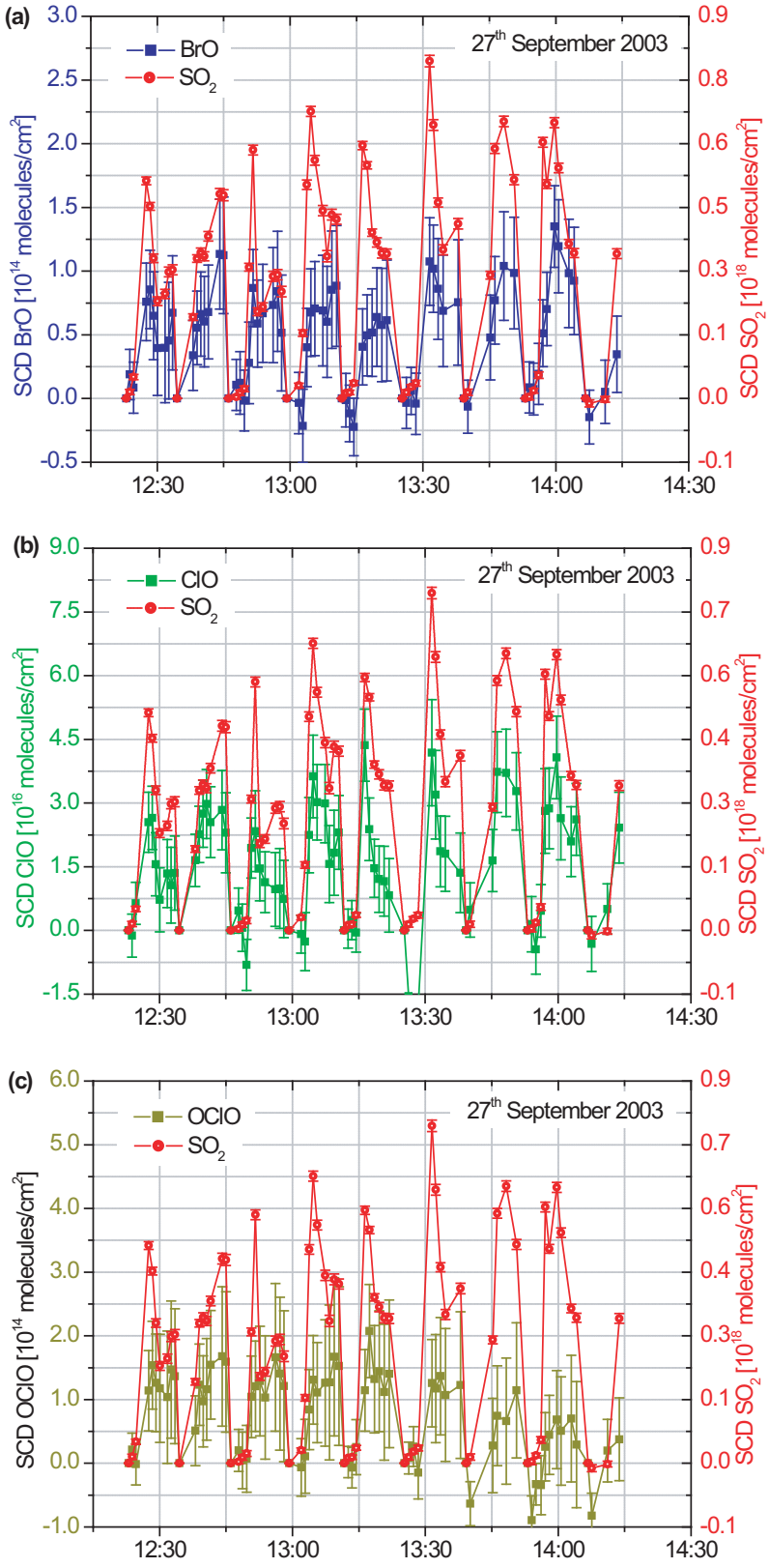

Figure A.9: *SCDs of BrO and SO_2 (a) and SCDs of ClO and SO_2 (b) OClO and SO_2 (c) are displayed. Measurement were carried out near the volcanic observatory on the 27th September 2003*

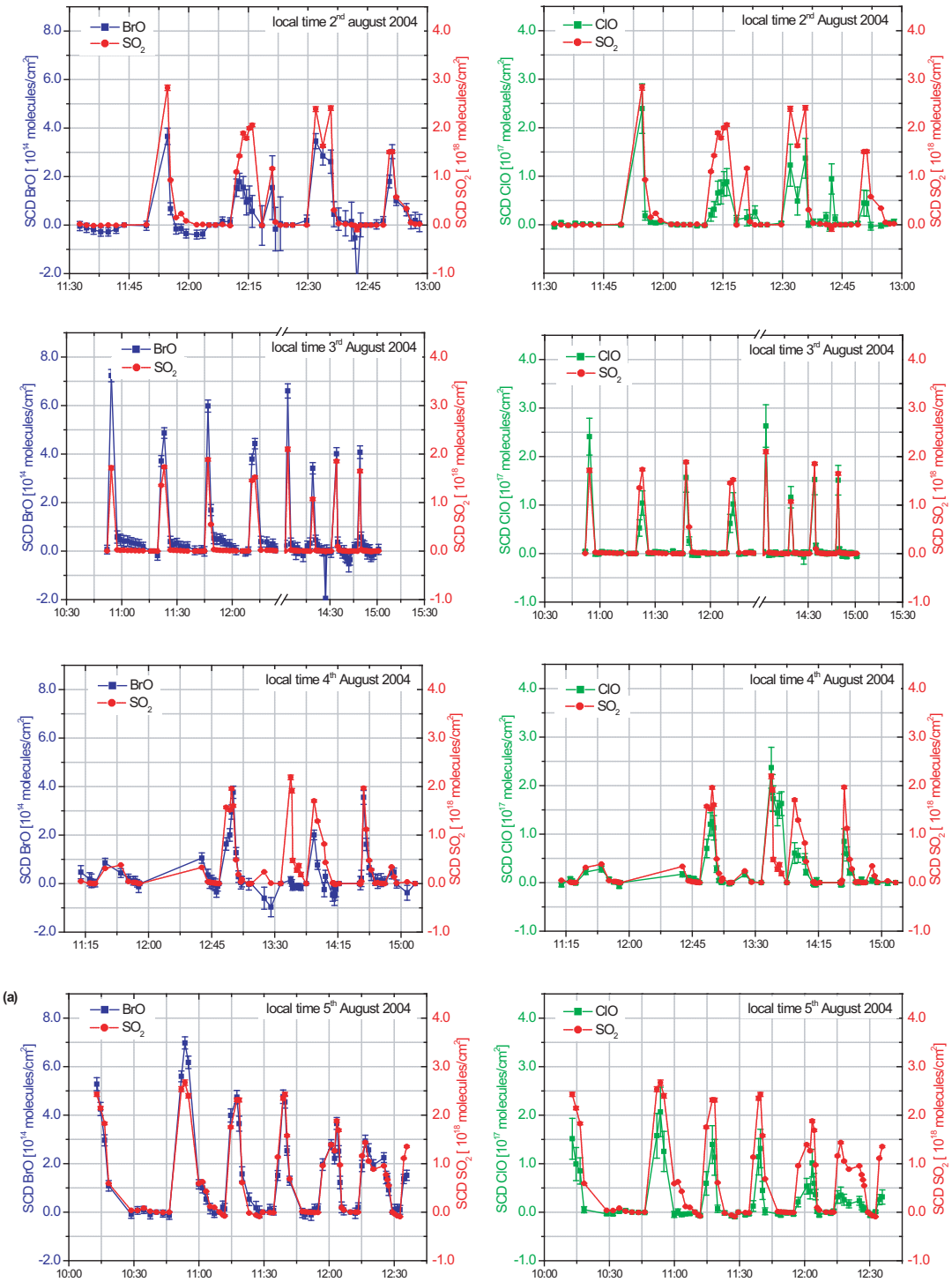

Figure A.10: *SCDs of ClO, BrO and SO_2 are displayed for the 4 measurement days in August 2004, for a better comparison of the days the y-axis were uniformly scaled*

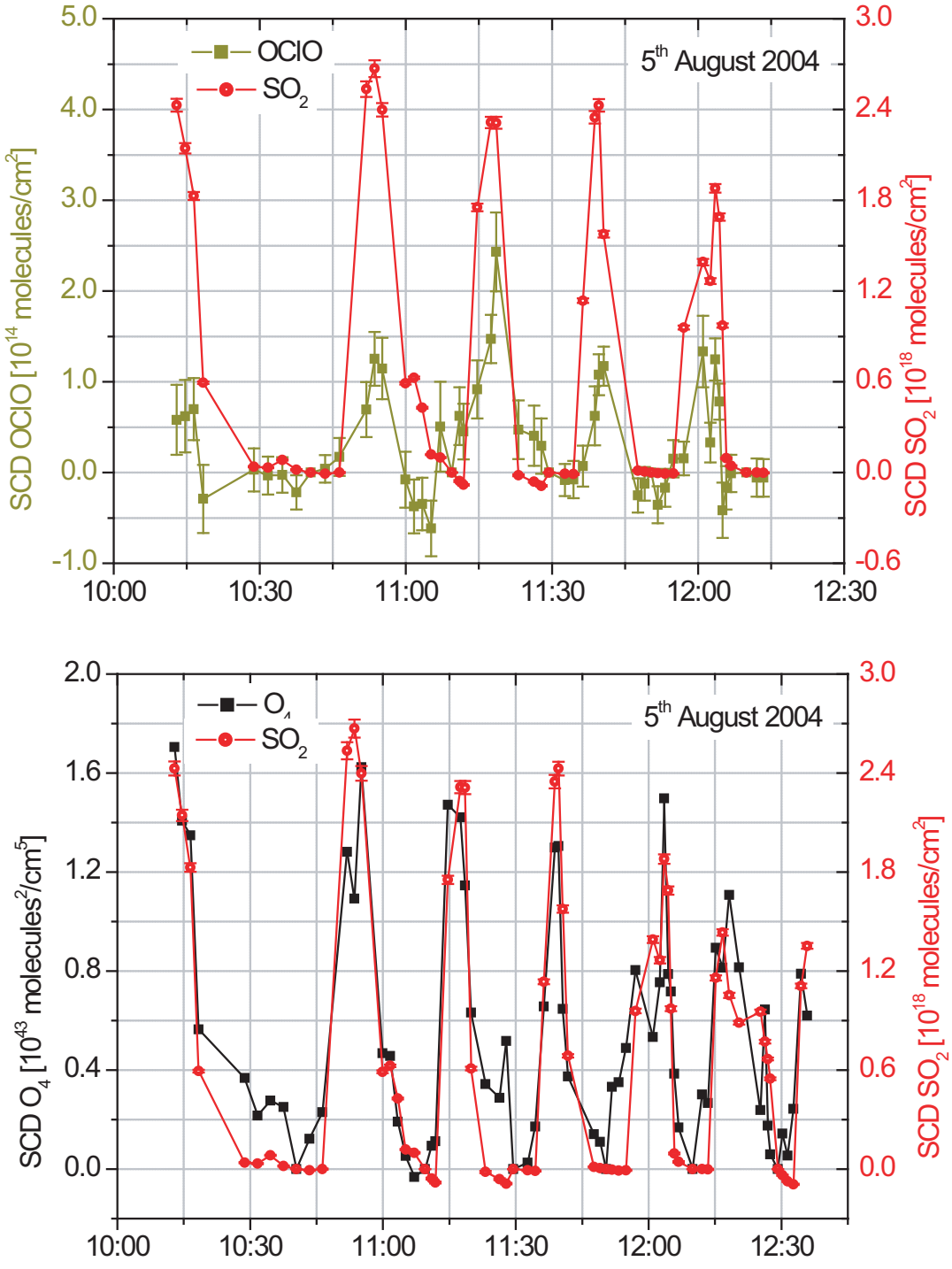

Figure A.11: *SCDs of OClO (dark yello), O_4(black) and SO_2(red) are displayed for the 5^{th} August 2004. Data was taken at Pizzi Deneri, Mt. Etna.*

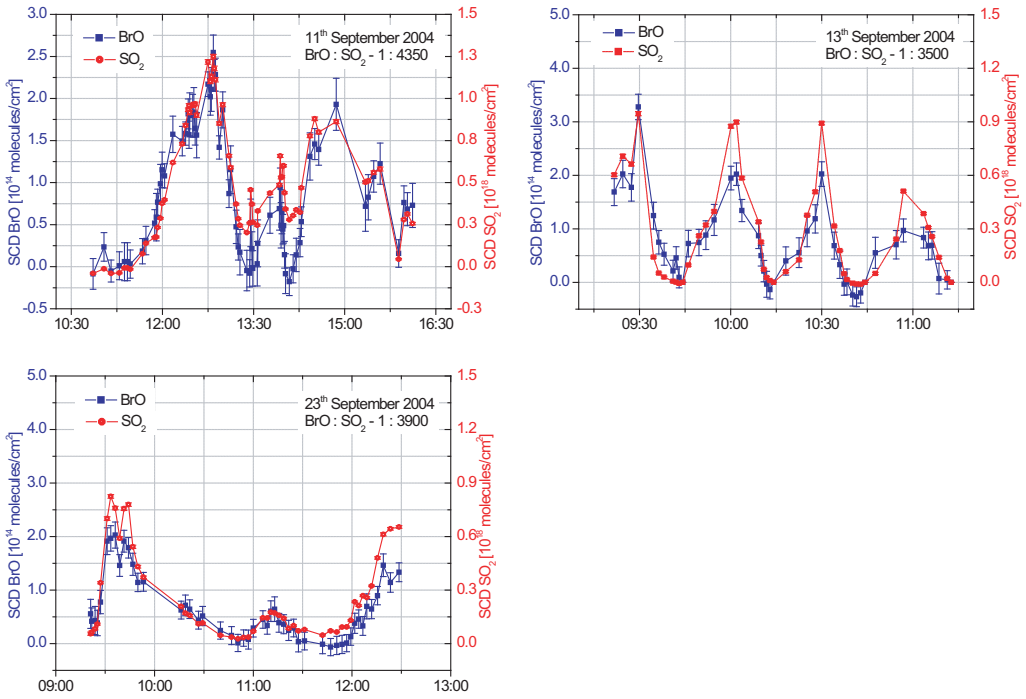

Figure A.12: *SCDs of SO_2 and BrO are plotted as a function of time for the 11^{th}, 13^{th} and 23^{th} September 2004. Data was taken 4 km from the summit of Mt. Etna.*

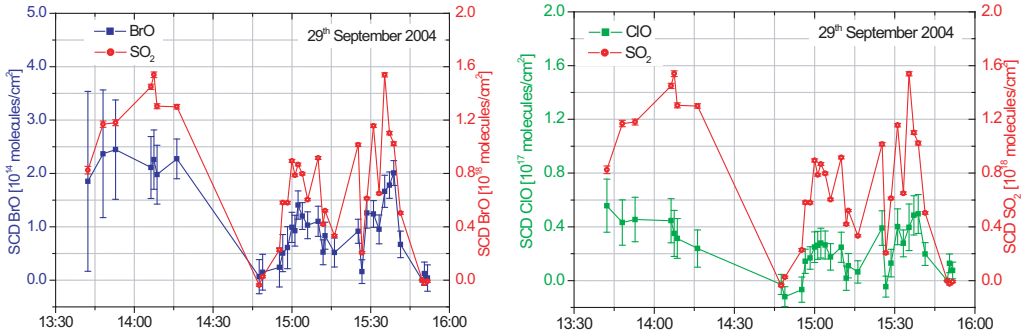

Figure A.13: *SCDs of SO_2 BrO and ClO are plotted as a function of time. Data was taken below the summit of Mt. Etna on the 29^{th} October 2004.*

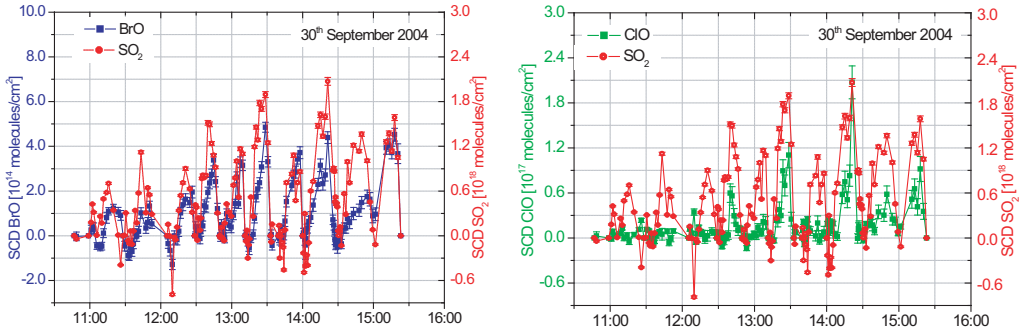

Figure A.14: *SCDs of SO_2 BrO and ClO are plotted as a function of time. Data was taken below the summit of Mt. Etna on the 30^{th} October 2004.*

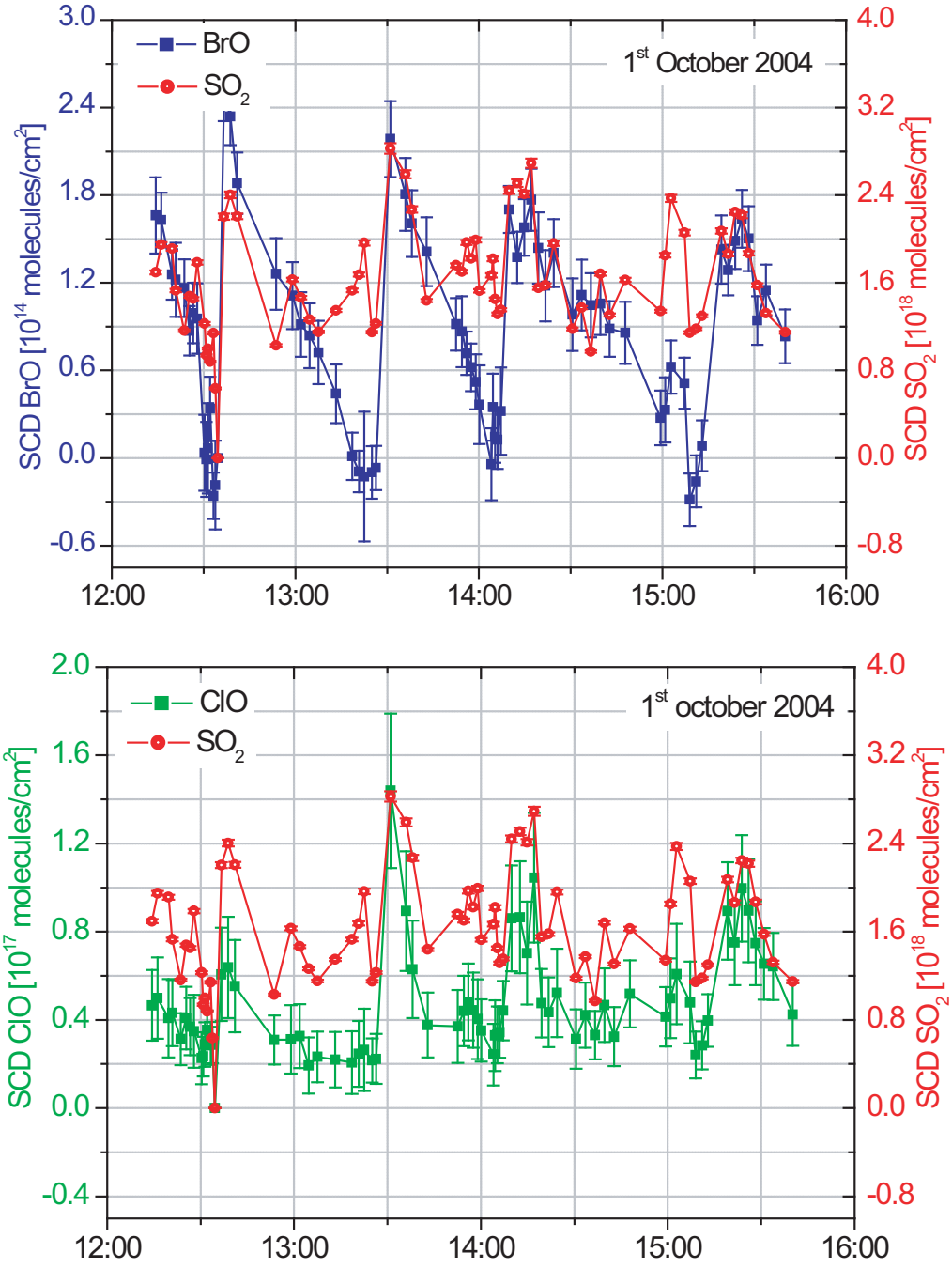

Figure A.15: *SCDs of SO_2, BrO and ClO below the summit region carried out on the 1st October 2004, attempt to separate the two main crater plumes (Crater centrale and North east crater).*

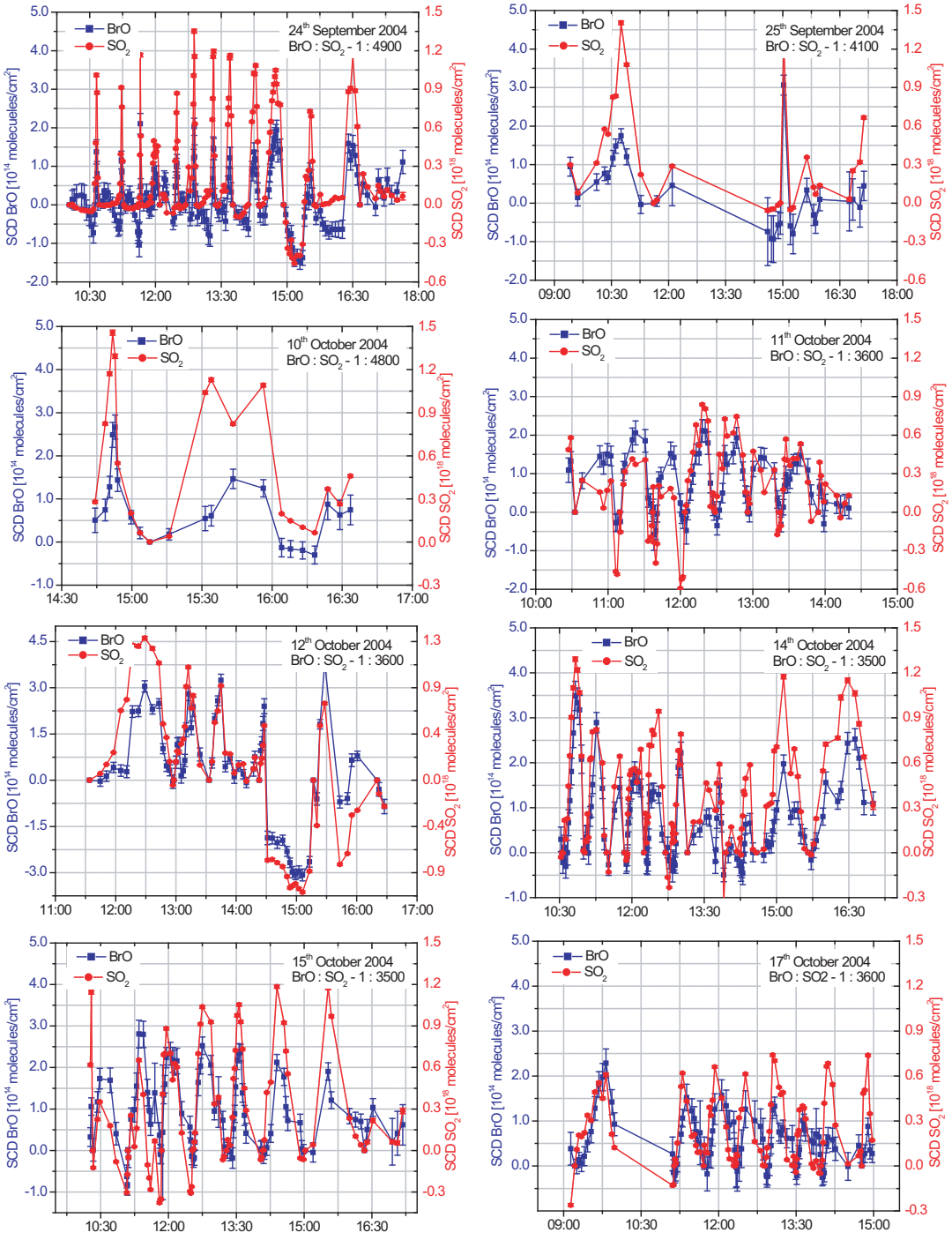

Figure A.16: *SCDs of BrO and SO_2 are displayed as a function of time. The measurements were carried out 6 km from the sumit at Rifugio Citelli during several days in September and October 2004.*

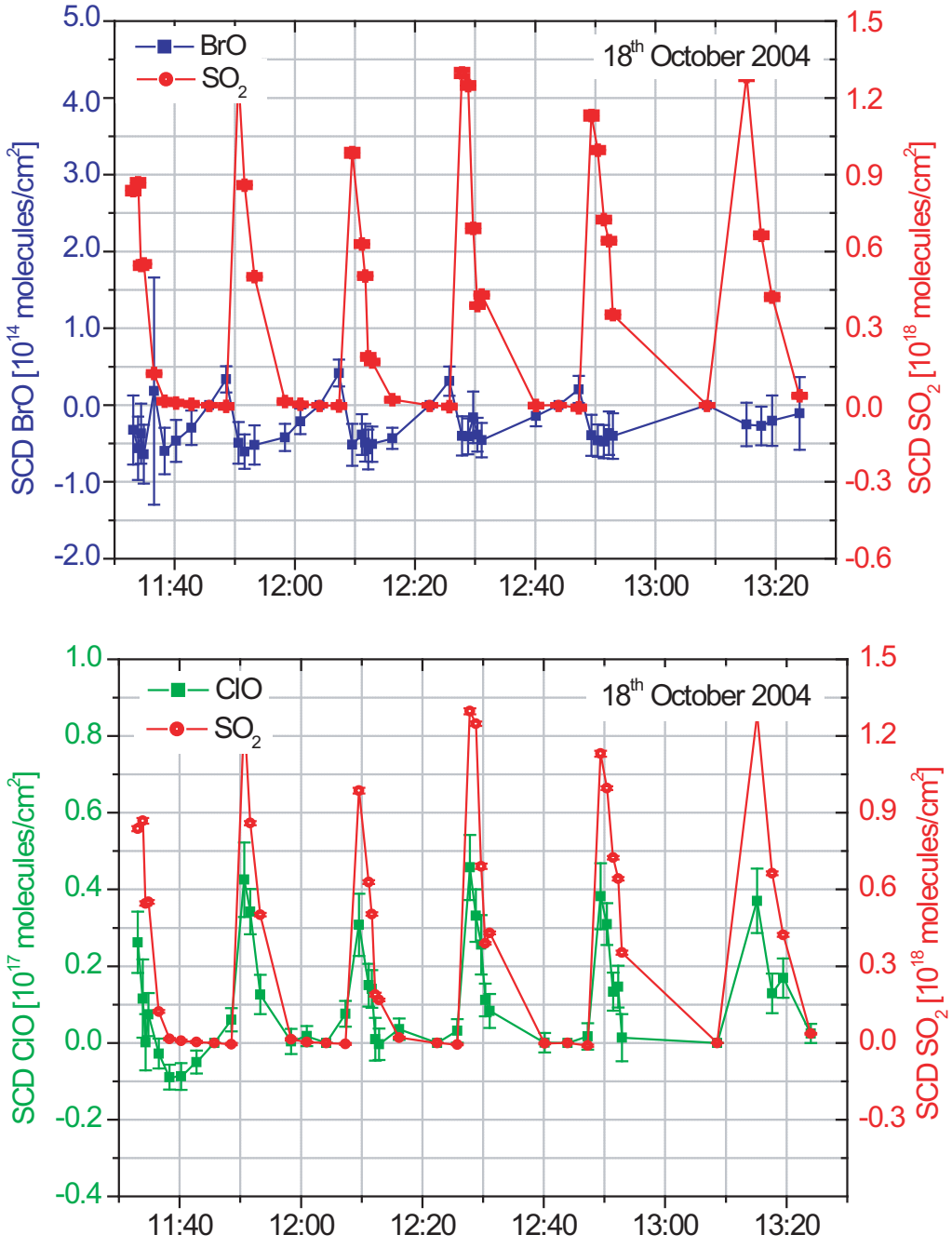

Figure A.17: *SCDs SO_2 (in red) and BrO (in blue) from measurements carried out in the summit region, 150 m from the plume of Voragine. Spectra taken on 18^{th} October 2004*

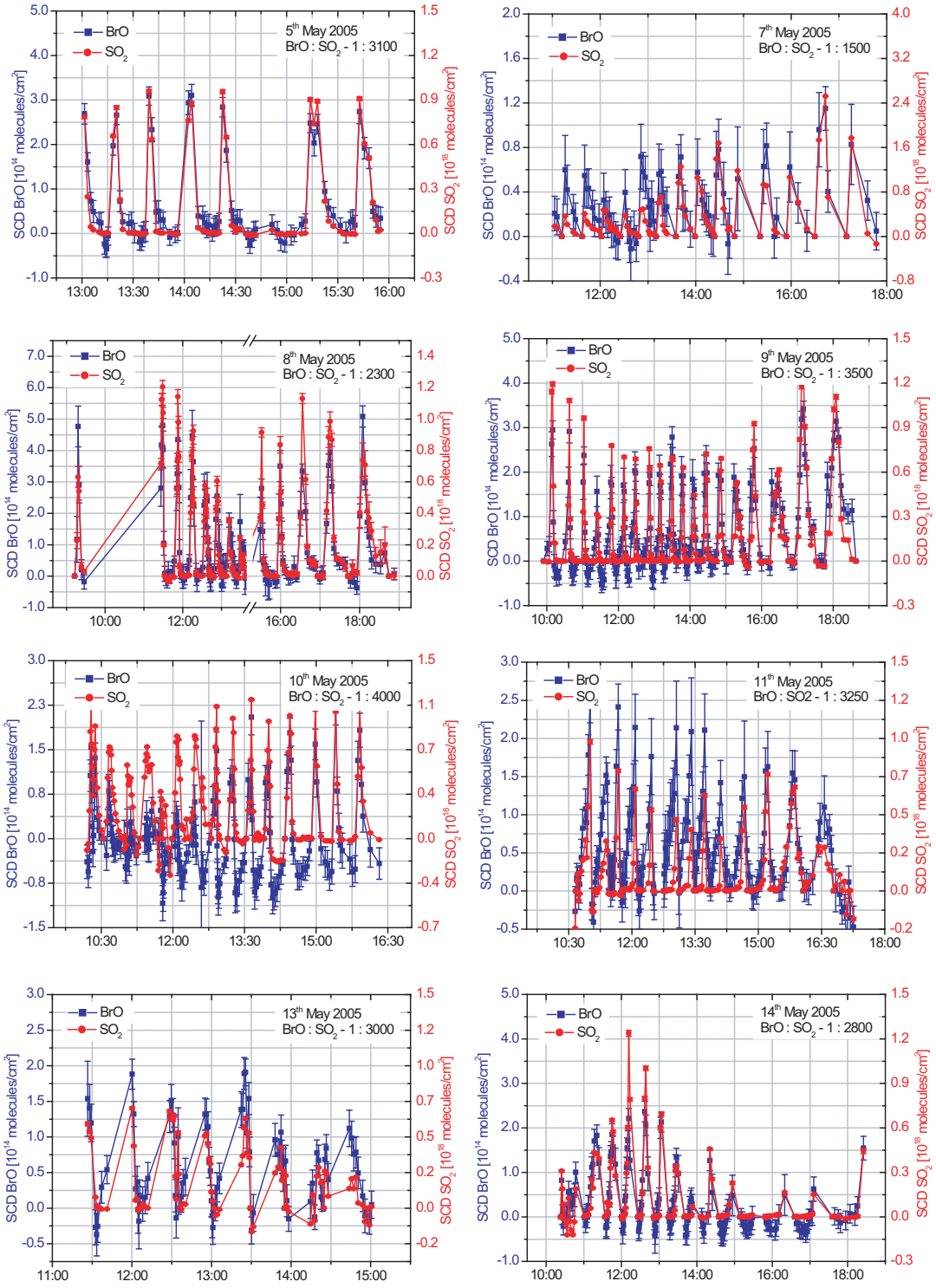

Figure A.18: *SCDs of SO_2 (in red) and BrO (in blue) are displayed as a function of time. The measurements were carried out 6 km from the summit at Rifugio Citelli during several days in May 2005.*

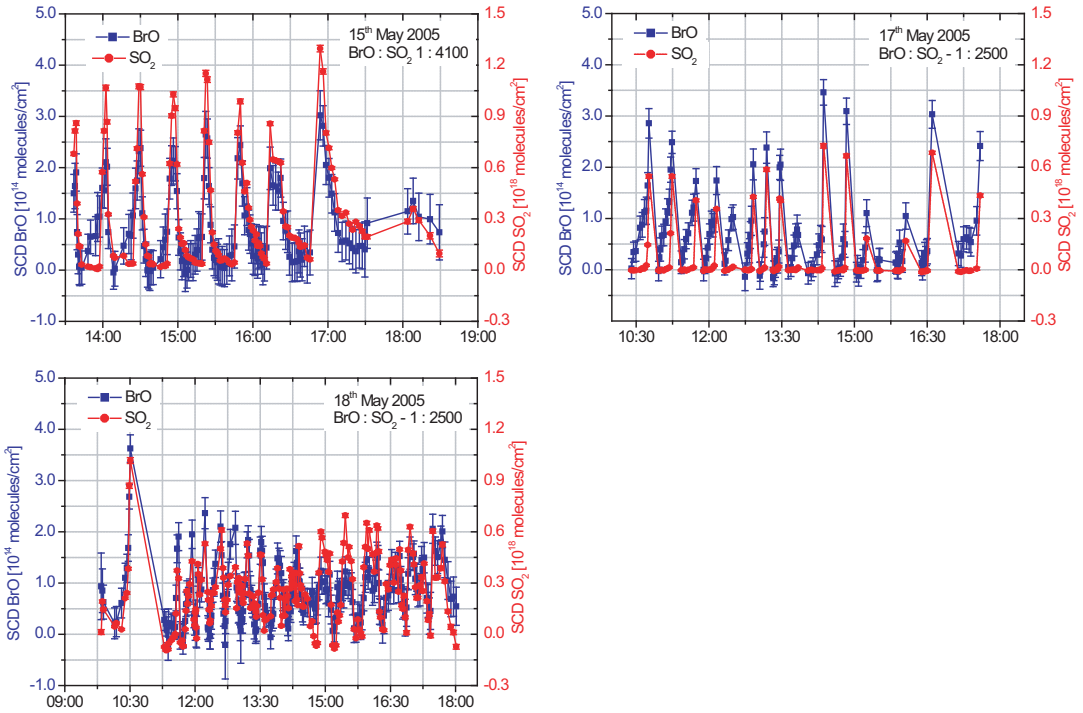

Figure A.19: *SCDs of SO_2 (in red) and BrO (in blue) are displayed as a function of time. The measurements were carried out 6 km from the summit at Rifugio Citelli during several days in May 2005.*

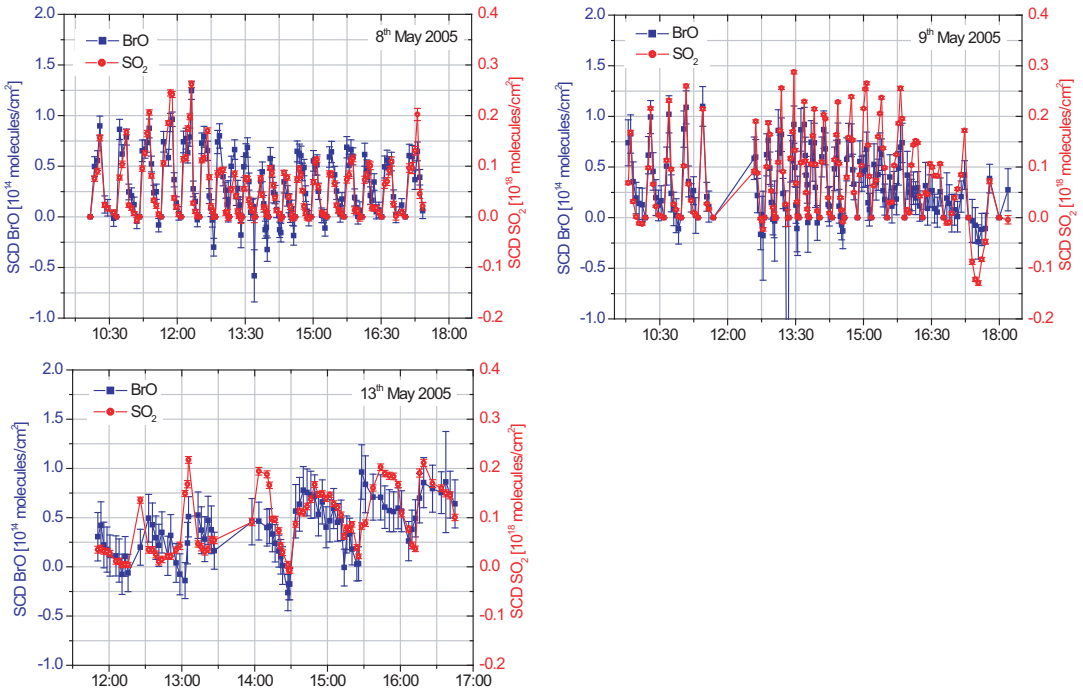

Figure A.20: *SCDs of SO_2 (in red) and BrO (in blue) are displayed as a function of time. The measurements were carried out 19 km from the summit near the town Riposto at the coast during several days in May 2005.*

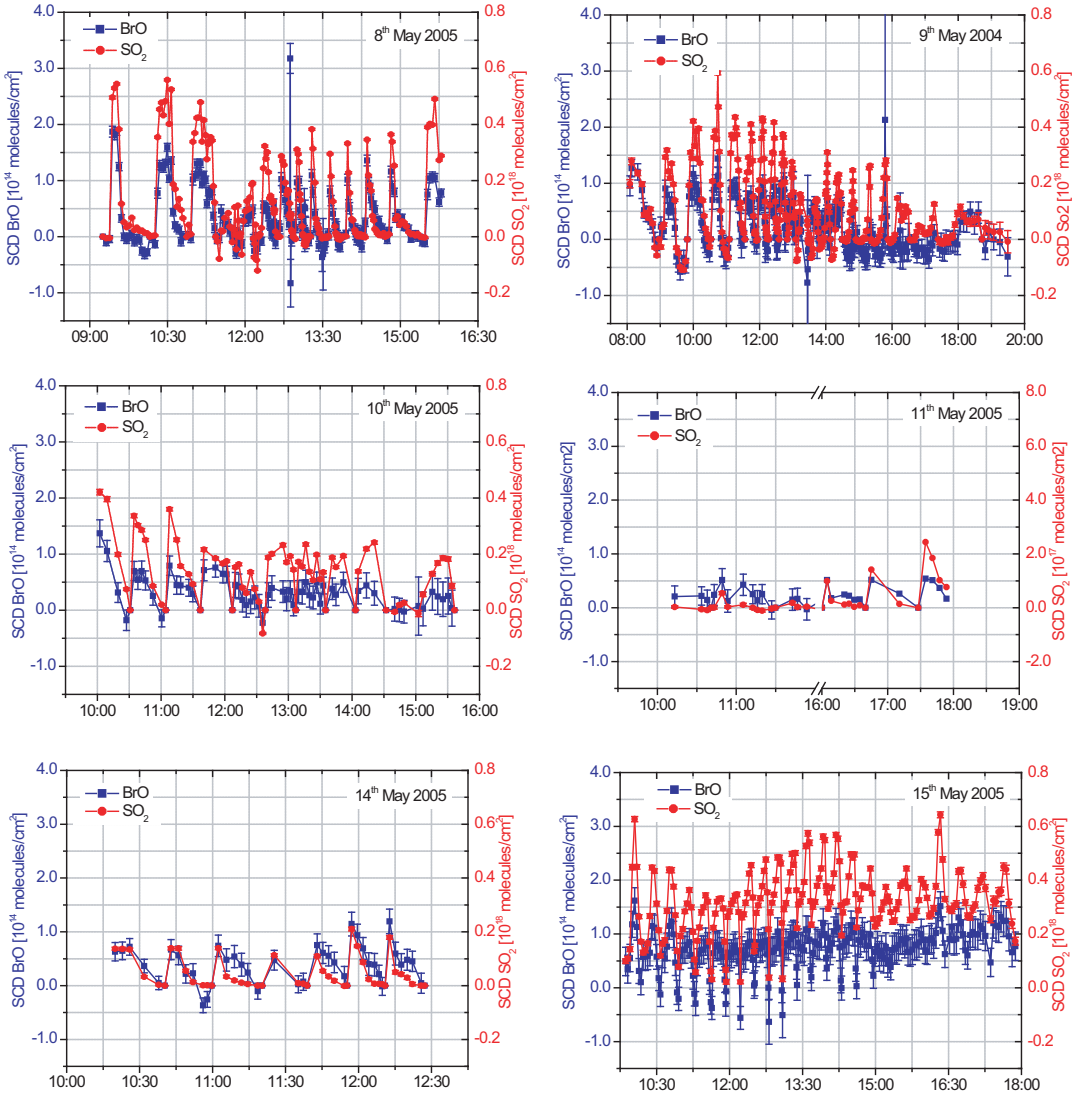

Figure A.21: *SCDs of SO_2 (in red) and BrO (in blue) are displayed as a function of time. The measurements were carried out 10 km from the summit at Milo during several days in May 2005.*

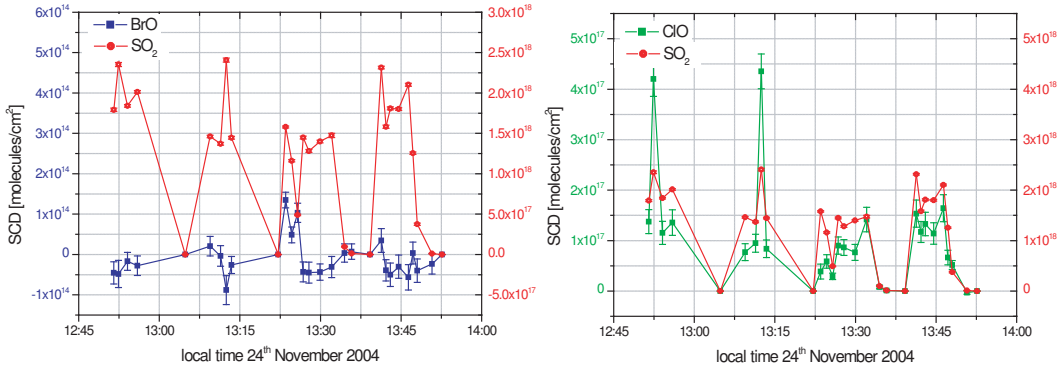

Figure A.22: *SO_2, BrO and ClO SCDs at Mt. Vilarica. The plume was scanned about three km downwind on the 17^{th} November 2004.*

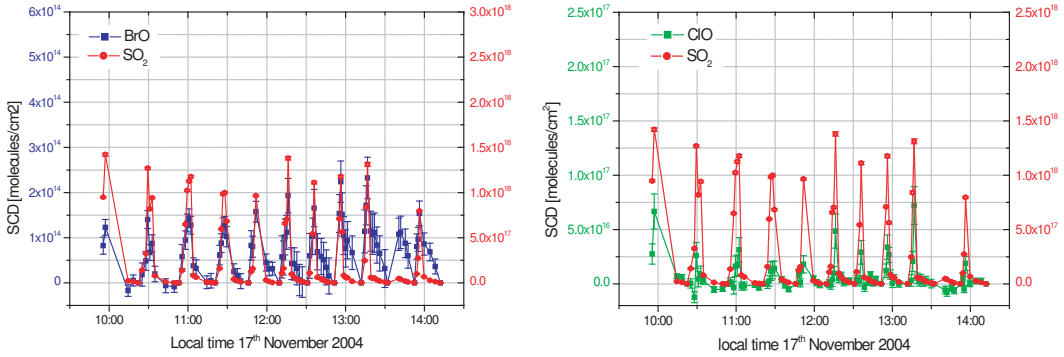

Figure A.23: *SO_2, BrO and ClO SCDs from the top of Mt. Villarica, carried out on 24^{th} November 2004.*

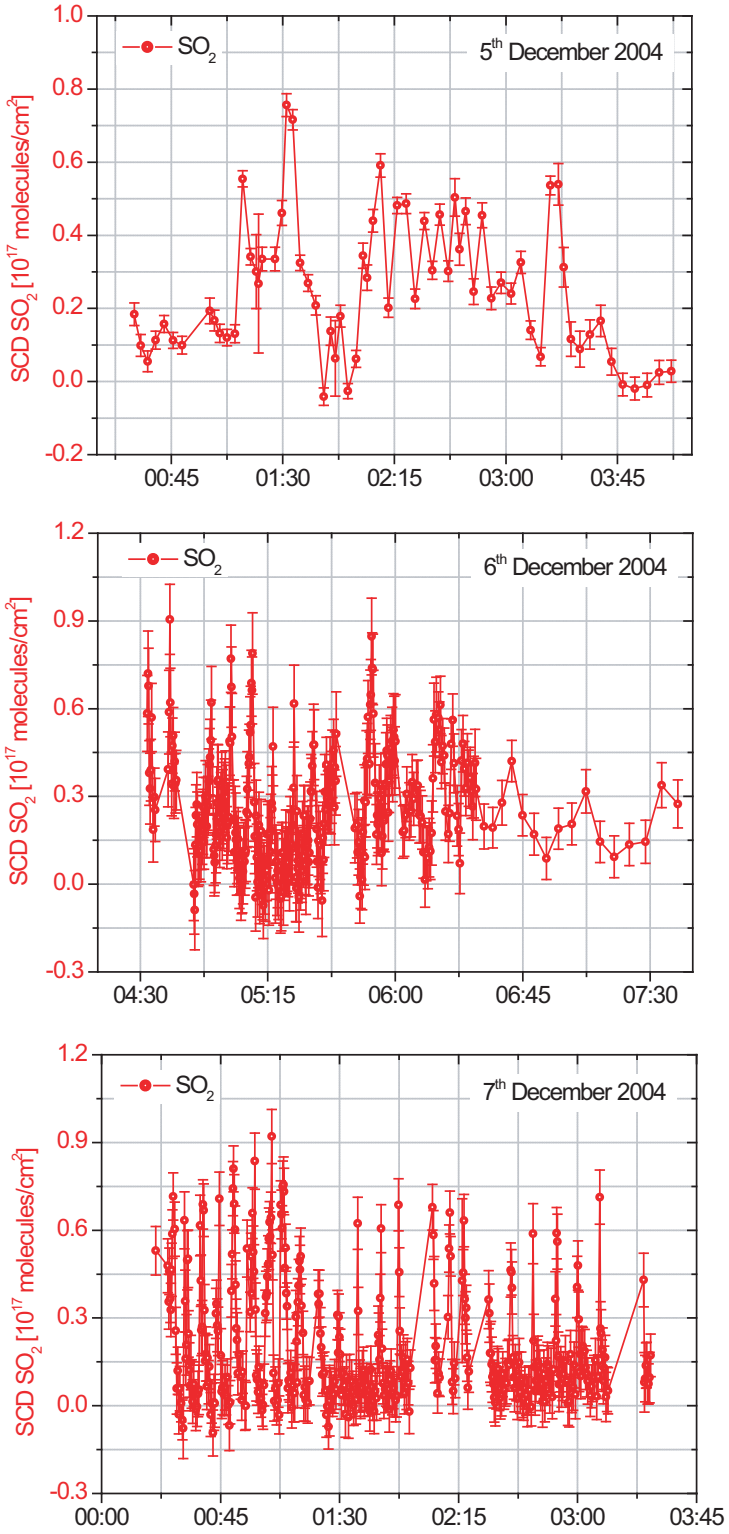

Figure A.24: *SCDs of SO_2. Measurements were undertaken in several distances from the emission source on the 5^{th}-7^{th} December 2004.*

List of Figures

List of Tables

References

Afe, O. T., A. Richter, B. Sierk, F. Wittrock, and J. Burrows (2004). BrO emissions from Volcanoes - a Survey using GOME and SCIAMACHY Measurements. *GRL,* Vol. 31, No. L24113, doi:10.1029/2004GL020994.

Aiuppa, A., C. Federico, A. Franco, G. Giudice, S. Gurrieri, S. Inguaggiato, M. Liuzzo, A. McGonigle, and M. Valenza (2005). Emission of Trace Halogens From A Basaltic Volcano: Mount Etna. *Geochem. Geophys. Geosyst.,* Vol. in press.

Aiuppa, A. and C. Frederico (2004). Anomalous magmatic degassing prior to the 5th April 2003 paroxysm on Stromboli. *GRL,* Vol. 31, doi:10.1029/2004GL020458.

Albritton, D. and L. Meira Filho (2001). Climate Change 2001: The Scientific Basis. In *Contribution of Working Group I to the Third Assesment Report of the Intergovernmental Panel on Climate Change*, pp. ISBN:0521014956.

Aliwell, S. R., M. V. Roozendael, P. V. Johnston, A. Richter, T. Wagner, D. W. Arlander, J. P. Burrows, D. J. Jones, K. K. Tornkvist, J.-C. Lambert, K. Pfeilsticker, and I. Pundt (2002). Analysis for BrO in Zenith-sky spectra: An intercomparision exercise for analysis improvement. *J. Geophys. Res.,* Vol. 107, No. D14, 10.1029/2001JD000329.

Allen, A. G., T. A. Mather, A. J. S. McGonigle, A. Aiuppa, P. Delmelle, B. Davison, N. Bobrowski, C. Oppenheimer, D. M. Pyle, and S. Inguaggiato (2005). Sources, size distribution and downwind grounding of aerosols from Mt. Etna. *JGR,*, in review.

Andrea, M. O., H. Berresheim, H. Bingemer, D. J. Jacob, and R. W. Talbot (1990). The cycle of biogenic sulfur compounds over the Amazon Basin II. Wet season. *J. Geophys. Res.,* Vol. 95, 16813–16824.

Andreae, M. O. and W. R. Barnard (1984). The marine chemistry of dimethylsulfide. *Mar. Chem.,* Vol. 14, 267–279.

Andreae, M. O. and H. Raemdonck (1983). Dimethyl sulfide in the surface ocean and the marine atmosphere: a global view. *Science,* Vol. 221, 744–747.

Andres, R. J. and A. Kasgnoc (1998). A time-averaged inventory of subaerial volcanic sulfur emissions. *J. Geophys. Res.,* Vol. 103, 25251–25261.

Arthur, M. A. (2000). *Volcanic contributions to the carbon and sulfur geochemical cycles and global change* (H. Sigurdsson and B. F. Houghton and S. R. McNutt H. Rymer and J. Stix, In Encyclopedia of Volcanoes ed.)., pp. 1046–1056. San Diego: Academic Press.

Atkinson, R., D. Baulch, R. Cox, R. H. Jr., J. Kerr, M. Rossi, and J. Troe (1997). Evaluated kinetic, photochemical and heterogeneous data for atmospheric chemistry. *J. Phys. Chem. Ref. Data,* Vol. 26 (3), 521–1011.

Barrie, L., J. Bottenheim, R. Schnell, P. Crutzen, and R. Rasmussen (1988). Ozone destruction and photochemical reactions at polar sunrise in the lower Arctic atmosphere. *Nature,* Vol. 334, 138–141.

Barrie, L. and U. Platt (1997). Arctic tropospheric chemistry: and overview. *Tellus,* Vol. 49B, 449–454.

Bass, A. M. and R. J. Paur (1985). The Ultraviolet Cross Section of Ozone, I. The Measurements. In Z. C. and A. Ghazy (Eds.), *Proc. of the Quadrennial Ozone Symposium*, Chalkidiki, Greece, pp. 606–616.

Bedjanian, Y., G. Poulet, and G. LeBras (1998). Low pressure study of the reactions of Br atoms with alkenes: reaction with propene. *J. Phys. Chem.,* Vol. 102, 5867–5875.

Behnke, W., V. Scheer, and C. Zetzsch (1993). Formation of $ClNO_2$ and HNO_3 in the presence of N_2O_5 and wet pure $NaCl-$ and wet mixed $NaCl/Na_2SO_4$-aerosol. *Journal of Aerosol Science,* Vol. 24, 115–116.

Berresheim, H. and W. Jaeschke (1983). The contribution of volcanoes to the global atmospheric sulfur budget. *J. Geophys. Res.,* Vol. 88, 3732–3740.

Berresheim, H., P. H. Wine, and D. D. Davis (1995). *Sulfur in the atmosphere, in Composition, Cemistry, and Climate of the Atmosphere.* New Yorck: H. B. Singh, Van Nostrand Reinhold.

Bilde, M., T. J. Wallington, C. Ferronato, J. J. Orlando, G. S. Tyndall, E. Estupinan, and S. Haberkorn (1998). Atmospheric chemistry of CH_2BrCl, $CHBrCl_2$, $CHBr_2Cl$, $CF_3CHClBr$ and CBr_2Cl_2. *J. Phys. Chem.,* Vol. 102, 1976–1986.

Bissoli, P. (1985). *Der Einfluss des Vulkanismus und der hypothetischen Variationen der Emission solarer Strahlung auf die Bodennahe Lufttemperatur 1881-1981.* Diploma thesis, Institut für Met. u. Geophys. d Universität Frankfurt a. M.

Bluth, G. J. S., S. D. Doiron, S. C. Schnetzler, A. J. Krueger, and L. S. Walter (1992). Global tracking of the SO2 clouds from the June 1991 Mount Pinatubo eruptions. *Geophys. Res. Lett.,* Vol. 19, 151–154.

Bluth, G. J. S., C. C. Schnetzler, A. J. Krueger, and L. S. Walter (1993). The contribution of explosive volcanism to global atmospheric sulphur dioxide concentrations. *Nature,* Vol. 366, 327–329.

Bobrowski, N. (2002). *Volcanic Gas Studies by Multi-AXis Differential Optical Absorption Spectroscopy.* Diploma thesis, Institut für Umweltphysik, Universität Heidelberg.

Bobrowski, N. and F. Filsinger (2005). *Mini-MAX-DOAS Manual.* Institut für Umweltphysik, Universität Heidelberg.

Bobrowski, N., G. Hönninger, B. Galle, and U. Platt (2003). Detection of bromine monoxide in a volcanic plume. *Nature,* Vol. 432, 273–276.

Bobrowski, N., G. Hönninger, F. Lohberger, and U. Platt (2005). IDOAS: A new monitoring technique to study the 2D distribution of volcanic gas emissions. *JGVR,*, accepted.

Bobrowski, N., I. Louban, R. von Glasow, O. I. Whaba, U. Platt, A. Aiuppa, and S. Inguaggiato (2005). Bromine Chemistry in Volcanic plumes. pp. in preparation.

Bobrowski, N. and U. Platt (2005). Bromine Monoxide Studies in Volcanic Plumes. *J. of Volc. and Geotherm. Res.,* Vol. 0, in review.

Bogumil, K., J. Orphal, T. Homan, S. Voigt, P. Spietz, O. Fleischmann, A. Vogel, M. Hartmann, H. Bovensmann, J. Frerick, and J. Burrows (2003). Measurements of molecular absorption spectra with the SCIAMACHY Pre-Flight Model: instrument characterization and reference data for atmospheric remote-sensing in the 230-2380 nm region. *Journal of Photochemistry and Photobiology A: Chemistry,* Vol. 157, 167–184.

Boucher, O. and U. Lohmann (1995). The sulfate-CCN-cloud albedo effect. *Tellus B,* Vol. 47, 281–300.

Boucher, O., C. Moulin, S. Belviso, O. Aumont, L. Bopp, E. Cosme, R. von Kuhlmann, M. Lawrence, M. Pham, M. Reddy, J. Sciare, and V. C. (2003). DMS atmospheric concentrations and sulphate aerosol indirect radiative forcing: a sensitivity study to the DMS source representation and oxidation. *Atmos. Chem. Phys.,* Vol. 3, 4965.

Bureau, H., H. Kepler, and N. Meternich (2000). Volcanic degassing of bromine and iodine: experimental fluid/melt portioning data and applications to stratospheric chemistry. *EPSL,* Vol. 183, 51–60.

Burnham, C. W. (1979). *The importance of volatile constituents, In The Evolution of Igneous Rocks: Fiftieth Anniversary Perspectives*, Volume 0. Princeton University.

Burrows, J. P., A. Dehn, B. Deters, S. Himmelmann, A. Richter, S. Voigt, and J. Orphal (1999). Atmospheric remote-sensing reference data from GOME: 2. temperature-dependent absorption cross sections of O_3 in the 231-794 nm range. *J. Quant. Spec. and Rad. Transf.,* Vol. 61, 509–517.

Burton, M., P. Allard, F. Mure, T. Caltabiano, G. di Grazia, M. Mattia, N. Metrich, D. Patane, and G. Salerno (2004). Four years of FTIR measurements of gas emissions from Mt. Etna: Comparison with volcanological and geophysical data. *IAVCEI conference, Pucon Chile,.*

Burton, M. R., P. Allard, F. Mure, and C. Oppenheimer (2003). FTIR remote sensing of fractional magma degassing at Mt. Etna, Sicily. *Volcanic degassing, Geological Society Special Publication,* Vol. 213, 281–293.

Bussemer, M. (1993). *Der Ring-Effekt: Ursachen und Einfluß auf die spektroskopische Messung stratosphärischer Spurenstoffe.* Diploma thesis, Institut für Umweltphysik, Universit"at Heidelberg.

Cadle, R. D. (1975). Volcanic emissions of halides and sulfur compounds to the troposphere and stratosphere. *Journal of Geophysical Research,* Vol. 80, 1650–1652.

Cadle, R. D. (1980). A comparison of volcanic with other fluxes of atmospheric trace gas constituents. *Reviews of Geophysics and Space Physics,* Vol. 18, 746–752.

Caltabiano, T., R. Romano, and G. Budetta (1994). SO_2 flux measurements at Mount Etna (Sicily). *J. Geophys. Res.,* Vol. 99, 12809–12819.

Carpenter, L., W. Sturges, S. Penkett, P. Liss, B. Alicke, K. Hebestreit, and U. Platt (1999). Observation of short-lived alkyl iodides and bromides at Mace Head, Ireland: links to biogenic sources and halogen oxide production. *J. Geophys. Res.,* Vol. 104, 1679–1689.

Carroll, M. R. and J. R. Holloway (1994). *Volatiles in Magmas.* Washington: Mineralogical Society of America.

Charlson, R. J., J. E. Lovelock, M. O. Andreae, and S. G. Warren (1987). Oceanic Phytoplankton, Atmospheric Sulphur, Cloud, Albedo and Climate. *Nature,* Vol. 326, 655–661.

Chin, M. and D. D. Davis (1993). Global sources and sinks of OCS and CS_2 and their distribution. *Global Bioceochem. Cycl,* Vol. 7, 321–337.

Chin, M., R. Rood, S.-J. Lin, J.-F. Müller, and A. Thompson (2000). Atmospheric sulfur cycle simulated in the global model GOCART: Model description and global properties. *J. Geophys. Res.,* Vol. 105 (D20) 24, 24671–24687.

Davies, J. (1970). Correlation Spectroscopy. *Analytical Chemistry,* Vol. 42, 101–112.

Delmelle, P., P. Baxter, A. Beaulieu, M. Burton, P. Francis, J. G.-A. L. Horrocks, M. Navarro, C. Oppenheimer, D. Rothery, H. Rymer, K. S. Amand, J. Stix, W. Strauch, and G. Williams-Jones (1999). Origin, effects of Masaya volcano's continued unrest probet in Nicargua. *EOS Transactions, American Geophysical Union,* Vol. 80, 575–581.

Dignon, J. and S. Hameed (1989). A Global emissions of nitrogen and sulfur oxides from 1860 to 1980 three dimensional model of the global ammonia cycle. *J. Air Pollut. Contr. Assoc.,* Vol. 39, 180–186.

Dudhia, A., A. Burgess, V. Payne, C. Picolla, and V. Jay (2003). Retrievel of minor species from MIPAS. *Geophysical Research Abstracts, 5, EGS-AGU_EUG Joint Assemble, Nice, France,.*

Ebinghaus, R., H. H. Kock, C. Temme, J. W. Einax, A. G. Löwe, A. Richter, J. P. Burrows, and W. H. Schroeder (2002). Antarctic springtime depletion of atmospheric mercury. *Environ. Sci. Technol.,* Vol. 36, 1238–1244.

Edmonds, M., D. M. Pyle, and C. Oppenheimer (2002). HCl emissions at Soufriere Hills Volcano, Montserrat, West Indies, during a second phase of dome building:November 1999 to October 2000. *Bull. Volcanol.,* Vol. 64, 21–30.

Edner, H., P. Ragnardson, S. Svanberg, E. Wallinder, R. Ferrara, R. Cioni, B. Raco, and B. Taddeucci (1994). Total fluxes of sulphur dioxide from the Italian volcanoes Etna, Stromboli and Vulcano measured by differential absorption lidar and passive differential optical absorption spectroscopy. *J. Geophys. Res.,* Vol. 99, 18827 – 18838.

Fan, S. and D. Jacob (1992). Surface ozone depletion in Arctic spring sustained by bromine reactions on aerosols. *Nature,* Vol. 359, 522–524.

Ferlemann, F., C. Campy-Peyret, R. Fitzenberger, H. Harder, T. Hawat, H. Osterkamp, D. Perner, U. Platt, M. Schneider, P. Vradelis, and K. Pfeilsticker (1998).

Stratospheric BrO Profile measured at Different Latitudes and Seasons: Measurement Technique. *Geophysical Research Letters,* Vol. 25, 3847–3850.

Fickert, S., J. W. Adams, and J. N. Crowley (1999). Activation of Br_2 and BrCl via uptake of HOBr onto aqueous salt solutions. *J. Geophys. Res.,* Vol. 104, 23719–23727.

Finlayson-Pitts, B. and S. Johnson (1988). The reaction of NO_2 with $NaBr$: Possible source of $BrNO$ in polluted marine atmospheres. *Atmos. Environ.,* Vol. 22, 1107–1112.

Finlayson-Pitts, B. J., F. E. Livingston, and H. N. Berko (1990). Ozone destruction and bromine photochemistry at ground level in the Arctic spring. *Nature,* Vol. 343, 622–625.

Fiocco, G., D. Fua, and G. Visconti (1996). The Mount Pinatubo Eruption. *NATO ASI Series I,* Vol. 42, Springer Berlin.

Fitzenberger, R., H. Bösch, C. Camy-Peyret, M. Chipperfield, H. Harder, U. Platt, B.-M. Sinnhuber, T. Wagner, and K. Pfeilsticker (2000). First profile measurement of tropospheric BrO. *Geophys. Res. Lett.,* Vol. 27, 2921–2924.

Francis, P., M. R. Burton, and C. Oppenheimer (1998). Remote measurements of volcanic gas composition by solar occultation spectroscopy. *Nature,* Vol. 396, 567–570.

Frank, H. (1991). *Ein Strahlungstransportmodell zur Interpretation von spektroskopischen Spurenstoffmessungen in der Erdatmosphäre.* Diploma thesis, University of Heidelberg.

Friedl, R. R., W. H. Brune, and J. G. Anderson (1985). Kinetics of SH with NO_2, O_3, O_2 and H_2O_2. *J. Phys. Chem,* Vol. 89, 5505 – 5510.

Friend, J. P. (1973). *The global sulfur cycle, in Chemistry of the Lower Atmosphere.* edited by S. I. Rasool.

Galle, B., N. Bobrowski, S. Carn, J. Durieux, M. Johansson, M. Kasereka, C. Oppenheimer, M. Yalire, and Y. Zhang (2005). Gas emissions from Nyiragongo volcano D. R. of Congo, measured by UV mini-DOAS spectroscopy. *EGU, Vienna,* Vol. 0, 0.

Gerlach, T. (2004). Volcanic sources of tropospheric ozone-depleting trace gases. *Geochem. Geophys. Geosys.,* Vol. 5, No. Q09007, doi:10.1029/2004GC000747.

Gerlach, T. M. (1991). Present day CO_2 emissions from volcanoes. *EOS Transaction AGU,* Vol. 72, 254–255.

Graf, H.-F., J. Feichter, and B. Langmann (1997). Volcanic sulfur emissions: Estimates of source strength and its contribution to the global sulfate distribution. *Journal of Geophysical Research,* Vol. 102, 10727–10738.

Grainger, J. and J. Ring (1962). Anomalous Fraunhofer line profiles. *Nature,* Vol. 193, 762.

Granat, L., H. Rodhe, and R. O. Hallberg (1976). The global sulphur cycle, in Nitrogen, Phosphorous and Sulphur-Global Cycles. *SCOPE Report 7, Ecological Bulletin,* Vol. 22, 89–134.

Greenblatt, G. D., J. J. Orlando, J. B. Burkholder, and A. R. Ravishankara (1990). Absorption Measurements of Oxygen between 330 and 1140 nm. *J. Geophys. Res.,* Vol. 95, 18577–18582.

Gribble, G. (2003). The diversity of naturally produced organohalogens. *Chemosphere,* Vol. 52(2), 289–297.

Gschwandtner, G., K. Gschwandtner, K. Eldridge, C. Mann, and D. Mobly (1986). Historic emissions ofsulfur and nitrogen oxides from 1900 to 1980. *JAPCA,* Vol. 36, 139.

Halmer, M., H. U. Schmincke, and H. F. Graf (2002). The annual volcanic gas input into the atmosphere, in particular into the stratosphere: A global data set of the past 100 years. *J. Volc. Geotherm. Res.,* Vol. 115, 511–528.

Harder, H., C. Camy-Peyret, F. Ferlemann, R. Fitzenberger, T. Hawat, H. Osterkamp, M. Schneider, D. Perner, U. Platt, P. Vradelis, and K. Pfeilsticker (1998). Stratospheric BrO profiles measured at different latitudes and seasons: Atmospheric observations. *Geophys. Res. Lett.,* Vol. 25, 3843–3846.

Hausmann, M. and U. Platt (1994). Spectroscopic measurement of bromine oxide and ozone in the high Arctic during Polar Sunrise Experiments 1992. *J. Geophys. Res.,* Vol. 99, 25399–25413.

Hebestreit, K. (2001). *Halogen Oxides in the Mid-Latitudinal Planetary Boundary Layer*. Dissertation, Institute für Umweltphysik, University of Heidelberg.

Hebestreit, K., J. Stutz, D. Rosen, V. Matveiv, M. Peleg, M. Luria, and U. Platt (1999). DOAS Mesurements of Tropospheric Bromine Oxide in Mid-Latitudes. *Science,* Vol. 283, 55–57.

Hermans, C., A. C. Vandaele, M. Carleer, S. Fally, R. Colin, A. Jenouvrier, B. Coquart, and M.-F. Mérienne (1999). Absorption Cross-Sections of Atmospheric Constituents: NO_2, O_2, and H_2O. *Environ. Sci. & Pollut. Res.,* Vol. 6, No. 3, 151–158.

Hoff, R. and M. Millán (1981). Remote SO_2 mass flux measurements using COSPEC. *JAPCA,* Vol. 31, 381–384.

Holland, H. D. (1978). *The Chemistry of the Atmosphere and Ocean*. New Yorck: Wiley-Interscience.

Hollwedel, J. (2005). *Observation of Tropospheric and Stratospheric Bromine Monoxide from Satelites*. Dissertation, Institute für Umweltphysik, University of Heidelberg.

Hönninger, G. (2002). *Halogen Oxide Studies in the Boundary layer by Multi Axis Differential Optical Absorption Spectroscopy and Active longpath-DOAS*. Phd thesis, Heidelberg University, Germany.

Hönninger, G., N. Bobrowski, E. Palenque, R. Torrez, and U. Platt (2004). Reactive bromine and sulfur emissions at Salar de Uyuni, Bolivia. *Geophysical Research Letters,* Vol. 31, L04101, doi:10.1029/2003GL018818.

Hönninger, G., C. von Friedeburg, and U. Platt (2004). Multi Axis Differential Optical Absorption Spectroscopy. *Atmospheric Chemistry and Physiks,*, 231–254.

Hönninger, G., C. von Friedeburg, and U. Platt (2004). Multi Axis Differential Optical Absorption Spectrospcopy (MAX-DOAS). *Atmospheric Chemistry and Physics,* Vol. 4, 231–254.

Huppert, R. (2000). *Theoretische und experimentelle Untersuchungen zum solaren I_0 Effekt*. Diploma thesis, Institut für Umweltphysik, Universität Heidelberg.

Janssen (1986). Sur le spectres d'absorption de l'oxygene. *Compte Rend.,* Vol. 102, 1352–1353.

Johnston, P. (1996). Making UV/Vis cross sections reference fraunhofer and synthetic spectra. unpublished manuscript.

Jordan, A. (2003). *Volcanic Formation of Halogenated Organic Compounds, in The Handbook of Environmental Chemistry*. Berlin-Heidelberg: Springer Verlag.

Kaiser, N. (1997). *Off-axis-Messungen von troposphärischen NO_3*. Diploma thesis, Institut für Umweltphysik, Universität Heidelberg.

Kellogg, W. W., R. D. Cadle, E. R. Allen, A. L. Lazrus, and E. A. Martell (1972). The sulfur cycle. *Science,* Vol. 175, 587–596.

Kirchner, U., T. Benter, and R. N. Schindler (1997). Experimental verification of gas phase bromine enrichment in reactions of HOBr with sea salt doped ice surfaces. *Ber. Bunsenges. Phys. Chem.,* Vol. 101, 975–977.

Kraus, S. (2001). *The DOASIS software*, Chapter Presentation at the 1^{st} international DOAS Workshop. Heidelberg.

Kritten, L. (2004). *Messung von Vulkangasen mit Multi-AXis DOAS am Kilauea*. Diploma thesis, Institut für Umweltphysik, Universität Heidelberg.

Kühl, S. (2005). *Quantifying Stratospheric Chlorine Chemistry by the Satellite Spectrometers GOME and SCIAMACHY*. Dissertation, Institut für Umweltphysik, Universität Heidelberg.

Lambert, G., M.-F. L. Cloarec, and M. Pennisi (1988). Volcanic output of SO2 and trace metals: A new approach. *Geochimica et Cosmochimica Acta,* Vol. 52, 39–42.

Le Guern, F. (1982). Es dèbits de CO_2 et de SO_2 volcaniques dans l'atmosphère. *L. Bulletin of Volcanology,* Vol. 45, 197–202.

LeBras, G. and U. Platt (1995). A possible mechanism for combined chlorine and bromine catalyzed destruction of tropospheric ozone in the arctic. *Geophys. Res. Lett.,* Vol. 22, 599–602.

Lee, C., H. Tanimoto, N. Bobrowski, U. Platt, T. Mori, K. Yamamoto, and Y. J. Kim (2005). Detection of halogen oxides in a volcanic plume and observation of surface ozone depletion. *GRL,*, in review.

Lelieveld, J., G.-J. Roelofs, L. Ganzeveld, J. Feichter, and H. Rodhe (1997). Terrestrial sources and distribution of atmospheric sulphur. *Phil. Trans. R. Soc. Lond.,* Vol. B 352 (1350), 149–158.

Leser, H. (2001). *Untersuchung troposphärischer Spurenstoffe mit Multiaxialer Differentieller Optischer Absorptionsspektroskopie von gestreutem Sonnenlicht (MAX-DOAS)*. Diploma thesis, Institut für Umweltphysik, Universität Heidelberg.

Lindberg, S. E., S. Brooks, C.-J. Lin, K. J. Scott, M. S. Landis, R. K. Stevens, M. Goodsite, and A.Richter (2002). Dynamic oxidation of gaseous mercury in the Arctic troposphere at Polar sunrise. *Environ. Sci. Technol.,* Vol. 36, 1245–1256.

Lohberger, F. (2003). *Abbildende Spektroskopie Atmosphärischer Spurenstoffe.* Diploma thesis, Institut für Umweltphysik, Universität Heidelberg.

Lohberger, F., G. Hönninger, and U. Platt (2004). Ground based Imaging Differential Optical Absorption Spectroscopy of Atmospheric Gases. *Applied Optics,* Vol. 43, No. 24, 4711–4717.

Lohmann, U. and J. Feichter (2005). Global indirect aerosol effects: a review. *ACP,* Vol. 5, 715–737.

Louban, I. (2005). *Zweidimensionale Spektroskopische Aufnahme von Spurenstoffverteilungen.* Diploma thesis, University of Heidelberg.

Lovelock, J. E., R. J. Maggs, and R. A. Rasmussen (1972). Atmospheric dimethyl sulfide and the natural sulphur cycle. *Nature,* Vol. 237, 452–453.

Martinez, M., T. Arnold, and D. Perner (1999). The role of bromine and chlorine chemistry for arctic ozone depletion events in Ny Ålesund and comparison with model calculations. *Ann. Geophys.,* Vol. 17, 941–956.

Matsuo, S. (1975). Chemistry of volcanic gases. *Bull. Volcanol. Soc. Jpn,* Vol. 20, 319–329.

Matveev, V., M. Peleg, D. Rosen, D. S. Tov-Alper, K. Hebestreit, J. Stutz, U. Platt, D. Blake, and M. Luria (2001). Bromine oxide - ozone interaction over the Dead Sea. *J. Geophys. Res.,* Vol. 106, No. D10, 10375–10387.

McFiggans, G., J. M. C. Plane, B. J. Allan, and L. J. Carpenter (2000). A modeling study of iodine chemistry in the marine boundary layer. *J. Geophys. Res.,* Vol. 105, 14371–14385.

McGonigle, A., P. Delmelle, C. Oppenheimer, V. I. Tsanev, T. Delfosse, H. Horton, and G. Williams-Jones (2004). SO2 depletion in tropospheric volcanic plumes. *Geophysical Research Letters,* Vol. 31, L13201, doi:10.1029/2004GL019990.

McGonigle, A., C. Oppenheimer, A. R. Hayes, B. Galle, M. Edmonds, T. Caltabiano, G. Salerno, M. Burton, and T. A. Mather (2003). Sulphur dioxide fluxes from Mount Etna, Vulcano, and Stromboli measured with an automated scanning ultraviolet spectrometer. *Journal of Geophysical Research-Solid Earth,* Vol. 108 (B9), doi:10.1029/2002JB002261.

McGonigle, A. J. S., D. R. Hilton, T. P. Fischer, and C. Oppenheimer (2005). Plume velocity determination for volcanic SO2 flux measurements. *Geophys. Res. Lett.,* Vol. 32, L11302, doi:10.1029/2005GL022470.

Meller, R. and G. K. Moortgat (2000). Temperature dependence of the absorption cross sections of formaldehyde between 223 and 323 K in the wavelength range 225-375 nm. *JGR,* Vol. 105 (D6), 7089–7101.

Mellouki, A., R. Talukdar, A.-M. Schmoltner, T. Gierczak, M. Mills, S. Solomon, and A. Ravishankara (1992). Atmospheric lifetimes and ozone depletions potential of

methyl bromine (CH_3Br) and dibromethane (CH_2Br_2). *Geophysical Research Letters,* Vol. 19, 2059–2062.

Millán, M., S. Townsend, and J. Davies (1969). *Study of the Barringer refractor plate correlation spectrometer as a remote sensing instrument.* Utias rpt. 146, m.a.sc. thesis, University of Toronto, Toronto, Ontario, Canada.

Moortgat, G. K., R. Meller, and W. Schneider (1993). Temperature dependence (256-296K) of the absorption cross-sections of bromoform in the wavelength range 285-360nm. In H. Niki and R. Becker (Eds.), *The Tropospheric Chemistry of Ozone in the Polar Regions*, pp. 359–370. Springer-Verlag, New York.

Mount, G., R. Sanders, A. Schmeltekopf, and S. Solomon (1987). Visible spectroscopy at McMurdo Station, Antarctica, 1. Overview and daily variations of NO_2 and O_3, austral spring, 1986. *Journal of Geophysical Research,* Vol. 92, 8320–8328.

Mozurkewich, M. (1995). Mechanisms for the release of halogen atom sea-salt particles by free radical reactions. *Journal of Geophysical Research,* Vol. 100, 14199–14207.

Mylona, S. (1996). Sulphur dioxide emission in Europe 1880-1991 and the effect on sulphur concentration and deposition. *Tellus,* Vol. 48B, 662–689.

Notsu, K., T. Mori, G. Igarashi, Y. Tohjima, and H. Wakita (1993). Infrared spectral radiometer: A new tool for remote measurement of SO_2 of volcanic gas. *Geochemical Journal,* Vol. 27, 361–366.

Oman, L., A. Robock, G. Stenchikov, G. A. Schmidt, and R. Ruedy (2005). Climatic response to high-latitude volcanic eruptions. *J. Geophys. Res.,* Vol. 110 (D13103), doi:10.1029/2004JD005487.

Oppenheimer, C., D. M. Pyle, and J. Barclay (2003). *Volcanic Degassing.* London: Geological Society, London, Special Publication.

Oppenheimer, C., V. I. Tsanev, C. F. Braban, R. A. Cox, J. W. Adams, A. Aiuppa, N. Bobrowski, P. Delmelle, J. Barclay, and A. J. McGonigle (2005). BrO formation in volcanic plumes. *Science,*, submitted.

Oum, K. W., M. J. Lakin, and B. J. Finlayson-Pitts (1998). Bromine activation in the troposphere by the dark reaction of O_3 with seawater ice. *Geophys. Res. Lett.,* Vol. 25, No. 21, 3923–3926.

Papp, S. (2004). *Aufbau eines Versuchs im Rahmen des F-Praktikums zur atmosphärischen Spurenstoffanalyse mittels der MAX - DOAS Methode und Ausarbeitung einer zugehörigen Dokumentation.* Diploma thesis, Institut für Umweltphysik, Universität Heidelberg.

Perner, D. and U. Platt (1980). Absorption of Light in the Atmosphere by Collision Pairs of Oxygen $(O_2)_2$. *Geophys. Res. Lett.,* Vol. 7, 1053–1056.

Peters, C. (2005). *Studies of Reactive Halogen Species (RHS)in the Marine and mid-Latitudinal Boundary Layer by Active Longpath Differential Optical Absorption Spectroscopy.* Phd thesis, Heidelberg University, Germany.

Pfeilsticker, K., D. Arlander, J.-P. Burrows, F. Erle, M. Gil, F. Goutail, C. Hermans, J.-C. Lambert, U. Platt, J.-P. Pommereau, A. Richter, A. Sarkissian, M. Van Roozendael, T. Wagner, and T. Winterrath (1999). Intercomparison of the influence of

tropospheric clouds on UV-visible absorption detected during the NDSC intercomparison campaign at OHP in June 1996. *Geophysical Research Letters,* Vol. 26, 1169–1173.

Pfeilsticker, K., F. Erle, O. Funk, L. Marquard, T. Wagner, and U. Platt (1998). Optical path modifications due to tropospheric clouds: Implications for zenith sky measurements of stratospheric gases. *Journal of Geophysical Research,* Vol. 103, 25323–25335.

Pinto, J. P., R. P. Turco, and O. B. Toon (1989). Self-Limiting Physical and Chemical Effects in Volcanic Eruption Clouds. *J. Geophys. Res.,* Vol. 94, 11165–11174.

Platt, U. (1994). Differential Optical Absorption Spectroscopy (DOAS). In M. W. Sigrist (Ed.), *Monitoring by Spectroscopic Techniques*. New York: John Wiley & Sons, Inc.

Platt, U. and G. Hönninger (2003). The role of halogen species in the troposphere. *Chemosphere, 52, 325-338,* Vol. 52, 325–338.

Platt, U. and E. Lehrer (1997). *Arctic Tropospheric Ozone Chemistry, ARCTOC, Final Report of the EU-Project No. EV5V-CT93-0318, Heidelberg.*

Platt, U., L. Marquard, T. Wagner, and D. Perner (1997). Corrections for Zenith Scattered Light DOAS. *Geophys. Res. Letters,* Vol. 24, No. 14, 1759–1762.

Platt, U. and D. Perner (1983). Measurements of Atmospheric Trace Gases by Long Path Differential UV/visible Absorption Spectroscopy. In D. K. Killinger and A. Mooradian (Eds.), *Optical and Laser Remote Sensing*, pp. 95–105. New York: Springer Verlag.

Platt, U., D. Perner, and H. W. Pätz (1979). Simultaneous Measurement of Atmospheric CH_2O, O_3 and NO_2 by Differential Optical Absorption. *J. Geophys. Res.,* Vol. 84, 6329–6335.

Platt, U. and J. Stutz (1998). *HALOTROP, Results from field, laboratory and modelling studies, Final Report of the EU-Project ENV4-CT95-0019-PL950049, Heidelberg.*

Pyle, D. M. and T. A. Mather (2003). The importance of volcanic emissions for te global atmospheric mercury cycle. *Atmospheric Environment,* Vol. 37, 5115–5124.

Rasch, P. J., M. C. Barth, J. T. Kiehl, S. E. Schwartz, and C. M. Benkovitz (2000). A description of the global sulfur cycle and its controlling processes in the National Center for Atmospheric Research Community Climate Model, Version 3. *J. Geophys. Res.,* Vol. 105 (D1), 1367–1386.

Reifenhäuser, W. and K. G. Heumann (1992). Determinations of methyl iodide in the Antarctic atmosphere and the south polar sea. *Atm. Env.,* Vol. 26a, 2905–2912.

Richter, A., F. Wittrock, M. Eisinger, and J. Burrows (1998). GOME Observations of Tropospheric BrO in Northern Hemispheric Spring and Summer 1997. *Geophys. Res. Lett.,* Vol. 25, 2683–2686.

Robock, A. (2000). Volcanic eruptions and climate. *Rev. Geophys.,* Vol. 38, 191–219.

Rodgers, C. D. (1976). Retrievel of atmospheric temperature and composition from remote measurements of thermal radiation. *Rev. Geophys. and Space Phys.,* Vol. 14, 609–624.

Roozendael, M. V. and C. Fayt (2001). WinDOAS 2.1. Software User Manuel.

Rothman, L. I., C. P. Rinsland, A. Goldman, S. T. Massie, D. P. Edwards, J.-M. Flaud, A. Perrin, C. Camy-Peyret, V. Dana, J.-Y. Mandin, J. Schroeder, A. McCann, R. R. Gamache, R. B. Watson, K. Yoshino, K. V. Chance, K. W. Jucks, L. R. Brown, V. Nemtchinov, and P. Varanasi (1996). The HITRAN molecular spectroscopic database HAWKS (HITRAN AtmosphericWorkstation). *J. Quant. Spectr. Rad. Transf.,* Vol. 60, 665–710.

Rowley, D. M., W. J. Bloss, R. A. Cox, and R. L. Jones (2001). Kinetics and Products of the IO+BrO Reaction. *J. of Phys. Chem. A,* Vol. 105, 7855–7864.

Sachs, P. M. and H. F. Graf (1998). *Die Rolle der Vulkane*. warnsignal Klima Wiss. Auswert., GEO, Hamburg: In Lozan, J. L., H. Gral, P. Hupfer.

Sander, R. and P. J. Crutzen (1996). Model study indicating halogen activation and ozone destruction in polluted air masses transported to the sea. *J. Geophys. Res.,* Vol. 101, 522–532.

Sander, S., R. R. Friedl, W. B. DeMore, G. D. M., M. J. Kurlo, H. R. F., R. E. Huie, G. K. Moortgat, A. R. Ravishank, C. E. Kolb, and M. M. J. (2000). Chemical Kinetics and Photochemical Data for Use in Stratospheric Modeling. *Technical Report JPL Publication 00-3,.Jet Propulsion Laboratory, Pasadena, CA.,.*

Sanders, R. W., S. Solomon, J. P. Smith, L. Perliski, H. L. Miller, G. H. Mount, J. G. Keys, and A. L. Schmeltekopf (1993). Visible and Near-Ultraviolet Spectroscopy at McMurdo Station Antarctica, 9. Obeservations of OClO from April to October 1991. *J. Geophys. Res.,* Vol. 98, No. D4, 7219–7228.

Schall, C. and K. Heumann (1993). GC determination of volatile organoiodine and organobromine compounds in seawater and air samples. *Fresenius Z. Anal. Chem.,* Vol. 346, 717–722.

Schmincke, H. U. (2004). *Volcanism*. Heidelberg: Springer.

Schroeder, W. H., K. G. Anlauf, L. A. Barrie, J. Y. Lu, A. Steffen, D. R. Schneeberger, and T. Berg (1998). Arctic springtime depletion of mercury. *Nature,* , No. 394, 331–332.

Schwandner, F. M., T. M. Seward, A. P. Gize, P. A. Hall, and V. J. Dietrich (2004). Diffuse emission of organic trace gases from the flank and crater of a quiescent active volcano (Vulcano, Aeolian Islands, Italy). *J. Geophys. Res.,* Vol. 109, doi:10.1029/2003JD003890.

Schwartz, S. E. (1988). Are global cloud albedo and climate controlled by marine phytoplankton? *Nature,* Vol. 336, 441.

Sebastian, O. (2004). *The relative contribution of free radicals to the oxidation chain of Dimethylsulphide in the marine boundary layer*. Ph.d. thesis, Institute for Environmental Physics, University of Heidelberg.

Seinfeld, J. H. and S. N. Pandis (1998). *Atmospheric Chemistry and Physics*. New Yorck, Chichester, Weinheim: Wiley.

Seisel, S. and M. Rossi (1997). The heterogeneous Reaction of HONO and HBr on Ice and on Sulfuric Acid. *Ber. Bunsenges. Phys. Chem.,* Vol. 101, 943.

Shanaka, L. d. S. and P. Francis (1991). *Volcanoes of the Central Andes*. Heidelberg: Springer Verlag.

Sigurdssun, H. (2000). *Encyclopedia of Volcanoes*. San Diego, San Francisco, New Yorck, Boston, London, Sydney, Toronto: Academic Press.

Simpson, W. R., L. Alvarez-Aviles, T. A. Douglas, M. Sturm, and F. Domine (2005). Halogens in the coastal snow pack near Barrow, Alaska: Evodence for active bromine in air-snow chemistry during springtime. *GRL,* Vol. 32, L04811, doi: 10.1029/2004GL021748.

Sinreich, R. (2003). *Höhenprofilmessung von NO_2 mit Multi-Axis-DOAS in Heidelberg*. Diploma thesis, Institute for Environmental Physics, University of Heidelberg.

Smith, J. and S. Solomon (1990). Atmospheric NO_3: 3. Sunrise Disappearance and the Stratospheric Profile. *J. Geophys. Res.,* Vol. 95, No. D9, 13819–13827.

Smith, J., S. Solomon, R. Sanders, H. Miller, L. Perliski, J. Keys, and A. Schmeltekopf (1993). Atmospheric NO_3: 4. Vertical Profiles at Middle and Polar Latitudes at Sunrise. *J. Geophys. Res.,* Vol. 98, No. D5, 8983–8989.

Solomon, S., A. Schmeltekopf, and R. Sanders (1987). On the interpretation of zenith sky absorption measurements. *Journal of Geophysical Research,* Vol. 92, 8311–8319.

Stachnik, R. A. and M. Molina (1987). Kinetics of the reactions of SH radicals with NO_2 and O_2. *J. Phys. Chem,* Vol. 91, 4603–4606.

Stoiber, R. and A. Jepsen (1973a). Sulfur dioxide contribution to the atmosphere by volcanoes. *Science,* Vol. 182, 577–578.

Stoiber, R. E. and A. Jepsen (1973b). Sulfur dioxide contributions to the atmosphere by volcanoes. *Science,* Vol. 182, 577–578.

Stoiber, R. E., S. N. Williams, and B. Huebert (1987). Annual contribution of sulfur dioxide to the atmosphere by volcanoes. *Journal of Volcanology and Geothermal Research,* Vol. 33, 1–8.

Stoiber, R. E., S. N. Williams, and B. J. Huebert (1986). Sulfur and halogen gases at Masaya caldera complex, Nicaragua: Total flux and variations with time. *Journal of Geophysical Research,* Vol. 91:B12, 1221–12231.

Stutz, J. (1996). *Messung der Konzentration troposhärischer Spurenstoffe mittels Differentieller-Optischer-AbsorptionsSpektroskopie: Eine neue Generation von Geräten und Algorithmen*. Ph. D. thesis, Institut für Umweltphysik, Ruprecht-Karls-Universität Heidelberg. D455.

Stutz, J., K. Hebestreit, B. Alicke, and U. Platt (1999). Chemistry of halogen oxides in the troposphere: comparison of model calculations with recent field data. *J. Atmos. Chem.,* Vol. 34, 65–68.

Sugiura, T. and S. O. Y. Mizutani (1963). Fluorine, chlorine and iodine in volcanic gases. *J. Earth Sci. Nagoya Univ.,* Vol. 11, 272–278.

Symonds, R. B., W. I. Rose, and M. H. Reed (1988). Contribution of Cl- and F-bearing gases to the atmosphere by volcanoes. *Nature,* Vol. 334, 415–418.

Tabazadeh, A., K. Drdla, M. R. Schoeberl, P. Hamill, and O. B. Toon (2002). From the Cover: Arctic "ozone hole" in a cold volcanic stratosphere. *PNAS,* Vol. 99, 2609 – 2612.

Textor, C., H. F. Graf, C. Timmreck, and R. A. (2004). *Emissions of Atmospheric Trace Compounds*, Chapter Emissions from volcanoes, pp. 269–303. Claire Grainer, Paulo Artaxo, and Claire Reeves, Eds. (Kluwer Dordrecht).

Thomas, V., J. Bedford, and R. Cicerone (1997). Bromine emissions from leaded gasoline. *Geophys. Res. Lett.,* Vol. 24, No. 11, 1371–1374.

Toumi, R. (1994). *BrO* as a sink for dimethylsulfide in the marine atmosphere. *Geophys. Res. Lett.,* Vol. 21, 117–120.

Tuckermann, M., R. Ackermann, C. Gölz, H. Lorenzen-Schmidt, T. Senne, J. Stutz, B. Trost, W. Unold, and U. Platt (1997). DOAS-observation of halogen radical-catalysed Arctic boundary layer ozone destruction during the ARCTOC campaign 1995 and 1996 in Ny-Alesund, Spitsbergen. *Tellus,* Vol. 49b, 533–555.

Turner, S. M. and P. S. Liss (1985). Measurements of various sulphur gases in a coastal marine environment. *J. Atmos. Chem,* Vol. 2, 223–232.

Van Roozendael, M., D. W. Arlander, J. Burrows, M. Chipperfield, C. Fayt, F. Hendrick, C. Hermans, P. Johnston, R. Jones, K. Kreher, J.-C. Lambert, N. Tahrin, D. Newnham, K. Pfeilsticker, U. Platt, J.-P. Pommereau, I. Pundt, A. Richter, B. Sinnhuber, A. South, K. Tørnkvist, and T. Wagner (2000). Lessons learned from 2 years of coordinated multi-platform UV-visible observations of atmospheric bromine monoxide. *Proceedings of the Quadrennial Ozone Symposium, Hokkaido University, Sapporo, Japan,*, 157–158.

Vandaele, A. C., T. C. Simon, J. M. Goilmont, C. M. Carleer, and R. Colin (1994). SO_2 Absorption Cross Section Measurement in the UV using Fourier Transform Spectrometer. *J. Geophys. Res.,* Vol. 99, 25599–25605.

Villemant, B. and G. Boudon (1999). H2O and halogen (F, Br, Cl) behaviour during shallow magma degassing process. *EPSL,* Vol. 168, 271–286.

Vogt, R., P. J. Crutzen, and R. Sander (1996). A mechanism for halogen release from sea-salt aerosol in the remote marine boundary layer. *Nature,* Vol. 383, 327–330.

Vogt, R., R. Sander, R. von Glasow, and P. J. Crutzen (1999). Iodine chemistry and its role in halogen activation and ozone loss in the marine boundary layer: a model study. *J. Atmos. Chem.,* Vol. 32, 375–395.

Voigt, S., J. Orphal, and J. P. Burrows (1999). UV-visible absorption cross-sections of NO_2 and O_3 at atmospheric temperatures and pressures by FTS. In *Proc. of the 1st Europ. Symp. Atmos. Meas. from Space (ESAMS-99), ESA-ESTEC, Noordwijk, The Netherlands, ESA WPP-161*, Volume 2, pp. 443–465.

von Friedeburg, C. (2003). *Derivation of Trace Gas Information combining Differential Optical Absorption Spectroscopy with Radiative Transfer Modelling.* Dissertation, Universit"at Heidelberg.

von Friedeburg, C., T. W. A. Geyer, N. Kaiser, B. Vogel, H. Vogel, and U. Platt (2002). Derivation of Tropospheric NO_3 Profiles Using Off-axis-DOAS Measure-

ments During Sunrise and Comparison with Simulations. *J. Geophys. Res.,*, doi:10.1029/2001JD000481.

von Glasow, R. and P. Crutzen (2003). Tropospheric Halogen Chemistry. In R. Keeling, H. Holland, and K. Turekion (Eds.), *Treatise on Geochemistry - Vol. 4 The Atmosphere*, pp. 21–64. Oxford: Elsevier/Pergamon.

Wagner, T. (1999). *Satellite observations of atmospheric halogen oxides*. Ph. D. thesis, University of Heidelberg, Heidelberg, Germany.

Wagner, T., B. Dix, C. v. Friedeburg, U. Frieß, S. Sanghavi, R. Sinreich, and U. Platt (2004). MAX-DOAS O4 measurements a new technique to derive information on atmospheric aerosols. (I) Principles and information content. *Journal of Geophysical Research,* Vol. 109, D22205, doi:10.1029/2004JD004904.

Wagner, T., C. Leue, M. Wenig, K. Pfeilsticker, and U. Platt (2001). Spatial and temporal distribution of enhanced boundary layer BrO concentrations measured by the GOME instrument aboard ERS-2. *J. Geophys. Res.,* Vol. 106, No. D20, 24225–24235.

Wagner, T. and U. Platt (1998). Satellite mapping of enhanced BrO concentrations in the troposphere. *Nature,* Vol. 395, 486.

Wardell, L. J., A. Peterson, J. Stix, and A. McGonigle (2004). Trace Element Flux Values from the Gas Plume of Masaya Volcano, Nicaragua. *AGU conference, Spring meeting in Montreal,*.

Watts, S. (2000). The mass budgets of carbonyl sulfide, dimethyl sulfide, carbon disulfide and hydrogen sulfide. *Atmos. Environ.,* Vol. 34 (5), 761–779.

Wayne, R., G. Poulet, P. Biggs, J. Burrows, R. Cox, P. Crutzen, G. Haymann, M. Jenkin, G. L. Bras, G. Moortgat, U. Platt, and R. Schindler (1995). Halogen oxides: radicals, sources and reservoirs in the laboratory and in the atmosphere. *Atmos. Environ., Special Issue,* Vol. 29, 2675 – 2884.

Weaver, A., S. Solomon, R. W. Sanders, K. Arpag, and H. L. Miller (1996). Atmospheric NO_3 5. Off-axis measuements at sunrise: Estimates of tropospheric NO_3 at 40°N. *J. Geophys. Res.,* Vol. 101, No. D13, 18605–18612.

Wennberg, P. (1999). Bromine explosion. *Nature,* Vol. 397, 299–300.

Williams, H. and A. R. McBirney (1983). *Volcanology*. San Francisco: Freeman, Cooper and Company.

Williams, S. N. (1983). *Geology and eruptive mechanisms of Masaya Caldera complex, Nicaragua*. Dissertation, Dartmouth College, United States.

Wilmouth, D. M., T. F. Hanisco, N. M. Donahue, and J. G. Anderson (1999). Fourier transform ultraviolet spectroscopy of the $A^2\Pi_{3/2} \leftarrow X^2\Pi_{3/2}$ transition of BrO. *J. Phys. Chem.,* Vol. 103, 8935–8945.

Witter, J., C. V. Kress, P. Delmelle, and T. G. Hersum (2001). Acid Gas Emissions Measured by COSPEC, Volatile Trap, and Filter Pack at Volcan Villarrica, South Chile. *AGU Fall Meeting,*.

Wofsy, S. C., M. B. McElroy, and L. Y. Yung (1975). The chemistry of atmospheric of atmospheric bromine. *Geophys. Res. Lett.,* Vol. 2, 215–218.

Woods, D., R. L. Chuan, and W. I. Rose (1985). Halite particles injected into the stratosphere by the 1982 El Chichon eruption. *Science,* Vol. 230, 170–172.

Yang, Q., P. A. Mayewski, G. A. Zielinski, and M. Twickler (1996). Depletion of atmospheric nitrate and chloride as a consequence of the Toba volcanic eruption. *Geophys. Res. Lett.,* Vol. 23, 2513–2516.

Yvon, S. and H. Butler (1996). An improved estimate of the oceanic lifetime of atmospheric CH_3Br. *Geophys. Res. Lett.,* Vol. 23, 53–56.

Zellner, J., H. Baumgärtel, W. Grünbein, and F. Ensel (1999). *Global Aspects of Atmospheric Chemistry.* Darmstadt: Springer.

Appendix B

Danke

Viele Menschen haben zu dieser Arbeit beigetragen, sie teilweise erst möglich gemacht, - unmöglich alle beim Namen zu nennen, aber danken möchte ich Euch trotzdem hiermit, selbst den manchmal ganz kurzen Begegnungen - manchmal war es vielleicht nur ein Lächeln was geholfen hat.

Zu allererst möchte ich Gerd danken, dem ich diese Arbeit widme und ich so sehr wünschte er könnte sie noch lesen. Schon zwei Wochen nach dem Beginn der Doktorarbeit wollte ich diese damals für beendet erklären. Es sollte nicht das einzigste mal bleiben, dass ich sehr gezweifelt habe die richtige Entscheidung getroffen zu haben, wobei es zumeist nicht an den fachlichen Problemen lag. Du warst immer erreichbar und die Diskussionen mit dir Gerd, dein Optimismus und Zuspruch waren es was mich überzeugt hat und noch heute tut die Arbeit fortzuführen.
Ich bin sehr viel gereist während der letzten drei Jahre und habe viele wundervolle Erfahrungen gesammelt auch ausserhalb der Physik, flüssiges Gestein, das durch den Erdboden bricht, Berge die in 6000 m Höhe hinaufragen, Blütenzauber aus Schwefel, Eis und Salz, etc. - nicht immer war es einfach, nicht immer Risikofrei - doch würde ich es jederzeit wieder tun. Die Teilnahme an Messkampagnen und internationalen Konferenzen hat mir ermöglicht Kontakte zu vielen Menschen zu knüpfen, die diesselbe Begeisterung für Vulkane haben und wissenschaftlichen Verbindungen sind sehr schnell entstanden und gewachsen. Möglich gemacht hat das Herr Platt und dafür ein ganz grosses und herzlichses Dankeschön, ohne ihn hätte es die Arbeit nicht gegeben. Danke für alle Unterstützung, für die Freiheit selbst entscheiden zu können und Verantwortung zu übernehmen.
Auch Herrn Mauersberger, der bereitwillig zustimmte meine Arbeit zu begutachten und sich die Zeit nahm sich auf das (für uns Atmosphärenforscher) eher ungewöhnliche Gebiet - Vulkane einzulassen, sei herzlichst gedankt.
Ein grosser Teil meiner Arbeit entstand im Rahmen des DORSIVA-Projekts. I like to thank all participants. Thanks especially to Bo for coordinating this project, thanks for sharing the fascination on volcanos, never to tired to look for the beautifulness of nature - climbing Etna at night to have a look on the red river, what could be more impressive ? Muchas Gracias - Jose, exceptionalmente para tu grande organizacion durante tiempo in Valencia y Alcaniz. Claudia, Matthias, Yan, Manne, Alexei, Johan, Vitchko, Ilia, Ossama and Wolfgang was nice to live together on Sicily. Thanks also to Lena, (even with wet

and cold Spain, I enjoyed your company in Spain), John, Jose and Jose.
In questo momento io vorrei dire molte grazie - Nuccio. Senza tu e possible io rinunciare, - molte problemi e io ho avuto no sufficiente forte. Tu tenti siempre ayuadare, grazie per non complicato appoggio in noi problemi (corrente, elettrica, posto per spectrometer....). Mt. Etna e il miglior luogo, fantastico, bellisimo e con molte forte. Ma acconto Mt. Etna grazie per tu parole e il possibilita palare con te.
To the best campaigns definitively belong the additionally campaigns in Italy autumn 2003 and summer 2004. Thanks Palermo for this possibility. Besides the scientific issue your company Greg, Dimitri, Giovanni, Andrew M., Andrew A., David, Tamsin, Ken, Martin, Manuela, Sandro, Salvo and Robertino it was great!! I wouldn't want to miss it. The adventures of flying with the helicopter, visiting the crater, seeing the sunset on the top of Stromboli,.. No other work was so much fun. Especially thank you for the organization Sandro and Salvo. The sun, the ice cream, granita ...unbelievible good. Molte grazie anche per Salvo G., Quenda, Franco, Fausto, Angela, Tomasso, Mike, Giuseppe, Filipo.
Thanks also to all participants on the IAVCEI Gasworkshop in Nicaragua/Costa Rica 2003 and Italy 2005, was great to meet you and thanks as well the participants of the IAVCEI workshop in Chile 2004 - I enjoyed it a lot. Momotombo was difficult - thanks Thor for the motivation on the last meters. Villarica, Llaima, Longymay, - my first experience with crampons and icepickel, thanks especially Nick for your help and company and Lois thanks for the time sharing in the evenings in Pucon - hot springs, chocolate fondue,...gracias Egidio para allogio y para mostri catarata, Eduardo thank you for your friendly hosting in La Paz, thanks to Marcello and Pedro - I know it was a hard trip for you as well on Ollague and cold nights, - thanks for doing this crazy adventure with me.
Vielleicht mag es erscheinen als wäre ich kaum in Heidelberg gewesen - manchmal kam es mir tatsächlich so vor. Trotz allem es gab und gibt viele Menschen die hier einfach da waren und mir wichtig sind.
Ronny, Stephen, Markward, Damian, Nadja, Damaris schade das oft zu wenig Zeit für unsere gemeinsamen Kochabende blieb in den letzten zwei Jahren. Seit wir hier zusammen angefangen haben zu studieren, haben wir vieles miteinander erlebt von dem ich nichts missen möchte, ich bin sehr froh dass wir uns schon im ersten Semester getroffen haben und hoffe Euch nie aus den Augen zu verlieren.
Meinen Mitbewohneren für die ich manchmal viel zu wenig Zeit hatte auch ein ganz ganz dickes grosses Dankeschön. Ich hätte nirgendwo anders wohnen wollen Nils, Hend, Nick, Sven und Kicki - ich werde Euch sehr vermissen.
Das Institut war mein zweites zu Hause, oft habe ich hier vermutlich die längste Zeit des Tages verbracht, dass ich gern da war lag an vielen lieben Menschen mit denen ich gerne zusammengearbeitet, zu Mittag gegessen, gequatscht oder Tee getrunken habe, vielen Dank den Satellites, Modellieren, den Balloneuren, Tropos, insbesondere auch meinen Zimmerkollegen Christian, Kai, Evelyn, Sam und auch den inzwischen Instituts ehemaligen Kai, Hansjörg, Hartmut, Oli S., Peter, Richi, Oli F., Björn, Andy and Hans - ihr alle habt für Ablenkung, Unterstützung, Kuchen und vieles andere gesorgt.
Vielen Dank auch an die Werkstatt und an die Verwaltung, ohne die vieles nicht möglich wäre, die praktischen Dinge im Leben fallen uns allen ja schon oft schwer.
Das letzte Jahr war wohl das schwerste. Tina sei an dieser Stelle besonders grosser Dank

sicher. Für Gespräche, Tee, Kaffee, Kochen - war für uns beide wohl nicht das beste Jahr und es ist schwer zu sagen welcher Monat der schlimmste war, - doch es ist einfach toll das Du da bist! Besonders in den letzten Wochen vor der Abgabe vielen Danke für's umsorgen, motivieren, da sein.
Anita - ein grosses herzliches Dankeschön, ohne Dich hätte ich nicht die Kraft gefunden nach Wien im April zu fahren oder Palermo im Mai, auch wenn es eine (zu) schwere Zeit scheint, die gemeinsame Zeit ist trotz allem auch schön/wertvoll, Frühstücken, Abendessen, gemeinsam Weinen und Lachen können, Du bist eine wundervolle Frau, kein Wunder das Gerd Dich geliebt hat.
Molte Grazie a Sicilia - voi siete fantastico amici Anna, Rosa, Nuccio, Alfia, Sandro e Egidio grazie per rinforzare, grazie per ayudarse, grazie per tutti e grazie per siete ci.
Vielen Dank an alle Korrekturleser von wenigen oder vielen Seiten meiner Arbeit, John, Barbara, Stephen, Ronny, Bill, Christoph, Tina P., Tina F., Roman, David, Frederik und Susanne.
Zu guter letzt aber nicht weniger von Herzen sei meiner Familie gedankt. Besonderen Dank an meinen Papa und meine Mama und an Dich Reni. Egal in welchem Teil der Welt ich bin, ich weiss dass Ihr da seid, danke für liebe Briefe, danke für alles Verständnis wenn ich mal wieder im Stress der Arbeit unterging.